Alma Mater Studiorum – Università di Bologna

Dottorato di Ricerca in
Fisica

Ciclo XXXII

Settore Concorsuale: 02/A1

Settore Scientifico Disciplinare: FIS/01

Higgs self-coupling measurements with the CMS detector at the LHC and at future colliders in the $\mathrm{HH} \to \mathrm{ZZ}(4\ell)\mathrm{b\bar{b}}$ decay channel

Presentata da: **Dott.ssa Lisa Borgonovi**

Coordinatore Dottorato:
Prof.ssa Silvia Arcelli

Relatore:
Prof.ssa Sylvie Braibant

Esame finale anno 2020

"Quando la tempesta sarà finita, probabilmente non saprai neanche tu come hai fatto ad attraversarla e a uscirne vivo.
Anzi, non sarai neanche sicuro se sia finita per davvero.
Ma su un punto non c'è dubbio.
Ed è che tu, uscito da quel vento, non sarai lo stesso che vi è entrato".

H. Murakami - Kafka sulla spiaggia

Sommario

Questa tesi presenta le prospettive sulla misura della produzione associata di una coppia di bosoni di Higgs (HH), sfruttando il canale di decadimento che presenta quattro leptoni e due b jet nello stato finale: $HH \to ZZ(4\ell)b\bar{b}$. La produzione HH consente un accesso diretto alla costante di accoppiamento trilineare del bosone di Higgs, la cui misura ha la duplice valenza di fornire una conferma del modello standard (SM) e sensibilità a possibili processi di fisica oltre il modello standard (BSM). Questo studio è stato effettuato in diversi scenari per quanto riguarda l'energia del centro di massa, la luminosità integrata e la configurazione degli apparati sperimentali. Partendo dallo studio dei dati di collisioni protone-protone, raccolti dal rivelatore CMS a LHC presso il CERN, ad un'energia del centro di massa di 13 TeV durante il 2018, la ricerca è stata estesa ad altri scenari sperimentali, ottenendo i risultati dell'analisi nel contesto del rivelatore CMS con gli interventi progettati in vista della fase di presa dati ad alta luminosità di LHC (HL-LHC) e alla possibile fase successiva ad alta energia (HE-LHC). Le prestazioni della stessa analisi sono dunque state studiate anche nel contesto di un futuro acceleratore adronico circolare (FCC-hh), fornendo così una panoramica unica sulla possibilità di confermare o smentire le predizioni del SM, sfruttando questo canale di decadimento. Il limite superiore sulla sezione d'urto di produzione di questo processo è di circa 230 volte il valore previsto dallo SM nel caso dell'analisi svolta sui dati raccolti nel 2018, e si abbassa a 6.5 e 1.5 volte quello previsto dallo SM rispettivamente per gli scenari di HL-LHC e HE-LHC. Per quanto riguarda invece la misura nello scenario di FCC-hh, sarà possibile raggiungere una precisione del 17% sulla misura della sezione d'urto. In aggiunta, gli effetti derivanti da processi BSM sono stati simulati e studiati per valutare la sensibilità a possibili modifiche del valore della costante di auto-accoppiamento.

Infine, dato che una parte consistente del lavoro di tesi descritto riguarda i miglioramenti che i rivelatori dovranno implementare nei prossimi anni, e progetti di futuri acceleratori, questa tesi descrive anche gli studi condotti su un innovativo rivelatore gassoso a micro-pattern, chiamato μ-RWELL,

che potrebbe essere impiegato in questi prossimi esperimenti. Sono dunque presentati studi di invecchiamento del rivelatore sfruttando una sorgente di raggi gamma, che hanno irraggiato un prototipo di μ-RWELL per capire la risposta del rivelatore quando sottoposto ad alti flussi di particelle ionizzanti, condizione prevista nei futuri esperimenti ad altissima luminosità. Inoltre, è stato eseguito un test di omogeneità su un altro prototipo di μ-RWELL con una grande superificie, per verificare la fattibilità dell'utilizzo di questi rivelatori di grandi dimensioni e la loro solidità, senza che ne siano compromesse le ottime prestazioni. Sebbene il primo test necessiti di approfondimenti per comprendere a pieno il risultato ottenuto, il secondo ha indubbiamente confermato che le prestazioni del rivelatore anche su grandi superfici non dipendono dalla posizione della particella incidente, con un'efficienza di rivelazione superiore al 97% su tutto il rivelatore.

Abstract

This thesis presents the perspectives on the Higgs boson pair production (HH) measurements in the four-lepton plus two b jets decay channel: $HH \rightarrow ZZ(4\ell)b\bar{b}$. The HH production gives a direct access to the Higgs boson trilinear self-coupling, providing confirmation to the standard model (SM) predictions and sensitivity to possible physics processes beyond the standard model (BSM). This study has been performed in different scenarios in terms of center-of-mass energy, integrated luminosity and detector layouts. Starting from proton-proton collision data collected at a center-of-mass energy of 13 TeV with the CMS detector at the CERN LHC during 2018, the search has been extended to future experimental scenarios obtained with the upgrade layout of the CMS detector for the High Luminosity (HL-LHC) and the possible subsequent High Energy (HE-LHC) phases of the LHC accelerator. The analysis has been repeated with a very high energy hadronic Future Circular Collider (FCC-hh), resulting in a unique overview of the capabilities, exploiting this channel, to confirm or disprove the SM predictions.

The upper limits on the HH production cross section range from 230 times the SM expectations for the 2018 analysis, to about 6.5 and 1.5 times for the HL- and HE-LHC scenarios, while with the FCC-hh, a 17% precision on the cross section measurement could be possible. Furthermore, BSM effects have been modeled and studied taking into consideration possible variations of the Higgs boson self-coupling.

Finally, since future upgrades of existing detectors and even future accelerator projects have been a consistent part of the work described, this thesis presents also the studies performed on innovative micropattern gaseous detectors (MPGD) called μ-RWELL, that could be suitable for these future experiments. Longevity studies exploiting a gamma source irradiating a μ-RWELL prototype have been conducted to understand the detector behavior in a high radiation environment, foreseen for future implementations in high energy physics experiments. In addition, a homogeneity test on a large area μ-RWELL prototype, to verify the feasibility and robustness of large surface detectors realized with this technology, without compromising the excellent

performances, is described. Although the first test pointed out the need of more in depth studies to understand the results obtained, the second one verified the excellent performances of this technology even in large area prototypes, since the response of the detector is proved to be independent on the position of the incident particle, and the detection efficiency is higher than 97% across all the surface of the detector.

Contents

Introduction

The discovery of the Higgs boson, announced in 2012, was an extraordinary achievement of the high energy physics community, the conclusion of several decades of extensive searches aimed at completing the standard model of particles and interactions (SM) with its last missing piece. The existence of this boson was introduced in 1964 with the BEH mechanism, as called from the names of the physicists that proposed it: R. Brout, F.Englert and P. Higgs. This mechanism postulates the presence of a complex scalar doublet field that causes a spontaneous electroweak symmetry breaking (EWSB), generating the masses of the vector bosons, mediators of the weak interaction, and providing the mass terms for the fermions.

The Large Hadron Collider (LHC) at the European Organization for Nuclear Research (CERN) was designed and realized to give a final answer about the existence of the Higgs boson, since previous experiments such as the Large Electron-Positron collider (LEP) at CERN and the Tevatron at Fermilab could only set exclusion limits to the possible Higgs boson mass. The LHC is a 27 km circumference collider designed to collide protons at a center-of-mass energy of 14 TeV in four interaction points where detectors are placed: the two multipurpose experiments, A Toroidal LHC Apparatus (ATLAS) and the Compact Muon Solenoid (CMS), and the Large Ions Collider Experiment (ALICE) and the Large Hadron Collider beauty (LHCb) for complementary specific measurements. After three years from the first collisions, started in 2009, the ATLAS and CMS Collaborations announced the discovery of a new boson, with a mass close to 125 GeV, compatible with the SM Higgs boson. In the following years, new measurements concerning the new boson spin-parity and its coupling to the other SM particles strongly indicated that the newly discovered particle was indeed the Higgs boson. Now it is fundamental to extend our knowledge on this scalar boson properties, especially for what concerns its couplings, performing studies with a large variety of production and decay modes.

The Higgs boson self-interaction is of particular interest, since it provides a unique way to directly access the trilinear Higgs coupling (or self-coupling),

and reconstruct the shape of the scalar potential, characterizing the scalar sector of the SM. However, many are the indications of physics processes beyond the standard model (BSM), from both theoretical and experimental considerations: the SM does not explain the observed matter-antimatter asymmetry, and does not provide any model for dark matter particles nor energy, for example. BSM physics could give a solution to these and other issues, still preserving the SM capability to describe the majority of the known physics processes. Being a unique particle in the SM, the Higgs boson is fundamental to investigate extensions of the SM, since BSM physics could produce effects on the coupling with anomalous effects, or manifest with the rise of new particles produced in the quantum loops responsible for the double Higgs production.

In this context, the work presented in my thesis aims at giving a prospect on the Higgs self-coupling measurements, in particular in a very rare decay process where of the two produced Higgs bosons, one decays in a pair of Z bosons, each decaying in a pair of opposite sign leptons (muons or electrons), and the other one decays in a pair of b jets: the $HH \rightarrow ZZ(4\ell)b\bar{b}$ decay channel. This decay mode is chosen for its clean final state, provided by the four isolated leptons, taking advantage of the high branching fraction of the $b\bar{b}$ decay, partially compensating for the large yield reduction brought by the 4ℓ decay. This process has been studied in different scenarios, in terms of center-of-mass energy, integrated luminosity, detector and accelerator layouts, to give an overall and unique prospect of the capability, given by this decay channel, to prove the SM prediction or give indications of BSM processes, in the short and very long term. For this reason, studies have been performed comparing the SM predictions, modeled with Monte Carlo (MC) simulated processes, to the data acquired by the CMS experiment during the last year of the so-called Run 2 data taking period(2018). Then, prospects have been studied in two different configurations foreseen for the LHC accelerator: the High Luminosity (HL-LHC) and High Energy (HE-LHC) phases, with a center-of-mass energy of 14 and 27 TeV respectively, and an estimated integrated luminosity at the end of each period of 3 and 15 ab^{-1}. Finally, the same study has been extended to a far future scenario, simulating the response of a multipurpose detector in a hadronic Future Circular Collider (FCC-hh) with a center-of-mass energy of 100 TeV and an integrated luminosity of about 30 ab^{-1} at the end of its lifespan.

The importance of increasing energy and luminosity to better access rare processes like the one described, and give reasonable indications of the validity of the SM predictions, is an evidence of the need for upgrades to existing accelerators (and detectors) and of future projects like the FCC. A research and development effort is ongoing to study new detector technologies capable

of withstanding the high radiation conditions foreseen in these future LHC and FCC environments, and cover huge surfaces with robust and affordable detectors.

One of the investigated technologies is the μ-RWELL, an innovative micropattern gaseous detector composed of a single amplification stage realized coupling a well-patterned polymide foil to the readout plane, via a resistive layer to evacuate the charge and avoid potentially damaging sparks. To verify the feasibility of large surface detectors, the work of this thesis consisted also in homogeneity studies performed on a large area μ-RWELL prototype, and longevity studies on the same type of technology, to understand the response of the detector in a high-radiation environment. Both these tests were performed at CERN, exploiting one of the SPS secondary beam lines, and the Gamma Irradiation Facility (GIF++) hosting a ^{137}Cs gamma source.

The contents of this thesis are organized as follows.

Chapter 1 introduces the theory of the SM of particles and interactions, focusing on the BEH mechanism and the double Higgs production.

Chapter 2 defines the experimental context, describing the CMS detector at LHC, but also its foreseen upgrades for the HL- and HE-LHC phases, and an introduction to the hadronic FCC collider and its associated baseline detector.

The three subsequent chapters describe my personal contribution to the topic of this thesis, that represents the main part of the research activities performed during my PhD.

In Chapter 3 the method developed for the modeling of physics processes exploited to simulate the SM expectation are described, together with the related systematic uncertainties, in all the four considered scenarios: Run 2 (2018), HL-LHC, HE-LHC and FCC-hh, together with the techniques applied for the optimized selection of the events.

In Chapter 4 the results for the $\mathrm{HH} \to \mathrm{ZZ}(4\ell)\mathrm{b\bar{b}}$ search and their interpretation are presented, in terms of signal sensitivity and limit, or precision, on the SM double Higgs production cross section.

Finally, in Chapter 5 an introduction to gaseous detectors and the state of the art on micropattern gaseous detectors is given, with a focus on the μ-RWELL technology. Moreover, the results of my research activity on longevity and homogeneity studies performed on large μ-RWELL prototypes are presented and discussed.

Chapter 1

Higgs boson pair production

The standard model of particle physics (SM) is a quantum field theory which describes three of the four known fundamental forces of the universe, the electromagnetic, weak and strong interactions, and classifies all known elementary particles. In order to include the mechanism responsible for particles to acquire mass, the theory introduces a new scalar boson, the so-called Higgs boson, and the corresponding field, responsible for the spontaneous symmetry breaking (SSB) of the electroweak theory [1, 2, 3].

In the past decades, collider experiments provided several evidences of the SM consistency through direct observation of particles predicted by the theory, among which the most famous, and long-awaited, is the discovery of the Higgs boson in 2012. However, many are the indications of missing pieces in the SM, both from the experimental and theoretical side. Beyond standard model (BSM) physics could modify the theory keeping it consistent with existing data, but at the same time addressing its deficiencies. Since BSM physics could appear in the scalar sector, the production of Higgs boson pairs is one of the best way to explore new phenomena and deviation from the SM, evaluating possible enhancement of the cross section due to additional BSM processes.

This chapter gives an overview of the theory of the SM and the symmetry breaking of the electroweak sector, describes the Higgs boson properties, focusing on the di-Higgs production as predicted by both SM and by BSM theories, and discusses the Higgs boson phenomenology at the Large Hadron Collider (LHC) at CERN.

Fermions	1st family	2nd family	3rd family	charge (e)	spin	interactions
Leptons	e	μ	τ	-1	1/2	EM + weak
	ν_e	ν_μ	ν_τ	0	1/2	weak
Quarks	u	c	t	+2/3	1/2	All
	d	s	b	-1/3	1/2	All

Table 1.1: Classification of fermions in the SM [4]

1.1 The standard model of elementary particles and interactions

Elementary particles can be divided into two categories, based on their spin: fermions and bosons.

Fermions have half-integer spin and obey to the Fermi-Dirac statistics; they consist in leptons and quarks and can be grouped in three families, each one composed of a quark doublet, a charged lepton and its associated neutrino, as shown in Table 1.1. Every fermion has a corresponding anti-particle, characterised by the same quantum numbers with opposite sign. Leptons, electron (e), muon (μ), tau (τ), and associated neutrinos (ν_e, ν_μ, ν_τ), can be found in nature as free particles, and are subjected to the electromagnetic (e, μ, τ) and weak (all) interactions. Quarks, up (u), down (d), charm (c), strange (s), top (t), bottom (b), are subjected to the electromagnetic and weak interactions, and thanks to an additional quantum number, the color, to the strong interaction; due to the characteristics of this interaction, quarks can not be found in nature as free particles but only in bound states called mesons, if composed of a pair of quark and anti-quark, or (anti-)baryons if composed of three (anti-)quarks.

Bosons have integer spin and obey to the Bose-Einstein statistics; they act as the force mediators: the massless photon (γ) for the electromagnetic interaction, three massive gauge bosons (W^+, W^- and Z) for the weak interaction, and eight massless gluons (g) for the strong interaction, as described in Table 1.2. The gravitational force is mediated by the graviton (G), but it is not described in the SM because at the scale of high energy particle physics the gravitational force can be neglected. The SM predicts the existence of an ultimate scalar boson, the Higgs boson (H), necessary for the spontaneous symmetry breaking mechanism through which fermions and massive bosons (W^+, W^- and Z) acquire mass, as will be explained in more details in what follows.

The SM is a quantum field theory (QFT) based on a gauge symmetry. Since it is a QFT, its fundamental objects are quantum fields defined in any

Guage bosons	charge (e)	spin	mass (GeV)	interaction
γ	0	1	0	EM
$W^{\pm}$	±1	1	80.4	weak
Z	0	1	91.2	weak
g	0	1	0	strong
H	0	0	125	-

Table 1.2: Classification of bosons in the SM [4]

point of the spacetime:

- fermion fields, ψ;
- electroweak boson fields, W_1, W_2, W_3, and B;
- gluon fields, G_a;
- Higgs field, ϕ.

Being a gauge symmetry instead means that the Lagrangian density ($\mathcal{L}$), usually called Lagrangian, which is the function that describes the dynamic of a quantum state and the fundamental fields, is invariant under a local symmetry. The gauge group of the SM is:

$$SU(3)_C \otimes [SU(2)_L \otimes U(1)_Y] \tag{1.1}$$

In particular, the quantum chromodynamics (QCD) which is the theory that describes the strong interaction, relies on the color group $SU(3)_C$, where the index C stands for color (red, blue, green) which is the generator of the group; the electroweak theory, which unifies the electromagnetic and weak interactions [5, 6, 7], is based on the $SU(2)_L \otimes U(1)_Y$ group: the generator of the electroweak interaction is the third component of the weak isospin, I_3, which applies to left-handed (L) fermions. In this unified theory, the generator of the electromagnetic interaction is not simply the electric charge Q but the weak hypercharge Y defined by the Gell-Mann-Nishijima relation, $Q = I_3 + \frac{1}{2}Y$

Strong interaction

QCD describes the interaction between quarks and gluons, based on the $SU(3)_C$ group. The Dirac Lagrangian of the quark fields is:

$$\mathcal{L}_{QCD} = \overline{q}_j(x)(i\gamma^\mu \partial_\mu - m)q_j(x) \tag{1.2}$$

where q_j represent the three color charges associated to the quarks: for simplicity, in the following only one color will be considered. In Eq. 1.2, the first term represents the kinetic energy of the matter field q at the space-time coordinate x, and the second term, which is bilinear in q, is proportional to the mass m of the field q; γ^μ are the Dirac matrices. The quark field transforms, under the $SU(3)_C$ group, as:

$$q(x) \rightarrow e^{i\alpha_a(x)\frac{\lambda_a}{2}} q(x) \tag{1.3}$$

where $\frac{\lambda_a}{2}$ are the Gell-Mann matrices that generate the group. The group is non-Abelian, since not all the generators of the group commute:

$$\left[\frac{\lambda_a}{2}, \frac{\lambda_b}{2}\right] = i f_{abc} \frac{\lambda_c}{2} \tag{1.4}$$

where f_{abc} are real constants called "structure contants" of the group. Since the space-time derivative $\partial_\mu q(x)$ does not transform in the same way as the quark field, the only way to keep the Lagrangian 1.2 invariant under the transformation 1.3 is to replace the derivative ∂_μ with a covariant derivative defined as:

$$\mathcal{D}_\mu = \partial_\mu + i g_s \frac{\lambda_a}{2} G^a_\mu \tag{1.5}$$

where G^a_μ, with $a = 1, ..., 8$ are eight gauge fields transforming as:

$$G^a_\mu \rightarrow G^a_\mu - \frac{1}{g_s}\partial_\mu \alpha_\mu - f_{abc} G^a_{\mu\nu} G^{\mu\nu}_a \tag{1.6}$$

Including a gauge invariant kinetic term for each of the G^a_μ field, the Lagrangian 1.2 can be re-written as:

$$\mathcal{L}_{QCD} = \overline{q}(x)(i\gamma^\mu \partial_\mu - m)q(x) - g_s\left(\overline{q}(x)\gamma^\mu \frac{\lambda_a}{2} q(x)\right) G^a_\mu - \frac{1}{4} G^a_{\mu\nu} G^{\mu\nu}_a \tag{1.7}$$

where

$$G^a_{\mu\nu} = \partial_\mu G^a_\nu - \partial_\nu G^a_\mu - g_s f_{abc} G^b_\mu G^c_\nu \tag{1.8}$$

This is the Lagrangian for interacting colored quarks q and vector gluons G_μ required to be massless for the local gauge invariance, with coupling g_s. The first term is the free Dirac Lagrangian 1.2 that describes the free propagation of quarks, the second term describes the interactions between quark and gluon fields, the last term includes the description of the free propagation of the gluon field, and introduces trilinear and quadrilinear terms corresponding to vertices with three and four gluons: this is possible since gluons carry the color charge and can interact due to the non-Abelian nature of the $SU(3)_C$ group.

Electroweak interaction

The electroweak interaction is based on the $\mathrm{SU(2)_L} \otimes \mathrm{U(1)_Y}$ gauge symmetry group and describes the electromagnetic and weak interactions. The quantum numbers associated to this group are the weak isospin $\mathrm{I_3}$ and the weak hypercharge Y. A peculiar characteristics of the electroweak theory is that parity is violated and therefore fermions with opposite chirality have different interactions. The left and right chiral component of a fermion field are defined using the operator $\gamma^5 \equiv i\gamma^0\gamma^1\gamma^2\gamma^3$: the left- and right-handed component of a field can be obtained with the operators $\frac{1-\gamma^5}{2}$ and $\frac{1+\gamma^5}{2}$ respectively. In the limit of massless particles, chirality corresponds to helicity, that is the projection of the spin vector in the direction of the momentum vector. Fields can be described by means of one left-handed doublet Ψ_L and two right-handed singlets ψ_R and ψ'_R defined as:

$$\begin{aligned} \Psi_L = \begin{pmatrix} \psi_L \\ \psi'_L \end{pmatrix} &\equiv \frac{1-\gamma^5}{2} \begin{pmatrix} \psi \\ \psi' \end{pmatrix} \\ \psi_R &\equiv \frac{1+\gamma^5}{2}\psi \\ \psi'_R &\equiv \frac{1+\gamma^5}{2}\psi' \end{aligned} \tag{1.9}$$

The Lagrangian can be written as:

$$\mathcal{L}_{EW} = i\overline{\Psi}_L\gamma^\mu\partial_\mu\Psi_L + i\overline{\psi}_R\gamma^\mu\partial_\mu\psi_R + i\overline{\psi}'_R\gamma^\mu\partial_\mu\psi'_R \tag{1.10}$$

The doublet and singlets transform under the local gauge symmetry similarly as what described for the strong interaction:

$$\begin{aligned} \Psi_L &\to e^{i\alpha_i(x)\frac{\sigma_i}{2}+i\beta(x)\frac{Y}{2}}\Psi_L \\ \psi_R &\to e^{i\beta(x)\frac{Y}{2}}\psi_R \\ \psi'_R &\to e^{i\beta(x)\frac{Y}{2}}\psi'_R \end{aligned} \tag{1.11}$$

where σ_i are the Pauli matrices that are the generators of the SU(2). To ensure the gauge invariance, the partial derivative needs to be replaced with:

$$\mathcal{D}_\mu = \partial_\mu + ig'\frac{Y}{2}B_\mu + \frac{ig}{2}W^a_\mu T_a \tag{1.12}$$

where $T_a = \frac{\sigma_a}{2}$ are the Pauli matrices for the doublet Ψ_L and 0 for the singlets ψ and ψ'. The gauge fields B_μ and W^a_μ transform as:

$$B_\mu \;\to\; B'_\mu = B_\mu - \frac{1}{g'}\partial_\mu\alpha(x); \tag{1.13}$$

$$W^a_\mu \;\to\; W'^a_\mu = W^a_\mu - \frac{1}{g}\partial_\mu\varepsilon^a(x) - \varepsilon^{abc}\varepsilon^b(x)W^c_\mu \tag{1.14}$$

where ε^{abc} is the total antisymmetric tensor which is the structure constant of the group. The connection between these two fields and the weak vector boson fields $W_\mu^\pm$ and $\mathcal{Z}_\mu$, and the photon field $\mathcal{A}_\mu$ will be explained in the next section. The Lagrangian 1.10 thus becomes:

$$\begin{aligned}
\mathcal{L}_{EW} &= i\overline{\Psi}_L\gamma^\mu\mathcal{D}_\mu\Psi_L + i\overline{\psi}_R\gamma^\mu\mathcal{D}_\mu\psi_R + i\overline{\psi}'_R\gamma^\mu\mathcal{D}_\mu\psi'_R - \frac{1}{4}W_a^{\mu\nu}W^a_{\mu\nu} - \frac{1}{4}B^{\mu\nu}B_{\mu\nu} \\
&= i\overline{\Psi}_L\gamma^\mu\partial_\mu\Psi_L + i\overline{\psi}_R\gamma^\mu\partial_\mu\psi_R + i\overline{\psi}'_R\gamma^\mu\partial_\mu\psi'_R + \\
&\quad - g\overline{\Psi}_L\gamma^\mu\frac{\sigma_a}{2}\Psi_L W^a_\mu - g'\overline{\Psi}_L\gamma^\mu\frac{Y}{2}\Psi_L B_\mu \\
&\quad - g'\overline{\psi}_R\gamma^\mu\frac{Y}{2}\psi_R B_\mu - g'\overline{\psi}'_R\gamma^\mu\frac{Y}{2}\psi'_R B_\mu \\
&\quad - \frac{1}{4}W_a^{\mu\nu}W^a_{\mu\nu} - \frac{1}{4}B^{\mu\nu}B_{\mu\nu}
\end{aligned} \tag{1.15}$$

where the kinetic terms of the gauge fields:

$$B_{\mu\nu} = \partial_\mu B_\nu - \partial_\nu B_\mu \tag{1.16}$$

$$W^a_{\mu\nu} = \partial_\mu W^a_\nu - \partial_\nu W^a_\mu - g\varepsilon^{abc}W^b_\mu W^c_\nu \tag{1.17}$$

have been added. The first three terms in Eq. 1.15 are the Dirac Lagrangian 1.10 and represent the free propagation of fermions; the fourth, fifth, sixth and seventh terms describe the interaction between fermions and the mediators of the electroweak interaction (γ, $W^\pm$ and Z); the last two terms represent the trilinear and quadrilinear interactions between the gauge bosons. No quadratic terms for the gauge fields are present, therefore they are massless and explicit mass terms would break the gauge invariance. Same goes for fermions, since their mass terms would not be invariant under the gauge transformation.

1.2 The BEH mechanism

The solution to provide mass to the mediators of the weak interaction and to fermions, keeping the mediator of the electromagnetic interaction massless, is the Brout-Englert-Higgs (BEH) mechanism, that is the spontaneous symmetry breaking (SSB) of $\mathrm{SU(2)_L}\otimes\mathrm{U(1)_Y}$ without explicit violation of the local gauge invariance. This mechanism was proposed in 1964 independently by F. Englert and R. Brout [8], P. Higgs [9], and by G. Guralnik, C. R. Hagen and T. Kibble [10, 11] to introduce fermion and vector boson masses. In 1967-1968 S. Weinberg and A. Salam formulated the electroweak theory

including the Higgs mechanism, and the theory was proved to be renormalizable in 1971 by G.'t Hooft [12]. The spontaneous symmetry breaking is realized introducing a self-interacting scalar doublet, with hypercharge Y=1:

$$\varphi = \begin{pmatrix} \varphi^a \\ \varphi^b \end{pmatrix} \tag{1.18}$$

where:

$$\varphi^a = \frac{1}{\sqrt{2}}(\varphi_1 + i\varphi_2) \tag{1.19}$$

$$\varphi^b = \frac{1}{\sqrt{2}}(\varphi_3 + i\varphi_4) \tag{1.20}$$

The corresponding Lagrangian is:

$$\mathcal{L}_{BEH} = (\mathcal{D}_\mu \varphi)^\dagger (\mathcal{D}^\mu \varphi) - V(\varphi^\dagger \varphi) \tag{1.21}$$

where the covariant derivative is defined as:

$$\mathcal{D}_\mu = \partial_\mu + \frac{ig'}{2} B_\mu \mathbb{1} + \frac{ig}{2} W_\mu^a \sigma_a \tag{1.22}$$

and the potential $V(\varphi^\dagger \varphi)$ has the same form of the Ginzburg-Landau potential in the theory of superconductivity, used as model [13]:

$$V(\varphi^\dagger \varphi) = \mu^2 \varphi^\dagger \varphi + \lambda (\varphi^\dagger \varphi)^2 \tag{1.23}$$

where μ^2 and λ are complex constants. If $\mu^2 > 0$, the potential 1.23 has a parabolic shape, with a unique minimum; however, if $\mu^2 = -|\mu^2| < 0$, the potential 1.23 has the form of the so-called "Mexican Hat". This form is due to the fact that the potential does not have a unique minimum and the ground state with $\varphi = 0$ corresponds to a local maximum of the potential, that is to an unstable equilibrium. Minima of the potential 1.23 are all doublet satisfying the condition:

$$\varphi^\dagger \varphi = -\frac{\mu^2}{2\lambda} \equiv \frac{v^2}{2} \tag{1.24}$$

obtained with $\varphi_1 = \varphi_2 = \varphi_3 = 0$ and $\varphi_3 = \sqrt{\frac{\mu^2}{2\lambda}}$, where $v = \sqrt{\frac{\mu^2}{\lambda}}$ is the vacuum expectation value (VEV) of the Higgs potential. The choice of a specific ground state is responsible for the spontaneous symmetry breaking of the Lagrangian, which still remains gauge invariant. The scalar field can be expanded around the ground state:

$$\varphi(x) = e^{i\xi_a(x)\cdot\sigma_a} \begin{pmatrix} 0 \\ v + h(x) \end{pmatrix} \tag{1.25}$$

where $\xi_a(x)$ are real fields corresponding to the so-called massless Goldstone bosons [14]. The Goldstone theorem states that the SSB of any continuous global symmetry implies the existence of as many massless spinless bosons as there are broken generators of the symmetry. The Goldstone bosons do not have a physical meaning and they can be removed with an appropriate rotation, as in this case:

$$\varphi(x) \to e^{-i\xi_a(x)\cdot\sigma_a}\varphi(x) = \begin{pmatrix} 0 \\ v + h(x) \end{pmatrix} \tag{1.26}$$

On the contrary, the scalar field $h(x)$ represents a new real massive particle, the Higgs boson (H). Defining:

$$W_\mu^\pm = \frac{1}{\sqrt{2}}(W_\mu^1 \mp W_\mu^2) \tag{1.27}$$

$$\mathcal{Z}_\mu = \cos\theta_W W_\mu^3 - \sin\theta_W B_\mu \tag{1.28}$$

$$\mathcal{A}_\mu = \sin\theta_W W_\mu^3 + \cos\theta_W B_\mu \tag{1.29}$$

where θ_W is the Weinberg angle, that is the mixing angle introduced in order to remove mixed products between W_μ^3 and B_μ ($\tan\theta_W = \frac{g'}{g}$), and substituting the covariant derivative 1.22, the Lagrangian 1.21 becomes:

$$\begin{aligned}\mathcal{L}_{BEH} = \frac{1}{2}(\partial_\mu h)(\partial^\mu h) - \frac{1}{2}(-2\mu^2)h^2 \\ + \frac{g^2v^2}{4}W_\mu^- W^{+\mu} + \frac{g^2v^2}{8\cos^2\theta_W}\mathcal{Z}_\mu\mathcal{Z}^\mu \\ + \frac{g^2v}{2}hW_\mu^- W^{+\mu} + \frac{g^2v}{4\cos^2\theta_W}h\mathcal{Z}_\mu\mathcal{Z}^\mu \\ + \frac{g^2}{4}h^2W_\mu^- W^{+\mu} + \frac{g^2}{8\cos^2\theta_W}h^2\mathcal{Z}_\mu\mathcal{Z}^\mu \\ + \frac{\mu^2}{v}h^3 + \frac{\mu^2}{4v^2}h^4 + \frac{\lambda}{4}v^4\end{aligned} \tag{1.30}$$

The Higgs mass, that appears in the first line of this equation, is not predicted by the theory, since it is directly related to μ which is an external parameter of the scalar potential. It is also clear that the Higgs boson does not couple with the massless gauge field $\mathcal{A}_\mu$ that can be identified as the photon: $m_\gamma = 0$. On the contrary, the bosons that are the weak mediators $W^\pm$ and Z, associated to the gauge fields $W_\mu^\pm$ and $\mathcal{Z}_\mu$ respectively, acquire mass:

$$m_W^2 = \frac{g^2v^2}{4} \tag{1.31}$$

$$m_Z^2 = \frac{g^2v^2}{4\cos^2\theta_W} = \frac{m_W^2}{\cos^2\theta_W} \tag{1.32}$$

The Higgs boson mass arises from the second term of the first line in the Lagrangian 1.30:

$$m_H = \sqrt{-2\mu^2} = \sqrt{2\lambda}v \tag{1.33}$$

The coupling of the Higgs boson to the vector bosons $W^{\pm}$ and Z is proportional to the square of their mass, as extracted from the third line. From the third and fourth lines the interaction of weak bosons with the Higgs field, with HWW, HZZ, HHWW and HHZZ vertices arises. The last line represents the trilinear and quadrilinear Higgs self-interaction terms with coupling constant λ_{HHH} and λ_{HHHH} that can be defined as:

$$\lambda_{\mathrm{HHH}} = \lambda_{\mathrm{HHHH}} = \lambda = \frac{m_H^2}{2v^2} \tag{1.34}$$

Since the Higss boson self-couplings are related to the Higgs mass and the VEV, their measurement is a crucial test of the validity of this theory in the SM.

Until now, fermions appear massless: the theory needs to be completed with the interaction between the Higgs boson and the fermion fields, through a Yukawa interaction. The Yukawa Lagrangian, that needs to be included in the SM Lagrangian, is:

$$\mathcal{L}_{Yukawa} = -g_{si}\varphi(\overline{\psi_L}\psi_R + \overline{\psi_R}\psi_L) \tag{1.35}$$

where i stands for all types of fermions and the coupling constants g_{si} are arbitrarily chosen in order to reproduce the known physical masses of the fermions. Expanding the Higgs field around the ground state (as in Eq. 1.25), the Lagrangian 1.35 becomes:

$$\mathcal{L}_{Yukawa} = -g_{si}\frac{v}{\sqrt{2}}(\overline{\psi_L}\psi_R + \overline{\psi_R}\psi_L) - g_{si}\frac{h}{\sqrt{2}}(\overline{\psi_L}\psi_R + \overline{\psi_R}\psi_L) \tag{1.36}$$

The first term represents the mass for each fermion:

$$m_{f_i} = g_{si}\frac{v}{\sqrt{2}} \tag{1.37}$$

and the second term expresses the coupling between the fermion fields and the Higgs boson field:

$$\frac{g_{si}}{\sqrt{2}} = \frac{m_{f_i}}{v} \tag{1.38}$$

From Eq. 1.38 it is clear that the Higgs coupling constants to fermions are proportional to the corresponding fermion masses.

The complete Lagrangian of the SM is then expressed as:

$$\mathcal{L}_{SM} = \mathcal{L}_{QCD} + \mathcal{L}_{EW} + \mathcal{L}_{BEH} + \mathcal{L}_{Yukawa} \tag{1.39}$$

where the different terms are given by Eq. 1.7, 1.15, 1.30 and 1.36 respectively.

1.3 Search and discovery of the Higgs boson at LHC

One of the main motivation for the Large Hadron Collider (LHC) at CERN was the search for an experimental confirmation of the theory of the BEH mechanism. This collider allowed to considerably extend the search for the Higgs boson far beyond what was previously achieved at other colliders such as the Large Electron Positron collider, LEP [15] at CERN or the Tevatron [16] at FermiLab, leading to the discovery of the new scalar boson at a mass of approximately 125 GeV, identified as the Higgs boson, announced on the 4$^{\text{th}}$ of July 2012 by the ATLAS [17] and CMS [18] Collaborations.

1.3.1 Higgs production mechanisms

The SM Higgs boson can be produced in many different production modes: the main four are represented in Figure 1.1 and briefly introduced in the following [19].

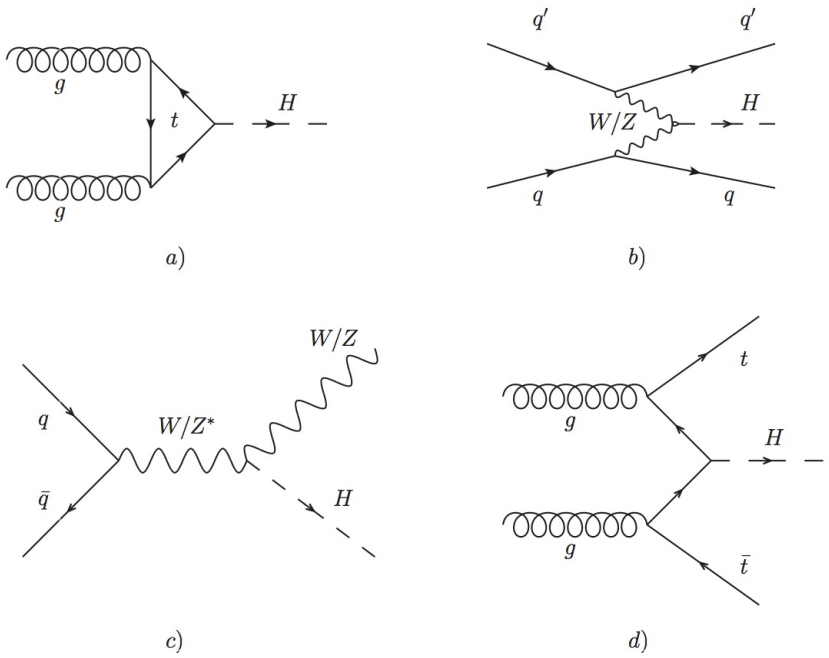

Figure 1.1: Feynman diagrams of the main four SM Higgs production modes: (a) gluon fusion, (b) vector boson fusion, (c) associated production with a vector boson, (d) associated production with a top quark pair.

Gluon fusion (ggF) The gg $\rightarrow$ H process, where two gluon fuse through a loop of quarks to produce the Higgs boson, represented in Figure 1.1 (a) is the process with the dominant cross section in the whole mass range. The top quark contribution in the loop is significantly higher ($\sim 90\%$) than the contributions from all the other fermions, thanks to the larger coupling constant, proportional to the fermion mass.

Vector boson fusion (VBF) The qq $\rightarrow$ qqH process illustrated in Figure 1.1 (b), where two fermions exchange a virtual vector boson (W or Z) which fuses into a Higgs boson, represents the second contribution to the total Higgs production. Its clear signature, due to the presence of two hadronic jets in the forward region, makes this channel very important to reject SM backgrounds and ggF production in association with two jets.

Associated production with a vector boson (VH) The qq $\rightarrow$ VH where V = $W^{\pm}$, Z production mode is shown in Figure 1.1 (c): a fermion and anti-fermion produce a vector boson which then radiates a Higgs boson. Also called Higgs-strahlung, this process produces a boosted Higgs in association with leptonic or hadronic products of the vector boson and represents the third contribution to the H production.

Associated production with a top quark pair (ttH) The lowest contribution is provided by the gg $\rightarrow$ $t\bar{t}$H process, that occurs when a pair of top and anti-top, each produced in a gluon decay, fuse to produce a Higgs boson, as shown in Figure 1.1 (d). The presence of the $t\bar{t}$ pair in the final state provides an interesting and profitable signature.

Other production modes are represented by the associated production of the Higgs boson with a pair of b quarks (bbH), and the single top production (tqH). In Figure 1.2 the Higgs boson production cross section for each production mechanism is shown as a function of the center-of-mass energy ($\sqrt{s}$) for a 125 GeV Higgs boson.

1.3.2 Higgs decay modes

The Higgs boson may decay in many final states with different branching fractions (BR), as shown in Figure 1.3 as a function of its mass, where the branching fraction is defined as the fraction of the Higgs bosons decaying in a given channel with respect to the total number of Higgs bosons produced. These final states are fundamental in the Higgs searches at LHC since its

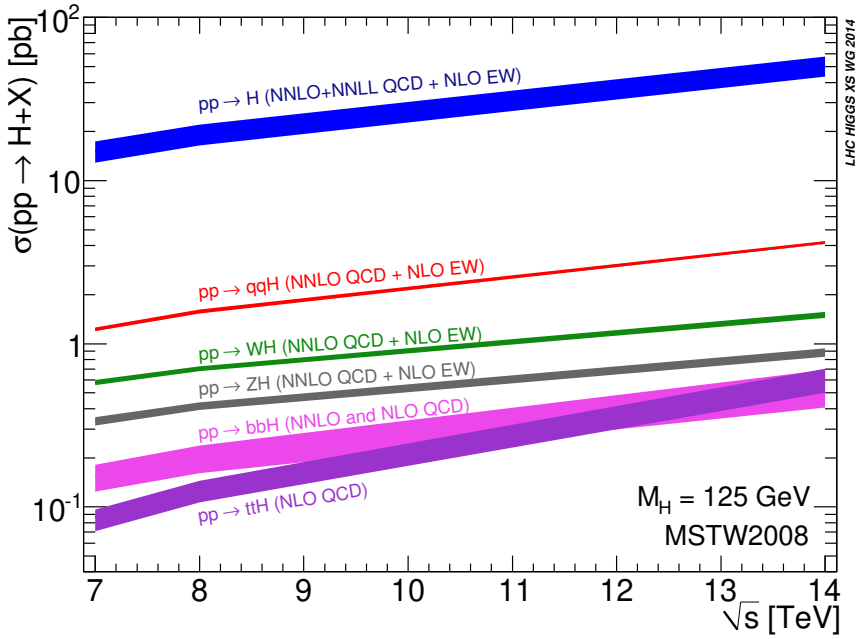

Figure 1.2: Total production cross section for a 125 GeV SM Higgs boson as a function of the center-of-mass energy [20].

short lifetime, about $1.6 \cdot 10^{-22}$ s for $m_{\mathrm{H}} = 125$ GeV [21] is not enough large to make it reach the detectors: only its decay products are thus detectable and studied by the LHC experiments.

At low Higgs mass ($m_{\mathrm{H}} < 130$ GeV) fermion decay channels are dominant, especially $\mathrm{H} \to \mathrm{b\bar{b}}$, since the quark b is the most massive fermion kinematically accessible, followed by $\mathrm{H} \to \tau^+\tau^-$. At higher masses ($m_{\mathrm{H}} > 130$ GeV), the Higgs boson decay to gauge bosons would be preferred, such as $\mathrm{H} \to \mathrm{WW}^{(*)}$ or $\mathrm{H} \to \mathrm{ZZ}^{(*)}$ in all possible final states produced by the decay of the vector bosons. At very high masses ($m_{\mathrm{H}} > 350$ GeV), the $\mathrm{H} \to \mathrm{t\bar{t}}$ decay would become possible. Among the many different signatures searched at LHC, the lepton and photon final states are favored with respect to hadronic final states, due to the clear signature and the complete reconstruction of the final state, with a good experimental resolution achieved on the invariant mass and the high signal over background ratio. For this reason, two important decay channels are $\mathrm{H} \to \mathrm{ZZ}^{(*)} \to 4\ell$ and $\mathrm{H} \to \gamma\gamma$, that despite their small branching fraction ($\sim 2.6\%$ and $\sim 0.2\%$), were fundamental for the Higgs boson discovery at the LHC.

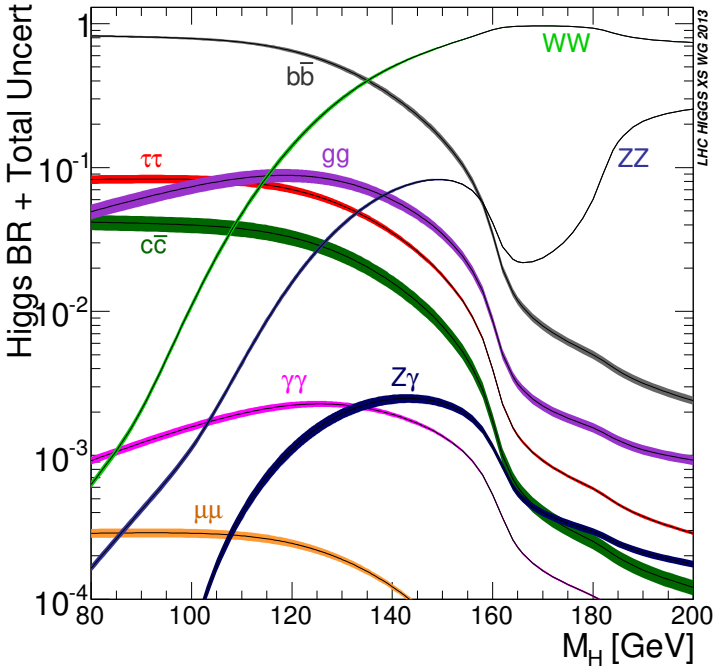

Figure 1.3: Decay branching fraction with uncertainties for the SM Higgs boson as a function its mass [20].

1.3.3 Higgs boson discovery and recent measurements at LHC

The experimental searches for a Higgs boson started at the LEP at CERN in the nineties: they lead to no evidence of a new scalar particle, but allowed to put a lower limit on the mass of the Higgs boson, which is not predicted by the theory, of $m_{\mathrm{H}} > 114.4$ GeV at the 95% confidence level (CL) [15]. The Tevatron at Fermilab, instead, excluded the region $158 \div 173$ GeV at the 95% CL [16]. In 2011, with a center-of-mass energy of 7 TeV, the LHC general purpose experiments ATLAS and CMS collected an integrated luminosity of 5.1 fb^{-1}. Analyzing those data in five decay channels, $\mathrm{H} \to \gamma\gamma$, $\mathrm{H} \to \mathrm{ZZ}^*$, $\mathrm{H} \to \mathrm{W}^+\mathrm{W}^-$, $\mathrm{H} \to \tau^+\tau-$, and $\mathrm{H} \to \mathrm{b\bar{b}}$, they were able to exclude the region $129.2 \div 541$ GeV and $129 \div 525$ GeV respectively [22]. In 2012, when the center-of-mass energy was increased to 8 TeV, more data became available: adding a new data sample of 5.3 fb^{-1} to the data collected in the previous year, both experiments observed an excess of events above the expected background, with a local significance of 5.1 σ (ATLAS) and 5.0 σ (CMS), at a mass near 125 GeV as shown in Figure 1.4 for the two discovery channels: $\mathrm{H} \to \gamma\gamma$ and $\mathrm{H} \to \mathrm{ZZ} \to 4\ell$.

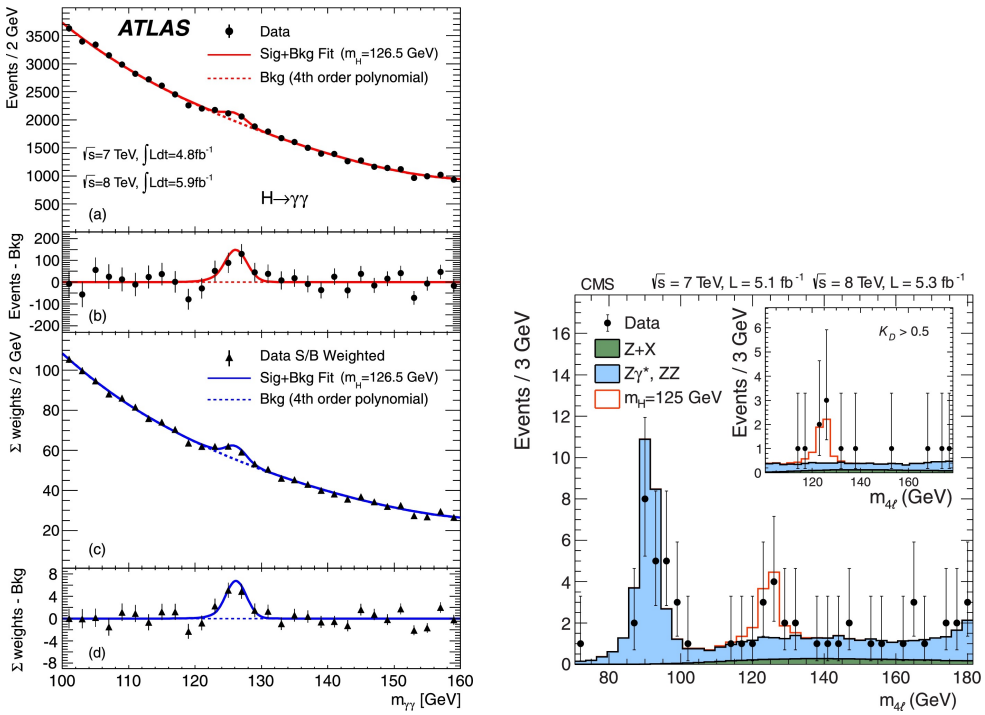

Figure 1.4: ATLAS photon pair invariant mass (left) and CMS four-lepton invariant mass (right) distributions obtained with 5.1 fb^{-1} at $\sqrt{s} = 7$ TeV and 5.3 fb^{-1} at $\sqrt{s} = 8$ TeV [17, 18].

With the complete dataset at $\sqrt{s} = 7$ and 8 TeV, the mass of the new boson was measured combining ATLAS and CMS results, obtaining the value $m_{\mathrm{H}} = 125.09 \pm 0.21(\mathrm{stat.}) \pm 0.11(\mathrm{sys.})$ GeV [23] and the spin-parity was found to be $J^P = 0^+$ [24]; the new scalar boson turned out to be compatible with the SM Higgs boson also in terms of its coupling strength to SM particles [25, 26, 27]. In the last data-taking period, at 13 TeV, extensively measurements and analyses were performed to discover all of the main production mechanisms and decay modes of the Higgs boson, and study its properties with high precision, in order to exclude, or discover, possible beyond the SM (BSM) physics. The ggF, VBF, VH [28] and ttH [29, 30] production mechanisms have been observed, and the same goes for the five Higgs decay channel previously mentioned: ZZ, WW, $\gamma\gamma$, bb [28, 31] and $\tau\tau$ [32, 33]. No indication of deviations from the SM prediction has been found up to now. Figure 1.5 shows the value of the signal strength $\mu = \sigma_{\mathrm{H}}/\sigma_{\mathrm{H}}^{SM}$, where σ_{H} (σ_{H}^{SM}) is the observed (expected) H production cross section, for the individual decay modes using CMS data, which is compatible with the SM expectations [34, 35].

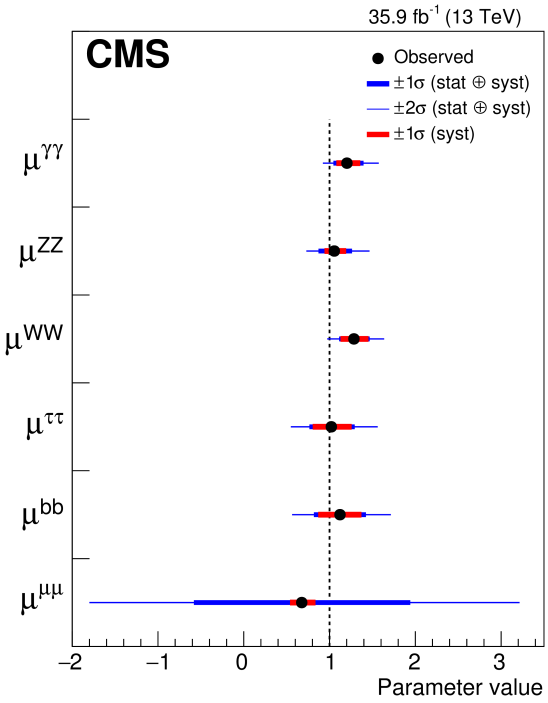

Figure 1.5: Values of the signal strength $\mu = \sigma_{\mathrm{H}}/\sigma_{\mathrm{H}}^{SM}$ for individual decay modes obtained by the CMS experiment [35].

1.4 Higgs boson pair production in the SM

The trilinear Higgs boson self-coupling λ_{HHH} can be extracted from the measurement of the Higgs boson pair (HH) production cross section [36]. However, a pair of Higgs bosons can be produced in many different ways, not all involving the trilinear coupling: the main di-Higgs production mechanisms at LHC are four, listed below in decreasing order of cross section magnitude [37, 38].

Gluon fusion (ggF) The gluon fusion gg $\rightarrow$ HH, shown in Figure 1.6, is the main production mechanism: the Higgs boson pair is produced by a triangle top-loop through the trilinear self-coupling or in a box top-loop with the radiation of two Higgs bosons from the heavy quark in the loop, with smaller contribution from bottom quarks in both cases (smaller than 1% at leading order, LO). However, since the two processes have amplitude with the same order of magnitude but interfere destructively, the ggF cross section is considerably reduced, nevertheless remaining the main production mode. The cross section of this process depends on λ_{HHH} and on the top Yukawa

coupling y_t.

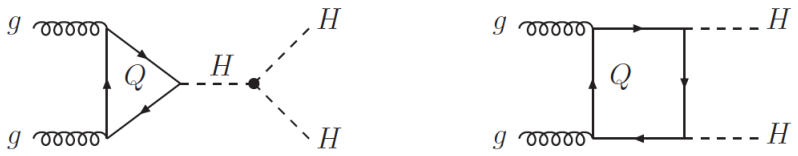

Figure 1.6: Feynman diagrams of the di-Higgs gluon fusion production modes.

Vector boson fusion (VBF) The vector boson fusion (VBF) $qq' \to jjHH$ is the second production mechanism, and is shown in Figure 1.7. It consists in the exchange in the t-channel of the vector bosons W and Z, where the Higgs boson pair is produced either from a single off-shell Higgs boson generated in the VBF process, involving the trilinear coupling, or from the radiation of Higgs bosons from the W or Z bosons. In this latter process, the quadrilinear couplings of the Higgs boson pair to the vector boson pair, and the coupling of a single Higgs boson to vector bosons are involved.

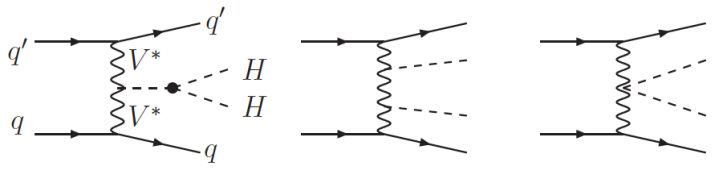

Figure 1.7: Feynman diagrams of the di-Higgs vector boson fusion production modes.

Top quark pair associated production (ttHH) The $qq'/gg \to t\bar{t}HH$ production mechanism is represented in Figure 1.8 and consists in the associated production of a Higgs pair with a top quark pair, where the two Higgs bosons originate either from the single Higgs produced in the $t\bar{t}H$ process, or from the top quarks. For high HH transverse momenta or center-of-mass energies, the $t\bar{t}HH$ cross section exceeds the VBF one.

Vector boson associated production (VHH) The $qq' \to VHH$ process, with $V = W^{\pm}, Z$, also referred to as double Higgs-strahlung production, consists in the associated production of a Higgs pair with a W or Z boson.

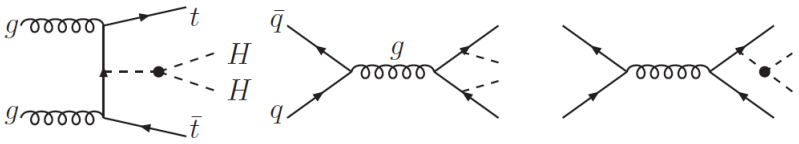

Figure 1.8: Feynman diagrams of the di-Higgs associated production with a pair of top quarks production modes.

The cross section depends on the same couplings just mentioned for the VBF process, but is considerably lower. This process is shown in Figure 1.9.

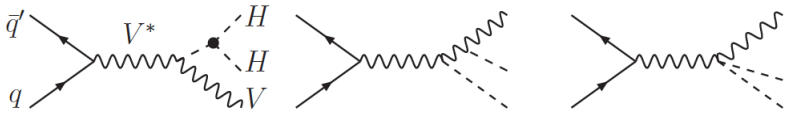

Figure 1.9: Feynman diagrams of the di-Higgs associated production with a vector boson production modes.

The cross sections of these production mechanisms are summarized in Table 1.3 at different center-of-mass energies and graphically shown in Figure 1.10 as a function of the center-of-mass energy. Due to the rarity of the process, LHC searches focus on the main production mechanism, the gluon fusion. Apart from being the production mode with the higher cross section, the destructive interference between the two diagrams makes the HH production sensitive to BSM physics that could change the interference and enhance the total production cross section.

1.5 Higgs boson pair production in BSM models

In light of many theoretical and experimental considerations, the SM appears to be incomplete: apart from not being able to describe gravity, the existence of dark matter and the matter-antimatter asymmetry, it results insufficient to provide any explanation about the reason for three fermion families with couplings to the Higgs boson that varies in a wide range; furthermore, it does not explain which mechanism to use to stabilize the radiative corrections to the mass of the Higgs boson which are quadratically

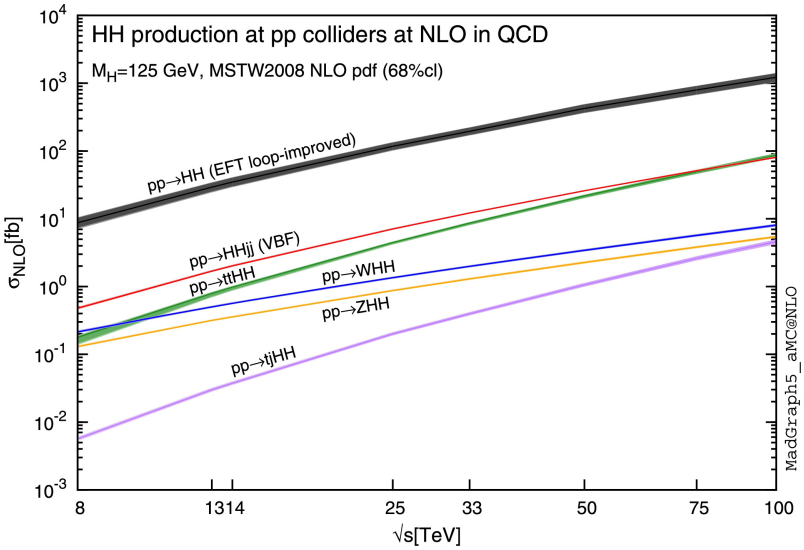

Figure 1.10: Di-Higgs total production cross section as a function of the center-of-mass energy [38].

divergent; finally it does not provide a stable vacuum condition thus not assuring the validity of the theory up to the Planck scale. BSM physics could provide a solution to these issues: being an extension of the SM, it could still preserve all its capabilities of describing the majority of the phenomenology, while adding the explanation to unsolved problems. For what concerns the Higgs pair production, BSM physics can produce consequences on the couplings of the Higgs boson with anomalous effects, or can manifest itself via new particles that can be produced or contribute to the quantum loops responsible for the di-Higgs production.

1.5.1 Resonant BSM HH production

Many BSM theories predict the existence of heavy particles that can couple to a pair of Higgs bosons, appearing in a resonance X of mass $m_X > 2m_{\mathrm{H}}$ that consequently decays in a pair of Higgs bosons. This could thus increase significantly the production cross section of the di-Higgs process with respect to the SM expectations. Resonances are postulated by many models, either with an extended scalar sector, or with warped extra dimensions: some of them are briefly introduced in the following.

Warped extra dimensions models Warped extra dimensions models (WED), proposed by Randall and Sundrum (RS) [39], postulate the existence

Production mode	σ (fb)
	$\sqrt{s} = 13$ TeV
ggF	$33.53\ ^{+4.3}_{-6.0}$(scale)$\pm$2.1(PDF)$\pm$2.3(α_S)$\pm$5.0%(top)
VBF	$1.64\ ^{+2.0}_{-2.5}$(scale)$\pm$2.3(PDF + α_S)
ttHH	$0.775\ ^{+1.5}_{-4.3}$(scale)$\pm$3.2(PDF + α_S)
ZHH	$0.363\ ^{+3.4}_{-2.7}$(scale)$\pm$1.9(PDF + α_S)
W^+HH	$0.329\ ^{+0.32}_{-0.41}$(scale)$\pm$2.2(PDF + α_S)
W^-HH	$0.173\ ^{+1.2}_{-1.3}$(scale)$\pm$2.8(PDF + α_S)
	$\sqrt{s} = 14$ TeV
ggF	$39.64\ ^{+4.4}_{-6.0}$(scale)$\pm$2.1(PDF)$\pm$2.2(α_S)$\pm$5.0%(top)
VBF	$1.94\ ^{+2.3}_{-2.6}$(scale)$\pm$2.3(PDF + α_S)
ttHH	$0.949\ ^{+1.7}_{-4.5}$(scale)$\pm$3.1(PDF + α_S)
ZHH	$0.415\ ^{+3.5}_{-2.7}$(scale)$\pm$1.8(PDF + α_S)
W^+HH	$0.369\ ^{+0.33}_{-0.39}$(scale)$\pm$2.1(PDF + α_S)
W^-HH	$0.198\ ^{+1.2}_{-1.3}$(scale)$\pm$2.7(PDF + α_S)

Table 1.3: Di-Higgs production cross section for different modes, assuming $m_{\mathrm{H}} = 125$ GeV, at center-of-mass energies of 13 and 14 TeV. The ggF cross section is computed at NNLO perturbative QCD calculation, with NNLO corrections and including top quark mass effects to NLO; the VBF and $t\bar{t}$HH ones are computed at NLO QCD, and the VHH ones at NNLO QCD [20].

of an extra spatial dimension compactified between two "branes", which are four-dimensional hypersurfaces, one corresponding to the Planck scale M_{Pl} and the other one to the electroweak scale. The region between the branes is called "bulk" and is warped via the exponential metric kl, where k is the warp factor which represents the curvature, and l is the coordinate of the extra spatial dimension. These models predict two new resonances: the spin-0 radion (R) and the spin-2 Kaluza-Klein graviton (KK graviton), that can decay into a pair of Higgs bosons. The free parameters of these models are: $\widetilde{k} = k/\bar{M}_{Pl}$, where $\bar{M}_{Pl} = M_{Pl}/\sqrt{8\pi}$ is the reduced Planck scale, and the ultraviolet cutoff, near the TeV scale $\Lambda_R = \sqrt{6}e^{-kl}\bar{M}_{Pl}$. The radion production cross section is proportional to $1/\Lambda_R^2$ while the graviton cross section is proportional to $\widetilde{k}^2$ [40]. The expected branching fractions of radion and graviton decaying in a pair of Higgs bosons is 23% and 10% respectively [41].

Higgs singlet model This model contemplate the existence of an additional singlet S to the SM Higgs doublet [42, 43]. After the EWSB they both acquire a vacuum expectation value and thus can be considered as real physical fields corresponding to a light (h) and heavy (H) particles: $m_H > m_h \simeq m_{\mathrm{H}} = 125$ GeV. The lighter one is thus interpreted as the Higgs

boson, while the heavier H represents the new resonance that could enhance the di-Higgs cross section.

Two-Higgs-doublet models In the two-Higgs-doublet models (2HDM), a second doublet of complex scalar fields is introduced, in addition to the SM Higgs one. Two different cathegories of models constitute the 2HDM: the type I 2HDM, in which all quarks couple with the same doublet, and the type II 2HDM, in which right-handed quarks with charge +2/3 and -1/3 couple to two different doublets [44]. The second one represents the Higgs sector of the minimal supersymmetric extension of the SM (MSSM) [45]. In this model, five additional new particles are predicted: two neutral scalars (the light field h interpreted as the Higgs field and a heavier field H), a pseudoscalar A and two charged scalars H^+ and H^-. This model is particularly interesting because the assumption of the existence of two Higgs doublets is also postulated in supersymmetric (SUSY) scenarios.

Spin-0 resonances predicted by the models with an extended scalar sector have the same Lorentz structure of the effective couplings to gluons as the radion predicted in WED models: in the case of spin-0 narrow resonances, the kinematic for its production and the production of a radion are the same, and can therefore be studied together.

1.5.2 Nonresonant BSM HH production

The study of the di-Higgs production is fundamental to understand the shape of the potential of the Higgs field. The SM does not directly predicts the Higgs boson mass, but gives a precise indication about the potential and other observables, provided the Higgs mass itself. Since many experiments have now measured this property of the Higgs boson, and other couplings in the electroweak sector, the SM can be tested to understand if it describes correctly the Higgs sector or if it needs to be extended with BSM effects. These effects could arise with contributions in the quantum loops responsible for the di-Higg production, thanks to modifications to the trilinear Higgs self-coupling [46] that can enhance the cross section and modify the kinematic properties of the Higgs bosons pair, as shown in Figure 1.11.

Instead of computing the di-Higgs production cross section in many specific BSM models, an effective field theory (EFT) framework can be introduced, to summarize deviations that may appear in various models [47]. In this approach, the Lagrangian can be written with an enumerable set of parameters, and thus gives an effective description of many models [20].

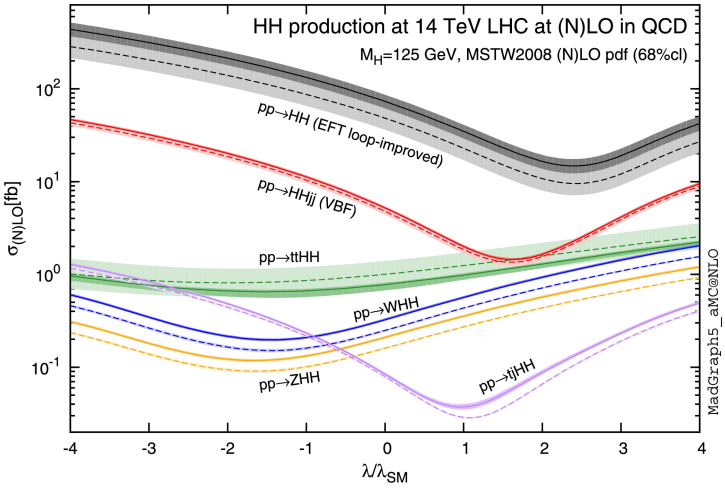

Figure 1.11: Di-Higgs production cross section as a function of the coupling modifier $\kappa_\lambda = \frac{\lambda_{\mathrm{HHH}}}{\lambda^{\mathrm{SM}}_{\mathrm{HHH}}}$ for several production mechanisms [38].

This theory is not renormalizable, but since it is only a representation at lower energies of a more extended theory, it can still be used to compute the parameters of the Lagrangian related to observables. The EFT Lagrangian is composed of the SM Lagrangian with the addition of BSM physics parametrized in terms of higher order operators (higher than the SM order 4), suppressed by powers of a scale Λ:

$$\mathcal{L} = \mathcal{L}_{\mathrm{SM}} + \sum_i \frac{c_i}{\Lambda^2}\mathcal{O}_i^6 + \cdots \tag{1.40}$$

where c_i are the Wilson coefficients. The dimension-5 operator that introduces neutrino masses has been neglected. This EFT Lagrangian can be re-written in the HH context using five parameters: κ_λ, κ_t, c_2, c_g and c_{2g}:

$$\begin{aligned}\mathcal{L}_{\mathrm{HH}} = \frac{1}{2}\partial_\mu \mathrm{H}\partial^\mu \mathrm{H} - \frac{1}{2}m_{\mathrm{H}}^2\mathrm{H}^2 - \kappa_\lambda\lambda_{SM}v\mathrm{H}^3 - \frac{m_t}{v}(v + \kappa_t\mathrm{H} + \frac{c_2}{v}\mathrm{HH})(\bar{t}_L t_R + h.c.) \\ + \frac{1}{4}\frac{\alpha_s}{3\pi v}(c_g\mathrm{H} - \frac{c_{2g}}{2v}\mathrm{HH})G^{\mu\nu}G_{\mu\nu}\end{aligned} \tag{1.41}$$

where m_t is the top quark mass, $\bar{t}_L$ and t_R are the left- and right-handed top quark fields, and "$h.c.$" stands for Hermitian conjugate. CP-violating BSM effects are not considered. In this Lagrangian, deviations from the SM values of the Higgs trilinear self-coupling and of the top Yukawa coupling are parametrized with the coupling modifiers κ_λ and κ_t defined as:

$$\kappa_\lambda = \frac{\lambda_{\mathrm{HHH}}}{\lambda^{\mathrm{SM}}_{\mathrm{HHH}}} \qquad \text{and} \qquad \kappa_t = \frac{y_t}{y_t^{\mathrm{SM}}} \tag{1.42}$$

The interaction of a Higgs boson with a pair of gluons, and of a pair of Higgs bosons with a pair of gluons or a pair of top quarks are not predicted by the SM and are parametrized by the absolute couplings c_g, c_{2g} and c_2 respectively. BSM effects are thus included with the possibility to modify the triangle and box diagrams of the gluon fusion and with the addition of three new diagrams at the same perturbative order, as shown in Figure 1.12. The di-Higgs cross section can thus be parametrized as:

$$\begin{aligned}\frac{\sigma_{\mathrm{HH}}}{\sigma_{\mathrm{HH}}^{SM}} = {} & A_1\kappa_t^4 + A_2c_2^2 + \big(A_3\kappa_t^2 + A_4c_g^2\big)\kappa_\lambda^2 + A_5c_{2g}^2 \\ & + \big(A_6c_2 + A_7\kappa_\lambda\kappa_t\big)\kappa_t^2 + \big(A_8\kappa_\lambda\kappa_t + A_9c_g\kappa_\lambda\big)c_2 \\ & + A_{10}c_2c_{2g} + \big(A_{11}c_g\kappa_\lambda + A_{12}c_{2g}\big)\kappa_t^2 \\ & + \big(A_{13}\kappa_\lambda c_g + A_{14}c_{2g}\big)\kappa_\lambda\kappa_t + A_{15}c_gc_{2g}\kappa_\lambda\end{aligned} \tag{1.43}$$

that in the limit $c_2 = c_{2g} = c_g = 0$ reduces to:

$$\frac{\sigma_{\mathrm{HH}}}{\sigma_{\mathrm{HH}}^{\mathrm{SM}}} = A_1\kappa_t^4 + A_3\kappa_\lambda^2\kappa_t^2 + A_7\kappa_\lambda\kappa_t^3 \tag{1.44}$$

that can be used for simplified approaches. The coefficients A_i are determined from a simultaneous fit of the cross section obtained at LO [48].

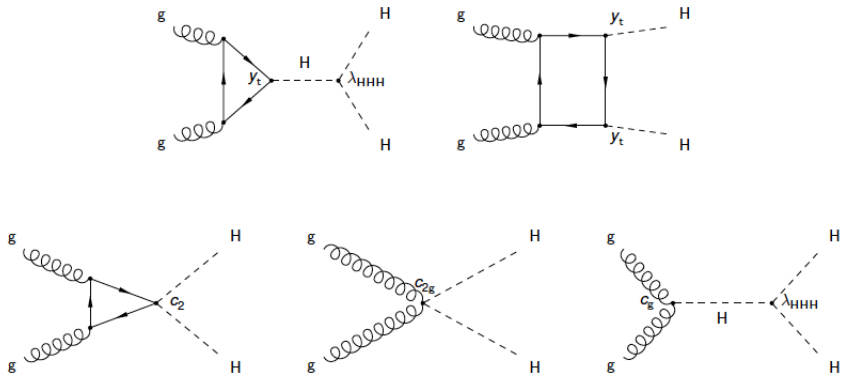

Figure 1.12: Feynman diagrams that contribute to the gluon fusion production mode at LO. Top diagrams correspond to SM-like processes, while bottom diagrams correspond to BSM only effects.

Anomalous values for the couplings have an impact not only on the HH production cross section, but also on the kinematic properties of the HH events. In order to study these effects, a finite set of "shape benchmarks"

covering the most typical kinematic features has been defined, since studying all the possible combinations of the couplings was computationally not possible [49]. A Monte Carlo simulation is used to generate 1507 samples, populating the parameter space of the couplings, that is in five dimensions, to provide a huge sampling of all possible distributions of the kinematic variables that describe the event. The points with similar kinematic properties are grouped together using a statistical Two-Sample test (TS-test), resulting in an optimal number of 12 benchmarks, whose corresponding shapes are shown in Figure 1.13, that best represent the phenomenology of the five-dimensional space of the couplings. The values of the five couplings for each benchmark are reported in Table 1.4; an additional benchmark called "box" has been added to represent the null Higgs self-coupling scenario. This approach based on the EFT and the grouping of all coupling combinations in benchmarks represents a useful model-independent way to parametrize BSM physics models.

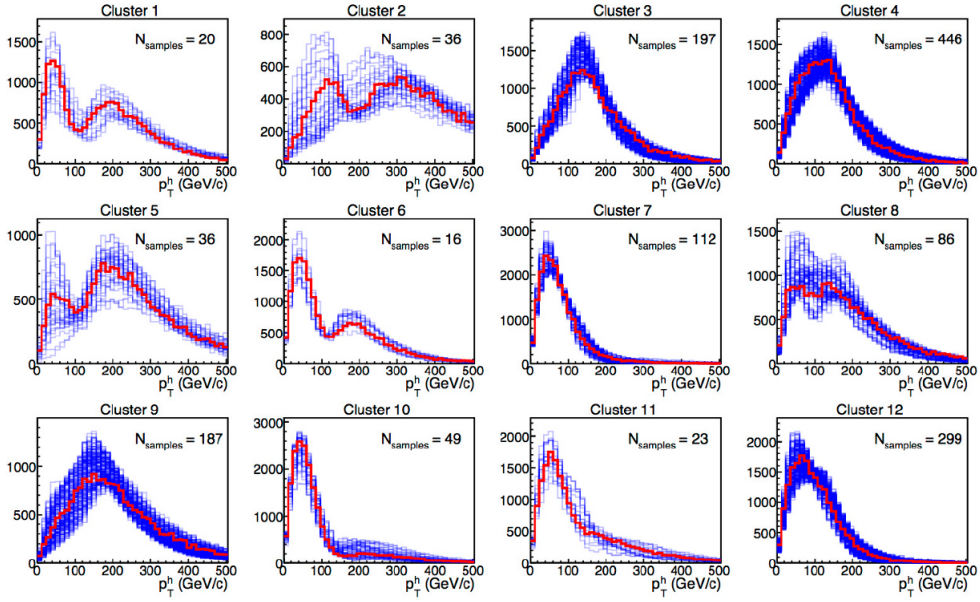

Figure 1.13: Generation-level distributions for the di-Higgs invariant mass m_{HH}: the red (blue) lines represent the benchmark (other members) distribution of each sub-group [49].

Benchmark	κ_λ	κ_t	c_2	c_g	c_{2g}
1	7.5	1.0	-1.0	0.0	0.0
2	1.0	1.0	0.5	-0.8	0.6
3	1.0	1.0	-1.5	0.0	-0.8
4	-3.5	1.5	-3.0	0.0	0.0
5	1.0	1.0	0.0	0.8	-1.0
6	2.4	1.0	0.0	0.2	-0.2
7	5.0	1.0	0.0	0.2	-0.2
8	15.0	1.0	0.0	-1.0	1.0
9	1.0	1.0	1.0	-0.6	0.6
10	10.0	1.5	-1.0	0.0	0.0
11	2.4	1.0	0.0	1.0	-1.0
12	15.0	1.0	1.0	0.0	0.0
box	0.0	1.0	0.0	0.0	0.0
SM	1.0	1.0	0.0	0.0	0.0

Table 1.4: Parameter values of nonresonant BSM 12 shape benchmarks, the "box" and the SM hypotheses [49].

1.6 Di-Higgs searches at LHC

The Higgs boson pair production can be studied in many different final states, since both Higgs bosons present a huge variety of exploitable decay channels. Since the SM Higgs pair production cross section is very small, decay channels with a higher branching fraction would be preferred; moreover, as just explained in the previous section, many BSM theories predict effects on the Higgs pair production cross section and kinematics, and depending on the model, the final states could have very different characteristics. For this reason the analysis searches need to be quite numerous and as complementary as possible, to be sure to explore all signal possibilities. In Figure 1.14, the branching fractions for some HH final states are shown. Up to now, the two general purpose experiments ATLAS and CMS at LHC have explored the more convenient of them, whose branching ratios are reported in Table 1.5:

- HH $\rightarrow b\bar{b}b\bar{b}$ profits from the highest branching fraction, 33.6% but is affected from a large multi-jet background produced by QCD processes;
- HH $\rightarrow b\bar{b}\gamma\gamma$ despite the very small branching fraction, it provides great separation of the signal from the background thanks to the high reconstruction efficiency of the photons and the excellent invariant mass resolution of the Higgs boson decaying into photons.
- HH $\rightarrow b\bar{b}\tau^+\tau^-$ is a compromise between the previous two decay channels, since it has a reasonable branching fraction and it is possible to

Final state	bbbb	bbVV	bb$\tau\tau$	WW*WW*	bb$\gamma\gamma$	WW$\gamma\gamma$
Branchig fraction	33.6%	28.0%	7.3%	4.6%	0.26%	0.098%

Table 1.5: Branching fractions for the HH decays studied by the ATLAS and CMS Collaborations; V stands for $W^{\pm}$, Z [20].

control the background contributions obtaining a good sensitivity on the signal.

- HH $\rightarrow$ b$\bar{\text{b}}$VV where V = $W^{\pm}$, Z, suffers from large background contamination coming mainly from t$\bar{\text{t}}$ and Drell-Yan processes but it has a considerable branching fraction that allows to consider all different sub-channels, depending on the decay of the V.

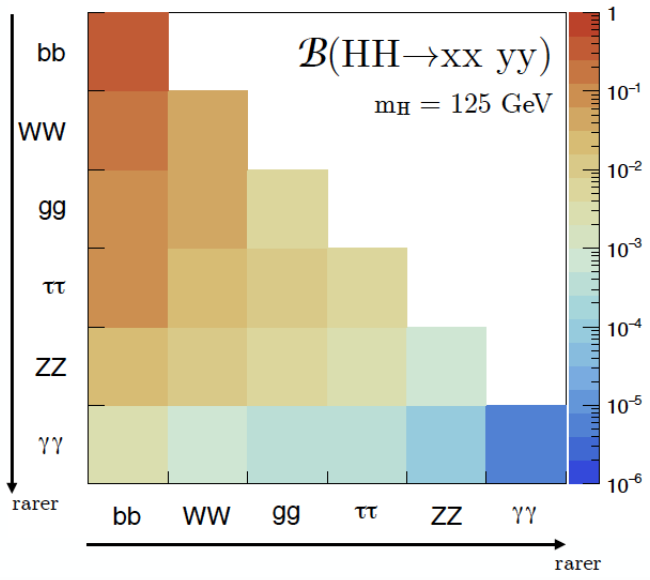

Figure 1.14: Branching fractions for some HH decays [20].

The other HH decay channels without b jets in the final state have smaller branching fractions, thus signal yields, and are higly contaminated by background processes. However, their sensitivity would improve with larger collected integrated luminosity since they are statistically limited; for this reason they would be extensively studied in future LHC data taking periods, like the High Luminosity era that, as will be discussed in the next chapter, will bring a huge integrated luminosity.

1.6.1 State of the art of Higgs boson pair searches

Both ATLAS and CMS experiments extensively studied the di-Higgs production with LHC data from Run 1 at 8 TeV and Run 2 at 13 TeV, testing both resonant and nonresonant HH production, in the decay channels previously described.

Resonant production For the resonant production, ATLAS and CMS explored both the spin-0 in the narrow width approximation and the spin-2 resonance hypotheses, in a wide range of the resonance mass, $250 < m_{\mathrm{HH}} < 3000$ GeV. ATLAS studied the $\mathrm{b\bar{b}b\bar{b}}$, $\mathrm{b\bar{b}}\tau^+\tau^-$, $\mathrm{b\bar{b}}\gamma\gamma$, $\mathrm{b\bar{b}WW^*}$, $\mathrm{WW^*}\gamma\gamma$ and $\mathrm{WW^*WW^*}$ decay channels [50], while CMS explored the $\mathrm{b\bar{b}b\bar{b}}$, $\mathrm{b\bar{b}}\gamma\gamma$, $\mathrm{b\bar{b}}\tau^+\tau^-$ and $\mathrm{b\bar{b}VV^*}$ considering dileptonic decays final states [51]. For the spin-0 resonance, the most sensitive channels are $\mathrm{b\bar{b}b\bar{b}}$, $\mathrm{b\bar{b}}\tau^+\tau^-$ and $\mathrm{b\bar{b}}\gamma\gamma$; however, no evidence of signal has been found up to now, and the upper limits at 95% CL set on the production cross section are shown in Figure 1.15 for ATLAS (top) and CMS (bottom). The spin-2 model has been tested for $k/\bar{M}_{Pl} = 1$, 2 for ATLAS and $k/\bar{M}_{Pl} = 0.5$ for CMS (for higher values the narrow width approximation used by CMS is no longer valid) as shown in Fig 1.16.

Nonresonant production For the nonresonant production the ATLAS Collaboration has studied the $\mathrm{b\bar{b}}\gamma\gamma$, $\mathrm{b\bar{b}b\bar{b}}$, $b\bar{b}\tau^+\tau^-$, $\mathrm{b\bar{b}WW^*}$, $\mathrm{WW^*}\gamma\gamma$ and $\mathrm{WW^*WW^*}$ final states, including only the single lepton final state for the $\mathrm{b\bar{b}WW^*}$ decay channel in the combination [50]. CMS has explored the $\mathrm{b\bar{b}}\gamma\gamma$, $\mathrm{b\bar{b}b\bar{b}}$, $\mathrm{b\bar{b}}\tau^+\tau^-$, and $\mathrm{b\bar{b}VV^*}$ in the dilepton channel [51]. Table 1.6 summarizes the 95% CL expected and observed limits on the signal strength $\mu = \sigma_{\mathrm{HH}}/\sigma_{\mathrm{HH}}^{\mathrm{SM}}$ for all the different channels separately, and for the combination result obtained by the two Collaborations. The best sensitive channel for ATLAS is the $\mathrm{HH} \to \mathrm{b\bar{b}}\tau^+\tau^-$, while for CMS it is the $\mathrm{b\bar{b}}\gamma\gamma$ final state: the differences between the performances of the two experiments in each channel is due to different analysis strategies and optimizations of the algorithms used to define the final states. The observed (expected) upper limit on the HH production has been set at 6.9 (10) times the SM by ATLAS, and at 22.2 (13) by CMS, using 2015 and 2016 data at 13 TeV. Models with BSM modifications to the Higgs self-coupling modifier κ_λ only has been also studied by both Collaborations, leading to an upper limit on the HH production cross section as a function of κ_λ shown in Figure 1.17 for the various channels studied and their combination by ATLAS and CMS respectively. The CMS Collaboration also studied the results obtained in the 12 benchmarks of the EFT theory, obtaining observed and expected exclusion limits on the HH

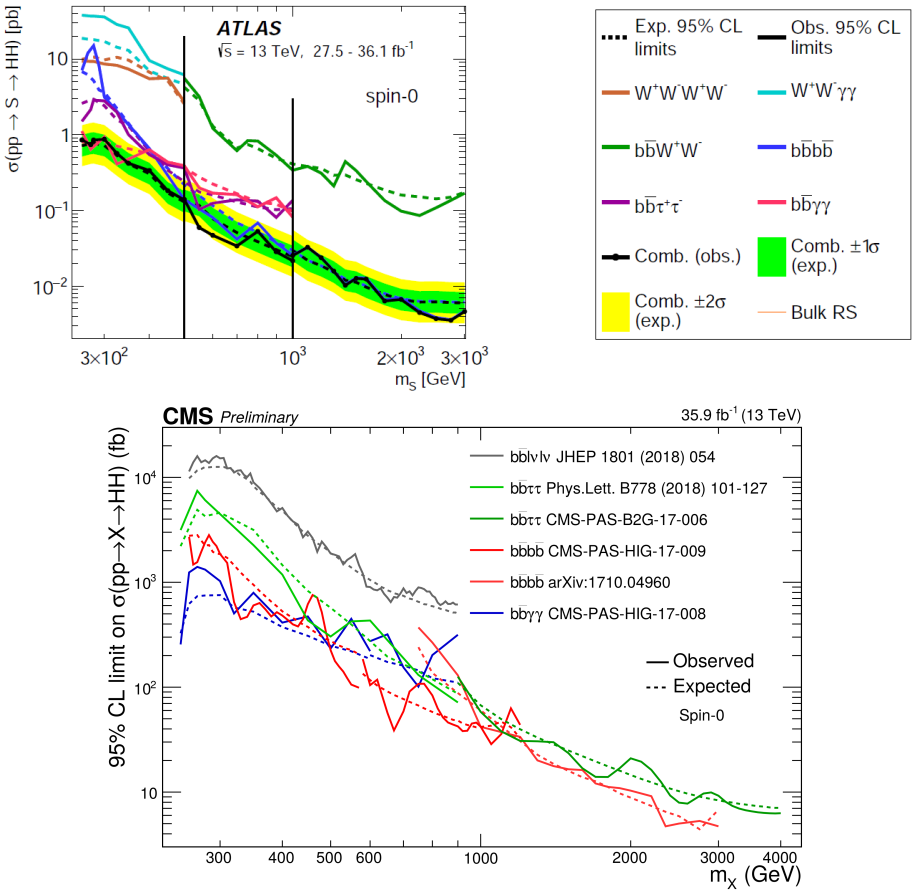

Figure 1.15: Expected and observed 95% CL exclusion limits on the production cross section of a narrow spin-0 resonance decaying into a pair of Higgs bosons for ATLAS (top) [50] and CMS (bottom) [51].

cross section for each benchmark [51], as shown in Figure 1.18.

Final state	Collaboration	95% CL upper limit on μ	
		observed	expected
$b\bar{b}b\bar{b}$	ATLAS	13	21
	CMS	75	37
$b\bar{b}\gamma\gamma$	ATLAS	20	26
	CMS	24	19
$b\bar{b}\tau^+\tau^-$	ATLAS	12	15
	CMS	32	25
$b\bar{b}\mathrm{VV}^*(\ell\nu\ell\nu)$	ATLAS	40	29
	CMS	79	89
$b\bar{b}\mathrm{WW}^*(\ell\nu\ell q)$	ATLAS	305	305
	CMS	-	-
$\mathrm{VV}^*\gamma\gamma$	ATLAS	230	160
	CMS	-	-
$\mathrm{WW}^*\mathrm{WW}^*$	ATLAS	160	120
	CMS	-	-
Combination	ATLAS	6.9	10
	CMS	22	13

Table 1.6: 95% CL upper limit on the SM HH signal strength obtained by the ATLAS and CMS Collaboration at LHC with pp collisions data at 13 TeV corresponding to an integretated luminosity of about 36 fb^{-1}. The ATLAS result obtained in the $\mathrm{b\bar{b}VV}^*(\ell\nu\ell\nu)$ channel is not included in the combinations and is obtained with 139 fb^{-1} [50, 51].

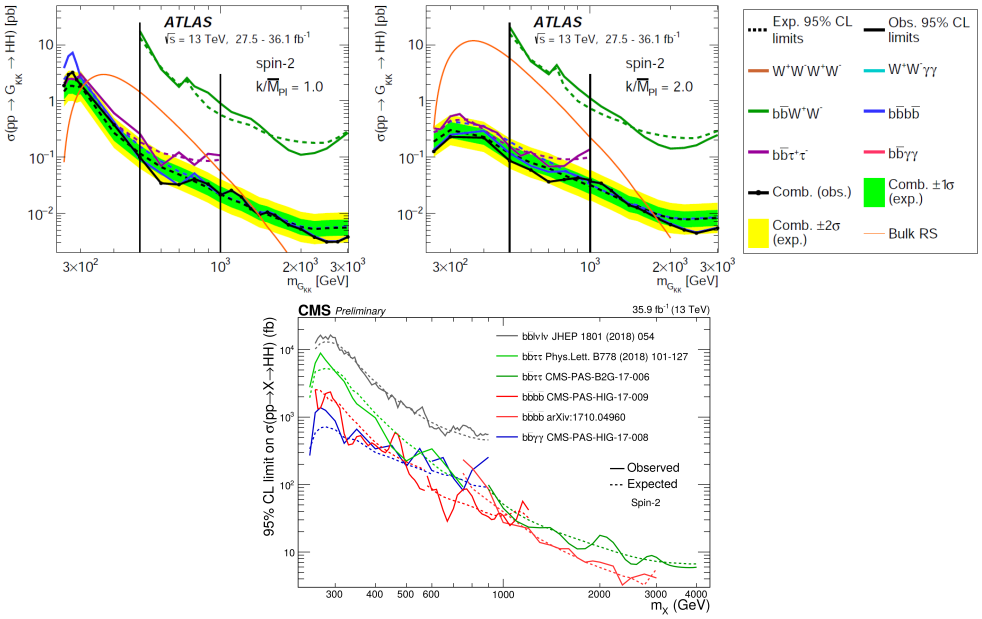

Figure 1.16: Expected and observed 95% CL exclusion limits on the production cross section of a spin-2 resonance decaying into a pair of Higgs bosons: ATLAS results for $k/\bar{M}_{Pl} = 1$ (top left) and $k/\bar{M}_{Pl} = 2$ (top right) [50], CMS results for $k/\bar{M}_{Pl} = 0.5$ (bottom) [51].

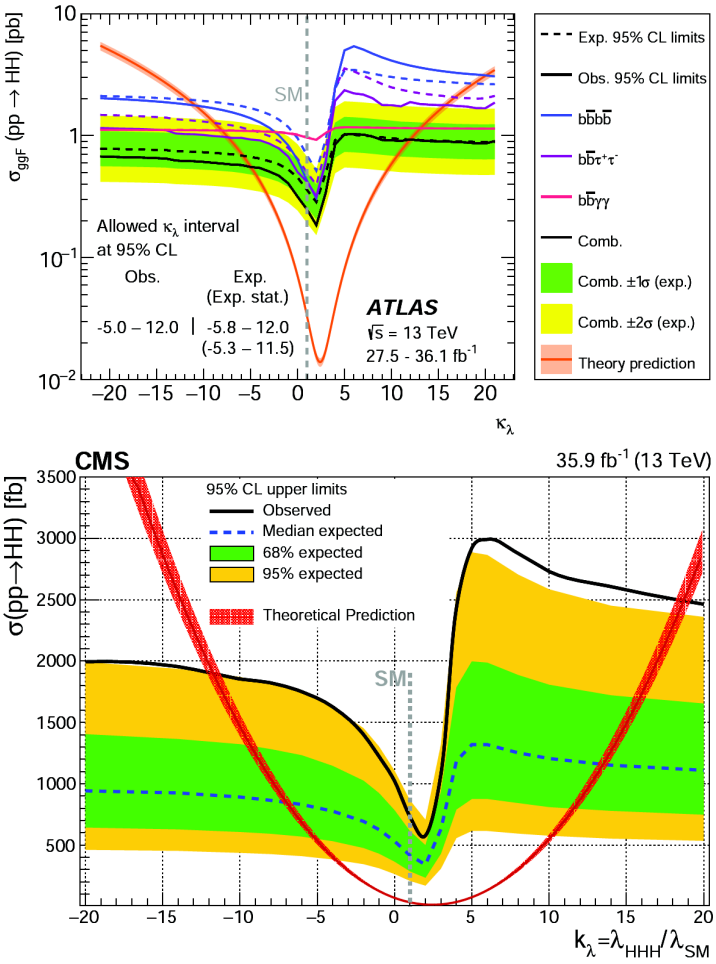

Figure 1.17: Expected and observed 95% CL upper limits on the di-Higgs production cross section as a function of the self-coupling modifier κ_λ for ATLAS (top) [50] and CMS (bottom) [51]. All other Higgs boson couplings are set to their SM values.

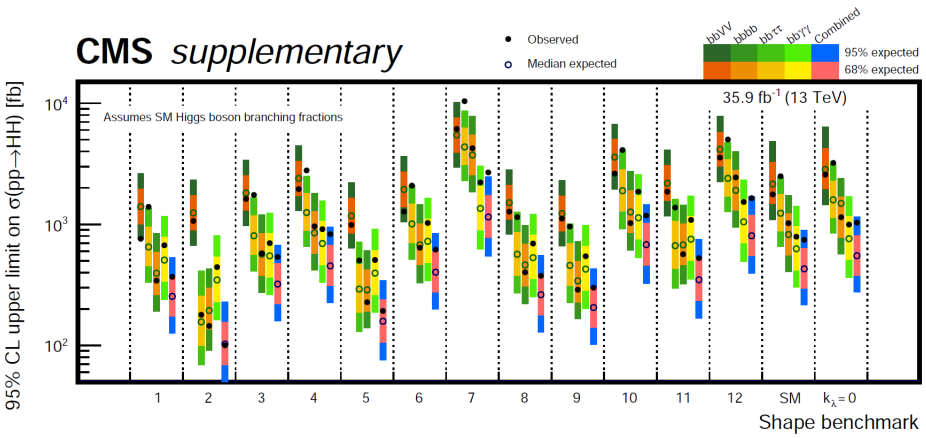

Figure 1.18: Expected and observed 95% CL upper limits on the non-resonant HH cross section for the different 12 EFT benchmarks (1 to 12), for the SM and the $\kappa_\lambda = 0$ hypothese obtained by CMS; the four final states are shown separately and with their combination [51].

Chapter 2

The experimental apparatus

2.1 The Large Hadron Collider

The European Organization for Nuclear Research (CERN), ratified on the 12 of September 1954 by 12 European countries, is now the largest particle physics laboratory in the world, located on the French-Swiss boarder near Geneva (Switzerland). CERN is run by 23 Member States, and counts 2500 staff members and more than 12200 users of 110 different nationalities from institutes in more than 70 countries.

The CERN laboratory hosts the largest and most powerful particle accelerator ever built, the Large Hadron Collider (LHC), conceived to discover the Higgs boson, demonstrate the validity of the SM and search for possible new physics phenomena [52, 53]. Inaugurated in 2008, it was designed to accelerate proton beams up to 7 TeV resulting in a center-of-mass energy of 14 TeV with an instantaneous luminosity of 10^{34} $\mathrm{cm}^{-2}\mathrm{s}^{-1}$ and was installed inside the 26.7 km long tunnel which was previously hosting the Large Electron Positron collider (LEP), about 100 m underground.

Performance

The collider contains two adjacent parallel beam pipes, separated by 194 mm, where beams circulate in opposite directions. The two pipes intersect only at four interaction points, where four main experiments have been placed to detect the particles resulting from the collisions. To keep the circular trajectory, a strong magnetic field of 8.3 T is provided by 1232 dipole magnets, each 14.3 m long and made with copper-clad niobium-titanium cables, installed inside the same mechanical structure and cryostat in order to reduce the amount of cold mass needed for operations. To focus the beams, 392 additional quadrupole magnets, 5 to 7 m long, are also employed, together

with special quadrupole magnets placed near the interaction points in order to increase the particle density and maximize the chances of collision. All the magnets are cooled with 96 tons of superfluid helium-4 maintained at the operational temperature of 1.9 K (-271.25 °C).

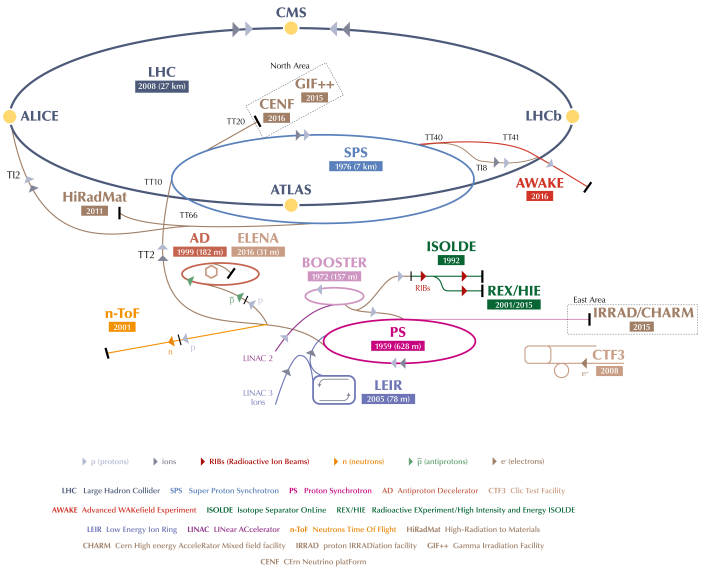

Figure 2.1: The CERN LHC ring with pre-accelerators and detectors layout [54].

Before the injection in the LHC tunnel, protons pass through an injection chain composed of several smaller accelerators that increase the proton energy in steps, schematically represented in Figure 2.1. First of all, hydrogen atoms are ionized to produce protons in a duo-plasmatron source and then accelerated up to 50 MeV in the Linear Accelerator (LINAC 2), which then feeds the Proton Synchrotron Booster (PSB) able to accelerate protons up to 1.4 GeV. They are then injected in the Proton Synchrotron (PS) and consequently in the Super Proton Synchrotron (SPS), where protons reach 26 GeV and 450 GeV respectively. Now the beam is ready to be injected in the LHC, where it is accelerated to the nominal energy thanks to 16 radiofrequency cavities with a frequency of 400 MHz. As soon as the beam is stable, at the nominal energy and correct bunch density, collisions start at the four interaction points. The event are produced at a rate (i.e. events per second) given by:

$$R = \mathcal{L}\sigma \tag{2.1}$$

Center-of-mass energy $\sqrt{s}$	14 TeV
Bunch spacing Δt_b	25 ns
Protons per bunch N_p	1.1×10^{11}
Bunches per beam n_b	2808
Revolution frequency f	11.2 kHz
Transverse beam emittance ε_n	3.75 μm
Beta function β^*	0.55 m
Crossing angle at IP θ_c	285 μrad
Transverse r.m.s. bunch size at IP σ_{xy}	16.7 μm
Longitudinal r.m.s.bunch size σ_z	7.55 cm

Table 2.1: Nominal parameters of the LHC machine for pp collisions [53].

where σ is the production cross section of the physics process and $\mathcal{L}$ is the luminosity [55], an accelerator machine characteristic which depends on the beam properties as:

$$\mathcal{L} = \frac{N_p^2 n_b f \gamma}{4\pi \varepsilon_n \beta^*} F \tag{2.2}$$

N_p is the number of protons per bunch, n_b is the number of bunches per beam, f is the revolution frequency, $\gamma = E/m$ is the relativistic factor, ε_n is the normalized transverse beam emittance, β^* is the beam beta function or focal length at the collision points, and F is a luminosity reduction factor due to the crossing angle at the interaction point (IP):

$$F = \left(1 + \frac{\theta_c \sigma_z}{2\sigma_{xy}}\right)^{-1/2} \tag{2.3}$$

where θ_c is the beam crossing angle, σ_z and σ_{xy} are the longitudinal and transverse r.m.s. bunch size at the interaction point. The nominal value of the LHC machine parameters are reported in Table 2.1: they lead to an instantaneous luminosity $\mathcal{L} \approx 1 \cdot 10^{34}$ cm^{-2}s^{-1}. The integrated luminosity, $L = \int \mathcal{L} dt$, represents the amount of collisions produced during a certain time interval, that is the number of events produced at a rate R with a cross section σ can be expressed as $N = L\sigma$.

As previously mentioned, collisions are produced in correspondence of four interaction points where four main detector have been installed. "A Thoroidal LHC Apparatus" (ATLAS) and "Compact Muon Solenoid" (CMS) are the two largest experiments, located in the diametrically opposite Point 1 and Point 5 respectively of the LHC ring, where the highest luminosity is reached. They are hermetic multipurpose detectors, in order to be able to study the Higgs sector and possible BSM physics. In Point 8 the "LHC beauty" (LHCb) experiment is placed, devoted to the study of CP violation in

b quark physics phenomena. "A Large Ion Collider Experiment" (ALICE) is located in Point 2, to study the quark-gluon plasma state of matter in heavy ion (Pb-Pb) collisions. Three other small experiments are hosted in the LHC: "LHC forward" (LHCf) that studies particles thrown forward by collisions to simulate cosmic rays, the "TOTal Elastic and diffractive cross section Measurement" (TOTEM) experiment devoted to cross section measurements, and the "Monopole and Exotics Detector at the LHC" (MoEDAL), looking for the hypothetical magnetic monopole.

Operations

On the 10^{th} of September 2008, the first proton (p) beam circulated in the LHC, but the first pp collisions were produced on November the 23^{rd}, 2009 after some repair works were needed due to an incident involving magnets. Some pilot runs where thus performed at a center-of-mass energy $\sqrt{s} = 900$ GeV and 2.36 TeV, then the energy was raised to 3.5 TeV per beam on the 30^{th} of March 2010, for a total center-of-mass energy of 7 TeV and with a bunch spacing of 50 ns, marking the beginning of the so-called Run 1. The increase in instantaneous luminosity is shown in Figure 2.2 together with the cumulative luminosity delivered to the CMS experiment in every year, until 2018.

In 2010 and 2011 about 45 pb^{-1} and 6 fb^{-1} respectively were collected by the CMS experiment, followed by 23 fb^{-1} collected in 2012 at $\sqrt{s} = 8$ TeV: with these data the discovery of the Higgs boson was finally possible, and announced on the 4^{th} of July, 2012. At the end of the year, the first technical long shutdown (LS1) took place to allow some maintenance and renovation work needed to increase the operation energy of LHC towards the design parameters. After two years, at the beginning of 2015, the accelerator restarted operations for the Run 2 data-taking period, with a center-of-mass energy of 13 TeV that was reached on the 10^{th} of April, and with a bunch spacing decreased from 50 ns to the nominal 25 ns during the summer period. Due to problems with the cooling of the magnet, the CMS experiment could collect only 2.9 fb^{-1} of data with magnetic field. In 2016 operations continued at 13 TeV and 25 ns bunch spacing but with nominal and even higher instantaneous luminosity, that reached up to $1.5 \cdot 10^{34}$ $\text{cm}^{-2}\text{s}^{-1}$, for a total integrated luminosity collected by CMS of 35.9 fb^{-1}. From 2017 the dimensions of the beam were reduced in correspondence of the interaction points, in order to maximize the number of collisions per bunch crossing, reaching $\mathcal{L} = 2 \cdot 10^{34}$ $\text{cm}^{-2}\text{s}^{-1}$, that lead to 44.98 and 63.67 fb^{-1} collected by CMS in 2017 and 2018 respectively as shown in Figure 2.3 that summarizes the delivered and collected integrated luminosity for the CMS experiment during Run 2.

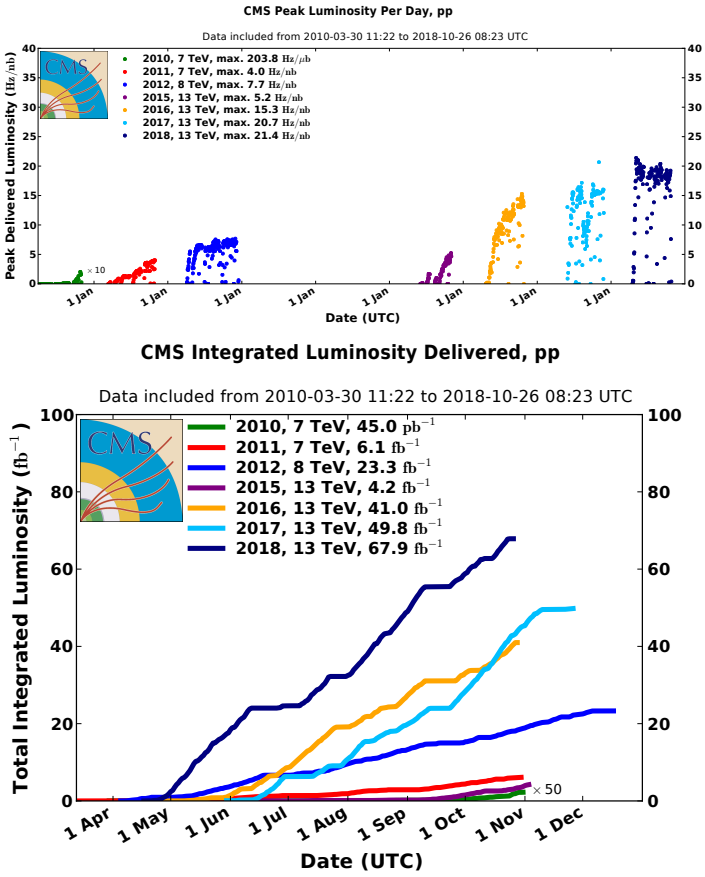

Figure 2.2: Peak luminosity (top) and integrated delivered luminosity (bottom) as a function of time for 2010-2012 and 2015-2018 with pp data only.

The LS2 started at the beginning of 2019, to allow the collider machine to be ready to operate at a center-of-mass energy of 14 TeV during Run 3 (2021-2023), to anticipate the upgrade of the injectors system, and to give time to the experiments to upgrade parts of the detectors for the so-called Phase-I upgrade. After Run 3, a major upgrade of LHC (and consequently of the detectors) will occur during LS3: since its instantaneous luminosity will significantly increase, this new regime of the accelerator machine is called High Luminosity LHC (HL-LHC), as shown in Figure 2.4.

2.1.1 High Luminosity LHC

The main motivations for a high luminosity era consist in the need for significantly large data sets, that would offer the possibility to improve the sensitivity of actual measurements and perform completely new ones, such as

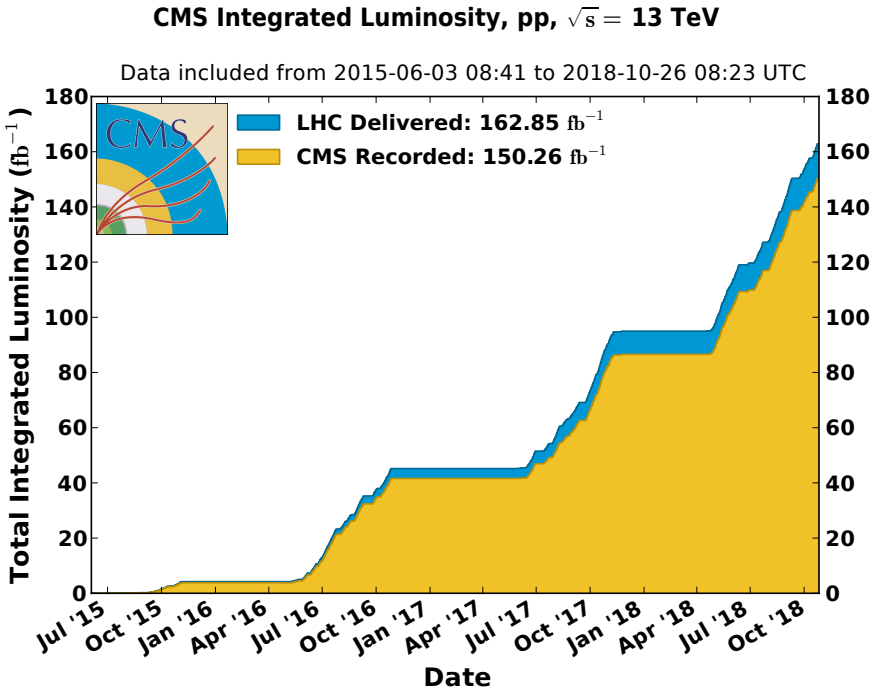

Figure 2.3: Cumulative delivered and recorded luminosity versus time for 2015-2018 with pp data only.

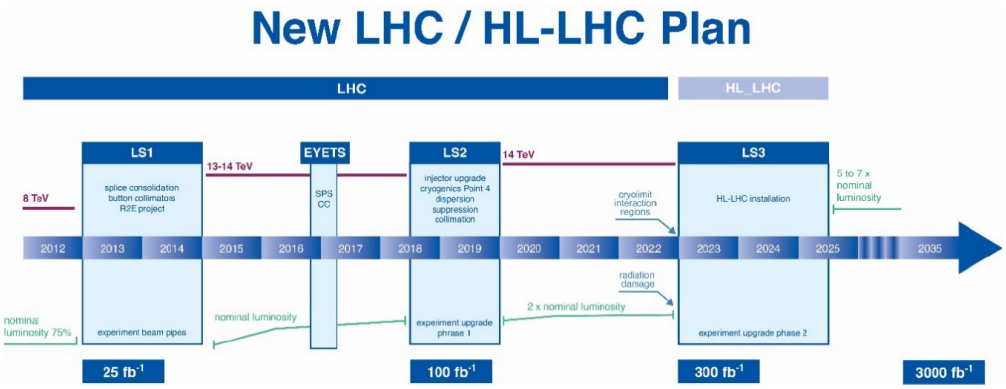

Figure 2.4: Baseline schedule of LHC and HL-LHC operations [56].

the Higgs trilinear self-coupling, impossible up to now because of the small cross section and the limited available statistics. These new capabilities will also allow to discriminate between SM predictions and many BSM theories. The High Luminosity LHC [57] will provide this opportunity, with a leveled instantaneous luminosity $\mathcal{L} = 5 \cdot 10^{34}$ cm^{-2}s^{-1} that will result in an

Parameter	unit	HL-LHC	HE-LHC
$\sqrt{s}$	TeV	14	27
Injection energy	TeV	0.45	0.45/0.9/1.3
Dipole field	T	8.33	16
N_b	10^{11}	2.2	2.2
Beam Current	A	1.12	1.12
Bunch spacing	ns	25	25 (12.5)
Luminosity per year	fb^{-1}	250	730

Table 2.2: Main operational parameters of the HL-LHC and HE-LHC machines [57, 58].

expected integrated luminosity of about 3000 fb^{-1} at the end of the HL-LHC programme. Even if the machine will be capable of providing a maximum peak luminosity of $2.2 \cdot 10^{35}$ $cm^{-2}s^{-1}$, it will be leveled to $5 \cdot 10^{34}$ $cm^{-2}s^{-1}$ in order to maximize the detectors efficiency limiting the peak pileup, defined as multiple overlapping collisions occurred in the same time window of 25 ns in which the proton bunches collide. This will result in an average luminosity just under the one obtained without leveling, but with significantly lower maximum peak, as shown in Figure 2.5, and with an average number of pileup events of about 140-200. In order to be able to operate with these new characteristics, the LHC systems will be significantly improved or substituted. In particular: the inner quadrupoles will be substituted due to accumulated radiation damage, a new cryogenic implant will be installed, the collimator system will be adapted to the increased beam intensity, dipole magnets will be upgraded to provide higher intensity magnetic field (11 T) with shorter dimensions, the quenching protection system will be improved to ensure safety operational conditions for the machine. The main operational parameters of the HL-LHC machine are summarized in Table 2.2.

2.1.2 High Energy LHC

A possible scenario after the HL-LHC era could be a new high energy phase, in which the accelerator would work at a center-of-mass energy of 27 TeV for a total integrated luminosity of 15 ab^{-1} after twenty years of operation: this configuration is called High Energy LHC (HE-LHC) [58, 59]. The physics reach would be significantly improved, since the extended mass region could lead to direct searches of new particles with respect to the HL-LHC scenario, as well as further improved precision measurements that would be performed at HL. To achieve this high energy, the HL-LHC should be upgraded starting from the dipole magnets, that should be able to provide

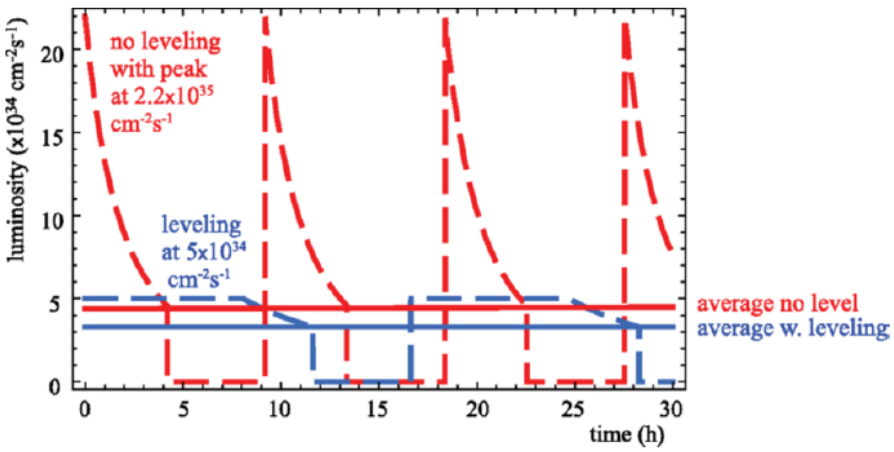

Figure 2.5: Luminosity profile for HL-LHC with (blue) and without (red) leveling [57].

an extremely high magnetic field (16 T) to keep the proton beams in circular orbit at 13.5 TeV. A beam screen would then be fundamental in order to stop the augmented synchrotron radiation ($5 - 20$ times higher than LHC) from being absorbed by the magnets and avoid a magnet quenching. To rotate the beam and provide head-on collisions, new optics electronics, still under study, will be deployed, together with a new injection system and new cryogenics with improved capacity. The main operational parameters of the accelerating machine needed for the HE scenario are reported in Table 2.2, compared to the HL ones; Figure 2.6 shows the instantaneous luminosity, the number of pileup events, the number of particles per bunch and the integrated luminosity as a function of time in the HE scenario.

2.2 The Compact Muon Solenoid experiment at LHC

The CMS detector [60] has been designed to explore physics at the TeV scale, discover the Higgs boson, and be able to detect many other different signatures, including possible BSM physics. For this reason it is a multi-purpose detector, instrumented with various sub-detectors specialized in the identification of different particles and the measurement of different particle characteristics. The detector needed to have: a fast response, to be able to cope with the high rate of collisions provided by the LHC ($25 - 50$ ns); high granularity of sub-detectors, since it is the best way to distinguish between

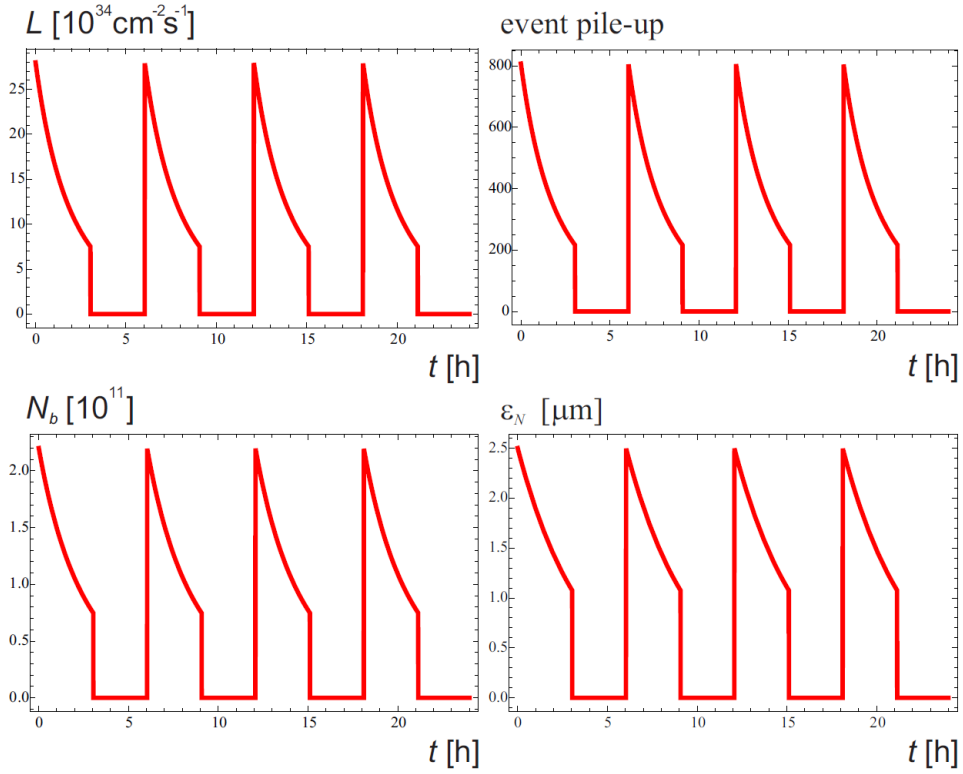

Figure 2.6: Instantaneous luminosity (top-left), pileup (top-right), number of particle per bunch (bottom-left), and integrated luminosity (bottom-right) as a function of time for the HE-LHC configuration [58].

particles produced in the main interaction point with respect to other pileup events; 4π-hermetical structure in order to detect all decay products resulting from the collisions; radiation hardness to maintain good enough capabilities after the high particle fluxes over the years. Part of its key characteristics are revealed in the name given to the detector: "Compact", that means high density of detector material without empty spaces between sub-detector parts; "Muon", since it has been designed to achieve high performances on muon detection with an advanced muon system; "Solenoid", due to the solenoidal superconducting magnet which allows a useful magnetic field inside the detector, as explained in the following.

The CMS detector has a cylindrical structure 21.6 m long with a diameter of 14.6 m, and a total weight o approximately 14000 tons, shown in Figure 2.7. It has been built in 15 sections at ground level, lowered in the cavern about 100 m below the village of Cessy in France and then assembled.

The detector can be divided in three main regions: the barrel, the central

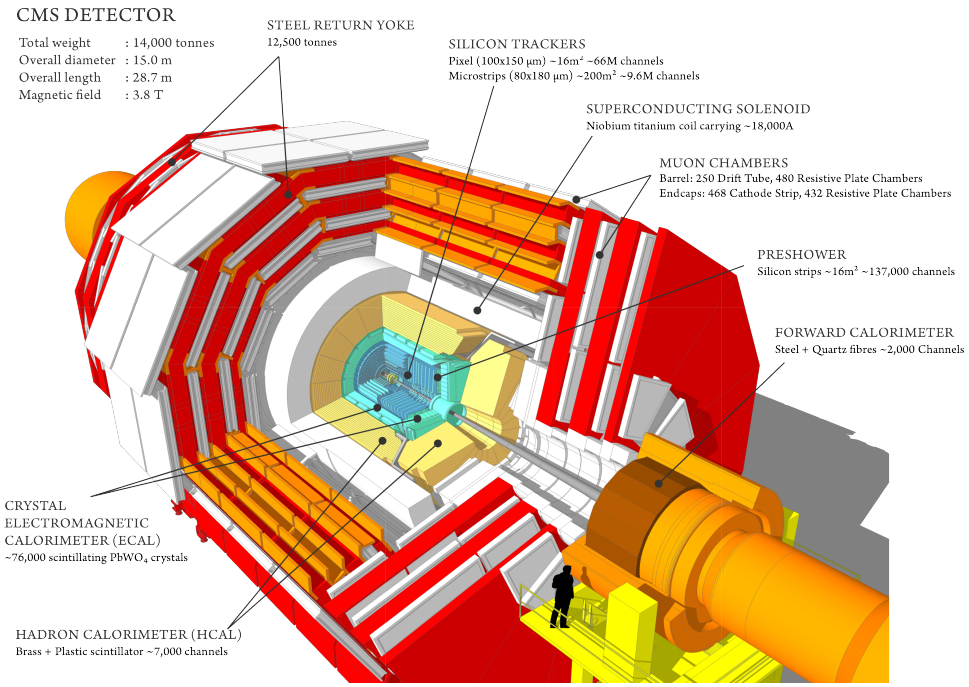

Figure 2.7: Perspective view of the CMS detector layout.

region composed of five wheels coaxial to the beam axis; the endcaps, two regions orthogonal to the beam axis that close the barrel at both ends, each one composed of three wheels; the very froward regions, close to the beam pipe, beyond the endcaps, with sub-detectors responsible to detect particles passing very close to the beam pipe. The core of the detector is the magnet, realized with a superconducting solenoidal coil cooled at -268.5 °C, providing a 3.8 T magnetic field. This is needed to bend charge particles and identify their momentum and charge. After being produced, particles pass through the tracker system which detects charged tracks thanks to silicon detectors, measures particle momentum and identifies primary and secondary vertices. After the tracker, particles arrive to calorimeters, designed to stop the particles and measure their energy, deposited in the active material. The inner part is composed of the electromagnetic calorimeter (ECAL), dedicated to photons and electrons, while the outer part is the hadron calorimeter (HCAL), designed to detect hadrons. If particles survive to calorimeters, they pass through the magnet and then arrive to the last sub-detector, the muon system, which is hosted in the iron of the return yoke of the magnet: it is composed of gas detectors designed to identify muons and measure their charge and transverse momentum. Since up to 40 million collisions happen

every second, a trigger system capable of selecting interesting events is in place. It is divided in two levels: the level 1 (L1) trigger based on fast hardware information that reduces the rate from ∼40 MHz to ∼100 kHz, and the high level trigger (HLT) based on software fast analyses, that reduces the rate to ∼100 Hz.

Coordinate frame

A right-handed Cartesian reference frame is used to describe the detector and the particles produced in the collisions, with the origin centered in the CMS interaction point, the x-axis horizontal, pointing towards the center of the LHC ring, the y-axis vertical, pointing upwards, the z-axis tangent to the beam line. The $x-y$ plane, which is orthogonal to the beam pipe, is called the transverse plane, while the z-axis direction is called longitudinal. Since the CMS detector has a cylindrical symmetry, polar coordinates can be used in reconstruction algorithms: r is the distance from the interaction point in the transverse plane $x-y$ ($r = \sqrt{x^2+y^2}$), ϕ is the azimuthal angle, measured from the x-axis in the transverse plane, and takes values in the range $[-\pi, \pi]$, and θ is the polar angle, measured from the z-axis in the longitudinal plane $z-y$, and takes values in the range $[0, \pi]$. The particle trajectories are often described in the transverse plane because the information in this plane is more interesting than the absolute value of particle characteristics. Using the above mentioned coordinates, many useful variables can be thus defined:

- the particle momentum can be split in the longitudinal and transverse components: $p = \sqrt{p_z^2 + \mathrm{p}_\mathrm{T}^2}$, where $\mathrm{p}_\mathrm{T} = \sqrt{p_x^2 + p_y^2}$;
- the transverse energy and mass can be defined respectively as $E_\mathrm{T} = E \cdot \sin\theta$ and $m_\mathrm{T} = \sqrt{\mathrm{p}_\mathrm{T}^2 + m^2}$;
- the missing transverse energy, according to momentum conservation, can be computed as $E_\mathrm{T}^{miss} = -\sum_i \vec{p}_\mathrm{T}^{\,i}$ where i represents every final state particle and accounts for the energy of particles escaping detection such as neutrinos;
- the rapidity of a particle, which is a Lorentz-invariant variable, is:
$$y = \frac{1}{2} \ln \frac{E + p_z}{E - p_z}; \tag{2.4}$$
- the pseudo-rapidity of a particle, which approximates the rapidity in the case of high energy particles, is defined as:
$$\eta = \frac{1}{2} \ln \left(\frac{p + p_z}{p - p_z} \right) = -\ln \left(\tan \frac{\theta}{2} \right). \tag{2.5}$$

2.2.1 Tracker

The CMS tracker [61], which is the largest tracker system ever built for a collider experiment, is the sub-detector located directly around the beam pipe, close to the interaction point. Its purpose is to reconstruct charged particle tracks, and to measure momentum and charge of particles, thanks to the strong magnetic field in which is embedded. It also needs to be able to distinguish the primary vertex, which is the hard scatter interaction producing the interesting event, from secondary vertices of in-fly decays of b hadrons or τ-leptons, and from additional interactions created by pileup events. The main requirements for this detector are then low occupancy and high detector granularity, fast detector and electronics response, and large redundancy to accurately reconstruct the particle trajectory. For these reasons, the silicon detector technology resulted the best choice: a charge particle passing through a thin layer of silicon cells produces electron-hole pairs that travel thanks to an applied electric field, giving rise to a pulse that is collected and used to reconstruct the particle track. Silicon sensors cover the region up to $|\eta| < 2.5$ with a radius $r < 1.2$ m around the beam pipe and for $|z| < 2.7$ m, for a total length of 5.8 m and a total surface of 210 m^2. The thickness of the silicon sensors changes as a function of the pseudo-rapidity, being 0.35 radiation lengths (X_0) at small η, 1.8 X_0 in the transition region between barrel and endcap, and 1.1 X_0 at $|\eta| \simeq 2.5$. Two types of silicon detectors are installed in the CMS tracker: pixel and strip sensors. The pixels provide very low occupancy, high resolution and precise vertex reconstruction thanks to the extremely high granularity, thus they are placed in the region closest to the beam pipe; microstrips instead cover the more extended region outside the pixels, since they allow to reduce the number of read-out channels, with an occupancy that decreases as the flux of particles with a $1/r^2$ dependence, maintaining a good resolution. To reduce the damage caused by ionizing radiation to the sensors, they are kept at a operation temperature of about -15 °C and -20 °C respectively, with an efficient cooling system that absorbs the heath produced by the on-board electronics.

Silicon pixel sensors The pixel sensors are the closest detector to the interaction point, where the particle flux is the highest ($\sim 10^7$ particles per second). The original system was composed of ~ 66 million pixel cells, each of 100×150 μm^2, grouped in 1400 sensors for a total surface of ~ 1.06 m^2. The barrel region (BPix), counts three layers, each 53 cm long and at a radius $r = 4.4$ cm, $r = 7.3$ cm, $r = 10.2$ cm respectively, while two disks constituted each endcap (FPix), made of 24 blades in a turbine-like shape each, at a radius $r = 7.3$ cm and $r = 15$ cm respectively, as schematically

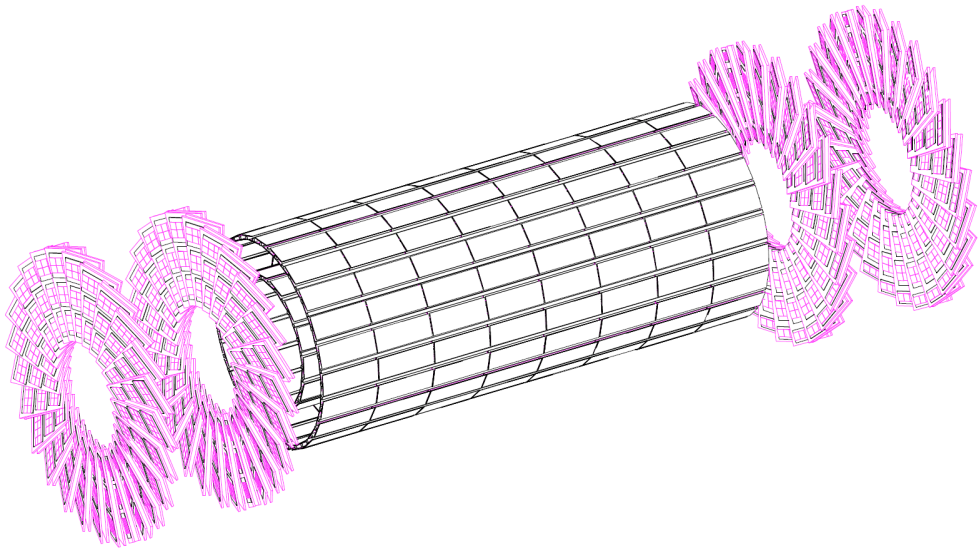

Figure 2.8: Schematic view of the pixel detector sub-system [61].

shown in Figure 2.8. Spatial resolutions of 10 μm in the transverse plane $r-\phi$ and 15 μm in the z-coordinate are achieved in the barrel region, while lower resolutions (15 μm and 20 μm respectively) are achieved in the endcaps. To face the challenging conditions foreseen for 2017 data taking in terms of high rate of collisions and elevated number of pileup events, the pixel tracker has been completely replaced during the usual technical stop at the end of 2016 with a completely new system able to sustain an instantaneous luminosity of $2 \cdot 10^{34}$ cm^{-2}s^{-1} and over 50 pileup events [62]. Figure 2.9 shows a comparison between the old pixel detector and the new one, which is composed of four disks in the barrel region and three disks in each endcap. The upgraded pixel detector is not only composed of an additional layer per region, but is also closest to the beam pipe (about 3 cm for the barrel section) and designed to be lighter (together with the support and services) than the previous one, reducing the material budget: this allowed to lower the weight of about 40% in the barrel region and 80% in the endcaps.

Silicon strip sensors The region of the strip sensors is composed of 9.6 million sensors that extend from $r = 20$ cm to $r = 120$ cm. They can be divided in two different regions, as shown in Figure 2.10: the inner region (20 cm $< r <$ 55 cm), which is composed of four layers in the barrel (TIB, Tracker Inner Barrel) and three disks in each endcap (TID, Tracker Inner Disk) with a minimum cell size of 10 cm $\times$ 80 μm; the outer region, ($r >$ 55 cm), which is composed of six barrel layers (TOB, Tracker Outer Barrel) and nine disks

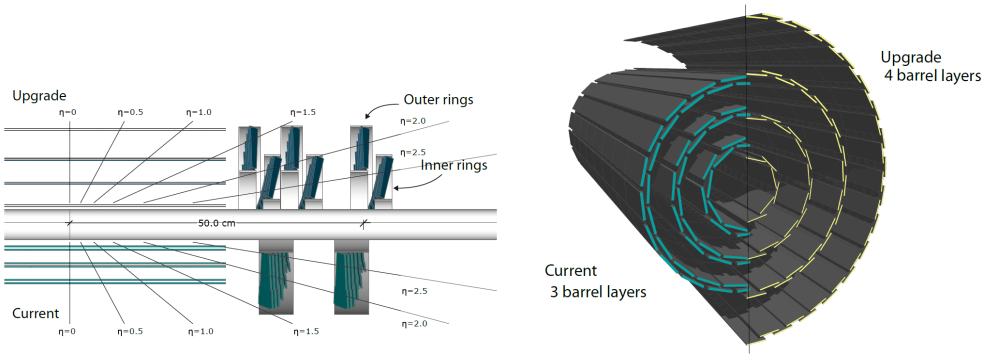

Figure 2.9: Longitudinal view of the current pixel detector (top, blue) and of the upgraded detector (bottom, green) installed for the 2017 data taking (left) and transverse-oblique view comparing the pixel barrel layers in the two detectors (right) [62].

in each endcap (TEC, Tracker EndCap) with a size of 25 cm $\times$ 180 μm. The spatial resolution ranges from 40 to 60 μm in the $r-\phi$ transverse plane, and from 200 to 500 μm in the z-coordinate.

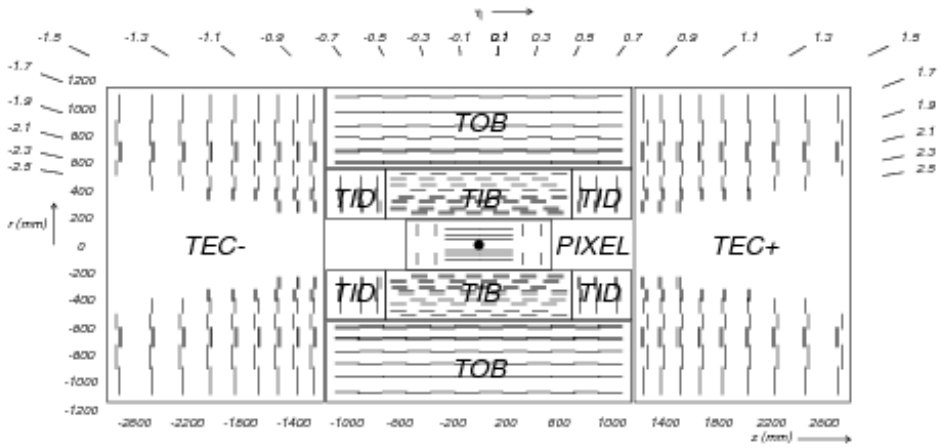

Figure 2.10: Transverse view of the CMS tracker, with focus on the silicon strip sensors part: each line represents a detector module [61].

2.2.2 Electromagnetic calorimeter

The CMS electromagnetic calorimeter (ECAL) [63] is a homogeneous, hermetic and highly granular calorimeter made of more than 75000 lead

tungstate ($PbWO_4$) crystals. This scintillating material detects the electromagnetic shower produced through Bremsstrahlung and pair production: since the intensity of the emitted light is proportional to the energy absorbed by the crystals, it is thus possible to measure the energy of incident photons or electrons studying the shower shape. The lead tungstate, which acts as dense interactive material and as active scintillating medium at the same time, was chosen for its high density ($\rho = 8.28$ g/cm^3), short radiation length ($X_0 = 0.89$ cm), small Molière radius[1] (2.2 cm) and very short scintillation time (in 25 ns almost 80% of the light is collected by silicon avalanche photo-diodes in the barrel and vacuum photo-triodes in the endcaps). These characteristics allow the ECAL to be compact, fast, with a fine granularity, and to ensure an excellent containment of the electromagnetic shower within the crystals, which have a length of approximately 25 X_0. ECAL is divided in two regions: barrel ECAL (EB) and endcap ECAL (EE), as shown in Figure 2.11.

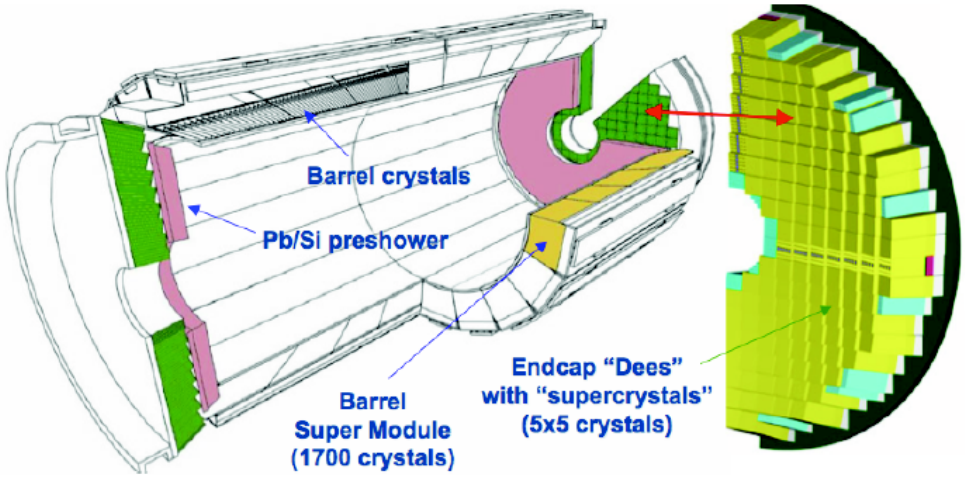

Figure 2.11: Schematic view of the electromagnetic calorimeter.

Barrel ECAL The EB covers the pseudo-rapidity range $|\eta| < 1.479$, with 61200 crystals contained in a thin-walled alveolar structure set at a radius $r = 1.29$ m. Each crystal has a surface of 22×22 mm^2 and a length of 230 mm which correspond to 25.8 X_0. The crystals, divided in 36 super-modules, are mounted in a truncated pyramid geometry, tilted of 3° with respect to the axis from the interaction vertex, in both the ϕ and η directions, to avoid

[1] $R_M = 21.2 \frac{X_0}{\varepsilon_c}$ MeV.

gaps between crystals (cracks) aligned with particle trajectories. However, small cracks are still present in the region $\eta = 0$ and between the barrel and endcap sections of the calorimeter.

Endcap ECAL The EE covers the pseudo-rapidity range $1.479 < |\eta| < 3$ and is composed of 7324 crystals 220 mm long (24.7 X_0) disposed in two "Dees" per endcap, as shown in Figure 2.11, with a surface of 30×30 mm^2, grouped in supercrystals. A preshower detector (ES) is placed in front of the EE to identify $\pi^0 \to \gamma\gamma$ decays in the pseudo-rapidity region $1.653 < |\eta| < 2.6$. The ES is a sampling calorimeter composed of two layers: lead radiators to initiate the shower and a 2 mm silicon strip sensors layer to measure the energy deposit and the transverse shower profiles.

The energy resolution of a calorimeter can be parametrized as:

$$\left(\frac{\sigma}{E}\right)^2 = \left(\frac{S}{\sqrt{E}}\right)^2 + \left(\frac{N}{E}\right)^2 + C^2 \tag{2.6}$$

where E is the particle energy; S is the stochastic term, which accounts for fluctuations in the number of photo-electrons produced and fluctuations in the shower-containment; N is the noise term, due to the electronics and pileup noise; C is a constant term, which is related to the calorimeter calibration, and to the energy leakage of the crystals. Using beam tests, the ECAL energy resolution was found to be:

$$\left(\frac{\sigma}{E}\right)^2 = \left(\frac{2.8\%}{\sqrt{E}}\right)^2 + \left(\frac{12\%}{E}\right)^2 + (0.3\%)^2 \tag{2.7}$$

where E is expressed in GeV.

To read out the scintillation light, detectors with excellent performances in a high magnetic field and high radiation regions are fundamental. For this reason, avalanche photodiodes (APDs) are used in the barrel and vacuum phototriodes (VPTs) in the endcap. Signals are amplified by the front-end electronics and sampled at a frequency of 40 MHz with a 12-bit analog-to-digital converter. Radiation has also an impact on crystals, that despite their resistance to radiation, are not insensitive to it. As a consequence, their optical transparency decreases due to ionization radiation and interactions of hadrons with the crystal lattice. The first effect is recovered with time when there are no collisions, but the second one cannot be neutralized. For this reason, a laser light injection system has been used to continuously monitor transparency loss during the data-taking, and time-dependant corrections are

computed and applied to maintain a good resolution on measured particle energy. Calibration of the calorimeter is also fundamental, to determine the absolute energy scale and the channel-to-channel intercalibration, that is the relative difference in scintillation light yields (up to $\sim$ 15% in EB crystals and $\sim$ 25% in EE crystals). Combined corrections computed from laboratory, cosmic-rays and in-situ measurements, lead to a precision of the percent level.

2.2.3 Hadron calorimeter

The hadron calorimeter (HCAL) [64] is fundamental to identify hadrons that pass through ECAL without being stopped. It is a hermetic and sampling calorimeter that measures hadron energy deposits giving the only measurement in the detector for neutral hadrons, and improving information on charged hadron tracks, in order to reconstruct jets. It is also important to measure the missing transverse energy (E_T^{miss}), being hermetic up to the maximum η region possible ($|\eta| = 5$), in order to provide the signature for neutrinos and other otherwise undetectable particles. CMS HCAL is made of layers of absorber material with alternating tiles of plastic scintillators. In the interaction of a particle with the absorber layer, many secondary particles are produced, which travel through the following absorber layers producing other secondary particles themselves. The result is a shower of particles that produce light in the interaction with the scintillating material: this light is then readout giving a measurement of the initial particle energy, if the shower is fully contained in the calorimeter. HCAL can be divided in four regions: barrel (HB), endcap (HE), forward (HF) and outer hadron calorimeters (HO), as shown in Figure 2.12.

Barrel and endcap hadron calorimeters The barrel hadron calorimeter (HB), composed of towers of $\Delta\eta\times\Delta\phi = 0.087\times0.087$, up to $|\eta| < 1.3$, and two endcap hadron calorimeters (HE), with dimensions $\Delta\eta \times \Delta\phi = 0.17 \times 0.17$ in the region $1.3 < |\eta| < 3$, are constrained between the ECAL and the magnet, from $r = 1.77$ m to $r = 2.95$ m. They are sampling calorimeters, made of brass layers as absorber material alternated to plastic scintillators, the active material, coupled to hybrid photo-diodes (HPDs) using wavelength-shifting fibers. Being non-magnetic and with a short interaction length (λ_0), the brass is particularly useful to obtain small shower dimensions.

Forward hadron calorimeter Two forward calorimeters (HF) are placed around the beam-pipe at $|z| = 11.2$ m which cover up to $|\eta| < 5$, to increase the hermeticity, built with radiation hard materials, being close to the beam

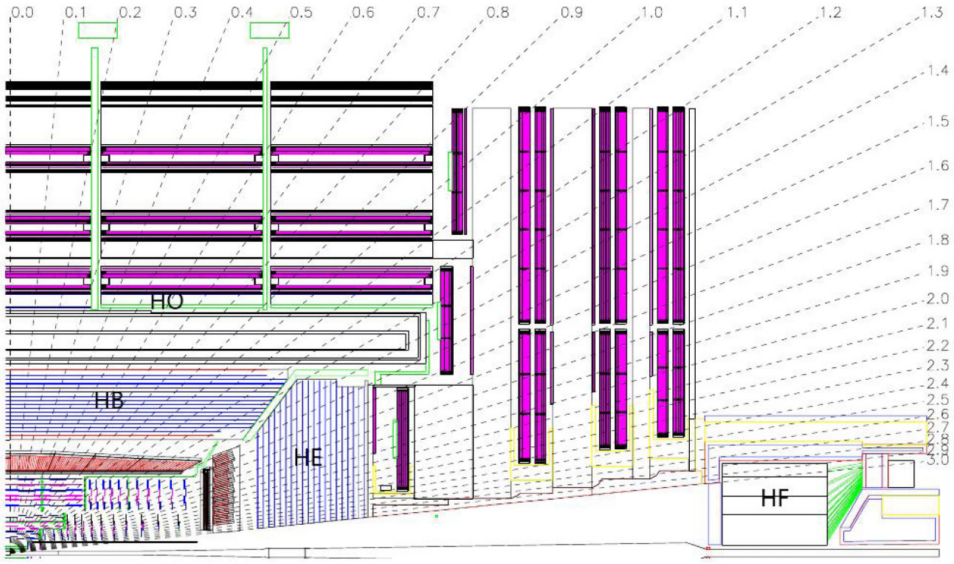

Figure 2.12: Longitudinal view of the hadron calorimeter [64].

line. Steel plates are used as absorbers, while quartz fibers are used as active material producing Cherenkov light at the passage of relativistic particles, measured by photomultiplier tubes (PMTs).

Outer hadron calorimeter The outer calorimeter (HO), outside the magnet coil, is added to improve the energy resolution of the barrel calorimeters, catching the tails of the hadron showers that are not fully contained in HB, increasing the total interaction length to $\simeq 10\ \lambda_0$.

The depth of the calorimeter is a function of the pseudo-rapidity, being $5.25\ \lambda_0$ at $|\eta| = 0$, $9.1\ \lambda_0$ at $|\eta| = 1.3$ and $10.5\ \lambda_0$ at $|\eta| \simeq 5$. The energy resolutions, for the different regions, are:

$$\begin{aligned} \frac{\sigma}{E} &\simeq \frac{65\%}{\sqrt{E}} \oplus 5\% \text{ for HB} \\ \frac{\sigma}{E} &\simeq \frac{85\%}{\sqrt{E}} \oplus 5\% \text{ for HE} \\ \frac{\sigma}{E} &\simeq \frac{100\%}{\sqrt{E}} \oplus 5\% \text{ for HF} \end{aligned}$$

where E is the energy of the particle measured in GeV and $\oplus$ stands for the sum in quadrature.

2.2.4 Magnet

The CMS magnet [65] consists of a superconducting solenoid made of niobium-titanium (NbTi) cables wrapped with copper. It provides a significant bending power, fundamental to be able to perform precise measurements of the transverse momentum of charged particles, both in the tracker and in the iron yoke. The magnet is kept at $T = 4$ K to maintain the superconducting mode in a vacuum cylinder which isolates it from the outside, allowing 19.14 kA of current to flow without almost any resistance. The magnet is able to provide a 4 T magnetic field, but it is lowered to 3.8 T in order to maximize the longevity of the material. The structure, 12.5 m long, with an inner diameter of 6 m and a total weight of 220 tons, is completed by an external iron yoke which is responsible for the return of the magnetic flux. The yoke is made of 5 layers in the barrel and 3 disks for each endcap, for a total weight of 10000 tons, that extends up to 14 m in length and absorbs all particles except for muons and neutrinos. A map of the magnetic field strength of the CMS magnet is shown in Figure 2.13.

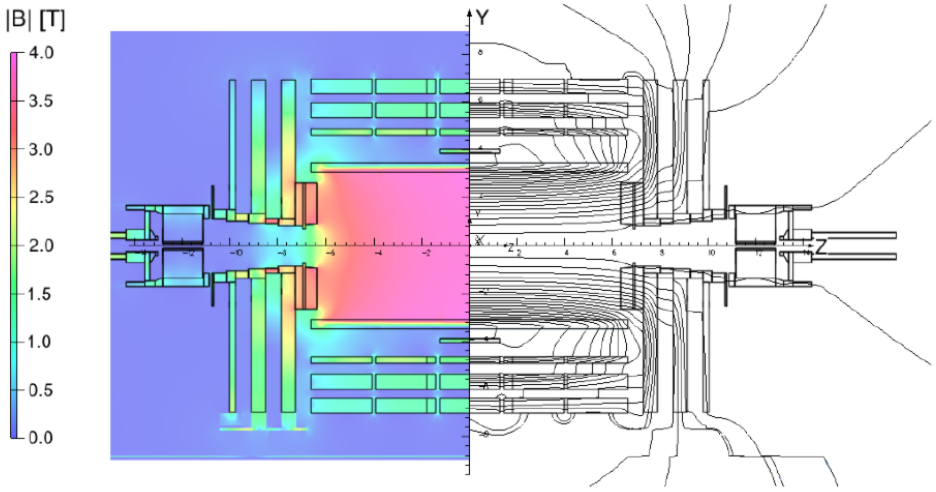

Figure 2.13: Map of the magnetic field intensity (left) and field lines (right) predicted for a longitudinal section of the CMS detector using a 3.8 T magnetic field model produced by the CMS solenoid [65].

2.2.5 Muon system

The CMS muon system [66], shown in Figure 2.14, is the outer part of the detector and is designed to identify muons, which are the only charged

particles that can fully penetrate the inner detector layers. Its goals are: to measure their transverse momentum and trajectory thanks to the magnetic field ($\simeq 1.8$ T) created by the return yoke; to complement the inner tracker information (even if muon system standalone measurements are also possible); to act as muon trigger. It covers the pseudo-rapidity region $|\eta| < 2.4$ and is entirely made of gaseous detectors, that use the ionization electrons created by the passage of charged particles in a gas volume immerse in an electric field to produce the signal. Three different types of gaseous detectors are employed, chosen accordingly to the expected background rate and the uniformity of the magnetic field in the various regions: drift tubes in the Muon Barrel region (MB) up to $|\eta| < 1.2$, cathode strip chambers in the Muon Endcap region (ME) where $0.9 < |\eta| < 2.4$, and resistive plate chambers in both MB and ME up to $|\eta| < 1.6$ to improve redundancy.

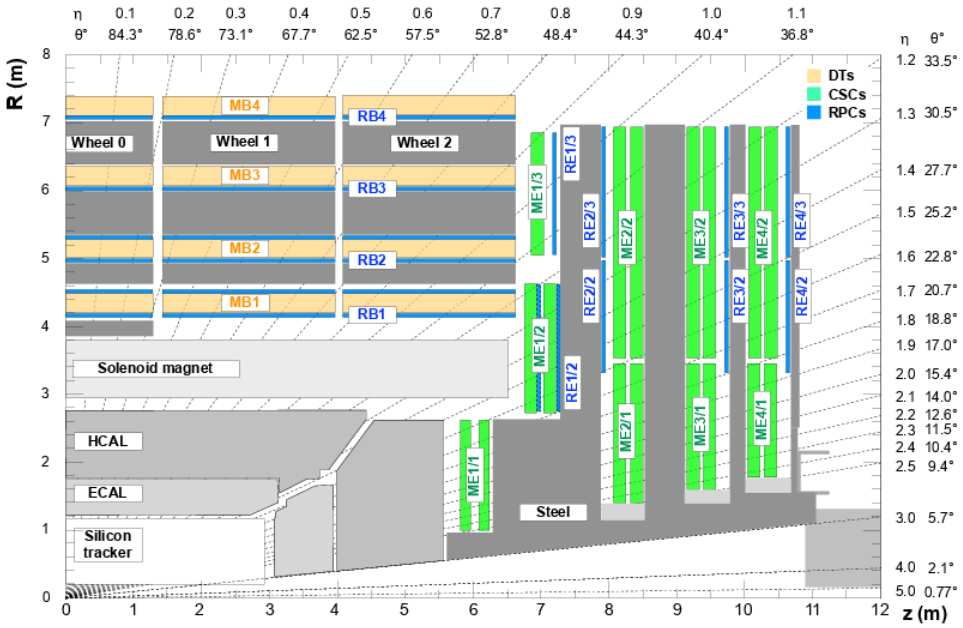

Figure 2.14: Longitudinal view of a quarter of the CMS detector, with DTs in orange, CSCs in green, and RPCs in blue regions [66].

Drift tubes Drift tube chambers (DTs) are rectangular (2×2.5 m^2) detectors organized in 5 barrel sections, "wheels", each consisting in four concentric rings of DT stations (MB1, MB2, MB3 and MB4), divided in 12 contiguous sectors, as shown in Figure 2.15. For the first three stations, each DT chamber is composed of three Super-Layers (SL), two composed of four layers of

drift cells each, oriented to measure the muon position in the $r-\phi$ plane, and one SL made of four layers of cells in the orthogonal direction, to measure the z-coordinate. In the MB4 stations these last layers are missing and the muon position is given in the $r-\phi$ plane only. The basic element of this detector is thus a DT cell, which has a transverse area of 4.2×1.3 cm^2 with a 50 μm stainless steel anode wire in the center. It is filled with a mixture of Ar (85%) and CO_2 (15%) that provides a 55 μm/ns drift velocity. When a muon passes through the detector, it ionizes the gas producing electrons which travel towards the anode wire: the measurement of the drift time provides the position and incident angle of the muon. The spacial resolution of each cell is $\simeq$ 200 μm, for a global resolution for the chamber of about $80-120$ μm. Consecutive layers are staggered by half a cell width to improve the coverage and efficiency (which reaches 99.8%) and provide an accurate bunch crossing (BX) identification [67].

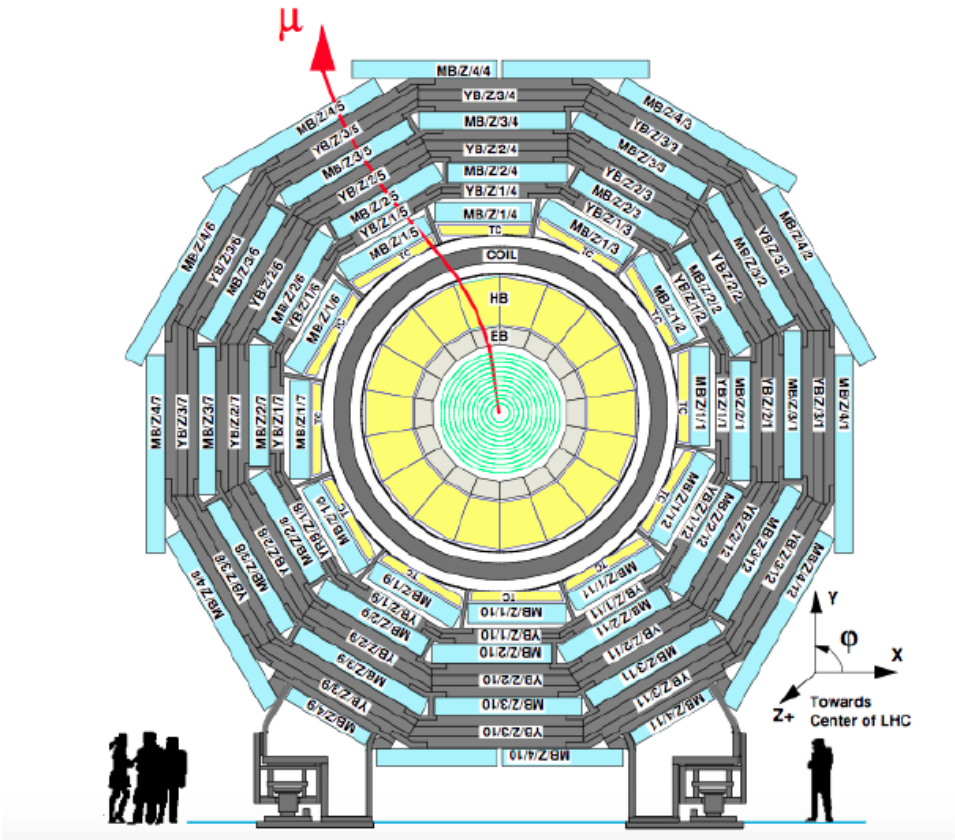

Figure 2.15: Transverse view of the CMS barrel muon system. Each wheel consists of twelve sectors formed by DTs (light blue) embedded in the yoke (gray) [66].

Cathode strip chambers Cathode strip chambers (CSCs) are multi-wire proportional chambers with the cathode planes segmented in negatively-charged strips orthogonal to positively-charged anode wires. Thanks to their fan-shape, consisting in trapezoidal panels mounted on eight disks, four in each endcap, partially overlapping in the $\phi-$plane to improve the coverage and efficiency, they can easily be arranged in the endcap regions. CSCs are filled with a mixture of Ar (40%), CO_2 (50%) and CF_4 (10%) gas that gets ionized upon the passage of a muon: the signal on wires and strips is interpolated to provide a measurement in the $r-\phi$ plane (from the wires) and in the z-direction (thanks to the strip segmentation), with a resolution ranging from 50 to 150 μm.

Resistive plate chambers Resistive plate chambers (RPCs) are made of four 2 mm Bakelite planes which form two gaps of 2 mm width filled with a mixture of $C_2H_2F_4$ (95.2%), i-C_4H_{10} (4.5%) and SF_6 (0.3%). These detectors are operated in avalanche mode, with the avalanche signal being readout by aluminum strips in the outer surface of the gaps, separated from the graphite by an insulating Polyethylene Terephtalate (PET) film. Their spacial resolution is very modest, from 0.8 to 1.2 cm, but their excellent time performance, of the order of the ns, makes them suitable for triggering purposes and precise time measurements. Furthermore, the presence of a double gap provides a high efficiency with lower electric fields, with respect to single gap chambers.

Combining the three above mentioned sub-detectors, the overall space resolution of the muon system is of the order of 250 μm in the $r-\phi$ plane and of 500 μm in the z-direction; the reconstruction efficiency is close to 100%.

2.2.6 Trigger and data acquisition

The CMS trigger and data acquisition system (DAQ) [68, 69] is designed to collect and analyze the detector information every 25 ns, that is at every bunch crossing: this would produce an amount of data of 70 terabytes. Since this quantity is too high to be handled by the storage system, the trigger is a fundamental part of the experiment, making a real-time selection of the events to store, choosing interesting collision events only. A multi-level trigger is adopted: the first level, called Level-1 trigger (L1), is based on custom hardware electronics while the second (L2) and third (L3) levels are software based, referred to as high-level trigger (HLT).

Level-1 trigger The L1 trigger needs to take a decision on accepting an event every 25 ns. For this reason it consists of a custom-designed programmable hardware that performs a rough identification of particles in the sub-detectors reducing the rate from 40 MHz to a maximum of 100 kHz. This trigger operates using a pipeline structure, which allows the temporary storage of the full event information in pipeline memories, for a latency up to 3.8 μs, after which the system needs to decide whether to discard the event or to accept it and send it to the HLT. Trigger information provided by the several subdetectors are sent to dedicated hardware in charge to build physics object candidates with coarse granularity: the L1 calorimetric trigger, which identifies electrons/photons objects (EG), jets and missing transverse energy, and the L1 Muon trigger, which identifies muons from the muon system. The candidate objects are sent to the L1 global trigger, which combines the information from the previous two and takes the final decision according to pre-defined algorithms. The L1 structure is shown in Figure 2.16. The Global Trigger performs its decision according to a "menu" where thresholds are set for candidate objects properties (i.e. pt, energy, isolation). Events accepted according to the L1 menu from the L1 Global Trigger serve as "seeds" for the HLT. During LS1, readout and electronics of the L1 trigger have been replaced, adding more sophisticated algorithms and new electronics boards mounting field-programmable gate arrays (FPGAs), to cope with higher pileup and luminosity conditions of Run 2 data taking. In particular, better position and energy resolution on jets and EG candidates have been achieved.

High-level trigger The HLT is a software system that performs event building, selected reconstruction and event selection on commercial processors (22 thousands CPU cores), reducing the rate below 1 kHz. It receives data filtered from the L1 trigger and performs a better reconstruction and selection of the events accessing the complete information of the collision at full granularity from all sub-detectors. In order to pass this trigger level, an event needs to satisfy the requirements of at least one of its paths, defined in the HLT menu, similarly to what was previously mentioned for the L1 trigger. Each trigger path targets a certain event topology, suitable for different studies such as the search for top-quarks, Higgs boson, supersymmetric particles, etc. and defines a sequence of modules which are run sequentially to optimize the computational execution time. The first step, L2, accesses calorimeter and muon system information only; the second step, L3, is conditioned to the L2 decision since it includes the reconstruction of the complete tracks in the tracker, a process that requires a large amount of CPU time. HLT too has

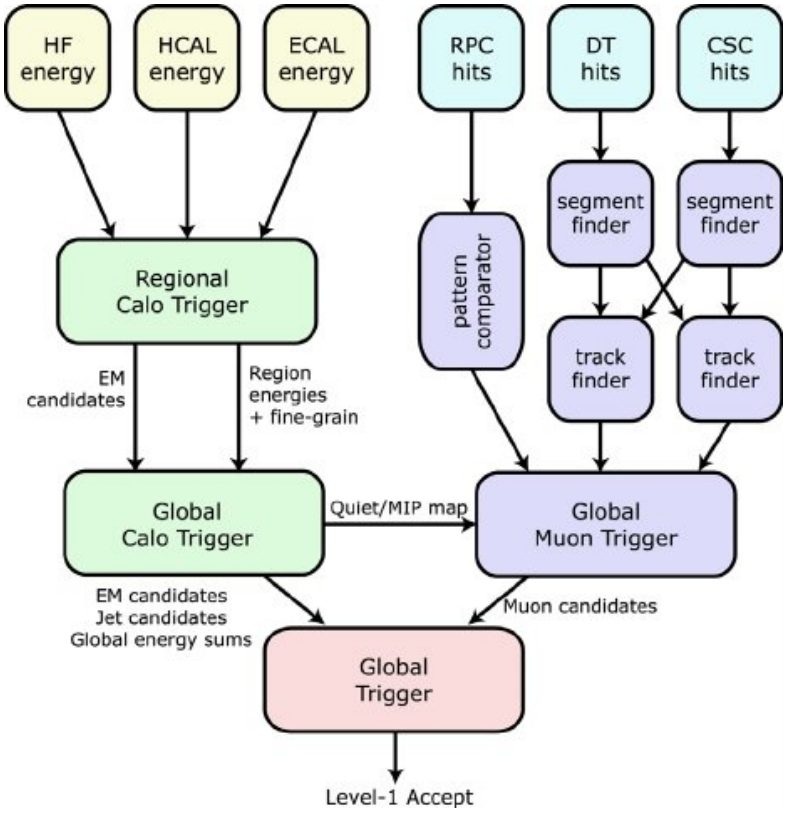

Figure 2.16: Schematic overview of the CMS L1 trigger.

been upgraded during the LS1, porting some offline algorithms, such as the particle-flow and the particle identification and isolation algorithms to the trigger level (see Section 2.3 for details about these algorithms). The result of the final selection is called raw data: they contain the event information, the L1 trigger and HLT results, and are stored on tape and sent to several data center spread all around the word that are connected in a worldwide computational GRID.

2.3 Physics objects reconstruction and identification in CMS

The raw data selected as coming from interesting events consist of electric signals such as hits in the tracker and muon chambers or energy deposits in the calorimeters, that need to be converted in physics objects or properties. This process is performed offline, in order to fully exploit CPU time and computation resources. In Figure 2.17 a simplified sketch of the typical

particle signatures are represented. All charged particles leave a series of hits in the tracker, which are reconstructed as part of a track; an electron leaves also an energy deposit in the ECAL, while a charged hadron in the HCAL; muons leave a track both in the tracker and in the muon system; neutral particles such as photons and neutral hadrons are reconstructed from an energy deposit in the ECAL or the HCAL respectively, and not matched to any track in the inner tracker. Elementary objects such as charged and neutral hadrons, electrons, photons, and muons are then subsequently combined to reconstruct more complex objects such as jets, missing transverse energy, etc. Since the above picture is an ideal situation, that does not occur in real collisions due to other effects of particles interacting with the detector material, such as Bremmstrhalung emission by electrons, or multiple scattering that affects muons, the particle-flow (PF) method is used to perform the best object reconstruction possible.

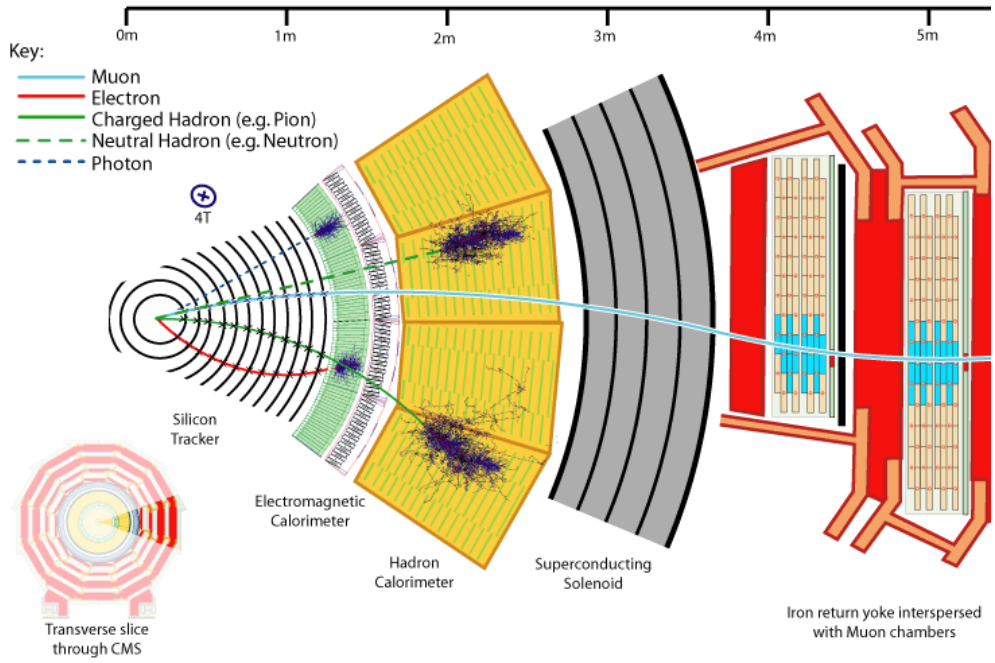

Figure 2.17: Schematic view of a transverse slice of the CMS detector, showing the specific signature of different types of detected particles.

2.3.1 The particle-flow algorithm

The particle-flow reconstruction [70] is a method that reconstructs the stable final-state particles in each event combining all sub-detectors informa-

tion, providing a global event description that leads to unprecedented CMS performances in reconstruction and identification of physics objects, together with a great pileup rejections capability. This is possible thanks to the properties of the detector itself, such as the highly segmentation of the tracker, the fine graining of the ECAL, the hermetic HCAL, the strong magnetic field, and the excellent muon spectrometer.

Tracking The algorithms implemented in CMS to reconstruct tracks use the hits of the charged particles in the silicon tracker to determine their helicoidal trajectories and measure their direction and momentum. The sequence of algorithms used in CMS is a combinatorial track finder based on Kalman Filtering (KF) [71] composed of three steps: track seeding, finding and fitting. The seeding step consists in looking for pairs of hits that can be candidates of charged tracks. The pixel information is used for better precision, except for the region $2 < |\eta| < 2.5$, where the information from the inner strips is added not to loose efficiency. The track finding stage is based on the Kalman Filter pattern recognition approach that starts from the seeds, extrapolates the track trajectory to the neighboring layers, and adds the compatible hits to the track. The track fitting process is obtained using again the Kalman Filter, applying the least-squares fit method in two ways: firstly from the interaction region to the outer hits and secondly from the outside to the inside, smoothing the trajectory and giving the best estimate of the track parameters. The combinatorial track finder is applied in an iterative procedure increasing moderately the efficiency at each step, but keeping the highest possible purity [72].

Clustering A specific clustering algorithm developed for the PF event reconstruction performs the clustering of energy deposit separetely in ECAL and HCAL, and separately for the barrel and endcap regions (no clustering is performed for HF where the energy deposits are directly transformed into clusters). It identifies local energy maxima, called seeds, and creates PF clusters aggregating neighbor cells that satisfy specific energy and topological criteria. The PF clusters are then calibrated to correct for energy loss in the dead material between ECAL and HCAL and other effects occurred in the clustering process.

The individual PF elements can be associated, or "linked", to create PF blocks with all sub-detectors information. For each block, the PF reconstruction and identification proceeds by analyzing the structure and properties of the block itself to identify the final physics objects:

1. Tracks corresponding to reconstructed and identified muons are removed from the block.

2. Electrons are reconstructed including the energy of all Bremmstrahlung photons emitted, procedure that allows also to distinguish and identify energetic and isolated photons. Then the same procedure described for muons is applied to electrons, for which also ECAL or preshower energy deposits are removed from the PF block.

3. Tracks with large uncertainties are removed.

4. Muons within jets[2] are identified exploiting the tracker information and removed from the block, since they can cause a disagreement between the sum of the cluster energy and the sum of the track momenta.

5. For each of the remaining tracks in the PF block, charged hadron candidates are created, and their momenta are set to the track momenta.

6. PF photons are created if there is an energy excess in the cluster energy with respect to the sum of track momenta that is equal or smaller than the ECAL energy, while PF neutral hadrons are created if the excess is greater than the ECAL energy.

7. Clusters that are not linked to tracks are used to create additional PF photons and neutral hadrons.

The output of the particle flow algorithm is then a list of mutually exclusive PF candidates, that are subsequently used for further data processing such as jet reconstruction, isolation and missing transverse energy calculation.

2.3.2 Muon reconstruction

Thanks to the unique interactions of muons in the muon spectrometer, they are reconstructed with a dedicated algorithm independent from the PF iterative tracking procedure described above. Their reconstruction is based on both tracker and muon system information, taking into account also the calorimeter energy deposit information. In the CMS muon reconstruction procedure, tracks are built from the tracker and from the muon system independently [73]. Different collections are produced: stand-alone muons, reconstructed using the muon system information only (DT, CSC and RPC hits); tracker muons, reconstructed starting from inner trackers tracks extrapolated

[2]a jet is a collection of particles produced by the hadronization of a quark or a guon, concentrated in a narrow cone, as will be explained in Section 2.3.4

to the muon system and matched to muon segments; global muons, that are reconstructed combining both stand-alone and tracker muons information. If the transverse momentum of the muon candidate is lower than 200 GeV, its charge and momentum are computed with the tracker information only, since it is more precise than the global muon informatiom, which becomes competitive at $p_T \geq 200$ GeV. Thanks to the high granularity of the tracker and to the high efficiency of the muon system, almost 99% of the muons produced in a collision are reconstructed as tracker or global muons.

2.3.3 Electron reconstruction

The electron reconstruction and identification are based on the tracker and ECAL information [74, 75]. PF clusters in ECAL and in the preshower are grouped in superclusters which merge the energy of Bremsstrahlung photons emitted by electrons in the active detector material. Then the tracking Gaussian Sum Filter (GSF) algorithm [76] is applied to take into account large Bremmstrahlung energy emission that could cause sudden curvature radius change to the electron candidate trajectory, and to approximate the radiation energy loss with a sum of gaussian distributions. This tracking is initiated with two different and independent procedures: the ECAL-seeding which estimates the expected track position from PF candidates with $E_T > 4$ GeV, and the tracker-seeding that starts from tracks with $p_T > 2$ GeV and look for matching PF superclusters; the first process is particularly efficient for high transverse momentum electrons ($p_T > 10$ GeV), while for low p_T electrons it has to be complemented with a tracker-driven approach. Once built, GSF tracks are associated to PF superclusters to form electron candidates. The electron transverse momentum is found using the GSF information.

2.3.4 Jet reconstruction

Jets are a set of hadrons and other particles inside a narrow cone that are produced from the ionization of a quark or a gluon: the goal of the jet reconstruction procedure is to compute the kinematics properties of the initial quark/gluon using jet components. Jet reconstruction [77] is based on the FASTJET package [78] and uses as inputs to reconstruction algorithms all possible PF candidates. The most exploited algorithm is the anti-k_t method [79]: it iteratively combines PF candidates that are close to each other around the hardest particles in the event, producing conic shape jet candidates, with radius of the cone defined by the parameter R. The jet four-momentum is computed combining the information of the particles in the cone using the vector sum of their four-momenta. Jet energy scale are

then applied to take into account pileup contributions and other effects linked to the detector response for hadrons [80].

2.4 The CMS upgrade for High Luminosity LHC

The upgrades foreseen during the LS3 to the LHC machine to prepare it for the HL phase will increase the instantaneous luminosity up to $5 \cdot 10^{34}$ $cm^{-2}s^{-1}$. This will lead to 140-200 additional interactions per bunch crossing (pileup), that will constitute a challenge for the detectors event reconstruction, together with the radiation damage. The basic goal of the Phase-II upgrade program of CMS is to maintain the excellent performance of the actual CMS detector for what concerns the efficiency, resolution and background rejection for the object reconstruction. As already said, the two main challenges to overcome are the high pileup and the radiation damage. At the nominal luminosity of the HL-LHC, the average number of interactions per bunch crossing will rise to 140-200. The majority of these events contains low p_T particles and produce small quantities of energy in the detector, and only a small fraction of all collisions contains high transverse momentum particles that may come from new high mass objects (called "hard" collisions). For this reason is essential to be able to reject the pileup events. For the so-called in-time pileup, that is the events or energy deposits from extra (with respect to the collision containing the hard scattering) pp collisions in the current bunch crossing, the granularity of the tracking system and of the calorimeters will be crucial to distinguish pileup tracks from the interesting tracks, preserving resolution and correct identification. For the out-of-time pileup, that is the events or energy deposits from previous or later bunch crossing with respect to the current one, timing measurements will be fundamental. The LHC will produce collisions at a rate of about $5 \cdot 10^9$ Hz. The particles emerging from the pp collisions and the radioactivity they induce in the material of the detectors and the electronics will cause significant damage to the detector material that could result in a progressive degradation of the detector performance. In fact, charged particles produce ionization and nuclear interactions causing shower of secondary particles that consequently interact with the detector producing additional radiation. Figure 2.18 shows the distribution of the absorbed dose of the CMS detector for an integrated luminosity of 3000 fb^{-1}.

To reduce these problems, and maintain good performance, all CMS subdetectors will undergo major upgrades and partial or total substitutions of their components.

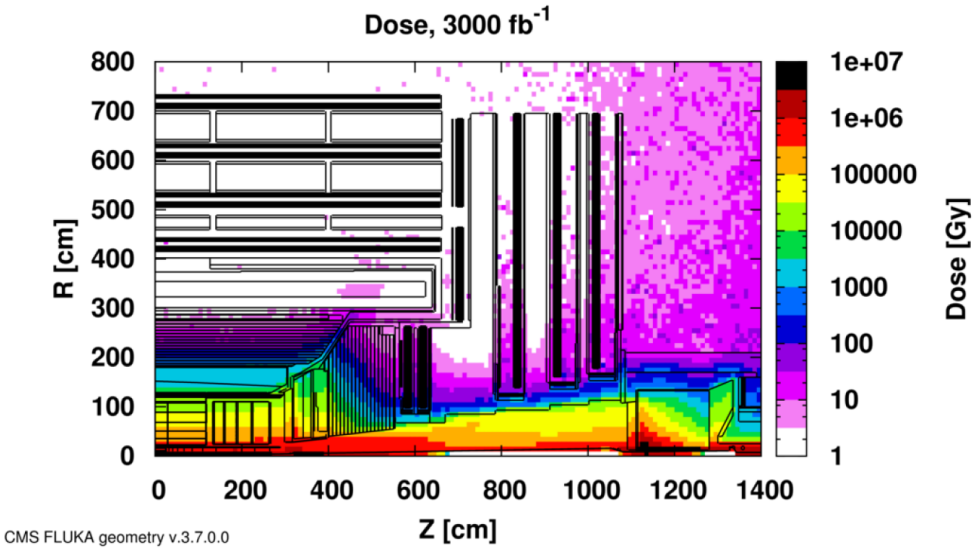

Figure 2.18: Absorbed dose in the CMS cavern after 3000 fb^{-1} of integrated luminosity: R is the transverse distance from the beam pipe, Z is the longitudinal distance along the beam pipe from the interaction point (Z=0) [81].

Trigger upgrade The entire trigger system will be replaced for the HL-LHC phase [82]: the detector readout electronics will be upgraded to allow a maximum L1 response rate of 750 kHz and a latency of 12.5 ms. In addition, the L1 trigger will also include tracking information from the silicon tracker and high-granularity calorimeter information, allowing real-time track fitting a particle-flow reconstruction of objects at the trigger level.

Tracker system upgrade Even if the present strip tracker is performing very well at the current instantaneous luminosities that are well above the design value of $1 \cdot 10^{34}$ cm^{-2}s^{-1}, its performance will worsen due to radiation damage after 500 fb^{-1}. The original pixel tracker has already been replaced with the Phase-I pixel tracker [62] during the extended year-end technical stop (EYETS) in 2016-2017 to address inefficiencies in the readout chip at high rates. During the LS3 both the strip tracker and the Phase-I pixel detector will be replaced due to the significant damage and performance degradation they would suffer during operations at the HL-LHC, and to cope with the more demanding operational conditions. The Phase-II tracker will consist of an Inner Tracker (IT) and an Outer Tracker (OT). The Inner Tracker is composed of pixel modules segmented into pixel sizes of 25×100 mm^2 or 50×50 mm^2. The barrel region of the IT is realized with four cylindrical layers while the endcap region of the IT is made of eight small

plus four large ring modules per side. The IT is inserted in the region $r < 200$ mm for $|z| < 1600$ mm and $r < 300$ mm for $|z| > 1600$ mm [83]. The Outer Tracker is composed of six cylindrical barrel layers in the central region ($|z| < 1200$ mm) and of five endcap double-disks per side ($1200 < |z| < 2700$ mm), between $r \approx 21$ cm and $r \approx 112$ cm, segmented in silicon modules called "p_T" modules, since they are able to reject signals from particles below a certain p_T threshold, implementing the L1 trigger functionality. The p_T modules appear in two versions: modules with two strip sensors with a length of about 5 cm (2-strip or 2S modules) and modules with one strip (2.4 cm long) and one macro-pixel sensor of about 1.5 mm length (pixel-strip or PS modules). The three inner (outer) layers of the barrel region of the OT are realized with PS (2S) modules while the endcap region of the OT is arranged in rings with the inner (outer) region composed of PS (2S) modules. The tracker upgrade will result in:

- radiation tolerance up to 3000 fb^{-1} with safety margin;
- increased granularity to maintain tracking efficiency at high pileup with an occupancy level of the per cent level (per mille level) in the Outer Tracker (Inner Tracker);
- reduced material budget to improve the impact of the tracker volume on the calorimeter and object reconstruction performance;
- extended tracking acceptance up to $|\eta| < 4$.

One quarter of the Phase-II tracker layout is shown in Figure 2.19.

Calorimeter upgrade The calorimeter will undergo different upgrades depending on the region: barrel ECAL (EB), barrel HCAL (HB), endcap calorimeter (EE and HE).

In order to accommodate the L1 trigger requirements on latency (from 4 μs to 12.5 μs) and rate (from 100 kHz to 750 kHz), provide more precise timing resolution and help mitigating the noise from the photodetectors, the barrel ECAL will feature an upgraded front-end electronics. With this electronics the EB will provide single-crystal information to the L1 trigger, and 160 MHz sampling to allow high precision timing capabilities useful for the determination of the production vertex of di-photon events. The noise will also be reduced thanks to an optimization of the preamplifier architecture and characteristics, and to lower supermodule operating temperature (from 18 to 9 °C) [84].

For what concerns the barrel HCAL, the Phase-I front-end electronics with silicon photo-multipliers (SiPMs) that are being installed during the

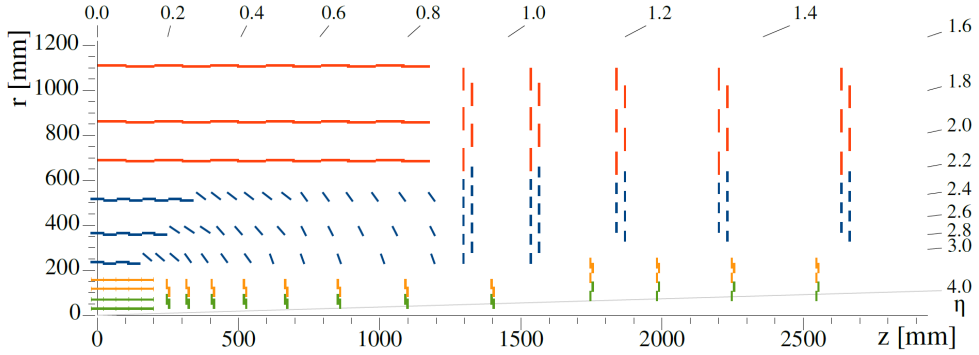

Figure 2.19: One quarter of the Phase-II tracker layout in the $r-z$ view. The green lines correspond to pixel modules made of two readout chips and the yellow lines to pixel modules with four readout chips of the Inner Tracker, while the blue and red lines represent the PS and 2S modules of the Outer Tracker [83].

current LS2 to replace the HPDs, will not be substituted during LS3 since they will be able to sustain HL levels of radiation. On the contrary, the back-end electronics based on the μTCA standard wil not be able to substain the 750 kHz L1 trigger rate, and will be therefore upgraded to the ATCA standard using the same boards developed for EB [84].

Both electromagnetic and hadron endcap calorimeters need to be replaced for the HL-LHC era. In fact the the $PbWO_4$-based EE and the plastic scintillator based HE were designed for an integrated luminosity of 500 fb^{-1} and will loose in physics performance beyond this integrated luminosity. They both will be substituted with a high granularity calorimeter (HGCAL), with silicon sensors as active material in the front section, more than capable to tolerate the expected fluence of around 10^{16} n_{eq}/cm^2 (where n_{eq}/cm^2 denotes the number of 1 MeV equivalent neutrons per square cm) and a maximum dose of around 2 MGy, and plastic scintillator tiles readout by SiPMs towards the rear, where the maximum expected fluence will be of about $8 \cdot 10^{13}$ n_{eq}/cm^2 and the dose of about 3 kGy [85]. In order to reliably operate silicon sensors after irradiation, and to keep the energy equivalent to the electronics noise sufficiently low, the whole calorimeter will be operated at around -30 °C. The HGCAL consists of an electromagnetic compartment (CE-E) followed by a hadron compartment (CE-H), as shown in Figure 2.20.

The CE-E consists of 28 sampling layers with a total thickness of 34 cm and a depth of approximately 26 X_0 and 1.7 λ. The active detector element is a 163 mm wide hexagonal silicon sensor sandwiched between a 1.4 mm thick WCu baseplate and a printed circuit board that carries the

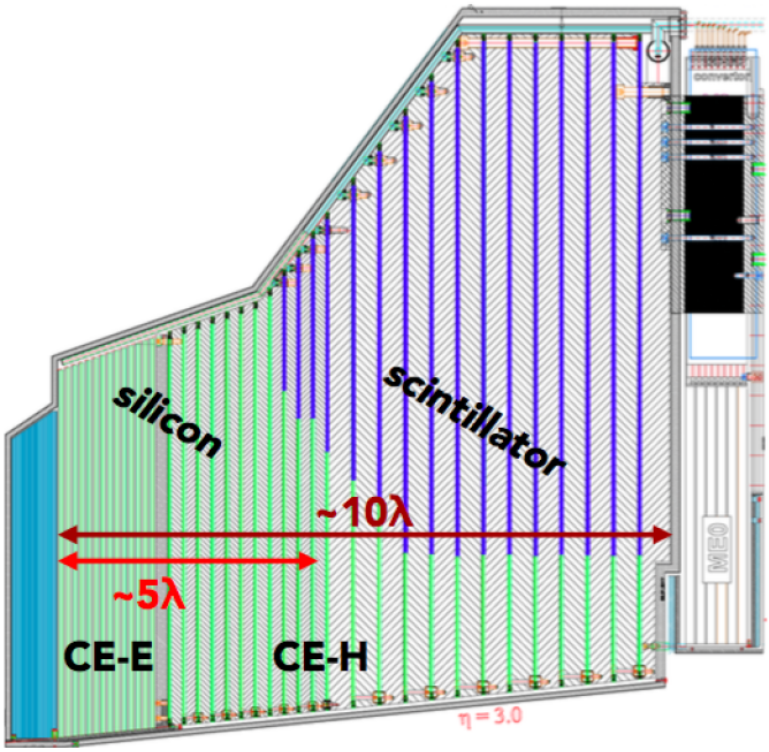

Figure 2.20: Longitudinal cross section of the upper half of one endcap calorimeter [86].

front-end electronics to form a silicon module, realized in three different sensitive thickness: 300, 200, and 120 mm, in regions of increasing fluence, respectively. The WCu baseplate and a 6 mm thick Cu cooling plate represent the absorber layer on one side of the active layer; on the other side, the absorber layer is composed of two 2.1 mm thick lead planes clad with 0.3 mm stainless steel sheets. Each plane of this structure is divided into 60 units called cassettes and 14 layers of these cassettes provide the full 28 sampling layers. The CE-H absorber is composed of 12 planes of 35 mm thick stainless steel plates followed by another 12 stainless steel planes, 68 mm thick. The active material is placed between the absorber plates, and is made of silicon modules and scintillator tileboards mounted on 6 mm thick copper cooling plates to form 30 wide cassettes. The total HGCAL thickness, perpendicular to the layers, is of about 10.7 λ. This kind of design will preserve the energy resolution and lateral compactness of the showers, with improved capability of two shower separation and fine sampling of the longitudinal shower development thanks to the extremely high granularity.

Muon system upgrade The existing muon system will be upgraded for HL-LHC, especially for what concerns the detector electronics, and will be provided with new muon stations as described in the following.

The existing DT, CSC, and RPC detectors will need an upgrade of the electronics [87]. The electronics attached to each DT chamber will be replaced to be able to cope with the 500 kHz of L1 trigger rate and with increased dose of radiations. Furthermore, the new back-end electronics will be placed outside the experimental cavern, thus more accessible, and will contain all trigger and event building logic. The CSC readout electronic boards will also need to be replaced in order to handle the more strict L1 trigger requirement and the higher chamber occupancy with higher speed optical links and faster processors. Since the new electronics will consume more power, both the low and high voltage systems will be upgraded. The link system of the RPC chambers, which send the data from the RP front-end electronics to the trigger and readout, will be completely replaced, since it is composed of obsolete components. This upgrade will make the RPC system robust against electromagnetic noise and improve the time resolution measurements.

The existing muon system will be also equipped with new detectors in the forward region, called RE3/1 and RE4/1 that will be added to the existing ME1/1 and ME2/1 stations, GE1/1 (installation during the ongoing LS2), GE2/1 and ME0 [87], covering the pseudorapity region up to 2.8, as shown in Figure 2.21.

The RPC upgrade extends the acceptance from $|\eta| = 1.9$ to 2.4, with the two rings of the RE3/1 and RE4.1 stations, that will exploit an improved version of the RPC technology, iRPC, to be able to cope with the high rate of 2 kHz/cm^2. The iRPCs will use thinner electrodes and a narrow gas gap, both of about 1.4 mm, to shorten the recovery time of the electrodes and reduce the total charge produced during discharge phenomena. To overcome the loss in gas gain, due also to the lowering of the high voltage, the front-end electronics will be improved to obtain higher signal amplification.

During the ongoing LS2, a new set of muon detectors, GE1/1, is being installed [88]: realized with the gas electron multiplier (GEM) technology, they will cover the first endcap muon station to improve the forward muon triggering and reconstruction capabilities of the CMS detector in the $1.6 < |\eta| < 2.2$ region in the face of High Luminosity. The GEM technology [89, 90, 91] consists of a 50 μm thick Kapton® foil, clad on both sides with a 5 μm thin copper layer. The foils are chemically perforated with holes of 70 (50) μm of external (internal) diameter, and a pitch of 140 μm. The detector is filled with gas that, applying an high electric field between the two side of the foil, is ionized by transpassing charge particles: the result is avalanche

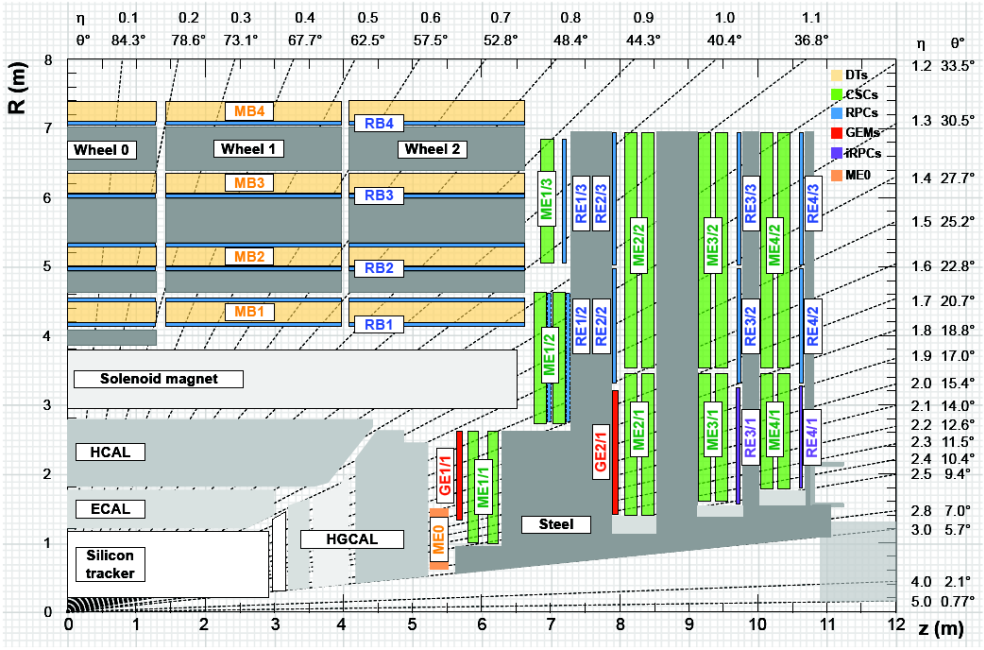

Figure 2.21: A $r-z$ cross section of a quadrant of the CMS detector, including the Phase-II upgrade new detectors RE3/1, RE4/1, GE1/1, GE2/1, ME0. The interaction point is at the lower left corner [87].

multiplication processes in the holes. Combining three foils in the Triple-GEM configuration, the gas gain is about 10^4. The electrical signal is then readout by a PCB equipped with strip electrodes, as shown in Figure 2.22.

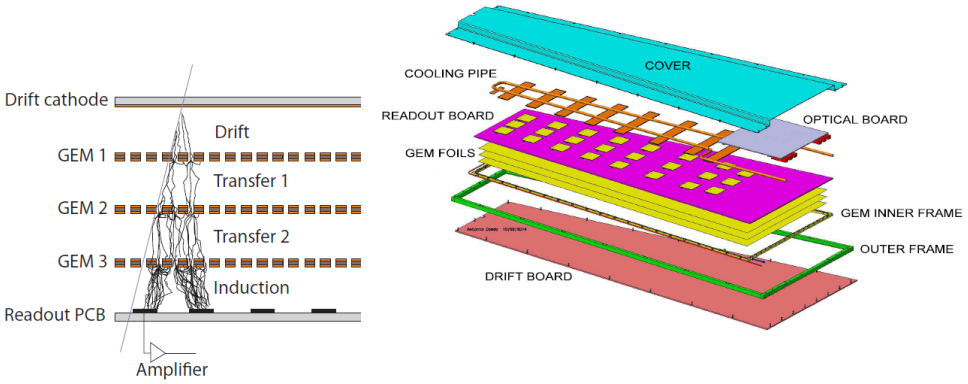

Figure 2.22: Scheme of a Triple-GEM chamber with three foils (left) and its exploded view of the mechanical design [88].

In the GE1/1 detector, two Triple-GEM chambers are combined to form

a "superchamber", that will provide two measurements planes. Each superchamber covers a 10° sector, for a total of 36 superchambers per endcap, installed in a ring shape structure with two alternate ϕ long ($1.55 < |\eta| < 2.15$) and short ($1.61 < |\eta| < 2.15$) versions, due to the mechanical constraint in the existing muon region. Each chamber has a drift gap 3 mm wide, while the induction and transfer gaps are 2 mm thick. The gas mixture employed is the non-flammable and environmentally-friendly Ar/CO_2 (70/30 %). Each chamber is segmented in both ϕ and η to obtain a total of 24 sectors per chamber, each of them divided into 128 strips readout by a 128-channel front-end electronic chip. During the LS3, the new GE2/1 and ME0 detectors will be then installed. The GE2/1 upgrade consists in a second ring of GEM detectors in the endcap region $1.6 < |\eta| < 2.4$, partially overlapping with the GE1/1 chambers, composed of two layers of Triple-GEM chambers, as shown in Figure 2.23. The GE2/1 chambers will each cover 20° in ϕ and will have the same technical characteristics of the GE1/1 chambers detailed previously. The ME0 station will instead increase the acceptance up to $|\eta| < 2.8$, which is the maximum possible range allowed by mechanical constraints, providing muon trigger inputs in this very forward region. This station will consist of six layers of Triple-GEM chambers, each covering 20° angle in the $2.0 < |\eta| < 2.8$ region, for a total of 108 chambers per endcap. The inner (outer) radius is 0.6 (1.5) m, with 8 sectors in η and 3 in ϕ for a total of 128 radial strip per ϕ sector. The same gas mixture used for GE1/1 and GE2/1 will be employed.

MIP Timing detector Since the calorimeter-based methods for track timing of hadrons are insufficient in terms of needed precision or efficiency, a hermetic timing detector dedicated to MIP detection will be installed during the LS3, to provide efficient time vertex reconstruction, and the use of timing in track-vertex association and in the object reconstruction [92]. The MIP timing detector (MTD) will be composed of a barrel ($|\eta| < 1.5$) and an endcap region ($|\eta| < 3.0$), as shown in Figure 2.24. In the barrel, a thin, actively cooled, standalone detector, based on lutetium-yttrium orthosilicate crystals activated with cerium (LYSO:Ce) of about 12×12 mm^2 read out by 4×4 mm^2 SiPMs will be installed, covering a surface of about 40 m^2. The crystal thickness will vary between about 3.7 mm ($|\eta| < 0.7$) and 2.4 mm ($|\eta| > 0.7$). The same technology cannot be implemented in the endcap due to radiation tolerance limitations. For this reason, in the endcap a hermetic single layer of MIP-sensitive silicon devices with high time resolution will be installed, covering the $1.6 < |\eta| < 3.0$ region, for a total area of about 6 m^2 per side. The time resolution that can be obtained with the MTD is of about

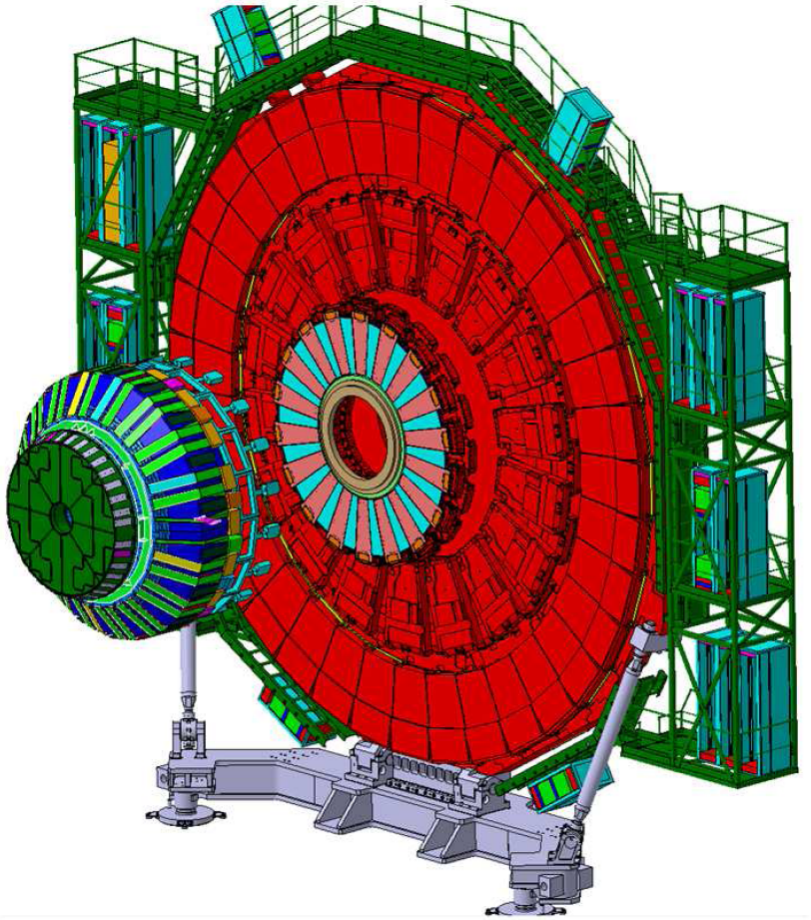

Figure 2.23: Location of the 18 GE2/1 detectors (light blue and red) on the back of the yoke disks [87].

30 ps in the barrel, and ranges from 30 to 50 ps in the endcap, depending on the η region (resolution decreases at greater pseudo-rapidities).

2.5 Future circular hadron collider

To extend the physics search currently conducted at the LHC, after the end of its lifespan (in 2035, including the HL-LHC period), the Future Circular Collider Study (FCC) is developing a new project for an unprecedented dimensions and physics reach: a future circular collider with an extremely high collision energies, in the search for new physics [93]. The FCC Study, hosted by CERN, is an international collaboration of more than 150 universities, research institutes and industrial partners from all over the world. The FCC

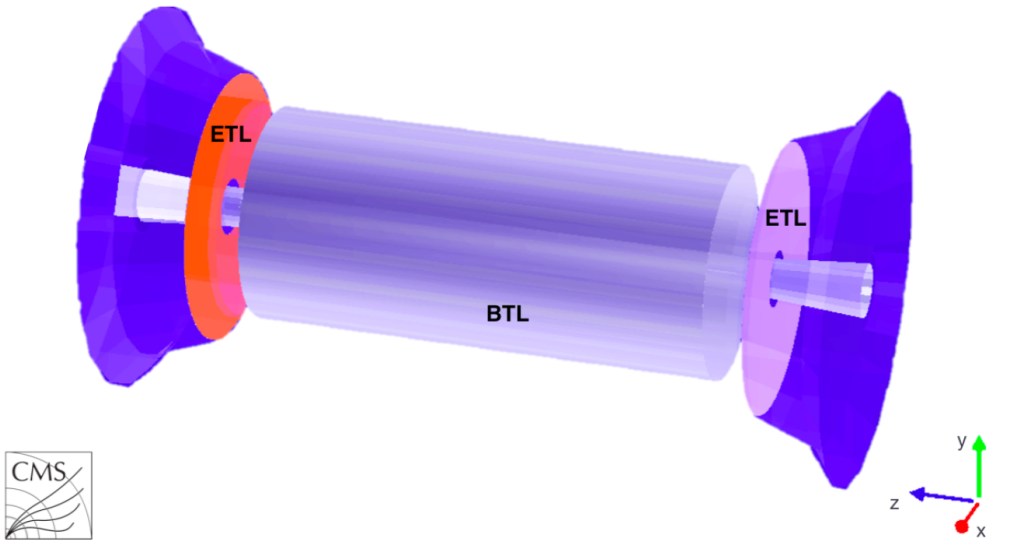

Figure 2.24: Simplified geometry of the new MTD layer: LYSO barrel (grey cylinder) between tracker and ECAL, and two silicon endcap (orange disks) layers in front of the CE-E calorimeter [92].

takes into consideration three different types of particle collisions: hadron (proton-proton and heavy ion) collisions, like in LHC; electron-positron collisions, as in LEP; and proton-electron collisions. For this reason, two different types of colliders are planned: a high luminosity electron-positron machine (FCC-ee) [94] and a high energy proton-proton collider with a center-of-mass energy of 100 TeV (FCC-hh) [95]. The latter is the ultimate goal of the project, and could be realized either after the FCC-ee, or independently directly after the HL-LHC era. The FCC-hh, that is the focus of this Section, will extend the current energy frontier by almost an order of magnitude, and the mass reach for direct discovery will reach several tens of TeV, with unprecedented possibility to discover new particles. Furthermore, with this collider the Higgs self-coupling will become completely accessible and its precise measurement will become possible, as well as other aspects of the EW symmetry breaking, or dark matter candidates, that could be discovered or ruled out.

2.5.1 The FCC-hh machine

The FCC-hh is designed to provide proton-proton collisions with a center-of-mass energy of 100 TeV and an integrated luminosity of almost 20 ab^{-1} after 25 years of operation of the two main experiments. The machine will also be able to provide proton-ion and ion-ion collisions.

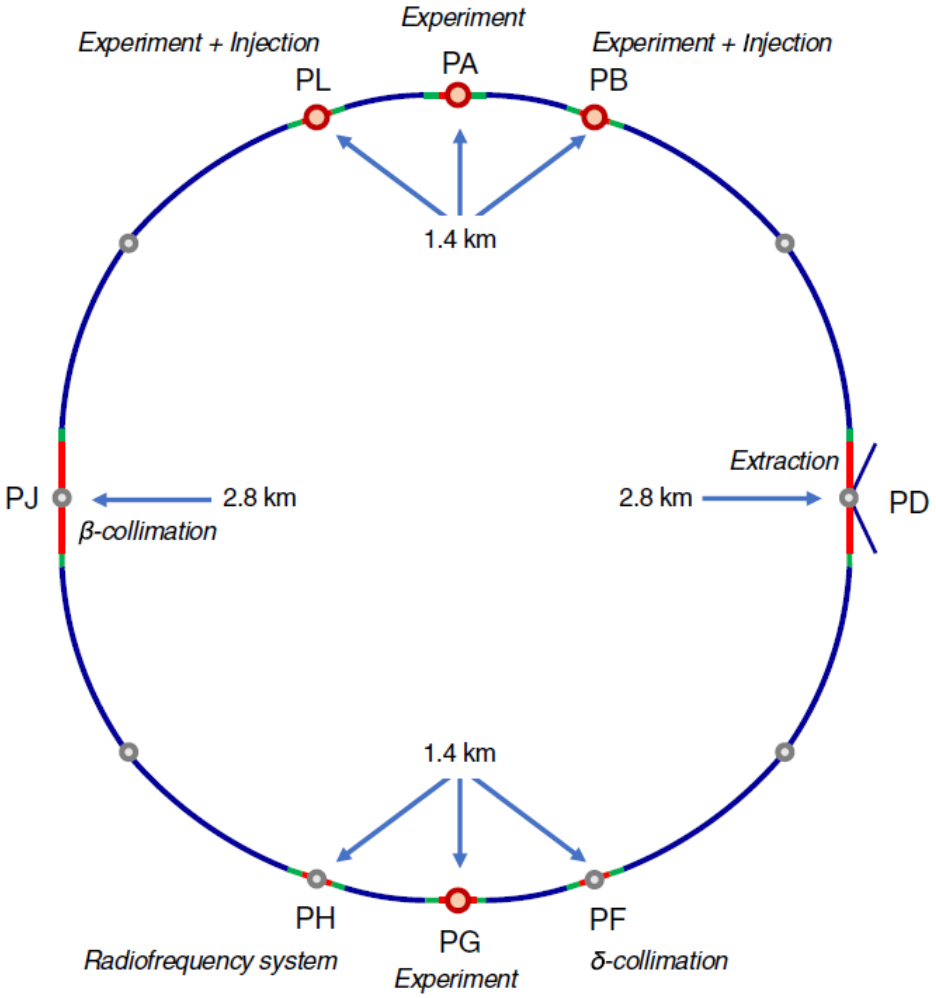

Figure 2.25: Conceptual layout of the FCC-hh collider ring: the experiment interaction points are at PA, PB, PG and PL; the injection points are at PL and PB; the beam extraction is at PD; the collimation takes place at PF and PJ; the radiofrequency and feedback systems are at PH. [95].

Layout and design Figure 2.25 shows the layout of the collider, that will have a 97.7 km long circumference, while Table 2.3 summarizes some key parameters. Two high luminosity experiments are located in opposite insertions (PA and PG), to ensures the highest luminosity and low beam-beam effects. Two additional lower luminosity experiments are located together with the injection systems in the insertions PB and PL, far enough from PA to avoid background from the collision debris in the main experiment. The total length of the arcs is 83.75 km. The lattice in the arc consists of

Center-of-mass energy $\sqrt{s}$	100 TeV
Peak luminosity $\mathcal{L}$	$< 30.0 \cdot 10^{34}$ cm^{-2}s^{-1}
Integrated luminosity per day L_{day}	8 fb^{-1}
Peak number of inelastic events/crossing	1026
Bunch spacing Δt_b	25 ns
Particles per bunch N_b	1.0×10^{11}
Bunches per beam n_b	10400
Transverse beam emittance ε_n	2.2 μm
Beta function β^*	0.3 m
Crossing angle at I.P. θ_c	200 μrad
Transverse r.m.s. bunch size at I.P. σ_z	3.5 μm
Longitudinal r.m.s.bunch size σ_z	8 cm

Table 2.3: Nominal parameters of the FCC-hh machine for pp collisions [95].

90 cells with a length of about 213 m and six 14 m long dipoles between quadrupoles. Since the dipole filling factor is about 0.8, a 16 T magnetic field is required from the Nb_3Sn dipoles to maintain the beam in circular orbit, kept at a temperature of 2 K. Fast transverse feedback and octupoles are used to stabilize the beam against parasitic electromagnetic interaction with the beamline components. The cryogenics system will be composed of active cryogenic components distributed around the ring with the cooling power required produced by 10 refrigeration plants at 6 technical sites, then distributed to the adjacent sectors over distances of up to 10 km. The baseline injection system concept exploits the CERN's Linac4, PS, PSB, SPS and the LHC at 3.3 TeV as pre-accelerators, connecting the LHC to the FCC-hh with transfer lines using 7 T superconducting magnets. This choice would permit the continuation of CERN's fixed-target physics programme in parallel with FCC-hh operation.

Planned operation The nominal phase of the FCC operation will be anticipated by an inital stage with a maximum luminosity of $5 \cdot 10^{34}$ cm^{-2}s^{-1} for the first year, with a corresponding integrated luminosity of about 2 fb^{-1} per day. Then the luminosity would be increased to the nominal $3 \cdot 10^{35}$ cm^{-2}s^{-1} reaching an integrated luminosity of 8 fb^{-1} per day.

Schedule The FCC-hh programme will start with a preparatory phase of 8 years, followed by the construction phase (civil and technical infrastructure, machines and detectors, including commissioning) of 15 years. Then a 25 years of operation period is planned, for a total of about 50 years of FCC-hh as a standalone project. If the FCC-hh will be preceded by the FCC-ee

machine, the global FCC project will cover about 70 years, until the end of the 21st century.

2.5.2 Reference detector at FCC-hh

The FCC-hh collider can be exploited both as a discovery machine as well as a precision measurement machine. The two main detectors will then need to be able to measure multi-TeV particles from heavy resonances with masses up to 50 TeV, and at the same time to measure known SM processes with high precision and be sensitive to a vast range of BSM signatures. To be able to detect SM particles, that have very low masses compared to the center-of-mass energy of 100 TeV, the detectors will need a very large acceptance both for the tracker and the calorimeter, to catch particles significantly boosted in the forward regions. A challenging question will be how to face the very high pileup foreseen, of about 1000 interactions per bunch crossing, and the development in the timing detectors sector will be crucial. A schematic conceptual FCC-hh reference detector is shown in Figure 2.26, that serves as an example for physics projection studies. The detector has a diameter of 20 m and a length of 50 m, and is divided in a central region for $|\eta| < 2.5$ equipped with the tracking system, the electromagnetic and hadron calorimeters inside a 4 T solenoid to provide the needed bending magnetic field. In the forward region ($|\eta| > 2.5$) the detector components are displaced from the interaction point along the beam axis, and two forward solenoid magnets provide the 4 T magnetic field in this region.

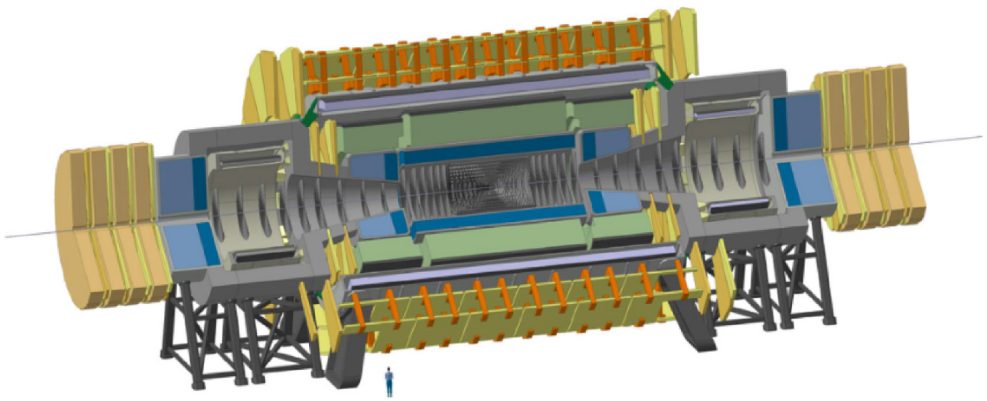

Figure 2.26: Scheme of the FCC-hh reference detector [95].

The tracking system has a radius of 1.7 m with the outermost layer at around 1.6 m from the beam in the central and the forward regions, up to $|\eta| = 3$. The calorimeter will extend from a radius of 8 cm at a z-distance of

16.6 m from the interaction point and will be divided in an electromagnetic (EMCAL) and a hadron calorimeters (HCAL). The EMCAL thickness is designed to cover 30 X_0 and together with the HCAL depth to provide more than 10.5 λ. The material planned for the EMCAL is liquid argon (LAr) since it has good radiation tolerance properties, while for the HCAL steel and lead absorbers are foreseen in the central region, and LAr in the forward region. The resolution targeted for the EMCAL (HCAL) is around $10\%/\sqrt{E}$ ($50\%/\sqrt{E}$). The muon system, thanks to the good performance of the inner tracker, will not be the focus of the layout, and will be important more for the trigger than for muon reconstruction. The reference detector does not assume any shielding of the magnetic field. However, since the shower and absorption processes inside the forward calorimeter produce a large quantity of low energy neutrons that can enter in the tracker volume, a heavy radiation shield is placed around the forward solenoid in order to keep these neutrons from entering the muon system and the detector cavern.

Chapter 3

$\mathrm{HH} \to \mathrm{ZZ}(4\ell)\mathrm{b\bar{b}}$ analysis: simulation and event selection

The modeling of the signal and background processes is a crucial part of the analysis, allowing a proper estimate of the rates and kinematics of the different processes and thus an optimization of the analysis strategy. Monte Carlo (MC) simulations can also be used to compare the observed results on data to the expectations from theory, looking for an excess of data in a region where signal is expected. The production of MC simulation samples starts with the generation of the hard physics process under study, the hadronization of quarks and gluons, the jet fragmentation and showering including the contribution of underlying events and overlapping pp collisions (pileup). Then the interaction of all generated particles with the material of the CMS detector is described, together with an emulation of the response of the HLT and the simulation of the reconstruction of events with the same algorithms used for data is performed. For performance studies regarding future upgrades of the experiment and their impact on the physics reach, this last step, which is the most time and CPU consuming can be substituted with a parametrized simulation of the detector response, that does not include the particle-material interaction but efficiently takes into account the detector performances. In this section the main tools exploited to simulate the samples used for this thesis analyses are briefly described.

3.1 Simulation tools

3.1.1 Event generation

An event generator is a tool that performs the generation of high energy physics events, based on a series of physics models which allow the evolution from a few-body process to a complex multi-particle final state. In this process they take into account many different processes such as QCD and electroweak interactions. The event generation process can be summarized in three basic steps:

1. the hard physics process of interest is generated with all four-momenta of outgoing particles calculated from the SM Lagrangian;

2. the hadronization of quarks and gluons, together with jet fragmentation and showering is performed, including the simulation of the underlying events, and the decay of unstable particles;

3. pileup interactions are included in the simulated process.

The event generators used in this thesis are MadGraph5_aMC@NLO [96], Powheg [97, 98] and Pythia8 [99].
MadGraph5_aMC@NLO and Powheg are programs capable of computing the tree-level and one-loop amplitude for arbitrary and coded processes respectively. These computations are then used to predict physics observables with different perturbative accuracies, and final-state descriptions, including NLO effects on cross sections and their matching to parton shower simulations. Since the latter include already NLO effects, the consequent double counting needs to be avoided: MadGraph5_aMC@NLO uses the MC@NLO approach that consists in subtracting from the exact NLO cross section its approximation as implemented in the Shower MC (SMC) program to which the NLO computation is matched. For this reason this method is SMC program dependent, but is process independent, since the term to be subtracted can be computed once per SMC and then applied to all processes. The Powheg (Positive Weight Hardest Emission Generator) generates the hard process first, with only positive-weighted events using the exact NLO matrix elements. In this way, it avoids the negative weights (that characterize instead a 10-15% of the events generated with MadGraph5_aMC@NLO) and is SMC independent. Pythia8 instead is a program for the generation of events in high-energy collisions, comprising a coherent set of physics models for the evolution from a few-body hard process to a complex multi-particle final state. It contains a library of hard processes, models for initial- and final-state parton showers, matching and merging methods between hard processes

and parton showers, multi-parton interactions, beam remnants, and particle decays. To better perform a proper event generation, a combination of these programs is used, favoring MadGraph5_aMC@NLO and Powheg for the generation of the hard process and the simulation of NLO effects to the process, and Pythia8 for the hadronization, showering and decay part of the process.

3.1.2 Detector simulation

After the generation of the event, the interaction of the particles with the detector material and the detector response need to be simulated. For the CMS detector, this is performed with Geant4 [100, 101] which is a program that accepts as input the output of event generators, and is based on a rich set of physics models that allow a complete description of the energy loss and interaction of particles in matter. Geant4 provides:

- the description of the detector geometry and material, distinguishing between active and passive material;
- a collection of physics processes that describe the interactions of particles with matter (Bremsstrahlung, pair production, nuclear interactions, multiple scattering, photon conversion, etc);
- the effect of the magnetic field on the tracking process;
- the simulation of the electronic response and digitization of the simulated hits;
- a correct management of pileup effects;
- the detector and particle trajectory visualization.

At the end of this complete simulation process, the simulated events are in the same format as the real data events. Therefore they can undergo the same reconstruction algorithms used for data described in Section 2.3.

For phenomenological studies, such as the comparison between several different configurations of a detector, the simulation of the aging of the detector materials due to radiation, or the response of a future detector not yet consolidated in its features, a complete simulation as the one described above is very demanding in terms of computing time and resources. For these purposes, Delphes, which is a modular framework for a parametrized and fast multipurpose detector simulation, has been developed and is described in its main features in the next section.

3.2 DELPHES for fast simulation

The DELPHES program has been developed by S. Ovyn, X. Rouby and V. Lemaître of the Center for Particle Physics and Phenomenology (CP3), Université Catholique de Louvain, Belgium in 2010 [102, 103]. To perform a parametrized and fast simulation of a detector response, DELPHES takes as input the event generators output, and produces collections of reconstructed objects such as charged leptons, photons, jets and missing energy, simulating the detector response of a tracking system embedded in a magnetic field, electromagnetic and hadron calorimeters with their granularity, and a muon identification system. Even if it does not perform the simulation of the interaction of particles with the detector material, and assumes the detector geometry to be ideal with no cracks nor dead materials, it can be easily tuned to reproduce the performances of any existing multipurpose detector such as CMS or detectors that could be used in future colliders.

3.2.1 Software implementation

In Figure 3.1 a simplified workflow chart is reported. As previously mentioned, DELPHES takes as input the most common event generators output files in various formats, which are decoded by a reader module. Then, the number of pileup events is randomly extracted using a user defined Poisson distribution from a pre-generated file containing only low-Q^2 QCD interactions, and randomly placed along the beam axis according to a user-defined longitudinal spread and overlaid to the hard scattering event; stable particles are then propagated from the tracker to the calorimeters, within the magnetic field. At this point, the objects are processed by a series of modules: muons, electrons, photons and particle-flow particles are reconstructed with user-defined efficiency and resolution, and pileup is subtracted to these collections of objects. Then the isolation variable is computed and the reconstruction of jets is performed. Finally, duplicates of reconstructed objects are removed, and the resulting collections of global event quantities and physics objects are stored in a ROOT Tree file format [104], together with the initial MC generated object collections.

Tracker The first step of the simulation is the propagation of particles through the inner tracker volume, embedded in a uniform magnetic field, parallel to the beam axis: charged particles follow a helicoidal trajectory, while neutral particles have a straight trajectory up to the calorimeters. As in real detectors, only charged particles have a user-defined probability to be reconstructed as tracks in the tracker volume; no smearing is applied to the

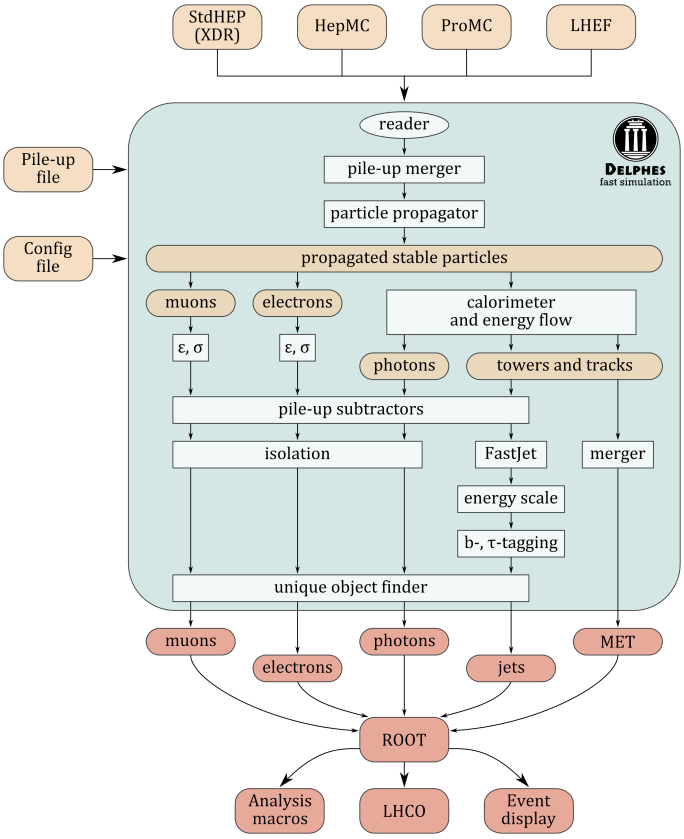

Figure 3.1: Simplified workflow scheme of the DELPHES simulation [103].

track parameters, except for the module of the transverse momentum, which is smeared at this point of the propagation. The user can specify the energy and momentum resolutions, as well as the tracking reconstruction efficiency, as a function of the particle type, of the transverse momentum and of the pseudo-rapidity.

Calorimeters For computational reasons, the default simulation of calorimeters in DELPHES provides electromagnetic calorimeter (ECAL) and the hadron calorimeter (HCAL) with the same segmentation. The design is such that the ECAL and the HCAL are perfectly overlaid so that one particle reaches exactly one cell in the ECAL and one cell in the HCAL. The segmentation is performed in the (η, ϕ) plane while no longitudinal segmentation is available. The size of the elementary unit of the calorimeters (*cell*) can be defined, while the segmentation in ϕ is set uniform, and the detector is assumed to be symmetric in ϕ and with respect to the $\eta = 0$ plane. The coordinate of

the energy deposit (*tower*) is computed at the center of the cell.

The particle energy loss can be shared by the ECAL and the HCAL according to pre-defined fractions (f_{ECAL} and f_{HCAL}) depending on the nature of the particle. By default, electrons and photons leave all their energy in the ECAL ($f_{ECAL}^{e\pm,\gamma} = 1$, $f_{HCAL}^{e\pm,\gamma} = 0$), hadrons deposit all their energy in the HCAL ($f_{ECAL}^{h} = 0$, $f_{HCAL}^{h} = 1$), kaons and Λs share their energy between the two calorimeters ($f_{ECAL}^{K,\Lambda} = 0.3$, $f_{HCAL}^{K,\Lambda} = 0.7$), while muons, neutrinos and neutralinos do not loose energy in the calorimeters. These values can be modified by the user to specify the energy loss fraction for every particle.

The resolutions of the electromagnetic and hadron calorimeters are independently parametrized as a function of the particle energy and pseudo-rapidity:

$$\left(\frac{\sigma}{E}\right)^2 = \left(\frac{S(\eta)}{\sqrt{E}}\right)^2 + \left(\frac{N(\eta)}{E}\right)^2 + C(\eta)^2, \tag{3.1}$$

where S, N and C are respectively the stochastic, noise and constant terms. The electromagnetic and hadronic energy deposits are independently smeared by a log-normal distribution, and the final tower energy is computed as:

$$E_{Tower} = \sum_{particles} \ln\mathcal{N}(f_{ECAL}\cdot E, \sigma_{ECAL}(E,\eta)) + \ln\mathcal{N}(f_{HCAL}\cdot E, \sigma_{HCAL}(E,\eta)). \tag{3.2}$$

where σ_{ECAL} and σ_{HCAL} are the resolutions for the ECAL and the HCAL respectively, and are computed using Eq. 3.1. The energy of each particle is concentrated in one single tower and all the particles that reach that tower are used to calculate the energy of this particular tower.

3.2.2 Object reconstruction

The object reconstruction and identification produce as output a collection of physics quantities with transverse momentum, energy, and other related quantities.

The particle-flow method DELPHES implements a simplified particle-flow (PF) approach based on the tracker and the calorimeters information. The particle momenta are always computed using the tracker information only (even if in real detectors the tracker resolution is better than the calorimeter one only if the particle energy is lower than a certain threshold).

In DELPHES the algorithm produces particle-flow tracks and particle-flow towers, starting from:

- E_{ECAL} and E_{HCAL}: the total energy deposit in ECAL and HCAL respectively;
- $E_{ECAL,trk}$ and $E_{HCAL,trk}$: the total energy detected in ECAL and HCAL that is associated to charged particles reconstructed in the tracker;

defining:

$$\Delta_{ECAL} = E_{ECAL} - E_{ECAL,trk} \qquad \Delta_{HCAL} = E_{HCAL} - E_{HCAL,trk} \quad (3.3)$$

and computing:

$$E_{Tower}^{eflow} = \max(0, \Delta_{ECAL}) + \max(0, \Delta_{HCAL}). \quad (3.4)$$

PF tracks are then built from particles reconstructed in the tracker, estimated with a good resolution while a PF tower is created with energy E_{Tower}^{eflow} if $E_{Tower}^{eflow} > 0$: it contains the information from neutral particles, charged particles with no corresponding reconstructed track and additional energy deposits, with degraded resolution. Pileup mitigation is performed using the PileUp Per Particle Identification (PUPPI) algorithm [105].

Muons and electrons Muons ($\mu^{\pm}$) and electrons ($e^{\pm}$) generated in the interaction are reconstructed with a user-defined probability (as a function of the transverse momentum and of the pseudo-rapidity), only if they are inside the tracker acceptance and have a transverse momentum higher than a certain threshold. The reconstructed momentum is the result of a Gaussian smearing of the generated momentum: the resolution can be defined by the user as a function of the transverse momentum and the pseudo-rapidity. For electrons, the information from the tracker is combined with the one from the calorimeter: at low energies the tracker resolution is more precise while at high energies the calorimeter energy resolution dominates.

Jets Jets are reconstructed using jet clustering algorithms and parameters included in the FASTJET package [78], the same used for the CMS event reconstruction, which is integrated in DELPHES. Many clustering algorithms are available, including the anti-k_t[79]. These methods can be used to produce jets starting from different collections of objects, depending on the user needs, and leading to: generated jets, which are clustered starting from the generator level particles; calorimeter jets, built using calorimeter towers; particle-flow jets, obtained from the clustering of particle-flow

tracks and towers. The reconstruction of jets that come from a b quark or from a τ lepton proceeds in two steps. Firstly, a jet is labeled as a b jet or τ jet if a b or τ is found within the distance from the jet axis $\Delta R = \sqrt{(\eta^{jet} - \eta^{b,\tau})^2 + (\phi^{jet} - \phi^{b,\tau})^2} < \Delta R^{min}$. Secondly, the b or τ jet is reconstructed depending on a user-defined efficiency. For b and τ jets, unlike for charged leptons and photons, a mis-tagging efficiency (the probability that a particle which is not a b nor a τ is reconstructed as a b or a τ) is implemented and can be modified by the user.

Isolation The isolation parameter, important to distinguish between an isolated lepton and a lepton inside a jet, which is surrounded by other particles, is fundamental in lepton-final states analyses. In DELPHES, the isolation parameter computed for a particle P is defined as:

$$I(P) = \frac{\sum_{i \neq P} p_T^{\text{charged}} + \max\left[\sum_{\text{i} \neq \text{P}} \text{p}_\text{T}^{\text{neutral}}(\text{i}) - \text{I}_\text{C}, 0\right]}{p_T(P)} \tag{3.5}$$

where I_C is the pileup subtraction term, applied only to neutral particles, defined as:

$$I_C = \frac{\rho \times \pi R^2}{p_T(P)} \tag{3.6}$$

with ρ indicating the pileup density, computed using the FastJet package. A cut on the isolation value $I(P)$ is then applied, to select only isolated leptons.

3.3 Analysis for Run 2

To study the performances of the HH $\rightarrow$ ZZ(4ℓ)b$\bar{\text{b}}$ analysis exploiting the 2018 data taking period, Monte Carlo samples of signal and background processes in pp collisions at $\sqrt{s} = 13$ TeV have been modeled, using the MC generators described before, and then the response of the detector and the interaction of its material with the particles produced has been simulated with GEANT4. A comparison with CMS observed data has been performed analyzing the data collected during 2018.

3.3.1 Modeling signal and background processes

The SM production cross section for HH process is

$$\sigma_{\text{HH}} = 31.05^{+2.2\%}_{-5.0\%}(\text{QCDscale}) \pm 2.1\%(\text{PDF}) \pm 2.1\%(\alpha_\text{S}) \pm 2.7\%(\text{top}) \text{ fb}$$

in proton-proton collisions at 13 TeV for a Higgs boson mass of 125 GeV, considering the main production mode only, which is the gluon-gluon fusion [106, 107, 108, 109].

Signal samples Signal samples of the SM gg →HH → ZZ(4ℓ)b$\bar{\text{b}}$ final state are generated using MadGraph5_aMC@NLO with an effective field theory description of the fermion loops, at the leading-order (LO) in QCD. Showering of parton-level events is done using Pythia8.209, with no specific matching requirements. Samples are generated with the NNPDF 3.1 NNLO parton distribution functions (PDFs) [110].

Background samples Descriptions of the SM Higgs boson production are obtained using the Powheg V2 generator for the five main production modes: gluon fusion (ggH) including quark mass effects [111], vector boson fusion (VBF) [112], and associated production (WH, ZH and t$\bar{\text{t}}$H [113]). In the case of WH and ZH the MiNLO HVJ extension of Powheg is used [114]. The description of the decay of the Higgs boson to four leptons is obtained using the JHUGen generator [115]. In the case of WH, ZH and t$\bar{\text{t}}$H, the Higgs boson is allowed to decay to H→ ZZ → 2ℓ2X such that 4-lepton events where two leptons originate from the decay of associated Z, W bosons or top quarks are also taken into account in the simulation. Showering of parton-level events is done using Pythia8, and in all cases matching is performed by allowing QCD emissions at all energies in the shower and vetoing them afterwards according to the Powheg internal scale. All samples are generated with the NNPDF 3.1 NLO parton distribution functions (PDFs) [110]. The list of the SM single Higgs production samples and their cross sections are shown in Table 3.1. Cross sections are calculated at N^{3}LO QCD and NLO EW for ggH, at NNLO QCD and NLO EW for VBF, WH and ZH, at NLO QCD and NLO EW for t$\bar{\text{t}}$H [20].

Process	Generator	$\sigma \times BR(\times\epsilon_{\text{filter}})$
gg → H → ZZ → 4ℓ	Powheg 2.0 + JHUGen V7	12.18 fb
qq′ → Hqq′ → ZZqq′ → 4ℓqq′	Powheg 2.0 + JHUGen V7	1.044 fb
q$\bar{\text{q}}$ → W$^+$H → W$^+$ZZ → 4ℓ + X	Powheg 2.0 + minlo HWJ + JHUGen V7	0.232 fb
q$\bar{\text{q}}$ → W$^-$H → W$^-$ZZ → 4ℓ + X	Powheg 2.0 + minlo HWJ + JHUGen V7	0.147 fb
q$\bar{\text{q}}$ → ZH → ZZZ → 4ℓ + X	Powheg 2.0 + minlo HZJ + JHUGen V7	0.668 fb
gg → t$\bar{\text{t}}$H → t$\bar{\text{t}}$ZZ → 4ℓ + X	Powheg 2.0 + JHUGen V7	0.393 fb
gg → b$\bar{\text{b}}$H → b$\bar{\text{b}}$ZZ → 4ℓ + X	Powheg + JHUGen V7	0.135 fb

Table 3.1: Run 2 analysis (2018) - SM Higgs boson background Monte Carlo samples and cross sections.

Production of ZZ via quark-antiquark annihilation is generated at next-to-leading order (NLO) using POWHEG V2 and PYTHIA8, with the same settings as for the Higgs signal. As this simulation covers a large range of ZZ invariant masses, dynamical QCD factorization and renormalization scales have been chosen, equal to m_{ZZ}. Since this process is generated at NLO, while the fully differential cross section has been computed at NNLO [116], but is

not yet available in a partonic level event generator, NNLO/NLO k-factors for the $q\bar{q} \to ZZ$ background process are applied to the Monte Carlo sample differentially as a function of m_{ZZ}. Additional NLO electroweak corrections which depend on the initial state quark flavor and kinematics are also applied to the $q\bar{q} \to ZZ$ background process in the region $m(ZZ) > 2m(Z)$ where the corrections have been computed.

The $gg \to ZZ$ process is simulated at leading order (LO) with MCFM [117, 118]. In order to match the $gg \to H \to ZZ$ transverse momentum spectra predicted by POWHEG at NLO, the showering for MCFM samples is performed with different PYTHIA8 settings, allowing only emissions up to the parton-level scale. This background is simulated at LO, and no exact calculations beyond the LO exist; however it has been shown [119] that the soft collinear approximation is able to describe the background cross section and the interference term at NNLO. The NNLO k-factor for the signal is obtained as a function of $m_{4\ell}$ using the HNNLO v2 Monte Carlo program [120, 121, 122] by calculating the NNLO and LO $gg \to H \to 2\ell 2\ell'$ cross sections at the small H boson decay width of 4.07 MeV and taking their ratios.

The reducible background (Z+X) originates from processes which contain one or more non-prompt leptons. The main sources of non-prompt leptons are non-isolated electrons and muons coming from decays of heavy-flavour mesons, mis-reconstructed jets (usually originating from light-flavor quarks) and electrons from γ conversions. In the following discussion a *fake lepton* is defined as any jet mis-reconstructed as a lepton or any lepton originating from a heavy meson decay. Similarly, any electron originating from a photon conversion will be considered a *fake electron*. The rate of these background processes is estimated by measuring the f_e and f_μ probabilities for fake electrons and fake muons which do pass the **loose** selection criteria (defined in Section 3.3.3) to also pass the final selection criteria (defined in Section 3.3.4). These probabilities, referred to as *fake rates*, are applied in dedicated control samples in order to extract the expected background yield in the signal region. An in depth explication about the determination process of this background is reported in Ref. [123]

Table 3.2 summarizes these MC simulation samples used for this analysis.

Pileup Reweighting Since pileup interactions are simulated exploiting first recorded data, and not the complete dataset, they do not reproduce accurately the actual pileup profile in data. For this reason, a reweighting procedure is performed. The average number of additional pileup interactions is computed either from the number of reconstructed primary vertices or from the measured instantaneous luminosity per bunch crossing. Then

Process	Generator	$\sigma \cdot BR$
$q\bar{q} \to ZZ \to 4\ell$	POWHEG 2.0	1.256 pb
$gg \to ZZ \to 4e$	MCFM	0.00159 pb
$gg \to ZZ \to 4\mu$		0.00159 pb
$gg \to ZZ \to 4\tau$		0.00159 pb
$gg \to ZZ \to 2e2\mu$		0.00319 pb
$gg \to ZZ \to 2e2\tau$		0.00319 pb
$gg \to ZZ \to 2\mu2\tau$		0.00319 pb
$Z \to \ell\ell$ + jets	MADGRAPH5_aMC@NLO	5765.4 pb
WWZ	MADGRAPH5_aMC@NLO	0.1651 pb
WZZ	MADGRAPH5_aMC@NLO	0.05565 pb
ZZZ	MADGRAPH5_aMC@NLO	0.01398 pb
TTZ($\ell\ell$)	MADGRAPH5_aMC@NLO	0.04695 pb
TTZ(jets)	MADGRAPH5_aMC@NLO	0.259 pb
TTW($\ell\nu$)	MADGRAPH5_aMC@NLO	0.2149 pb

Table 3.2: Run 2 analysis (2018) - Non-SM background Monte Carlo samples and cross sections.

a comparison between the pileup distribution from simulation and data is performed, to compute the weights that need to be applied to the simulation samples to match the pileup distribution in data. The reweighting procedure for 2018 data is shown in Figure 3.2.

3.3.2 Data

The analysis studied in the Run 2 scenario has been performed comparing the results obtained with the simulated samples previously described, to the ones obtained on the set of data recorded by the CMS experiment during 2018, corresponding to an integrated luminosity of 59.7 fb^{-1}. In order to select only interesting processes, a dedicated collection of HLT paths has been designed and optimized, listed in Table 3.3.

The data samples used are reported in Table 3.4.

The analysis relies on four different primary datasets (PDs), *DoubleMuon*, *MuEG*, *EGamma*, and *SingleMuon*, each of which combines a certain collection of high-level trigger (HLT) paths described before. In order to avoid duplicate events from different PDs, events are taken as follow:

- from *EGamma*, if they pass the *diEle* or *triEle* or *singleElectron* triggers,
- from *DoubleMuon*, if they pass the *diMuon* or *triMuon* triggers and fail the *diEle* and *triEle* triggers,

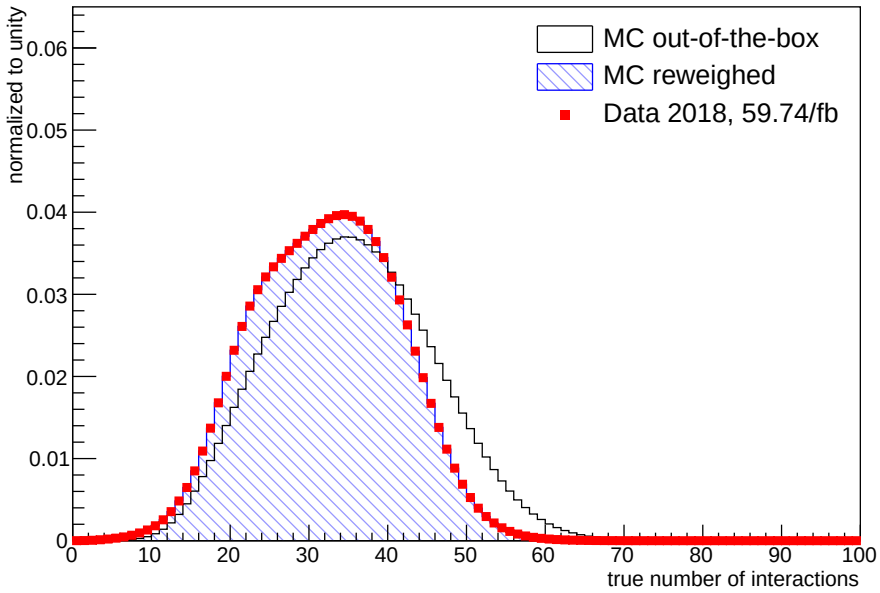

Figure 3.2: Run 2 analysis (2018) - Distribution of the number of pileup interactions in 2018 simulation before and after pileup reweighting, compared to that in data.

HLT path	primary dataset
HLT_Ele23_Ele12_CaloIdL_TrackIdL_IsoVL_v*	*EGamma*
HLT_DoubleEle25_CaloIdL_MW_v*	*EGamma*
HLT_Ele32_WPTight_Gsf_v*	*EGamma*
HLT_Mu17_TrkIsoVVL_Mu8_TrkIsoVVL_DZ_Mass3p8_v*	*DoubleMuon*
HLT_TripleMu_10_5_5_DZ_v*	*DoubleMuon*
HLT_TripleMu_12_10_5_v*	*DoubleMuon*
HLT_Mu23_TrkIsoVVL_Ele12_CaloIdL_TrackIdL_IsoVL_v*	*MuEG*
HLT_Mu8_TrkIsoVVL_Ele23_CaloIdL_TrackIdL_IsoVL_DZ_v*	*MuEG*
HLT_Mu12_TrkIsoVVL_Ele23_CaloIdL_TrackIdL_IsoVL_DZ_v*	*MuEG*
HLT_Mu23_TrkIsoVVL_Ele12_CaloIdL_TrackIdL_IsoVL_DZ_v*	*MuEG*
HLT_DiMu9_Ele9_CaloIdL_TrackIdL_DZ_v*	*MuEG*
HLT_Mu8_DiEle12_CaloIdL_TrackIdL_DZ_v*	*MuEG*
HLT_IsoMu24_v*	*SingleMuon*

Table 3.3: Run 2 analysis (2018) - Trigger paths used for 2018 CMS collision data.

- from *MuEG*, if they pass the *MuEle* or *MuDiEle* or *DiMuEle* triggers and fail the *diEle*, *triEle*, *singleElectron*, *diMuon*, and *triMuon* triggers,

- from *SingleMuon*, if they pass the *singleMuon* trigger and fail all the above triggers.

Run-range	Dataset	Integrated luminosity
315252-316995	/DoubleMuon/Run2018A-17Sep2018-v2/MINIAOD /MuonEG/Run2018A-17Sep2018-v1/MINIAOD /SingleMuon/Run2018A-17Sep2018-v2/MINIAOD /EGamma/Run2018A-17Sep2018-v2/MINIAOD	14.00 fb^{-1}
317080-319310	/DoubleMuon/Run2018B-17Sep2018-v1/MINIAOD /MuonEG/Run2018B-17Sep2018-v1/MINIAOD /SingleMuon/Run2018B-17Sep2018-v1/MINIAOD /EGamma/Run2018B-17Sep2018-v1/MINIAOD	7.10 fb^{-1}
319337-320065	/DoubleMuon/Run2018C-17Sep2018-v1/MINIAOD /MuonEG/Run2018C-17Sep2018-v1/MINIAOD /SingleMuon/Run2018C-17Sep2018-v1/MINIAOD /EGamma/Run2018C-17Sep2018-v1/MINIAOD	6.94 fb^{-1}
320673-325175	/DoubleMuon/Run2018D-PromptReco-v2/MINIAOD /MuonEG/Run2018D-PromptReco-v2/MINIAOD /SingleMuon/Run2018D-PromptReco-v2/MINIAOD /EGamma/Run2018D-PromptReco-v2/MINIAOD	31.93 fb^{-1}

Table 3.4: Run 2 analysis (2018) - 2018 CMS data.

3.3.3 Preselection of the objects

Electrons Electron candidates are preselected using loose cuts on track-cluster matching observables, in order to preserve the highest possible efficiency while rejecting part of the QCD background. To be considered for the analysis, electrons are required to have a transverse momentum $p_{\mathrm{T}}^{e} > 7$ GeV, a reconstructed $|\eta^{e}| < 2.5$, and to satisfy a loose primary vertex constraint defined as $d_{xy} < 0.5$ cm and $d_{z} < 1$ cm. Such electrons are called **loose electrons**.

Reconstructed electrons are identified and isolated by means of a Gradient Boosted Decision Tree (GBDT) multivariate classifier algorithm, which exploits observables from the electromagnetic cluster, the matching between the cluster and the electron track, observables based exclusively on tracking measurements as well as particle-flow (PF) isolation sums. The full list of observables used in the classifier, which is trained on Drell-Yan plus jets MC sample, can be found in the Table 3.5.

Table 3.6 lists the cut values applied to the GBDT score for the chosen working point.

In order to ensure that the leptons are consistent with a common primary vertex (PV), an associated track with a small impact parameter with respect to the event primary vertex is requested. The significance of the impact parameter to the event vertex, $\mathrm{SIP_{3D}} = \frac{\mathrm{IP}}{\sigma_{\mathrm{IP}}}$, is used: IP is the lepton impact parameter in three dimensions at the point of closest approach with respect to the primary interaction vertex, and σ_{IP} the associated uncertainty. Therefore, a "primary lepton" is a lepton satisfying $|\mathrm{SIP_{3D}}| < 4$.

Muons Muons that satisfy $p_{\mathrm{T}}^{\mu} > 5$, $|\eta^{\mu}| < 2.4$, and pass requirements on the impact parameter observables, such as $d_{xy} < 0.5$ cm, $d_{z} < 1$ cm, where d_{xy}

Observable type	Observable name
cluster shape	RMS of the energy-crystal number spectrum along η and φ: $\sigma_{i\eta i\eta}$, $\sigma_{i\varphi i\varphi}$
	super cluster width along η and ϕ
	ratio of the hadronic energy behind the electron supercluster to the supercluster energy, H/E
	circularity $(E_{5\times5} - E_{5\times1})/E_{5\times5}$ (*)
	sum of the seed and adjacent crystal over the super cluster energy R_9
	energy fraction in preshower divided by the supercluster energy E_{PS}/E_{raw}
track-cluster matching	energy-momentum agreement E_{tot}/p_{in}, E_{ele}/p_{out}, $1/E_{tot} - 1/p_{in}$
	position matching $\Delta\eta_{in}$, $\Delta\varphi_{in}$, $\Delta\eta_{seed}$
tracking	fractional momentum loss $f_{brem} = 1 - p_{out}/p_{in}$
	number of hits of the KF and GSF track N_{KF}, N_{GSF}
	reduced χ^2 of the KF and GSF track χ^2_{KF}, χ^2_{GSF}
	number of expected but missing inner hits
	probability transform of conversion vertex fit χ^2
isolation	particle-flow photon isolation sum
	particle-flow charged hadrons isolation sum
	particle-flow neutral hadrons isolation sum
For PU-resilience	mean energy density in the event: ρ

(*)$E_{5\times5}$ is the energy computed in the 5×5 block of crystal of the cluster seed
(*)$E_{5\times1}$ is the energy computed in the strip of crystals containing it

Table 3.5: Run 2 analysis (2018) - Overview of input variables to the identification classifier.

minimum BDT score	$\lvert\eta\rvert < 0.8$	$0.8 < \lvert\eta\rvert < 1.479$	$\lvert\eta\rvert > 1.479$
$5 < p_T < 10$ GeV	1.264	1.178	1.330
$p_T > 10$ GeV	2.364	2.078	1.080

Table 3.6: Run 2 analysis (2018) - Minimum GBDT score required for passing the electron identification.

and d_z are defined with respect to the PV and using the "muonBestTrack" are defined **loose muons**. Muons have to be reconstructed by either the Global Muon or Tracker Muon algorithm. Standalone Muon tracks that are only reconstructed in the muon system are rejected. Loose muons with $\mathrm{p_T}$ below 200 GeV are considered identified muons if they also pass the PF muon identification (PF ID). Loose muons with $\mathrm{p_T}$ above 200 GeV are considered identified muons if they pass the PF ID or the Tracker High-$\mathrm{p_T}$ ID, the definition of which is shown in Table 3.7.

Muon station matching:	muon is matched to segments in at least two muon stations
Good $\mathrm{p_T}$ measurement:	$\frac{\mathrm{p_T}}{\sigma_{\mathrm{p_T}}} < 0.3$
Vertex compatibility $(x-y)$:	$d_{xy} < 2$ mm
Vertex compatibility (z):	$d_z < 5$ mm
Pixel hits:	at least one associated pixel hit
Tracker hits:	hits in at least six tracker layers

Table 3.7: Run 2 analysis (2018) - Requirements for a muon to pass the Tracker High-$\mathrm{p_T}$ ID.

In the computation of the isolation parameter, a $\Delta\beta$ correction is applied in order to subtract the pileup contribution for the muons, where $\Delta\beta = \frac{1}{2}\sum_{\mathrm{PU}}^{\text{charged had.}} \mathrm{p_T}$ gives an estimate of the energy deposit of neutral particles (hadrons and photons) from pileup vertices. The relative isolation for muons is then defined as:

$$\mathcal{I}_{PF} = \frac{\sum^{\text{charged had.}} \mathrm{p_T} + \max(\sum^{\text{neutral had.}} \mathrm{E_T} + \sum^{\text{photon}} \mathrm{E_T} - \Delta\beta, 0)}{\mathrm{p_T^{lepton}}} \quad (3.7)$$

The isolation working point for muons is chosen to be $\mathcal{I}_{PF}(\Delta R = 0.3) < 0.35$ [124]. The same selection applied to electrons on the significance of the impact parameter is applied to muons: $|\mathrm{SIP_{3D}}| < 4$.

Photons for FSR recovery In this analysis, photons are considered only as possible candidates for final-state radiation (FSR) recovery. Since leptons coming from the Z bosons can radiate a high-$\mathrm{p_T}$ photon, its four-momentum need to be considered to assure the best accuracy in the reconstruction of the Z boson kinematics. The selection of FSR photons is performed per-lepton and does not depend on any Z mass criterion. Starting from the collection of "PF photons" provided by the particle-flow algorithm, the selection of photons and their association to a lepton proceeds as follows.

1. The preselection of PF photons is done by requiring $p_{\mathrm{T}}^{\gamma} > 2$ GeV, $|\eta^{\gamma}| < 2.4$, and a relative particle-flow isolation smaller than 1.8. The latter variable is computed using a cone of radius $R = 0.3$, a threshold of $p_{\mathrm{T}} > 0.2$ GeV on charged hadrons with a veto cone of 0.0001, and $p_{\mathrm{T}} > 0.5$ GeV on neutral hadrons and photons with a veto cone of 0.01, also including the contribution from pileup vertices (with the same radius and threshold as per charged isolation).

2. Supercluster veto: all PF photons that match with any electron passing both the loose ID and SIP cuts are removed. The matching is performed by directly associating the two PF candidates.

3. Photons are associated to the closest lepton in the event among all those passing both the loose ID and SIP cuts.

4. Photons that do not satisfy the following cuts are discarded: $\Delta R(\gamma, l) < 0.5$, $\Delta R(\gamma, l)/E_{T,\gamma}^2 < 0.012$.

5. If more than one photon is associated to the same lepton, the lowest-$\Delta R(\gamma, l)/E_{T,\gamma}^2$ is selected.

6. Each FSR photon that was selected is excluded from the isolation sum of all the leptons in the event that pass the kinematic and impact parameter cuts.

Jets Jets are reconstructed by using the anti-k_T clustering algorithm out of particle-flow candidates, with a distance parameter $R = 0.4$, after rejecting the charged hadrons that are associated to a pileup primary vertex.

To reduce instrumental background, the tight working point jet ID is applied [125]. In addition, jets from pileup are rejected using the PileUp jet ID criteria [126].

In this analysis, the jets are required to be within $|\eta| < 4.7$ and have a transverse momentum above 30 GeV. In addition, the jets are cleaned from any of the tight leptons (passing the SIP and isolation requirement computed after FSR correction) and FSR photons by a separation criterion: $\Delta R(\text{jet,lepton/photon}) > 0.4$.

In order to properly select the signal final state, b jets must be properly selected. For this purpose the b tagging *DeepCSV* algorithm is used. It combines impact parameter significance, secondary vertex and jet kinematics using tracks information. Furthermore, the b tag output discriminator is computed with a Deep Neural Network. In this analysis, a jet is considered to be b tagged if it passes the *medium* working point, i.e. if the discriminator score is larger than 0.4184 [127].

The requirements on all objects used for the analysis are summarized in Table 3.8.

A lepton is declared **loose** if it passes the reconstruction, kinematics and d_{xy}/d_z cuts, as described before, and declared **tight** if in addition it passes the identification, isolation and SIP_{3D} cut.

3.3.4 Event selection

First of all, the events are required to have fired the high-level trigger (HLT) paths described in section 3.3.2.

The events are then required to have at least one good primary vertex (PV) fullfilling some quality requirements, such as a small radius and collisions restricted along the z-axis.

The four-lepton candidates are built from the so-called *selected leptons*, which are the tight leptons (defined in Section 3.3.3). A lepton cross cleaning is applied by discarding electrons which are within $\Delta R < 0.05$ of selected muons.

Choice of the best ZZ candidate The construction and selection of four-lepton candidates proceeds according to the following sequence:

1. **Z candidates** are built as pairs of selected leptons of opposite charge and matching flavor (e^+e^-, $\mu^+\mu^-$) that satisfy $12 < m_{\ell\ell(\gamma)} < 120$ GeV/c^2, where the Z candidate mass includes the selected FSR photons, if any.

2. **ZZ candidates** are built as pairs of Z candidates not sharing the same lepton. The Z candidate with reconstructed mass $m_{\ell\ell}$ closest to the nominal Z boson mass is denoted as Z_1, and the second one is denoted as Z_2. ZZ candidates are required to satisfy the following list of requirements:

   - Ghost removal: $\Delta R(\eta, \phi) > 0.02$ between each of the four leptons.
   - Lepton p_T: two of the four selected leptons should pass $p_{T,i} >$ 20 GeV/c and $p_{T,j} > 10$ GeV/c.
   - QCD suppression: all the opposite-sign pairs that can be built with the four leptons (regardless of lepton flavor) must satisfy $m_{\ell\ell} > 4$ GeV/c. Here, selected FSR photons are not used in computing $m_{\ell\ell}$, since a QCD-induced low mass dilepton (eg. J/Ψ) may have photons nearby (from π_0, for example).
   - Z_1 mass: $m_{Z1} > 40$ GeV/c^2
   - Alternative pairing check: defining Z_a and Z_b as the mass-sorted alternative pairing Z candidates (Z_a being the one closest to the nominal Z boson mass), require the following condition not to be satisfied: ($|m_{Za} - m_Z| < |m_{Z1} - m_Z|$ and $m_{Zb} < 12$). Selected FSR photons are included in m_Z computations. This cut discards 4μ and $4e$ candidates where the alternative pairing looks like an on-shell Z + low-mass $\ell^+\ell^-$.

3. Events containing at least one selected ZZ candidate with the four-lepton invariant mass in the range $115 < m_{4\ell} < 135$ GeV/c^2, define the signal region.

The best ZZ candidate is chosen after all kinematic cuts reported above. If more than one ZZ candidate survives the above selection, the one with the highest value of the kinematic discriminant $\mathcal{D}^{\rm kin}_{\rm bkg}$ is chosen.

The full kinematic information from each event is extracted using the matrix element calculations. These discriminants use a complete set of mass and angular input observables $\vec{\Omega}$ [115, 128] to describe kinematics at LO in

QCD. The kinematic discriminant used in this analysis is computed exploiting the MELA package [18, 115, 128, 129], which uses JHUGEN V7 matrix elements for the signal and MCFM matrix elements for the background. The signal includes both the four-lepton decay kinematics in the processes gg or $q\bar{q} \to X \to ZZ$ / $Z\gamma^*$ / $\gamma^*\gamma^* \to 4\ell$, and kinematics of associated particles in production H+jet, H+2jets, VBF, ZH, WH, $t\bar{t}H$, or $b\bar{b}H$. The background includes gg or $q\bar{q} \to ZZ$ / $Z\gamma^*$ / $\gamma^*\gamma^*$ / $Z \to 4\ell$ processes. The discriminant sensitive to the gg / $q\bar{q} \to 4\ell$ kinematics is calculated as [18, 130]:

$$\mathcal{D}_{\text{bkg}}^{\text{kin}} = \left[1 + \frac{\mathcal{P}_{\text{bkg}}^{qq}(\vec{\Omega}^{H\to 4\ell}, m_{4\ell})}{\mathcal{P}_{\text{sig}}^{gg}(\vec{\Omega}^{H\to 4\ell}, m_{4\ell})}\right]^{-1} \tag{3.8}$$

where the denominator contains the probability for the $H \to 4\ell$ signal and the numerator includes the probability for the dominant $q\bar{q} \to 4\ell$ background process, all calculated either with the JHUGEN or MCFM matrix elements within the MELA framework.

Choice of the best $b\bar{b}$ candidate The pairs of jets candidates are built from the jets that pass all criteria described in Section 3.3.3 with the additional requirement $|\eta^{jet}| < 2.4$ in order to reduce the background coming from the vector boson fusion Higgs production mode. At least one of the two jets in the pair is required to be b tagged.

Different selection criterias are used in order to identify the best $b\bar{b}$ candidate, depending on how many b tagged jets are present in the final state, predilecting b tag requirements. If more than one pair with both jets b tagged is present in the event, the one with the highest p_T is selected, otherwise the only pair with both jets b tagged is selected. If there are no pairs with both jets b tagged, the best $b\bar{b}$ candidate is chosen among the jet pairs with one of the two jets b tagged, by selecting the pair with the highest p_T. This method has been compared to a similar one, where the best $b\bar{b}$ candidate is chosen among the jet pairs with one of the two jets b tagged, by selecting the pair with the mass closest to the nominal Higgs boson mass. Figure 3.3 shows the comparison between the two methods in terms of number of reconstructed jets in the $b\bar{b}$ candidate that are matched to the gen-level jets coming from the decay of the Higgs boson, while Figure 3.4 represents the reconstructed $b\bar{b}$ candidate mass with the two methods. From these distributions it is clear that choosing the highest p_T pair provides almost equivalent results to the other method, and has the advantage not to induce any bias in the mass spectrum of the $b\bar{b}$ candidate.

No cuts are applied on the invariant mass of the $b\bar{b}$ candidate, in order not to reduce the signal event selection efficiency.

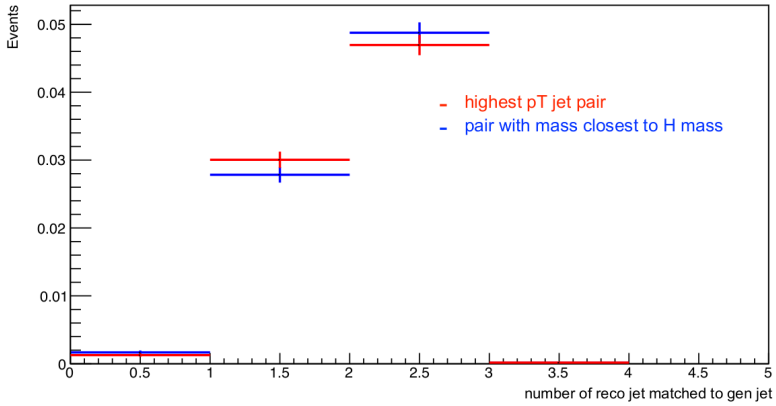

Figure 3.3: Run 2 analysis (2018) - Number of reconstructed jets in the selected $b\bar{b}$ candidate that are matched to a generator level jet coming from the decay of the Higgs boson, comparing the two methods for the $b\bar{b}$ candidate selection.

3.3.5 Systematic uncertainties

Experimental uncertainties There are different systematic uncertainties derived from experimental sources. The uncertainties that affect both signal and background processes are: the uncertainty on the integrated luminosity (2.5%), the uncertainty on the lepton identification and reconstruction efficiency (in the range $5.6 - 12.5\%$ on the overall event yield for the $4\mu b\bar{b}$ and $4eb\bar{b}$, respectively), the uncertainty on the b-tagging efficiency (estimated of about 20% due to the missing scale factors), and the uncertainty on the pileup reweighting (3%). The experimental uncertainty for the reducible background estimation, Z+X, amounts to 40% and it is due to the mismatch in the composition of backgrounds between the samples where the fake rate

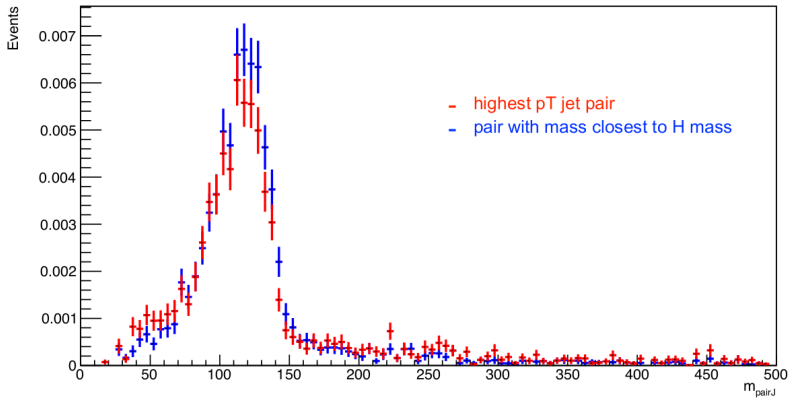

Figure 3.4: Run 2 analysis (2018) - Invariant mass spectrum of the b jet pair, comparing the two methods for the $b\bar{b}$ candidate selection.

is derived and where it is applied. The summary of experimental systematic uncertainties is reported in Table 3.9.

Theoretical uncertainties Theoretical uncertainties which affect both the signal and background estimation include uncertainties from the renormalization and factorization scale and choice of PDF set. The uncertainty from the renormalization and factorization scale is determined by varying these scales between 0.5 and 2 times their nominal value while keeping their ratio between 0.5 and 2. The uncertainty from the PDF set is determined by taking the root mean square of the variation when using different replicas of the default NNPDF set. An additional uncertainty of 10% (0.1%) on the k-factor used for the $gg \to ZZ$ ($qq \to ZZ$) prediction is applied. The summary of theory systematic uncertainty is reported in Table 3.10.

Electrons
$\mathrm{p_T^e} > 7\mathrm{GeV} \qquad \lvert\eta^e\rvert < 2.5$
$\mathrm{d_{xy}} < 0.5\,\mathrm{cm} \qquad \mathrm{d_z} < 1\,\mathrm{cm}$
$\lvert\mathrm{SIP_{3D}}\rvert < 4$
BDT ID with isolation
Muons
Global or Tracker Muon
Discard Standalone Muon tracks if reconstructed in muon system only
$\mathrm{p_T^\mu} > 5\ \mathrm{GeV} \qquad \lvert\eta^\mu\rvert < 2.4$
$\mathrm{d_{xy}} < 0.5\,\mathrm{cm} \qquad \mathrm{d_z} < 1\,\mathrm{cm}$
$\lvert\mathrm{SIP_{3D}}\rvert < 4$
PF muon ID if $p_T < 200$ GeV, PF muon ID or High-p_T muon ID if $p_T > 200$ GeV
$\mathcal{I}^\mu_{\mathrm{PF}} < 0.35$
FSR photons
$\mathrm{p_T^\gamma} > 2\ \mathrm{GeV} \qquad \lvert\eta^\gamma\rvert < 2.4$
$\mathcal{I}^\gamma_{\mathrm{PF}} < 1.8$
$\Delta R(\ell,\gamma) < 0.5 \qquad \frac{\Delta R(\ell,\gamma)}{(\mathrm{p_T^\gamma})^2} < 0.012\ \mathrm{GeV}^{-2}$
Jets
$\mathrm{p_T^{jet}} > 30\ \mathrm{GeV} \qquad \lvert\eta^{\mathrm{jet}}\rvert < 4.7$
$\Delta R(\ell/\gamma, \mathrm{jet}) > 0.4$
Cut-based jet ID (tight WP)
Jet pileup ID (tight WP)
Deep CSV b tagging (medium WP)

Table 3.8: Run 2 analysis (2018) - Summary of physics object selection criteria.

Experimental uncertainties	
Luminosity	2.5%
Muon reco and ID eff.	$3.0 - 5.6\%$
Electron reco and ID eff.	$5.1 - 13.8\%$
b tagging efficiency	20.0%
Pileup	$2.4 - 2.7\%$
Z+jets	40.0%

Table 3.9: Run 2 analysis (2018) - Summary of the experimental systematic uncertainties considered.

Theory uncertainties	
PDF set and α_s HH $\to 4\ell$bb	3.0%
QCD scale HH $\to 4\ell b\bar{b}$	$2.2 - 5.0\%$
PDF set and α_s ggH	3.2%
QCD scale ggH	$4.6 - 6.7\%$
PDF set and α_s VBFH	2.1%
QCD scale VBFH	$0.3 - 0.4\%$
PDF set and α_s ZH	2.2%
QCD scale ZH	3.8%
PDF set and α_s WH	2.2%
QCD scale WH	$0.7 - 1.5\%$
PDF set and α_s bbH	3.2%
QCD scale bbH	$4.6 - 6.7\%$
PDF set and α_s ttH	3.6%
QCD scale ttH	$5.8 - 9.2\%$
PDF set and α_s qqZZ	$3.1 - 3.4\%$
QCD scale qqZZ	$3.2 - 4.2\%$
Electroweak correction qqZZ	0.1%
PDF set ttW	2.0%
α_s ttW	2.7%
QCD scale ttW	$11.5 - 12.9\%$
PDF set and α_s VVV	3.6%
QCD scale VVV	$5.8 - 9.2\%$
PDF set ttZ	2.8%
α_s ttZ	2.8%
QCD scale ttZ	$9.6 - 11.3\%$
PDF set and α_s ggZZ	3.2%
QCD scale ggZZ	$4.6 - 6.7\%$
Electroweak correction ggZZ	10.0%

Table 3.10: Run 2 analysis (2018) - Summary of the theory systematic uncertainties considered.

3.4 Analysis at High Luminosity LHC

To study the impact of the High Luminosity phase on the HH $\to$ ZZ(4ℓ)b$\bar{\text{b}}$ analysis, Monte Carlo samples of signal and background processes in pp collisions at $\sqrt{s} = 14$ TeV have been modeled, using the MC generators described before. To simulate the CMS detector response in the HL configuration, they have been interfaced with the DELPHES software.

3.4.1 Modeling signal and background processes

Signal samples The SM HH $\to$ ZZb$\bar{\text{b}} \to 4\ell$b$\bar{\text{b}}$ signal has been simulated using MADGRAPH5_aMC@NLO at leading order (LO) accuracy, accounting for the full m_t dependence, considering only the gluon fusion production mechanism. In addition to the SM scenario ($\kappa_\lambda = 1$), twenty BSM samples corresponding to anomalous values of the λ_{HHH} coupling, ranging from $\kappa_\lambda = -10$ to $\kappa_\lambda = +10$, are modeled changing the κ_λ parameter in the MADGRAPH5_aMC@NLO program. The correspondent cross sections are computed using the parametrization of the di-Higgs cross section as a function of the κ_λ parameter, keeping the other EFT parameters fixed to their SM values ($\kappa_t = 1$, $c_2 = c_g = c_{2g} = 0$). The di-Higgs cross section for each value of κ_λ is obtained by multiplying the SM cross section for the factor $\sigma_{\text{HH}}/\sigma_{\text{HH}}^{\text{SM}}$ expressed in Eq. 1.44 computed in Section 1.5.2 that becomes:

$$\frac{\sigma_{\text{HH}}}{\sigma_{\text{HH}}^{\text{SM}}} = A_1\kappa_t^4 + A_3\kappa_\lambda^2\kappa_t^2 + A_7\kappa_\lambda\kappa_t^3 = A_1 + A_3\kappa_\lambda^2 + A_7\kappa_\lambda \tag{3.9}$$

with $A_1 = +2.100$, $A_3 = +0.287$ and $A_7 = -1.388$ at 14 TeV.

SM and BSM signal samples are hadronized and showered with PYTHIA8 that is used also to force the decay of one Higgs boson in a pair of Z bosons, and the subsequent decay of the Z bosons in pairs of leptons ℓ, where $\ell = \text{e}, \mu$.

Background samples The main background sources for this analysis are the single Higgs production processes and the top quark pair production in association with Z boson(s). The single Higgs boson production in gluon (ggH) and vector boson (VBFH) fusion is simulated with POWHEG, with the decay of the Higgs in four leptons generated using JHUGEN. The other background sources, t$\bar{\text{t}}$H, ZH, WH, t$\bar{\text{t}}$Z and t$\bar{\text{t}}$ZZ, are generated at LO using MADGRAPH5_aMC@NLO accounting for the full m_t dependence. The decays of the Higgs boson in a pair of Z bosons, and of the Z boson in two opposite-sign leptons ($\ell = \text{e}, \mu$) are forced to increase acceptance for the decay channel studied, using PYTHIA8, that is also used for hadronization and showering of all background samples. For the t$\bar{\text{t}}$H sample, the Higgs boson

has been forced to decay also into a pair of W bosons. The samples are normalized to the expected SM cross section, as recommended in [20]: the ggH production cross section is computed at the next-to-next-to-next-to-leading order (N^3LO) in perturbative QCD and at NLO in electroweak (EW) corrections, the VBF and WH processes cross sections are computed at NNLO QCD and NLO EW accuracies, the $t\bar{t}H$ cross section is computed at NLO QCD and NLO EW accuracies, the ZH cross section is computed at NNLO QCD and NLO EW accuracy for quark-initiated contributions and at NLO QCD accuracy with NLL effects for the gluon fusion-induced component.

Both the signal and background samples are processed with the DELPHES software to simulate the response of the upgraded CMS detector and account for the pileup contributions by overlaying an average of 200 minimum bias interactions. The resolution, efficiencies, and misidentification rates for the various objects have been extensively compared and tuned to reproduce the performance obtained with a full simulation of the CMS detector based on GEANT4 and the use of reconstruction algorithms tuned to the HL-LHC environment. In those cases where the reconstruction algorithms have not yet been developed or finalized, the parametrization follows assumptions based on the Run 2 object performance and on the studies prepared for the CMS detector Technical Design Reports [81].

For the presented study of the performance of the $HH \to ZZ(4\ell)b\bar{b}$ analysis in the HL-LHC scenario, three different configurations of the future CMS detector have been studied: the baseline configuration includes the improvement given by the MTD detector measurements only in the parametrized b tagging performance, with an average time resolution of 35 ps; the first alternative one excludes completely any improvement given by the MTD detector; the second alternative one includes the improvements given by the MTD detector, with a resolution of 35 ps, not only in the b tagging but also in the lepton reconstruction performances. This reflects in an efficiency gain, implemented in the DELPHES reconstruction procedure for each final state object, at constant rejection probability for the reducible backgrounds, of about $3-4\%$ for electrons and muons, $4-6\%$ for b jets.

Top quark pair production ($t\bar{t}$) and Drell-Yan (DY) lepton pair production in association with jets are a reducible background for this analysis. As their contamination is due to hadrons misidentified as leptons ("fake" leptons) or to the selection of non-prompt leptons, large suppression is expected with the selections used in this work. Nevertheless, their huge cross section, orders of magnitude larger than the signal, makes them a challenging background at the HL-LHC. The estimation of the $t\bar{t}$ and DY contributions in this work

is difficult because of the limited number of MC events available, leading to very large uncertainties related to the few or zero events satisfying the selections. Moreover, the actual impact of the $t\bar{t}$ and DY backgrounds on the analysis largely depends on reconstruction techniques and performance in the rejection of fake and non-prompt leptons that are not fully optimized in the parametric simulation implemented in DELPHES. Dedicated techniques and optimized algorithms will be available by the HL-LHC operations to have negligible contamination, deeming this assumption reasonable from studies performed on the MC simulation, given the fact that the size of MC samples will not represent an issue at the HL-LHC, and will allow to control the effective contamination in data control regions. For these reasons, $t\bar{t}$ and DY lepton pair production in association with jets processes are not included in this analysis. In Table 3.11 the product of the SM signal and considered background samples cross section and branching fraction ($\mathcal{B}\,\sigma$) is reported.

Process	$\mathcal{B}\,\sigma$ (fb)
HH $\to$ ZZbb $\to 4\ell$bb	0.0053
gg(H), H $\to$ ZZ(4ℓ) ($\cdot$)	15.007
VBF(H), H $\to$ ZZ(4ℓ) ($\cdot$)	1.169
$t\bar{t}$H, H $\to$ ZZ(4ℓ)	0.0761
$t\bar{t}$H, H $\to$ WW	131.15
ZH, Z $\to$ $b\bar{b}$, H $\to$ ZZ(4ℓ)	0.0183
WH, H $\to$ ZZ(4ℓ)	0.1876
$t\bar{t}$Z, Z $\to 2\ell$	69.224
$t\bar{t}$ZZ, Z $\to 2\ell$	0.0078

Table 3.11: HL-LHC analysis - Product of the cross section and branching fraction ($\mathcal{B}\sigma$) for the signal and considered background processes. In the Table, $\ell = \mathrm{e}, \mu$ except where indicated by ($\cdot$), where $\ell = \mathrm{e}, \mu, \tau$.

3.4.2 Event selection

Choice of the best ZZ candidate

The selection requirements implemented to select the four lepton candidate for the H $\to ZZ \to 4\ell$ decay are:

- events are required to have at least four identified and isolated ($\mathcal{I}(\ell) < 0.7$) leptons with $|\eta| < 2.8$;
- muons (electrons) are required to pass the loose (medium) working point with $p_T > 5(7)$ GeV;

- Z boson candidates are formed from pairs of opposite-charge leptons ($\ell^+\ell^-$) requiring a minimum angular separation between two leptons of 0.02;
- at least two di-lepton pairs are required;
- the Z candidate with the invariant mass closest to the nominal Z boson mass is denoted as Z_1;
- among all the other opposite-sign lepton pairs, the one with the highest p_T is labeled as Z_2;
- Z_1 candidates are required to have an invariant mass in the range $[50, 100]$ GeV
- Z_2 candidates are required to have an invariant mass in the range $[12, 60]$ GeV;
- the angular separation between the two Z bosons is required to be $\Delta R_{Z_1 Z_2} > 0.05$;
- at least one lepton is required to have $p_T > 20$ GeV and a second one is required to have $p_T > 10$ GeV;
- the four leptons invariant mass, $m_{4\ell}$, is requested to be in the range $[120, 130]$ GeV.

Choice of the best $b\bar{b}$ candidate

After the selection of events satisfying all criteria described above, with at least a Higgs boson reconstructed from four leptons, the selection of the other Higgs takes place:

- jets are required to be reconstructed with the anti-k_T algorithm inside a cone of radius $R = 0.4$;
- at least two identified b-tagged jets, exploiting the medium b tag working point, are required;
- the invariant mass of the b jets pairs, corrected assuming an improvement of 20% on the resolution on the $m_{b\bar{b}}$ peak, as expected for HL-LHC thanks to a proper b jet energy regression, is required to be in the range $[90, 150]$ GeV [131];
- the angular distance between the two b jets in each pair has to be $0.5 < \Delta R_{b\bar{b}} < 2.3$.

At the end of the two Higgs candidates selection, a missing transverse energy (MET) cut is fixed at $MET < 150$ GeV and a cut on the angular distance between the two reconstructed Higgs is required to be $\Delta R_{\mathrm{HH}} \geq 2.0$.

The same analysis requirements have been applied to all signal and background samples. In order to quantify the discriminant power of this workflow, a study of the efficiency at each step of the analysis has been made for the SM signal and main background processes, and reported in Figure 3.5 for the inclusive $4\ell\mathrm{b}\bar{\mathrm{b}}$ final state.

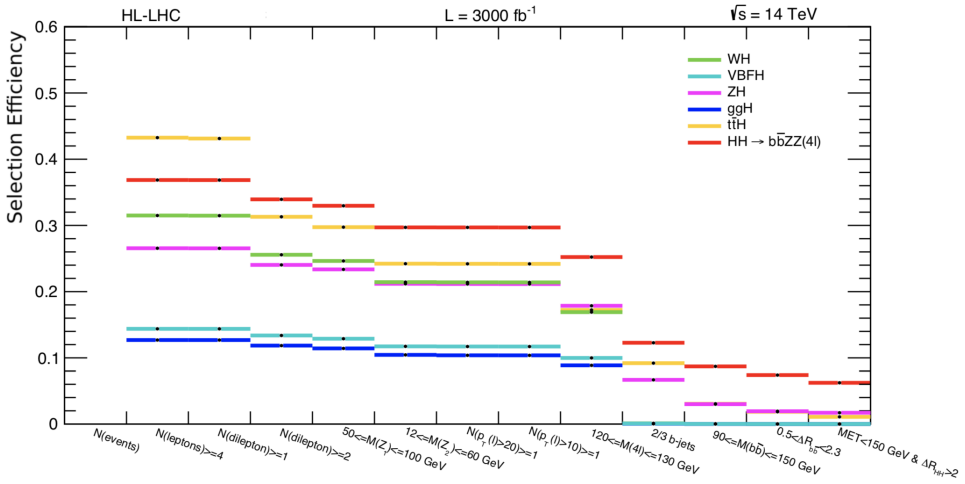

Figure 3.5: HL-LHC analysis - Percentage of events passing each step of the analysis workflow.

As anticipated in Section 3.4.1, the event selection for the HL-LHC study is performed in three different scenarios, depending on the inclusion of the MTD projected improvement on the object reconstruction. The "baseline" scenario includes the improvement given by the MTD detector measurements only in the parametrized b tagging performance, assuming an average MTD time resolution of 35 ps; the first alternative scenario excludes completely any improvement given by the MTD detector ("NO MTD") while the second alternative option includes the improvements given by the MTD detector not only in the b tagging but also in the leptons reconstruction performances ("MTD 35 ps"). For this reason, in the above list of requirements on the selected objects for the analysis, leptons are reconstructed and identified exploiting the MTD improvement only in the "MTD 35 ps" scenario, while b-tagged jets are selected exploiting the MTD improvement both in the "baseline" and in the "MTD 35 ps" options.

3.4.3 Systematic uncertainties

Systematic uncertainties in the modeling of the signal and background processes due to theoretical and experimental effects are considered. An uncertainty on the total integrated luminosity of 1% is considered for all processes. The uncertainty on the b tagging efficiency amounts to 2% while the uncertainty on the muon (electron) identification and isolation efficiency amounts to 0.5% (1%). Triggers are assumed to be fully efficient in the phase space considered, and the corresponding uncertainties are included in the object reconstruction and identification uncertainties. The uncertainties in the theoretical cross sections used for the normalization of simulated processes are assumed to be reduced by a factor of 0.5 with respect to the current values. Table 3.12 summarizes all systematic uncertainties implemented in the analysis.

Type	Systematic uncertainty
Luminosity	1.0%
Muon ID and isolation	0.5%
Electron ID and isolation	1.0%
b tagging efficiency	2.0%
HH $\rightarrow$ ZZ(4ℓ)b$\bar{\text{b}}$ QCD scale	2.7%
HH $\rightarrow$ ZZ(4ℓ)b$\bar{\text{b}}$ PDF and α_s	3.0%
t$\bar{\text{t}}$H QCD scale	$^{+6.0\%}_{-9.2\%}$
t$\bar{\text{t}}$H PDF and α_s	3.5%
WH QCD scale	$^{+0.4\%}_{-0.7\%}$
WH PDF and α_s	1.8%
ZH QCD scale	$^{+3.8\%}_{-3.3\%}$
ZH PDF and α_s	1.6%
t$\bar{\text{t}}$Z QCD scale	$^{+9.6\%}_{-11.2\%}$
t$\bar{\text{t}}$Z PDF	2.7%
t$\bar{\text{t}}$Z α_s	2.8%
ggH QCD scale	3.9%
ggH PDF and α_s	3.2%
VBFH PDF and α_s	2.1%

Table 3.12: HL-LHC analysis - Summary of all the systematic uncertainties considered.

3.5 Analysis at High Energy LHC

To study the impact of the possible High Energy phase after the HL one on the HH $\rightarrow$ ZZ(4ℓ)b$\bar{\text{b}}$ analysis, the same procedure described in the

previous section has been followed: MC samples of signal and background processes in pp collisions at $\sqrt{s} = 27$ TeV have been modeled and the CMS detector response in the HE configuration has been assumed the same as in the HL phase.

3.5.1 Modeling signal and background processes

Signal samples The SM HH $\to$ ZZb$\bar{\text{b}}$ $\to 4\ell$b$\bar{\text{b}}$ signal has been simulated using MadGraph5_aMC@NLO at leading order (LO) accuracy, accounting for the full m_t dependence, considering only the gluon fusion production mechanism. Similarly to the HL study, in addition to the SM scenario ($\kappa_\lambda = 1$), twenty-three BSM samples corresponding to anomalous values of the λ_{HHH} coupling, ranging from $\kappa_\lambda = -20$ to $\kappa_\lambda = +20$, are modeled, keeping $\kappa_t = 1$, $c_2 = c_g = c_{2g} = 0$. The corresponding cross sections are computed with Eq. 3.9 with $A_1 = +2.002$, $A_3 = +0.243$ and $A_7 = -1.247$ at 27 TeV.

SM and BSM signal samples are hadronized and showerered with Pythia8 that is used also to force the decay of one Higgs boson in a pair of Z bosons, and the subsequent decays of the Z bosons in pairs of leptons ℓ, where $\ell = \text{e}, \mu$.

Background samples The same background sources studied for the HL analysis have been considered for the analysis performed at the HE scale. The contribution from single Higgs boson production in gluon (ggH) and vector boson (VBFH) fusion is obtained scaling the results obtained at HL taking into account the different value of integrated luminosity (L) and cross section (σ):

$$\text{yield(HE)} = \text{yield(HL)} \times \frac{\sigma_{\text{HE}}}{\sigma_{\text{HL}}} \times \frac{L_{\text{HE}}}{L_{\text{HL}}} \tag{3.10}$$

This procedure is applied since these backgrounds have a huge statistics not easily reproducible in the HE scenario, and since the event selection efficiency, both for signal and background processes obtained in the HE scenario is comparable with the HL one. The other background sources, t$\bar{\text{t}}$H, ZH, WH, t$\bar{\text{t}}$Z and t$\bar{\text{t}}$ZZ, are generated, hadronized, showered and forced into the decay of the Higgs boson in a pair of Z bosons, and of the Z bosons in a pair of leptons in the same way as described for HL in Section 3.4.1. The samples are normalized to the expected SM cross section, as recommended in [20]: the ggH production cross section is computed at N^{3}LO in perturbative QCD and at NLO in EW corrections, the VBF, ZH and WH processes cross sections are computed at NNLO QCD and NLO EW accuracies, the t$\bar{\text{t}}$H cross section is computed at NLO QCD and NLO EW accuracies.

The baseline HL configuration of the CMS detector (including pileup) has been assumed for the HE scenario too, and has been simulated with

DELPHES as described in Section 3.4.1. For the same reasons explained before, top quark pair production and Drell-Yan lepton pair production in association with jets are not included in this study.

Table 3.13 summarizes the product of the SM signal and considered background samples cross section and branching fraction.

Process	$\mathcal{B}\,\sigma$ (fb)
HH $\to$ ZZb$\bar{\text{b}}$ $\to 4\ell$b$\bar{\text{b}}$	0.02
gg(H), H $\to$ ZZ(4ℓ) ($\cdot$)	40.592
VBF(H), H $\to$ ZZ(4ℓ) ($\cdot$)	3.277
t$\bar{\text{t}}$H, H $\to$ ZZ(4ℓ)	0.358
ZH, Z $\to$ b$\bar{\text{b}}$, H $\to$ ZZ(4ℓ)	0.047
WH, H $\to$ ZZ(4ℓ)	0.425
t$\bar{\text{t}}$Z, Z $\to 2\ell$	207.876
t$\bar{\text{t}}$ZZ, Z $\to 2\ell$	0.0383

Table 3.13: HE-LHC analysis - Product of the cross section and branching fraction ($\mathcal{B}\sigma$) for the signal and considered background processes. In the Table, $\ell = \text{e}, \mu$ except where indicated by ($\cdot$), where $\ell = \text{e}, \mu, \tau$.

3.5.2 Event selection

The event selection for the search of the HH $\to$ ZZ(4ℓ)b$\bar{\text{b}}$ decay in the HE-LHC scenario is performed following the same procedure applied in the HL scenario, with the differences listed below, due the optimization of the analysis for this scenario:

- Z_1 candidates are required to have an invariant mass in the range $[40, 120]$ GeV instead of $[50, 100]$ GeV;
- Z_2 candidates are required to have an invariant mass in the range $[12, 120]$ GeV instead of $[12, 60]$ GeV;
- the invariant mass of the b jets pairs is not corrected with the b jet energy regression and is required to be in the range $[80, 160]$ GeV instead of $[90, 150]$ GeV.

Figure 3.6 shows the efficiency at each step of the analysis flow, for the SM signal and main backgrounds in the inclusive 4ℓb$\bar{\text{b}}$ final state.

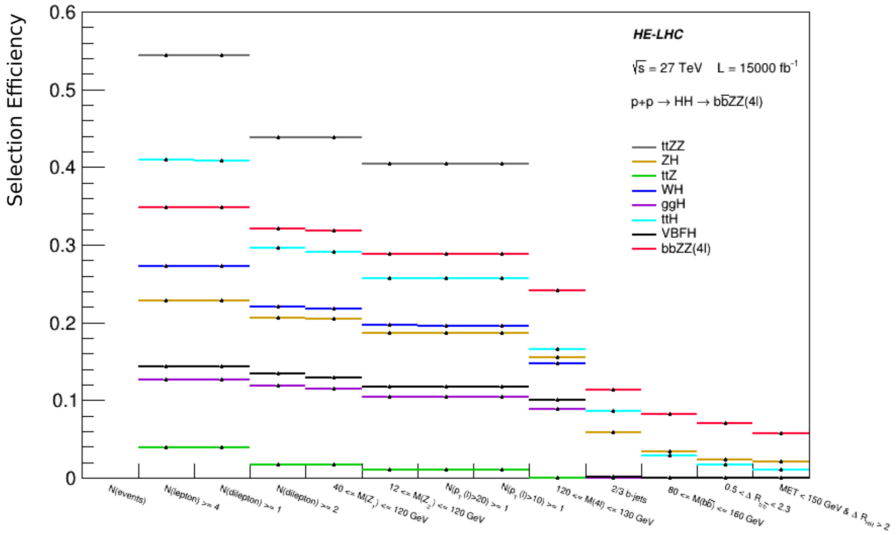

Figure 3.6: HE-LHC analysis - Percentage of events passing each step of the analysis workflow.

3.5.3 Systematic uncertainties

Systematic uncertainties related to the detector performance, such as for muon and electron identification and isolation, and b tagging, are assumed to be the same used for the HL study. A 1% uncertainty on the total integrated luminosity is considered for all processes. The uncertainties in the theoretical cross sections used for the normalization of simulated processes are reported in Table 3.14.

Type	Systematic uncertainty
Luminosity	1.0%
Muon ID and isolation	0.5%
Electron ID and isolation	1.0%
b tagging efficiency	2.0%
$HH \to ZZ(4\ell)b\bar{b}$ QCD scale	3.4%
$HH \to ZZ(4\ell)b\bar{b}$ PDF and α_s	2.5%
$t\bar{t}H$ QCD scale	$^{+7.8\%}_{-9.0\%}$
$t\bar{t}H$ PDF and α_s	2.8%
WH QCD scale	$^{+0.29\%}_{-0.72\%}$
WH PDF and α_s	1.37%
ZH QCD scale	$^{+5.42\%}_{-4.0\%}$
ZH PDF and α_s	2.24%
$t\bar{t}Z$ QCD scale	$^{+9.6\%}_{-11.2\%}$
$t\bar{t}Z$ PDF	2.7%
$t\bar{t}Z$ α_s	2.8%
ggH QCD scale	$^{+4.53\%}_{-6.43\%}$
ggH PDF	1.95%
ggH α_s	$^{+2.69\%}_{-2.64\%}$
VBFH PDF and α_s	2.1%

Table 3.14: HE-LHC analysis - Summary of all the systematic uncertainties considered.

3.6 Analysis at Future Circular Colliders

The HH $\rightarrow$ ZZ(4ℓ)b$\bar{\text{b}}$ analysis has been performed in the FCC-hh scenario, with the same procedure described in the previous sections: MC samples of signal and background processes in pp collisions at $\sqrt{s} = 100$ TeV have been modeled and the baseline configuration for a detector at the FCC-hh has been simulated.

3.6.1 Modeling signal and background processes

Signal samples The SM HH $\rightarrow$ ZZb$\bar{\text{b}}$ $\rightarrow$ 4ℓb$\bar{\text{b}}$ signal process has been generated at LO with MadGraph5_aMC@NLO, accounting for the full m_t dependence, considering only the gluon fusion production mechanism. In addition to the SM scenario ($\kappa_\lambda = 1$), BSM samples corresponding to anomalous values of the λ_{HHH} coupling, ranging from $\kappa_\lambda = -1$ to $\kappa_\lambda = +3$, in steps of 0.5 are generated, keeping $\kappa_t = 1$, $c_2 = c_g = c_{2g} = 0$. The correspondent cross sections are computed with Eq. 3.9 with $A_1 = +2.070$, $A_3 = +0.277$ and $A_7 = -1.347$ at 100 TeV.

Background samples The background processes considered for this analysis are: gluon fusion production of a single Higgs boson with an extra pair of b$\bar{\text{b}}$ jets added in the event to increase the contamination of jets, t$\bar{\text{t}}$H, ZH, t$\bar{\text{t}}$Z. They are generated at LO with MadGraph5_aMC@NLO, taking into account higher order radiative corrections applying k-factors to the cross section provided by the generator: k(t$\bar{\text{t}}H$) = 1.22, k(ggH) = 3.2 and k(ZH) = 1.1 [132].

Generated signal and background samples are hadronized and showered with Pythia8, that is used also to force the decay of one Higgs boson in a pair of Z bosons, and the subsequent decay of the Z bosons in pairs of leptons ℓ, where $\ell = \text{e}, \mu$, while the ideal parametrization of the FCC-hh detector has been implemented with a pileup 0 scenario using Delphes. Table 3.15 summarizes the product of the SM signal and considered background samples cross section and branching fraction.

3.6.2 Event selection

Similarly to the analysis flow followed in the HL and HE scenarios, for the study of the HH $\rightarrow$ ZZ(4ℓ)b$\bar{\text{b}}$ decay channel at FCC-hh the same event selection criteria have been requested, with the following exceptions with respect to the HL analysis:

Process	$\mathcal{B}\,\sigma$ (fb)
$HH \to ZZb\bar{b} \to 4\ell b\bar{b}$	0.178
$gg(H) + b\bar{b}$, $H \to ZZ(4\ell)$	0.369
$t\bar{t}H$, $H \to ZZ(4\ell)$	4.013
ZH, $Z \to 2\ell$, $H \to ZZ(4\ell)$	0.071
$t\bar{t}Z$, $Z \to 2\ell$	$2.594 \cdot 10^3$

Table 3.15: FCC-hh analysis - Product of the cross section and branching fraction ($\mathcal{B}\sigma$) for the signal and considered background processes.

- to be within the detector acceptance, events are required to have **exactly** four identified and isolated ($\mathcal{I}(\ell) < 0.7$) leptons with $|\eta| < 4.0$ instead of $|\eta| < 2.8$;
- Z_1 candidates are required to have an invariant mass in the range $[40, 120]$ GeV instead of $[50, 100]$ GeV;
- Z_2 candidates are required to have an invariant mass in the range $[12, 120]$ GeV instead of $[12, 60]$ GeV;
- the invariant mass of the b jets pairs is not corrected for the improvement due to the b jet energy regression and is required to be in the range $[80, 130]$ GeV instead of $[90, 150]$ GeV;
- the angular distance between the two b jets in each pair has to be $0.5 < \Delta R_{b\bar{b}} < 2.0$ instead of $0.5 < \Delta R_{b\bar{b}} < 2.3$.

The percentage of events passing the full analysis chain in the signal and considered background samples is shown in Figure 3.7 for the inclusive $4\ell b\bar{b}$ final state.

3.6.3 Systematic uncertainties

For this study, since the detector geometry is still being discussed and one cannot easily foresee the specific systematic uncertainties related to all quantities involved, two basic scenarios have been assumed on signal and background processes: 1% ($\frac{\Delta S}{S} = \frac{\Delta B}{B} = 1\%$) and 3% $\left(\frac{\Delta S}{S} = \frac{\Delta B}{B} = 3\%\right)$ systematic uncertainties.

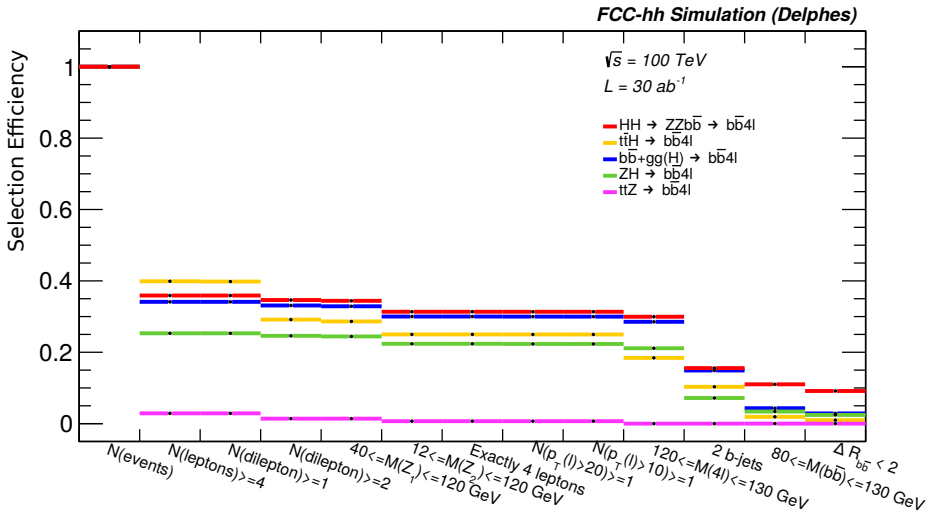

Figure 3.7: FCC-hh analysis - Percentage of events passing each step of the analysis workflow.

Chapter 4

Results for the $\mathrm{HH} \to \mathrm{ZZ}(4\ell)\mathrm{b\bar{b}}$ analysis

4.1 Statistical methods

A proper statistical method is needed in order to derive the results regarding the presence or absence of a signal and its significance, after the event selection, estimation of background contributions and systematic uncertainties. The procedure used is the same frequentistic approach developed by the ATLAS and CMS Collaborations at the beginning of Run 1 in the context of the LHC Higgs Combination Group [133].

4.1.1 The likelihood function

The first step of this method consists in building a likelihood function $\mathcal{L}(\text{data}|\theta)$, where θ is the set of m nuisance parameters $\theta = (\theta_1, ...\theta_m)$ that represent all sources of systematic uncertainties. Then the method of the maximum likelihood is applied, used to find the value of the model parameter of interest θ that maximizes the likelihood function $\mathcal{L}(\text{data}|\theta)$. In other words, this procedure chooses the value of the set of parameters that makes observed data most probable. The model used in this thesis introduces a parameter called signal strength μ that is defined as the measured cross section of the physics process under study normalized to the SM cross section, as already mentioned in Chapter 1: $\mu = \sigma/\sigma^{\mathrm{SM}}$. This parameter is used to quantify the expected number of events (yield): $\mu \cdot s(\theta) + b(\theta)$, where s and b denote the signal and total background yield respectively. They are both function of the nuisance parameters that need to be estimated from a priori considerations or auxiliary measurements, on different sets of data with respect to the ones used for the statistical analysis. The frequentistic

probability $\mathrm{p}(\widetilde{\theta}, \theta)$ to measure a value $\widetilde{\theta}_i$ of the i-th parameter, given its true value θ_i is then considered. Since all systematic uncertainties are assumed to be uncorrelated, the combined probability density function (PDF) $p(\widetilde{\theta}, \theta)$ of a sample of N events is defined as:

$$p(\widetilde{\theta}|\theta) = \prod_{i=1}^{N} p_i(\widetilde{\theta}_i|\theta_i). \tag{4.1}$$

The likelihood can be therefore defined, given the data (actual data or a pseudo-experiment), as:

$$\mathcal{L}(\text{data}, \widetilde{\theta}|\mu, \theta) \equiv \mathcal{L}_{ext}(\text{data}|\mu \cdot s(\theta) + b(\theta)) \cdot \prod_{i=1}^{N} p_i(\widetilde{\theta}_i|\theta_i). \tag{4.2}$$

The extended likelihood function $\mathcal{L}_{ext}$ is expressed as:

$$\begin{aligned}\mathcal{L}_{ext}(\text{data}|\mu \cdot s(\theta) + b(\theta)) =& \frac{(\mu \cdot s(\theta) + b(\theta))^N e^{-(\mu \cdot s(\theta) + b(\theta))}}{N!} \\ & \cdot \prod_{i=1}^{N} (f_s P_s(x_i|\theta) + f_b P_b(x_i|\theta)) \\ =& \frac{e^{-(\mu \cdot s(\theta) + b(\theta))}}{N!} \cdot \prod_{i=1}^{N} (\mu \cdot s(\theta) P_s(x_i|\theta) + b(\theta) P_b(x_i|\theta))\end{aligned} \tag{4.3}$$

where the first term represents the Poisson distribution of the number of events, which is a random variable, and the second term is the likelihood of the measured values x_i in a process that is composed of signal and background contributions:

$$\begin{aligned} f_s =& \frac{\mu \cdot s(\theta)}{\mu \cdot s(\theta) + b(\theta)} \\ f_b =& \frac{b(\theta)}{\mu \cdot s(\theta) + b(\theta)} \end{aligned}$$

are the expected signal and background fractions respectively and P_s and P_b are the PDF of the variable x_i for signal and background respectively [134].

4.1.2 Hypothesis test

The hypothesis testing procedure profits from the likelihood formalism in order to discriminate between two hypotheses (in this case the presence

or absence of the signal process) in observed experimental data. The two opposite hypotheses are defined as $H_{\mu s+b}$, that includes the presence of the signal, and H_b that describes the background only hypothesis. To quantify a signal excess in data, or set un upper limit on the presence of the signal, a "test statistics" need to be defined starting from Eq. 4.3. The test statistics is usually built as the ratio of two likelihood functions, evaluated for the observed data under two different hypotheses, H_0 and H_1, since the Neyman-Pearson lemma states that such a test statistics allows the best discrimination between the two hypotheses [135]. This choice, added to the Wilks' theorem [136] that states that for a model with m parameters, the distribution of $-2\Delta \ln \mathcal{L}$ approaches the χ^2 distribution with m degrees of freedom in the limit of a large data sample, leads to the following definition of the test statistics:

$$q(\text{data}) - 2\Delta \ln \mathcal{L} = -2 \ln \frac{\mathcal{L}(\text{data}|\theta, H_0)}{\mathcal{L}(\text{data}|\theta, H_1)}. \tag{4.4}$$

Quantifying an excess

The test statistics q_0 that is built to quantify a signal excess in data is defined as:

$$q_0 \equiv -2 \ln \frac{\mathcal{L}(\text{data}, \widetilde{\theta}|\mu_0, \hat{\theta}_0)}{\mathcal{L}(\text{data}, \widetilde{\theta}|\hat{\mu}, \hat{\theta})} \tag{4.5}$$

where $\mu_0 = 0$ denotes the background only hypothesis, $\hat{\theta}_0$ in the numerator is the conditional maximum likelihood estimator of θ in the background only hypothesis, that is the value of θ that maximizes the likelihood of Eq. 4.3 for a fixed μ, while $\hat{\mu}$ and $\hat{\theta}$ in the denominator are the global minimum of the likelihood function, that is the values obtained minimizing the likelihood on both parameters simultaneously. The significance of an excess is quantified by the p-value, that is the probability that the test statistics q_0 is larger than or equal to the observed q_0^{obs}, assuming the background only hypothesis:

$$p \equiv \mathcal{P}(q_0 \geq q_0^{obs}|H_b) \tag{4.6}$$

This corresponds to the probability of the background to fluctuate giving an excess at least as large as the one observed on data, and can be evaluated comparing the observed value of q_0^{obs} with the expected distribution of q_0, obtained with pseudo-experiments according to the statistical method defined. The p-value is usually converted in the significance Z of the excess, with a Gaussian one-sided tail integral:

$$p = \int_Z^{+\infty} \frac{1}{\sqrt{2\pi}} e^{-x^2/2} dx \tag{4.7}$$

The conventional significance of 3 σ ($Z = 3$, $p = 1.3 \cdot 10^{-3}$) is required to claim for an "evidence" of signal, while 5 σ ($Z = 5$, $p = 2.8 \cdot 10^{-7}$) are required to claim for a "discovery" of signal in data.

Setting exclusion limits

The test statistics q_μ that is built to set exclusions limits is defined as:

$$q_\mu \equiv -2 \ln \frac{\mathcal{L}(\text{data}, \widetilde{\theta}|\mu, \hat{\theta}_\mu)}{\mathcal{L}(\text{data}, \widetilde{\theta}|\hat{\mu}, \hat{\theta})} \tag{4.8}$$

where $\hat{\theta}_\mu$ in the numerator is the conditional maximum likelihood estimator of θ, while $\hat{\mu}$ and $\hat{\theta}$ in the denominator are the global minimum of the likelihood function. The value of $\hat{\mu}$ is constrained between 0 and μ: $\hat{\mu} \geq 0$ indicates that the signal contribution cannot be negative, while $\hat{\mu} \leq \mu$ ensures that upward fluctuations of the data larger that the one expected for a signal of strength μ do not provide evidence against the signal hypothesis itself. With this definition, larger values of q_μ represent increasing incompatibility between data and the chosen value of μ. The exclusion limits are then derived starting from the test statistics using the modified frequentistic criterion CL_s [137, 138]. Under the two hypotheses $H_{\mu s+b}$ and H_b, and given an observed value q_μ^{obs} of the test statistics, the probability for q_μ to be larger than or equal to q_μ^{obs} is defined, respectively, as:

$$\text{CL}_{s+b}(\mu) \equiv \mathcal{P}(q_\mu \geq q_\mu^{obs}|H_{\mu s+b}) \tag{4.9}$$

$$\text{CL}_b(\mu) \equiv \mathcal{P}(q_\mu \geq q_\mu^{obs}|H_b) \tag{4.10}$$

The CL_s quantity is then defined as:

$$\text{CL}_s(\mu) \equiv \frac{\text{CL}_{s+b}(\mu)}{\text{CL}_b(\mu)}. \tag{4.11}$$

When measuring one single parameter μ, the 68% and 95% CL intervals are deduced from the conditions $-2\Delta \ln \mathcal{L} < 1$ and $-2\Delta \ln \mathcal{L} < 3.84$ respectively. In general, the results are both quoted as central values with 68% CL intervals, and displayed graphically as scans of $-2\Delta \ln \mathcal{L}$. Expected results can also be provided for some nominal values of the parameters, which is very useful to estimate the sensitivity of a given measurement. A very good approximation alternative to the generation a large number of pseudo-experiments and determination of each one of their median outcome is provided by the Asimov data set [139], that is one single representative data set in which the

observed rates and distributions coincide with predictions under the nominal set of nuisance parameters. This choice with respect to the exclusion based on $CL_{s+b}(\mu)$ is justified since it avoids underfluctuations in the background that could lead to the exclusion of a signal even if the latter is absent.

4.2 Results of the analysis for Run 2

In this section the full event selection is presented, with emphasis on the inputs to the final results, namely the event yields, and the distributions of the main kinematic variables in data and MC samples.

The expected yields of the backgrounds and the HH signal in the $4\ell b\bar{b}$ final state, together with the observed yields in 2018 data (59.7 fb^{-1}), are summarized in Table 4.1, after the full event selection.

Channel	4μbb	4ebb	2e2μbb	4ℓbb
gg$\bar{H}$	0.192	0.098	0.244	0.534
VBF$\bar{H}$	0.038	0.026	0.051	0.116
Z$\bar{H}$	0.054	0.029	0.077	0.160
W$\bar{H}$	0.026	0.013	0.035	0.075
t$\bar{t}$H	0.258	0.157	0.361	0.776
b$\bar{b}$H	0.022	0.011	0.026	0.058
q$\bar{q}$ZZ	0.0	0.012	0.026	0.038
ggZZ	0.002	0.002	0.002	0.006
t$\bar{t}$Z	0.053	0.073	0.099	0.224
t$\bar{t}$W	0.005	0.010	0.018	0.033
VVV (WWZ, WZZ, ZZZ)	0.0	0.0	0.0	0.0
Z+jets	0.505	0.153	0.790	1.448
Sum of backgrounds	1.155	0.584	1.729	3.468
HH $\rightarrow 4\ell b\bar{b}$ signal	0.008	0.005	0.013	0.026
Total expected	1.163	0.589	1.742	3.494
Observed	1	0	3	4

Table 4.1: Run 2 analysis (2018) - Number of expected background and signal events, and number of observed candidates after the full event selection for an integrated luminosity of 59.7 fb^{-1}.

The main kinematic distributions for the $4\ell b\bar{b}$ final state are shown after all the requirements described above, except for the cut on the four-lepton mass, comparing 2018 data (59.7 fb^{-1}) to the signal and background expectations. Figure 4.1 and Figure 4.2 show the invariant mass distributions of Z_1 and Z_2 respectively; Figure 4.3, Figure 4.4 and Figure 4.5 show the four-lepton transverse momentum, pseudorapidity and invariant mass distribu-

tions respectively; Figure 4.6 and Figure 4.7 show the transverse momentum and invariant mass of the reconstructed b jet pair. The partial disagreement observed between data and MC distributions is likely due to the absence of jet energy corrections and b tagging scale factors. In fact, a much better agreement is achieved up to the best ZZ candidate selection, as shown in Figure 4.8 where the four-lepton invariant mass is displayed after the reconstruction of the H $\rightarrow$ ZZ only. Adding requests on jets causes the discrepancy observed. A study is ongoing to implement these corrections in the analysis.

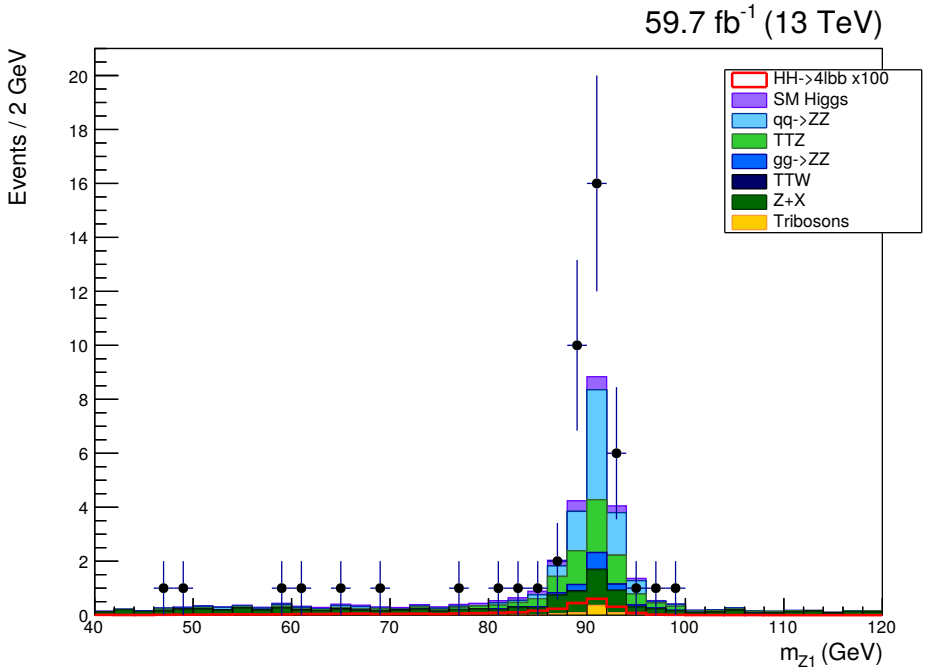

Figure 4.1: Run 2 analysis (2018) - Distribution of the Z_1 reconstructed invariant mass in the inclusive $4\ell b\bar{b}$ final state for an integrated luminosity of 59.7 fb^{-1}; data are represented by black dots.

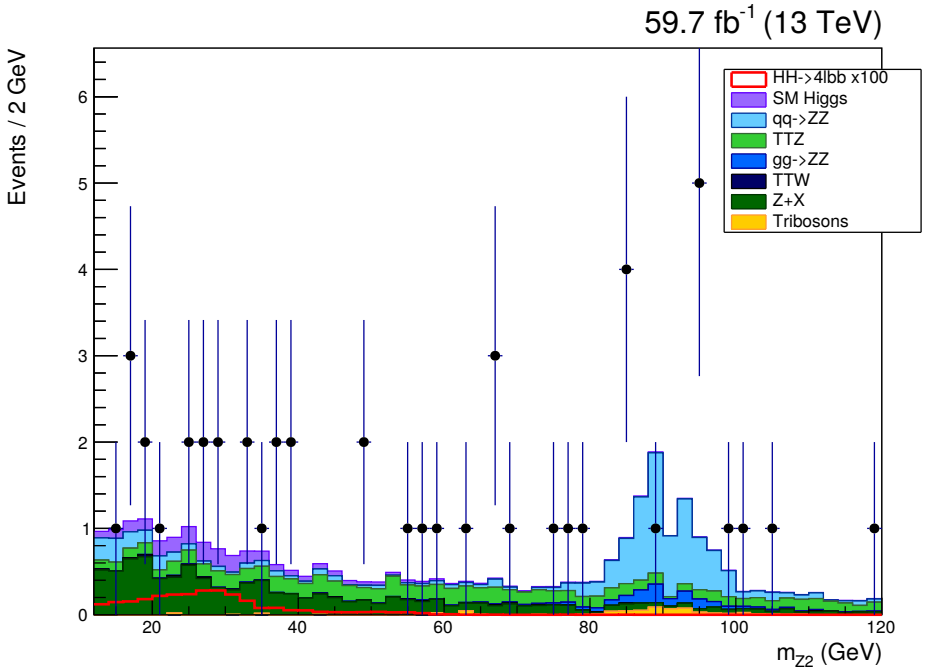

Figure 4.2: Run 2 analysis (2018) - Distribution of the Z_2 reconstructed invariant mass in the inclusive $4\ell b\bar{b}$ final state for an integrated luminosity of 59.7 fb^{-1}; data are represented by black dots.

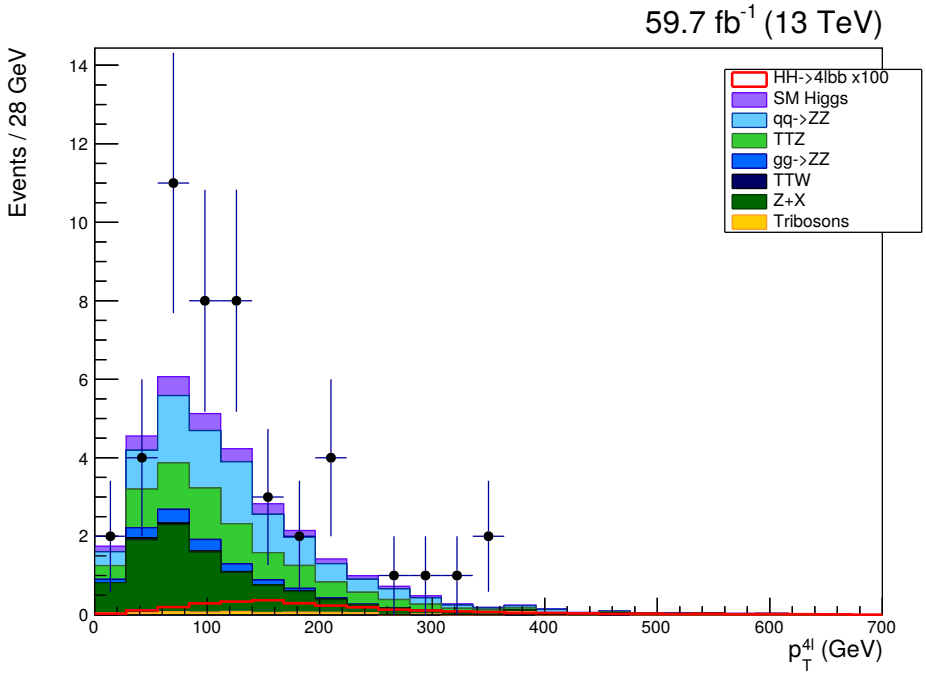

Figure 4.3: Run 2 analysis (2018) - Distribution of the four-lepton reconstructed transverse momentum in the inclusive $4\ell b\bar{b}$ final state for an integrated luminosity of 59.7 fb^{-1}; data are represented by black dots.

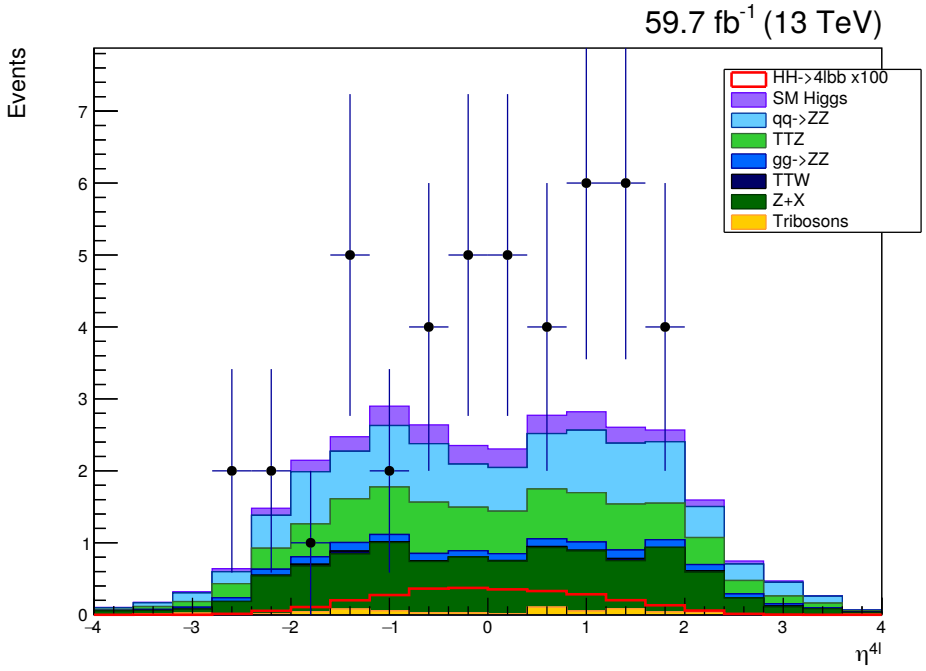

Figure 4.4: Run 2 analysis (2018) - Distribution of the four-lepton reconstructed pseudorapidity in the inclusive $4\ell b\bar{b}$ final state for an integrated luminosity of 59.7 fb^{-1}; data are represented by black dots.

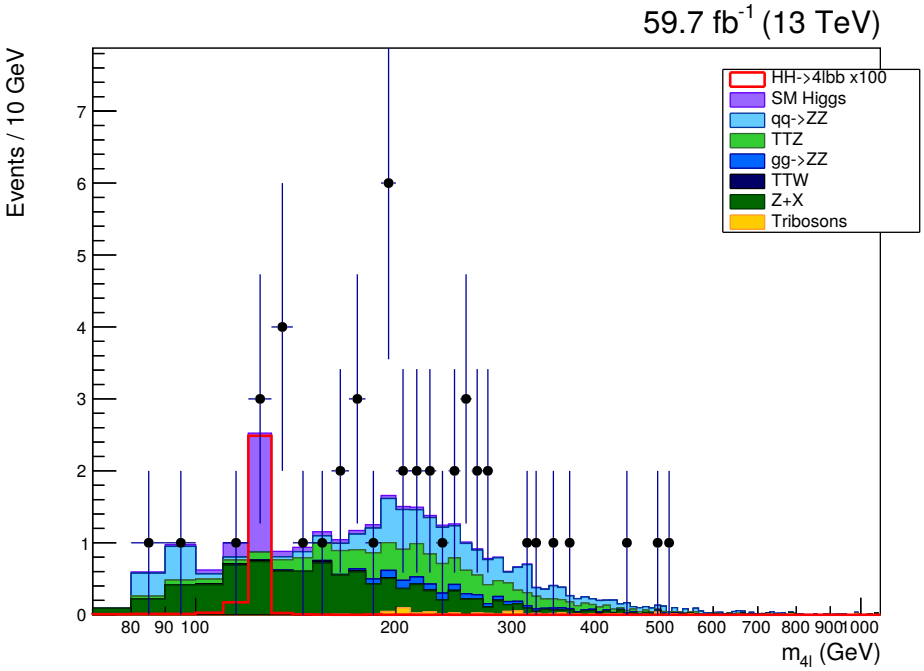

Figure 4.5: Run 2 analysis (2018) - Distribution of the four-lepton reconstructed invariant mass in the inclusive $4\ell b\bar{b}$ final state for an integrated luminosity of 59.7 fb^{-1}; data are represented by black dots.

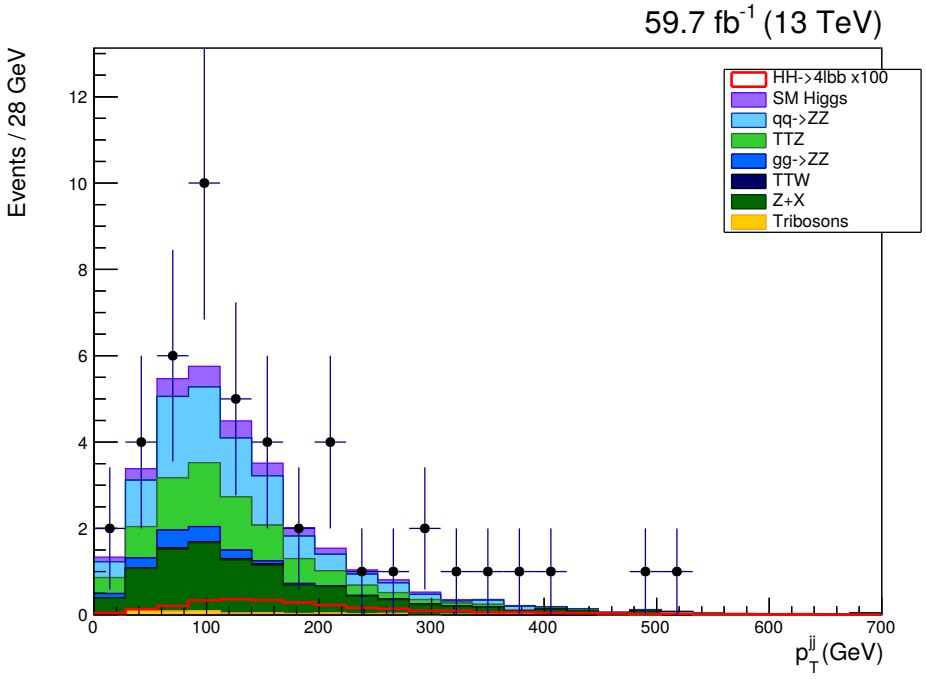

Figure 4.6: Run 2 analysis (2018) - Distribution of the b jets pair reconstructed transverse momentum in the inclusive $4\ell b\bar{b}$ final state for an integrated luminosity of 59.7 fb^{-1}; data are represented by black dots.

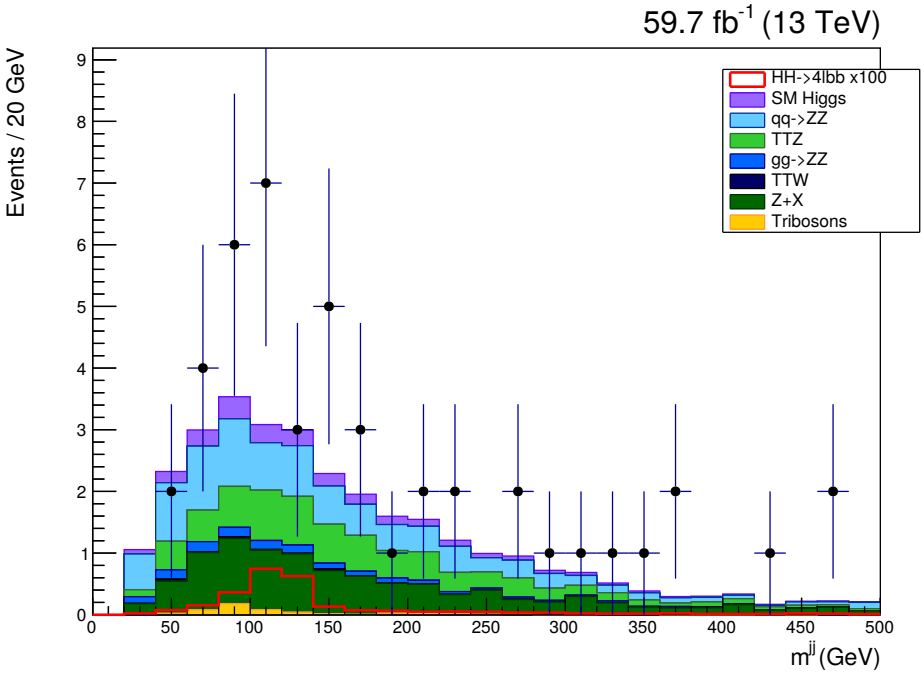

Figure 4.7: Run 2 analysis (2018) - Distribution of the b jets pair reconstructed invariant mass in the inclusive $4\ell b\bar{b}$ final state for an integrated luminosity of 59.7 fb^{-1}; data are represented by black dots.

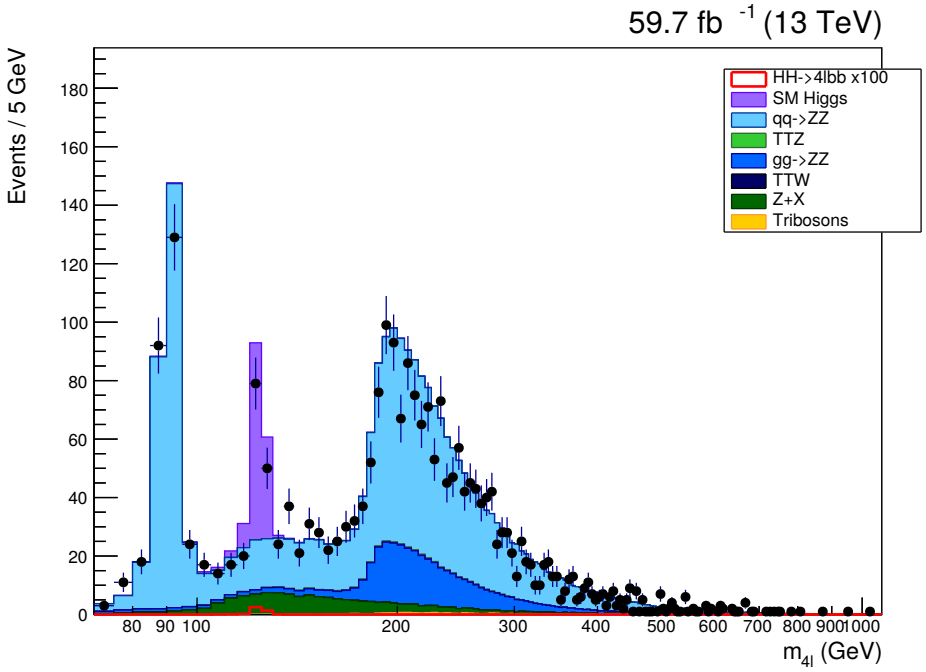

Figure 4.8: Run 2 analysis (2018) - Distribution of the four-lepton reconstructed invariant mass after the reconstruction of the H $\rightarrow$ ZZ only, in the inclusive $4\ell b\bar{b}$ final state for an integrated luminosity of 59.7 fb^{-1}; data are represented by black dots.

In Table 4.2, the expected yields for the backgrounds and the HH signal after the full event selection, obtained by rescaling the MC samples to the full Run 2 luminosity (137.2 fb^{-1}), are reported, to give an indication of the results that could be achieved analyzing the full Run 2 data set. Distributions for the full Run 2 luminosity projection are presented: Figure 4.9 shows the four-leptons invariant mass distribution, while Figure 4.10 shows the invariant mass of the reconstructed b jets pair.

Channel	$4\mu b\bar{b}$	$4eb\bar{b}$	$2e2\mu b\bar{b}$	$4\ell b\bar{b}$
ggH	0.441	0.224	0.561	1.226
VBFH	0.087	0.061	0.117	0.265
ZH	0.124	0.067	0.176	0.367
WH	0.059	0.031	0.081	0.172
$t\bar{t}H$	0.592	0.361	0.830	1.783
$b\bar{b}H$	0.049	0.025	0.059	0.133
$q\bar{q}ZZ$	0.0	0.028	0.060	0.088
ggZZ	0.004	0.006	0.004	0.014
$t\bar{t}Z$	0.121	0.168	0.227	0.516
$t\bar{t}W$	0.012	0.023	0.040	0.075
VVV (WWZ, WZZ, ZZZ)	0.0	0.0	0.0	0.0
Z+jets	1.161	0.352	1.816	3.328
Sum of backgrounds	2.650	1.346	3.971	7.967
$HH \rightarrow 4\ell b\bar{b}$ signal	0.018	0.011	0.030	0.059
Total expected	2.668	1.357	4.001	8.026

Table 4.2: Run 2 anaysis (full Run 2 projection) - Number of expected background and signal events after the full event selection scaled to an integrated luminosity of 137.2 fb^{-1}.

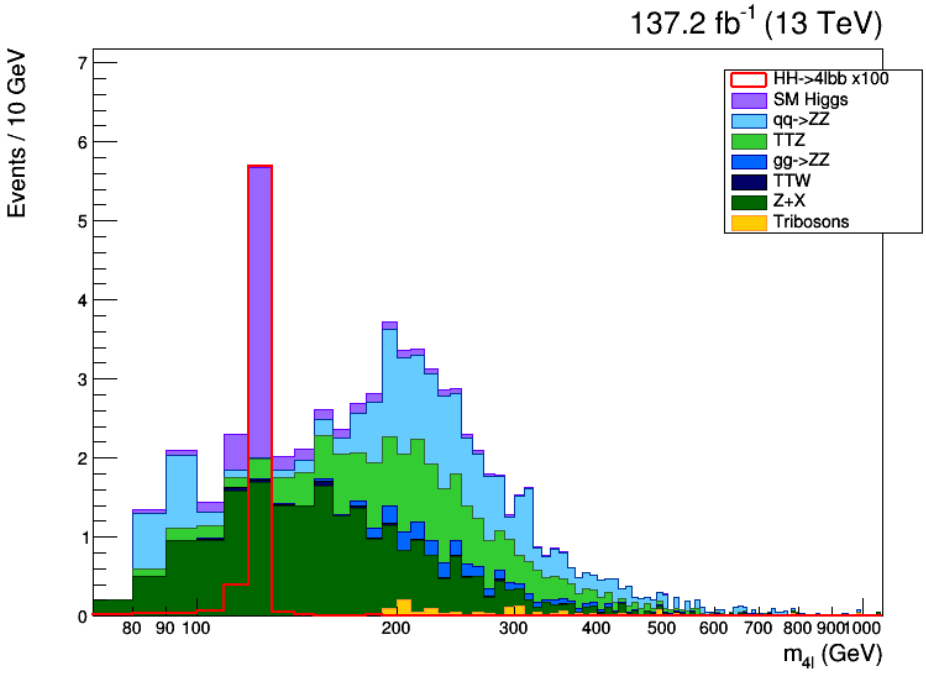

Figure 4.9: Run 2 analysis (full Run 2 projection) - Distribution of the four-lepton reconstructed invariant mass in the inclusive $4\ell b\bar{b}$ final state scaled to the full Run 2 integrated luminosity of 137.2 fb^{-1}.

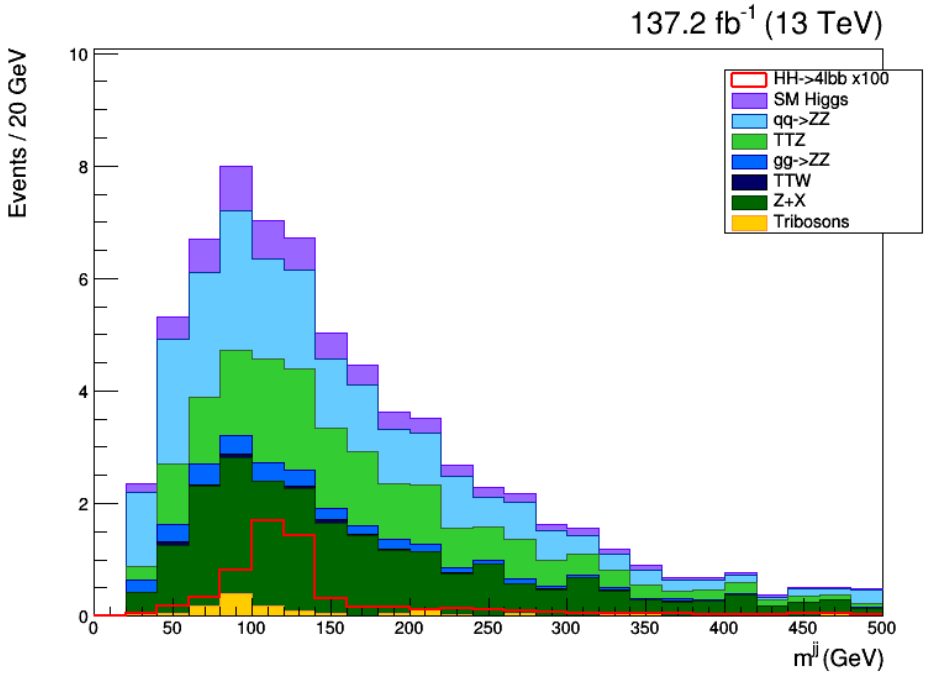

Figure 4.10: Run 2 analysis (full Run 2 projection) - Distribution of the b jets pair reconstructed invariant mass in the inclusive $4\ell b\bar{b}$ final state scaled for the full Run 2 integrated luminosity of 137.2 fb^{-1}.

Signal strength and significance

A multi-dimesional fit is performed, considering the yields at the end of the full event selection, in order to extract the significance for the SM HH signal and the upper limit at the 95% confidence level (CL) on the signal strength modifier, $\mu = \sigma_{\mathrm{HH}}/\sigma_{\mathrm{HH}}^{\mathrm{SM}}$. For the 2018 data set, the observed and expected significance and upper limit are reported in Table 4.3, while in Table 4.4 the expected significance and upper limit at the 95% CL on μ obtained scaling the 2018 MC expectations to the full Run 2 integrated luminosity are reported. All results have been computed in two different uncertainty assumptions: statistical uncertainties only, and statistical and systematic uncertainties on signal and background processes.

The negative log-likelihood on the SM cross section is shown in Figure 4.11 for the 2018 data set while the projection of the 2018 MC expectations scaled to the Run 2 luminosity is shown in Figure 4.12 for the two different uncertainty scenarios.

4ℓbb final state		Signal Significance (σ)		95% CL upper limit on μ	
2018 Data (L = 59.7 fb^{-1})		observed	expected	observed	expected
Uncertainty	Stat. only	0.280	0.014	195.5	195.5
	Stat. + Sys.	0.244	0.012	229.5	230.0

Table 4.3: Run 2 analysis (2018) - Observed and expected significance and upper limit at the 95% CL on the signal strength μ in the inclusive $4\ell\mathrm{b\bar{b}}$ final state, in two different uncertainty assumptions, for the 2018 data set (59.7 fb^{-1}).

4ℓbb final state		Signal Significance (σ)		95% CL upper limit on μ	
Run 2 (L = 137.2 fb^{-1})		observed	expected	observed	expected
Uncertainty	Stat. only	-	0.020	-	118.0
	Stat. + Sys.	-	0.015	-	155.5

Table 4.4: Run 2 analysis (full Run 2 projection) - Expected significance and upper limit at the 95% CL on the signal strength μ in the inclusive $4\ell\mathrm{b\bar{b}}$ final state, in two different uncertainty assumptions, obtained scaling the 2018 MC expectations to the full Run 2 integrated luminosity of 137.2 fb^{-1}.

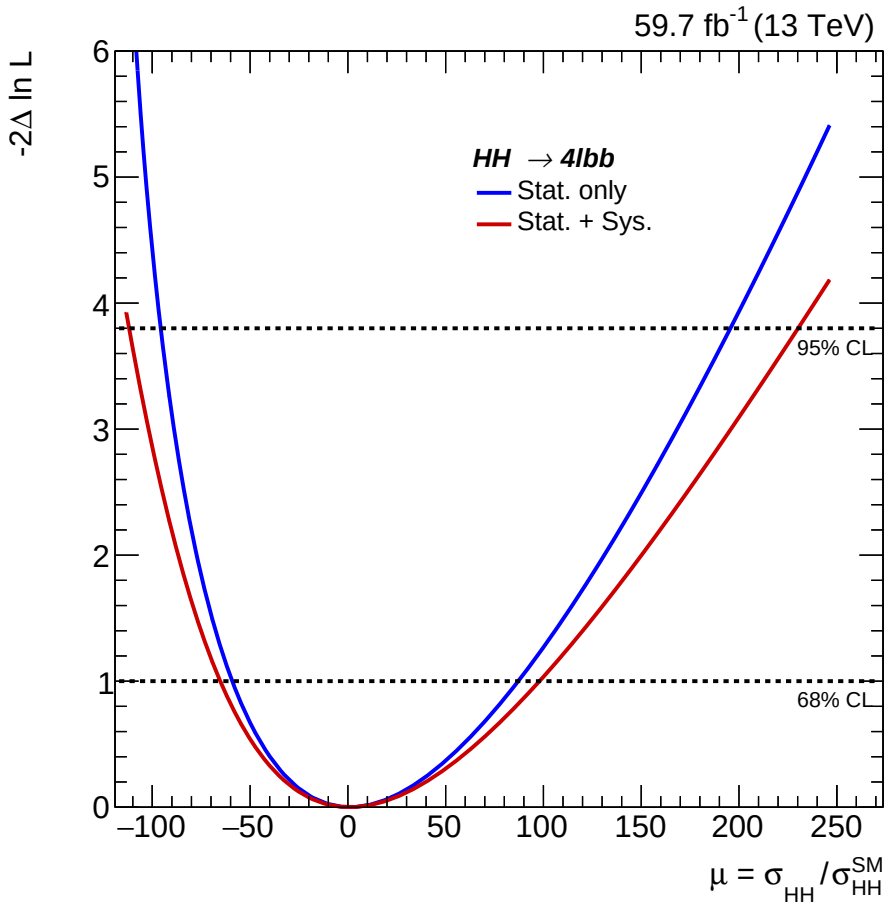

Figure 4.11: Run 2 analysis (2018) - Expected negative log-likelihood on μ for the 2018 data in two different uncertainty assumptions for the inclusive $4\ell b\bar{b}$ final state and an integrated luminosity of 59.7 fb^{-1}.

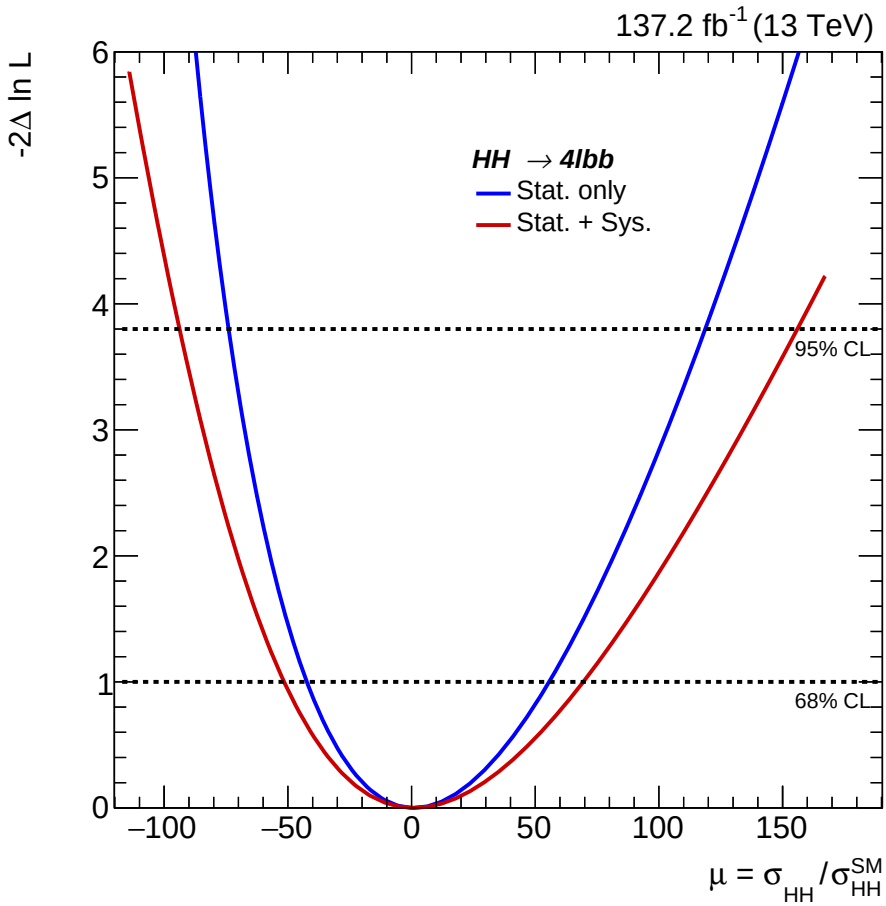

Figure 4.12: Run 2 analysis (full Run 2 projection) - Expected negative log-likelihood on μ in two different uncertainty assumptions for the inclusive $4\ell b\bar{b}$ final state, obtained scaling the 2018 MC expectations to the full Run 2 integrated luminosity of 137.2 fb^{-1}.

4.3 Results of the analysis at HL-LHC

The expected event yields for the HH $\rightarrow$ ZZ(4ℓ)b$\bar{\text{b}}$ signal and background processes, normalized to an integrated luminosity of 3000 fb^{-1}, are reported in Table 4.5. Considering the channels investigated, 1 HH signal event is expected to be selected, for a total number of background events of 6.8 in the inclusive 4ℓb$\bar{\text{b}}$ final state. The invariant mass spectrum of the four leptons after the full event selection, is shown in Figure 4.13. Due to the lack of statistics of the t$\bar{\text{t}}$Z background MC sample, only few events passed all the requirements fulfilling the analysis criteria; however, since the cross section of this process is clearly not negligible, the t$\bar{\text{t}}$Z contribution has been reported in Figure 4.13 considering a flat distribution, which is the one followed by the t$\bar{\text{t}}$Z events in the mass region, to a first approximation, normalized to the expected yield.

Channel	4μbb	4ebb	2e2μbb	4ℓbb
t$\bar{\text{t}}$H	1.3	0.2	1.0	2.5
ggH	0.69	0.053	0.76	1.5
ZH	0.49	0.069	0.38	0.094
WH	0.022	0.003	0.015	0.04
VBFH	0.11	0.011	0.049	0.17
t$\bar{\text{t}}$Z	0.81	0	0.79	1.6
Sum of backgrounds	3.4	0.34	3.0	6.8
HH $\rightarrow$ 4ℓb$\bar{\text{b}}$ signal	0.49	0.088	0.42	1.0
Total expected	3.9	0.42	3.4	7.8

Table 4.5: HL-LHC analysis - Number of expected background and signal events after the full event selection for an integrated luminosity of 3000 fb^{-1}.

Signal strength and significance

The negative log-likelihood on the SM cross section in the inclusive 4ℓb$\bar{\text{b}}$ final state is shown in Figure 4.14 for two different scenarios, both applied to signal and all backgrounds:

- statistical uncertainties only;
- statistical and systematic uncertainties.

The impact of the systematic uncertainties on the analysis is found to be almost negligible. The upper limit at 95% CL on the signal strength μ is computed and shown in Table 4.6, together with the signal significance, for

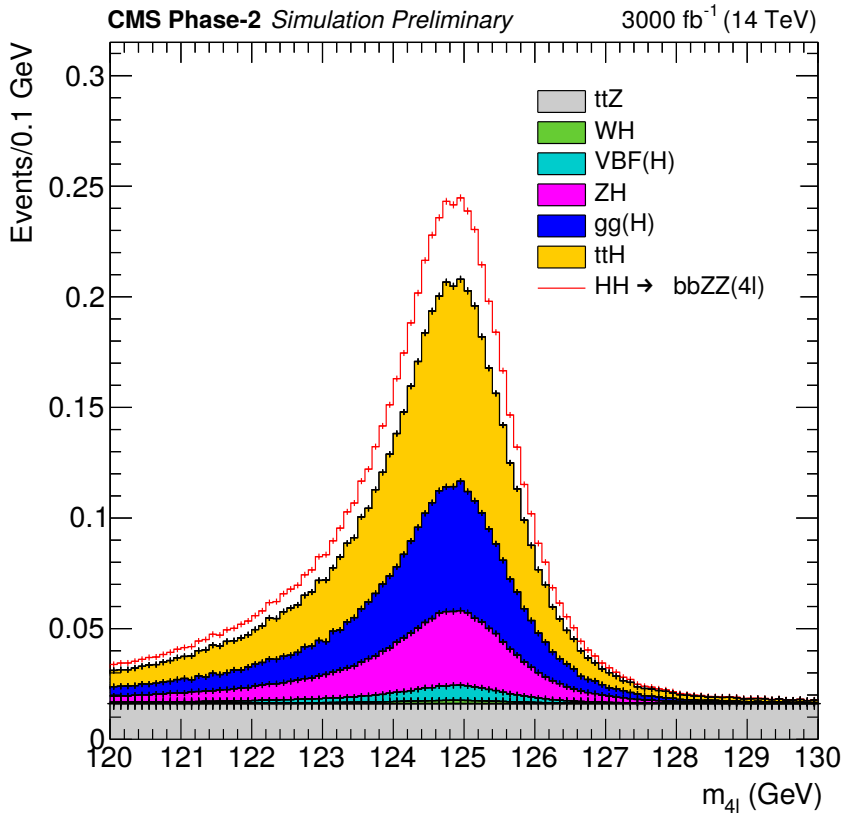

Figure 4.13: HL-LHC analysis - Distribution of the four-lepton reconstructed invariant mass in the inclusive $4\ell b\bar{b}$ final state for an integrated luminosity of 3000 fb^{-1}.

the inclusive final state $4\ell b\bar{b}$ both with statistical uncertainties only and statistical and systematic uncertainties. In Table 4.7 the upper limit at 95% CL on the signal strength μ and the signal significance, for all final states, are reported in the scenario with both statistical and systematic uncertainties.

$4\ell b\bar{b}$ final state HL-LHC (L = 3000 fb^{-1})		Signal Significance (σ) expected	95% CL upper limit on μ expected
Uncertainty	Stat. only	0.37	6.5
	Stat. + Sys.	0.37	6.6

Table 4.6: HL-LHC analysis - Expected significance and upper limit at the 95% CL on the signal strength μ for the inclusive $4\ell b\bar{b}$ final state, in two different uncertainty assumptions, for HL-LHC (3000 fb^{-1}).

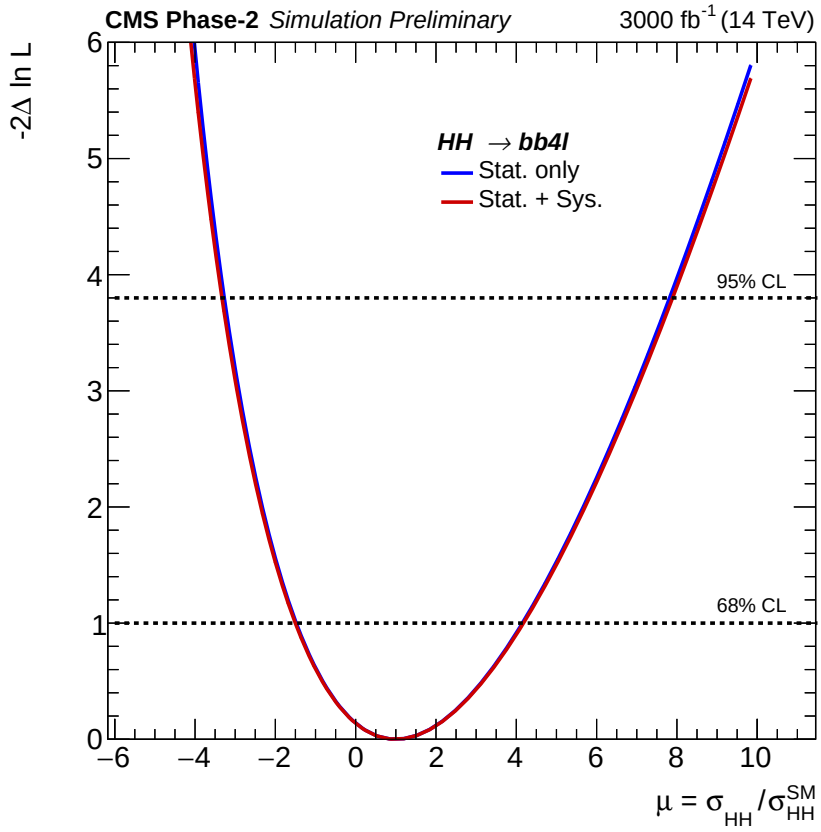

Figure 4.14: HL-LHC analysis - Expected negative log-likelihood on μ in two different uncertainty assumptions for the inclusive $4\ell b\bar{b}$ final state and an integrated luminosity of 3000 fb^{-1}.

	Signal Significance (σ)	95% CL limit on μ
$4\mu bb$	0.3	10.2
$4eb\bar{b}$	0.2	30.5
$2e2\mu b\bar{b}$	0.2	11.7
$4\ell bb$	0.37	6.6

Table 4.7: HL-LHC analysis - Expected significance and upper limit at the 95% CL on the signal strength μ for the four final states studied, in two different uncertainty assumptions, for HL-LHC (3000 fb^{-1}).

Prospects for λ_{HHH}

Assuming that a HH signal exists with the properties predicted by the SM, prospects for the sensitivity of the analysis to the measurement of the Higgs self-coupling λ_{HHH} are derived. The scan of the likelihood as a function of the κ_λ coupling is shown in Figure 4.15 for the inclusive $4\ell\mathrm{b}\bar{\mathrm{b}}$ final state: the projected confidence interval on this coupling corresponds to $[-2.0, +8.0]$ at 68% CL and to $[-3.9, +9.9]$ at 95% CL considering stastistical and systematic uncertainties. Table 4.8 summarizes the confidence intervals on κ_λ at 68% CL and 95% CL in all four final states, considering both statistical and systematic uncertainties. The peculiar likelihood function structure, characterized by two local minima, is related to the dependence of the total cross section and HH kinematic properties on κ_λ, while the relative height of the two minima depends on the capability of the analyses to access differential $\mathrm{m_{HH}}$ information. In fact, the total HH cross section has a quadratic dependence on κ_λ with a minimum at $\kappa_\lambda \approx 2.45$. Consequently, a partial degeneracy exists between the $\kappa_\lambda = 1$ value, that is assumed for the expected signal plus background modeling in the results of Fig 4.15, and a second κ_λ value. The exact position of this second minimum depends on the interplay between the changes in the cross section and in the acceptance as a function of κ_λ. Since this analysis is not sensitive to the differential $\mathrm{m_{HH}}$ measurement, it is not possible to remove the degeneracy between $\kappa_\lambda = 1$ and another valure of κ_λ.

	68% CL intervals on κ_λ	95% CL intervals on κ_λ
$4\mu\mathrm{b}\bar{\mathrm{b}}$	$[-2.8, +8.8]$	$[-5.1, +11.2]$
$4\mathrm{eb}\bar{\mathrm{b}}$	$[-6.5, +13.3]$	$[-12.6, +18.6]$
$2\mathrm{e}2\mu\mathrm{b}\bar{\mathrm{b}}$	$[-3.3, +9.3]$	$[-6.3, +12.3]$
$4\ell\mathrm{bb}$	$[-2.0, +8.0]$	$[-3.9, +9.9]$

Table 4.8: HL-LHC analysis - Confidence intervals on κ_λ at 68% CL and 95% CL in the four final states studied, considering both statistical and systematic uncertainties.

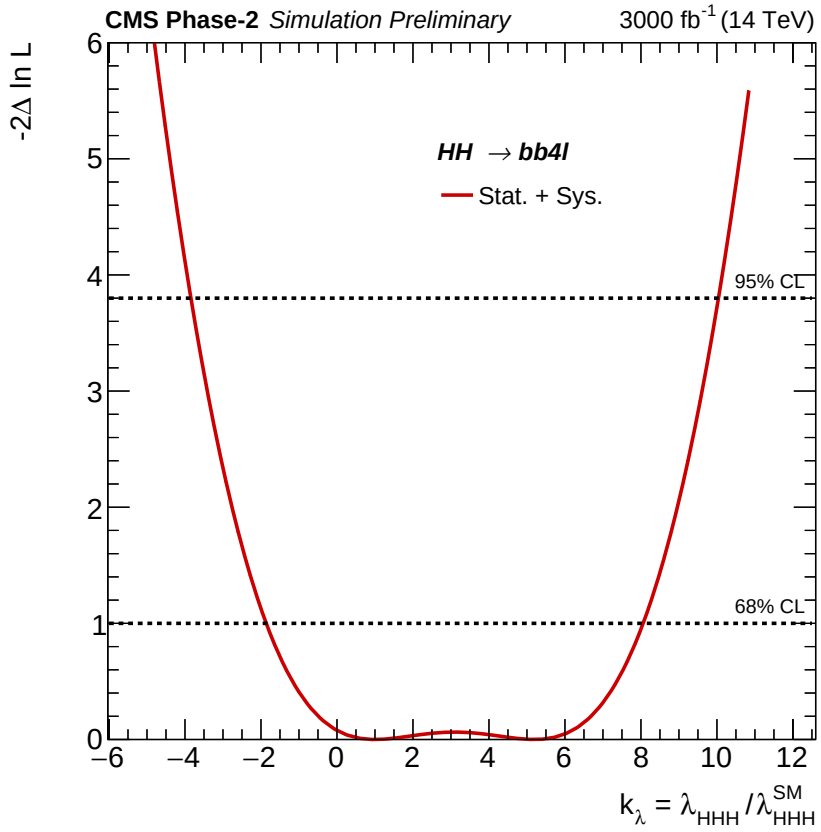

Figure 4.15: HL-LHC analysis - Expected negative log-likelihood on the self-coupling modifier κ_λ considering both statistical and systematic uncertainties for the inclusive $4\ell b\bar{b}$ final state and an integrated luminosity of 3000 fb^{-1}.

4.3.1 Combination with other channels

The results obtained in the baseline HL scenario in the $4\ell b\bar{b}$ final state have been combined statistically with the ones achieved in other four decay channels: HH $\rightarrow$ bbbb, HH $\rightarrow$ bb$\gamma\gamma$, HH $\rightarrow$ bb$\tau\tau$, HH $\rightarrow$ bbWW($\ell\nu\ell\nu$), assuming the SM branching fractions for HH decays to the final states studied. The analyses of the five decay channels have been designed to be orthogonal thanks to the mutually exclusive requirements in the objects used, or to have negligible overlap due to tight object identification criteria and the efficient separation achieved by the multivariate methods used in most of the channels. Systematic uncertainties associated to the same objects (such as the b tag efficiency uncertainties and the leptons reconstruction efficiency) and to the same processes (including common backgrounds and the HH signal) are correlated across the corresponding decay channels, while the others are left uncorrelated.

Table 4.9 summarizes, for the five channels and their combination, the upper limit at the 95% CL and the significance for the SM HH signal. The combined 95% CL upper limit on the SM HH cross section is about to 0.77 times the SM prediction, with a corresponding significance of the signal of 2.6 σ [131]. These results significantly improve over previous projections thanks to the dedicated optimization of the analysis strategies applied to the HL-LHC data set. To give a comparison, the extrapolation to an integrated luminosity of 3000 fb^{-1} of the current Run 2 combination, obtained with a data set of 35.9 fb^{-1} collected at $\sqrt{s} = 13$ TeV [51], yields to a projected SM HH significance of 1.8 σ in the statistical uncertainties only scenario.

Channel	Significance (σ)		95% CL limit on $\sigma_{HH}/\sigma_{HH}^{SM}$	
	Stat. + syst.	Stat. only	Stat. + syst.	Stat. only
bbbb	0.95	1.2	2.1	1.6
bb$\tau\tau$	1.4	1.3	1.4	1.6
bbWW($\ell\nu\ell\nu$)	0.56	0.59	3.5	3.3
bb$\gamma\gamma$	1.8	1.8	1.1	1.1
$4\ell b\bar{b}$	0.37	0.37	6.6	6.5
Combination	2.6	2.8	0.77	0.71

Table 4.9: HL-LHC analysis (combination) - Expected significance and upper limit at the 95% CL on the signal strength μ for the five channels studied and their combination, in two different uncertainty assumptions, for HL-LHC (3000 fb^{-1}) [131].

The combination of the five channels has been also performed for the sensitivity of the analyses to the measurement of the Higgs self-coupling

λ_{HHH}, assuming that a HH signal exists with the properties predicted by the SM. The combined result is shown in Figure 4.16: the projected confidence interval on κ_λ corresponds to $[0.35, 1.9]$ at the 68% CL and to $[-0.18, 3.6]$ at the 95% CL. The analyses that retain sensitivity on the differential $\mathrm{m_{HH}}$ distribution, such as bbbb and bb$\tau\tau$ where this information is used as input to the multivariate methods, partially removes the degeneracy between $\kappa_\lambda = 1$ and another value of κ_λ, while in the case of the bb$\gamma\gamma$ analysis, with a good acceptance and purity in the low $\mathrm{m_{HH}}$ region and a dedicated $\mathrm{m_{HH}}$ categorization, a better discrimination of the second minimum is achieved. The combination of the five channels largely removes the degeneracy, and results in a plateau in the likelihood function for κ_λ values between 4 and 6.

Under the assumption that no HH signal exists, instead, combined 95% CL upper limits on the SM HH production cross section are derived as a function of κ_λ. Figure 4.17 shows the result: a variation of the excluded cross section, directly related to changes in the HH kinematic properties, can be observed as a function of λ_{HHH}.

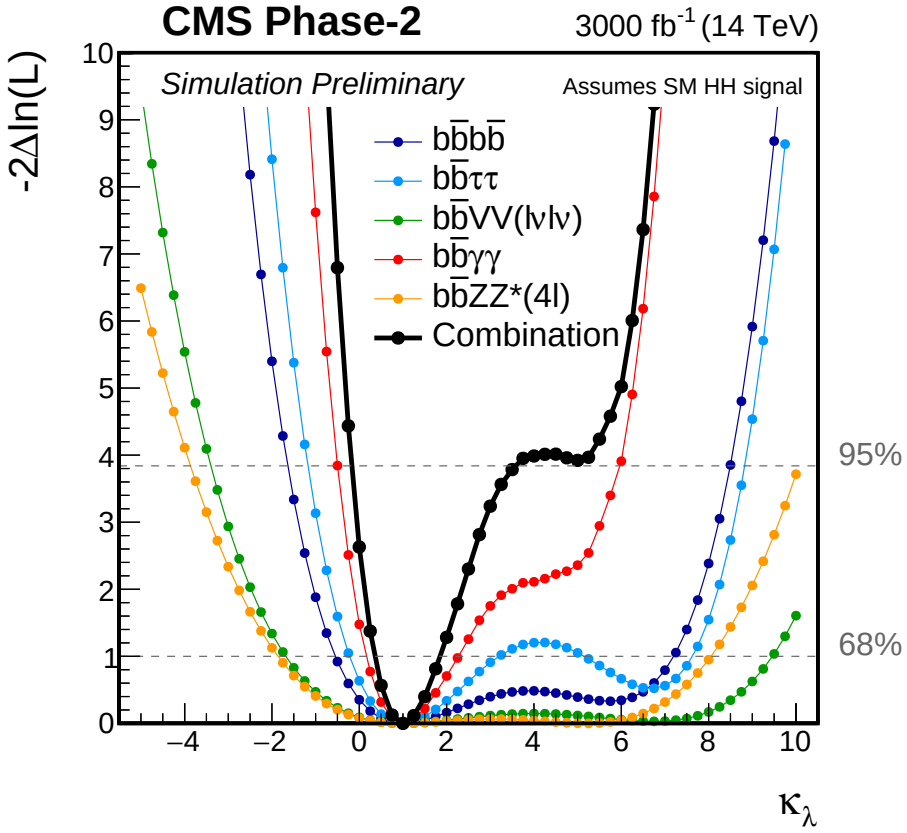

Figure 4.16: HL-LHC analysis (combination) - Expected likelihood scan as a function of κ_λ. The functions are shown separately for the five decay channels studied and for their combination [131].

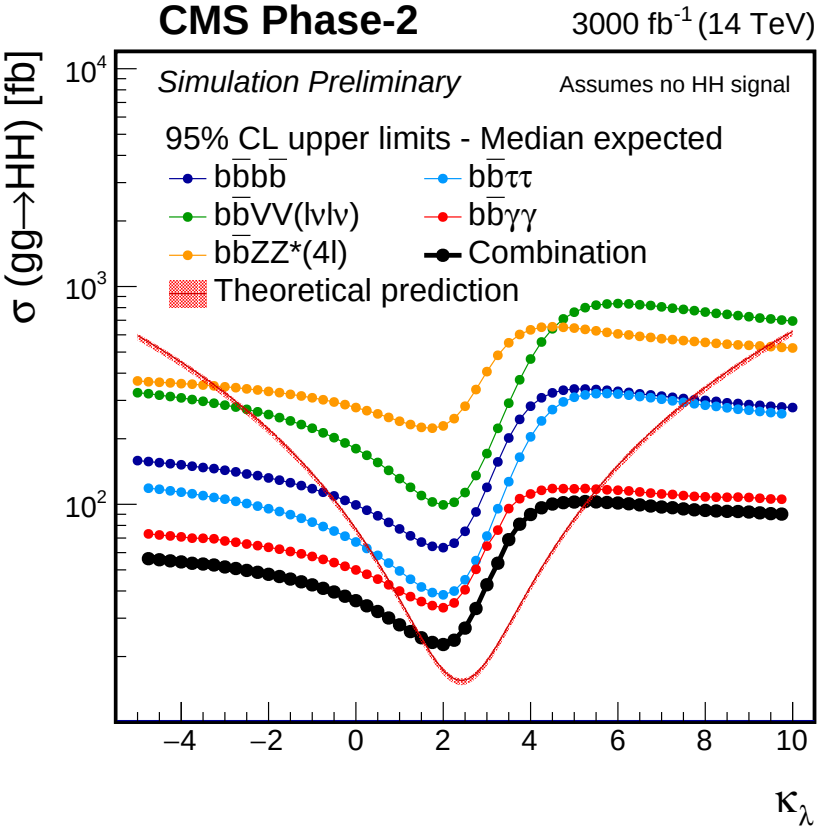

Figure 4.17: HL-LHC analysis (combination) - Upper limit at 95% CL on the HH production cross section as a function of κ_λ for the five decay channel investigated and their combination. The red band indicates the theoretical production cross section [131]

4.3.2 MTD improvement study

The results obtained in the baseline scenario, that exploit the MTD improvement only in the b tagging efficiency, have been compared to the results obtained with no information provided by the MTD ("NO MTD"), and to the ones obtained with a time resolution of the MTD of about 35 ps ("MTD 35 ps") that reflects in an in improvement both on the lepton reconstruction and on the b-tagging efficiency. Table 4.10 summarizes the results obtained for the limit on the signal strength μ and the signal sensitivity in the three scenarios, while Figure 4.18 shows the expected limit on the signal strength μ comparing the "Baseline" and the "MTD 35 ps" scenarios. The inclusion of the MTD information also in the lepton reconstruction brings a sizable improvement up to 0.42 σ for a limit on μ of 5.7 times the SM prediction, with respect to both the other two scenarios, that are almost compatible. The likelihood scan as a function of the self-coupling modifier κ_λ is shown in Figure 4.19 comparing the "Baseline' and the "MTD 35 ps" scenarios.

	Significance (σ)	95% CL limit on μ
"Baseline"	0.37	6.6
"NO MTD"	0.38	6.5
"MTD 35 ps"	0.42	5.7

Table 4.10: HL-LHC analysis (MTD study) - Expected significance and upper limit at the 95% CL on the signal strength μ for the inclusive $4\ell b\bar{b}$ final state, in the three different scenarios ("Baseline", "NO MTD", "MTD 35 ps") considering statistical and systematic uncertainties and an integrated luminosity of 3000 fb^{-1}.

As proceeded for the baseline scenario, the results obtained in the $4\ell b\bar{b}$ final state in the two alternative scenarios have been combined to the ones obtained in the other four channels. The gains in the single objects reconstruction efficiency translates into an increase in the signal yield at constant reducible background ranging between 15 and 30% depending on the final state. In Table 4.11 the expected signal sensitivity for the five channels separated and their combination is reported.

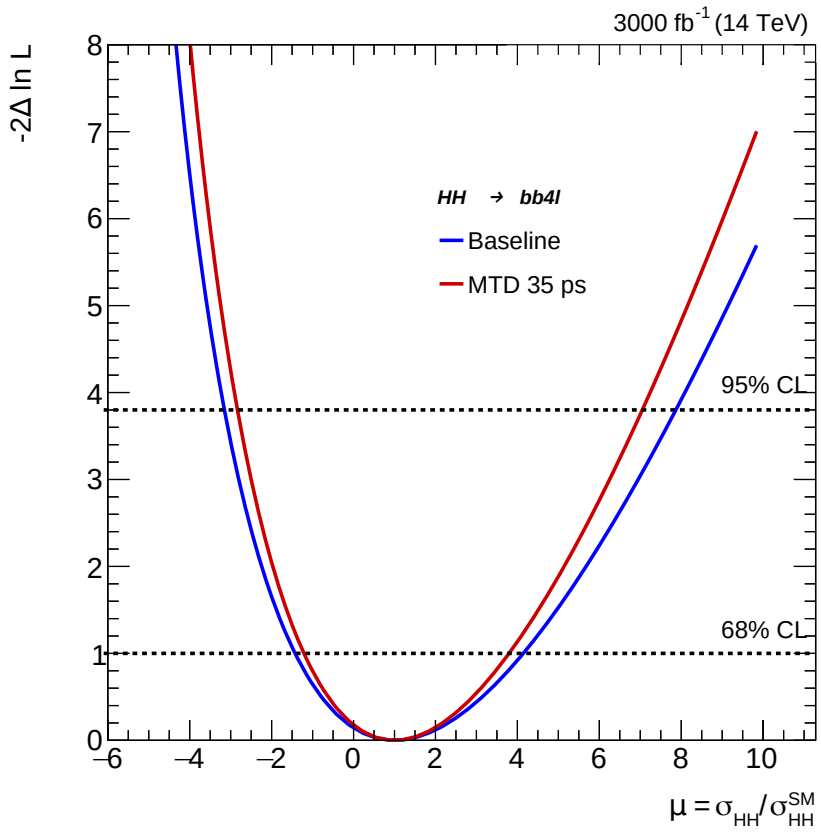

Figure 4.18: HL-LHC analysis (MTD study) - Expected negative log-likelihood on μ for the inclusive $4\ell b\bar{b}$ final state in the "Baseline" (blue) and "MTD 35 ps" (red) scenarios considering statistical and systematic uncertainties and an integrated luminosity of 3000 fb^{-1}.

Significance (σ)	Baseline	"NO MTD"	"MTD 35 ps"
bbbb	0.95	0.88	0.95
bb$\tau\tau$	1.4	1.3	1.6
bbWW($\ell\nu\ell\nu$)	0.56	0.53	0.58
bb$\gamma\gamma$	1.8	1.7	1.9
$4\ell b\bar{b}$	0.37	0.38	0.42
Combination	2.6	2.4	2.7

Table 4.11: HL-LHC analysis (MTD study) - Projection for the HH signal significance in the "Baseline", "NO MTD" and "MTD 35 ps" scenarios for the five decay channels and their combination, including statistical and systematics uncertainties.

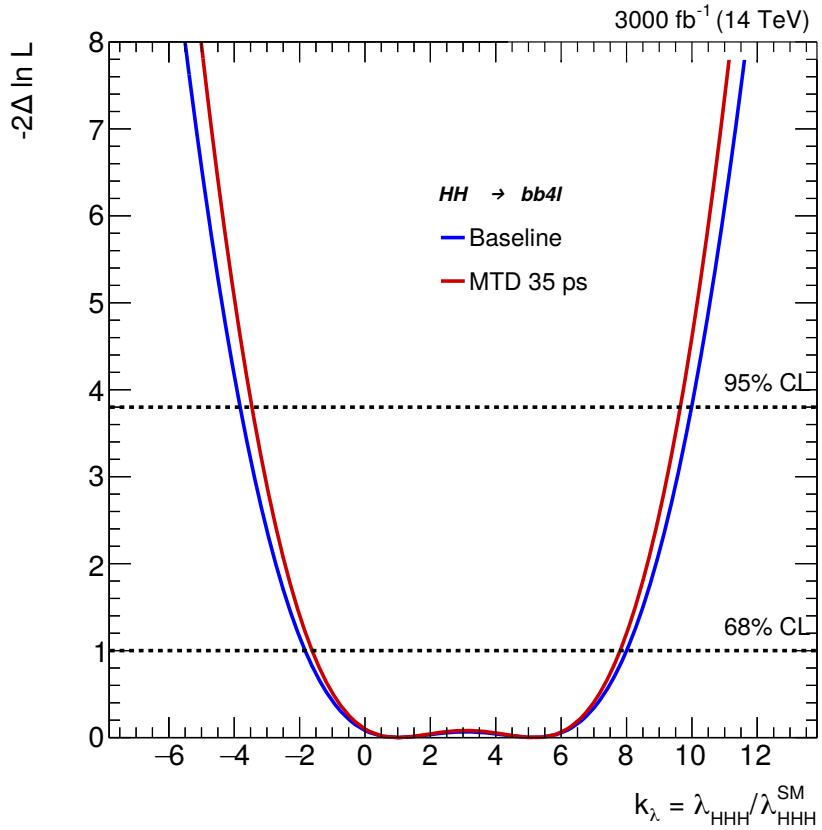

Figure 4.19: HL-LHC analysis (MTD study) - Expected negative log-likelihood on the self-coupling modifier κ_λ for the inclusive $4\ell b\bar{b}$ final state in the "Baseline" (blue) and "MTD 35 ps" (red) scenarios considering statistical and systematic uncertainties and an integrated luminosity of 3000 fb^{-1}.

4.4 Results of the analysis at HE-LHC

Similarly to the HL-LHC scenario, for the analysis at HE-LHC the expected event yield for the HH $\rightarrow$ ZZ(4ℓ)b$\bar{\text{b}}$ signal and background processes, normalized to an integrated luminosity of 15000 fb^{-1}, has been computed and reported in Table 4.12. After 15000 fb^{-1}, 17 HH signal events are expected, over a total of 106 background events in the 4ℓb$\bar{\text{b}}$ final state. The four-lepton invariant mass distribution, after the full event selection, is shown in Figure 4.20. The main background contribution is represented by the t$\bar{\text{t}}$H, ggH, ZH and t$\bar{\text{t}}$Z processes, followed by minor contributions from VBFH and WH. The t$\bar{\text{t}}$ZZ background is found to be negligible. The same procedure described in the previous section on results obtained in the HL scenario has been adopted to graphically represent the t$\bar{\text{t}}$Z background.

Channel	4μb$\bar{\text{b}}$	4eb$\bar{\text{b}}$	2e2μb$\bar{\text{b}}$	4ℓb$\bar{\text{b}}$
t$\bar{\text{t}}$H	27.3	4.6	21.5	53.0
ggH	9.3	0.71	10.0	20.1
ZH	7.4	1.1	5.8	14.3
WH	0.26	0.4	0.2	0.5
VBFH	1.5	0.15	0.69	2.4
t$\bar{\text{t}}$Z	10.7	1.8	3.6	16.0
Sum of backgrounds	56.6	8.8	41.8	106.3
HH $\rightarrow$ 4ℓb$\bar{\text{b}}$ signal	8.5	1.5	7.2	17.2
Total expected	65.0	10.3	49.0	123.5

Table 4.12: HE-LHC analysis - Number of expected background and signal events after the full event selection for an integrated luminosity of 15000 fb^{-1}.

Signal strength and significance

The negative log-likelihood of the SM cross section in the inclusive 4ℓb$\bar{\text{b}}$ final state is shown in Figure 4.21 in the two scenarios: statistical uncertainties only, and statistical and systematic uncertainties included. The upper limit at 95% CL on the signal strength μ is computed and shown in Table 4.13, together with the signal significance, for the inclusive final state 4ℓb$\bar{\text{b}}$ both with statistical uncertainties only and statistical and systematic uncertainties. In Table 4.14 the upper limit at 95% CL on the signal strength μ and the signal significance, for all final states are reported, in the scenario with both statistical and systematic uncertainties.

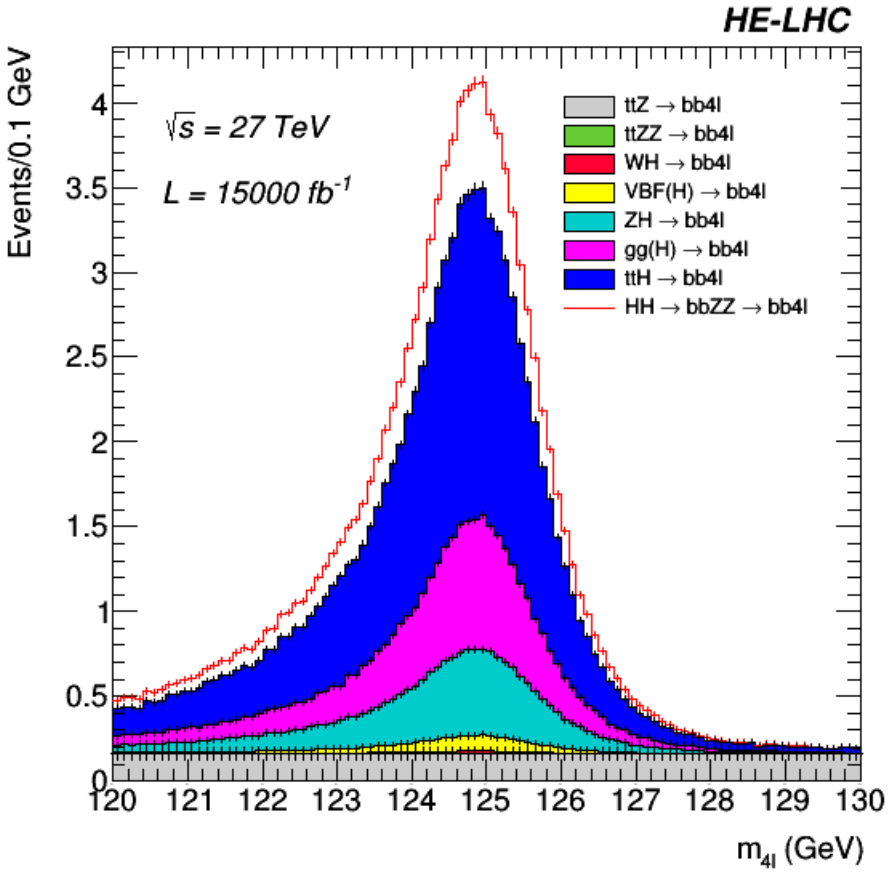

Figure 4.20: HE-LHC analysis - Distribution of the four-lepton reconstructed invariant mass in the inclusive $4\ell b\bar{b}$ final state for an integrated luminosity of 15000 fb^{-1}.

$4\ell b\bar{b}$ final state HE-LHC (L = 15000 fb^{-1})		Signal Significance (σ) expected	95% CL upper limit on μ expected
Uncertainty	Stat. only	1.63	1.25
	Stat. + Sys.	1.43	1.45

Table 4.13: HE-LHC analysis - Expected significance and upper limit at the 95% CL on the signal strength μ for the inclusive $4\ell b\bar{b}$ final state, in two different uncertainty assumptions, for HE-LHC (15000 fb^{-1}).

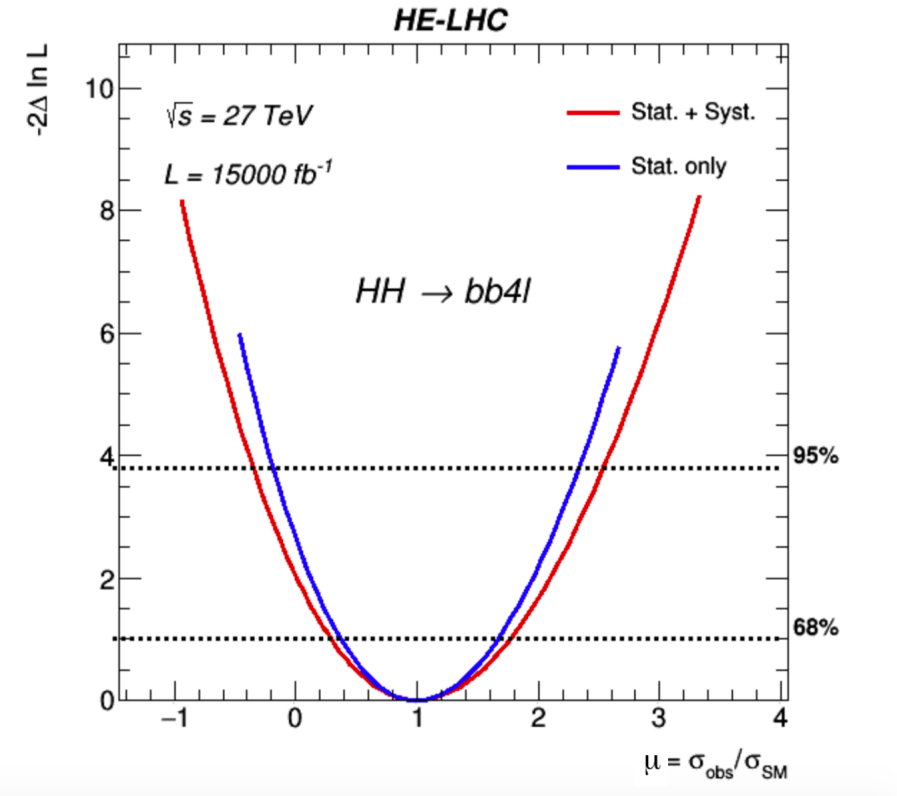

Figure 4.21: HE-LHC analysis - Expected negative log-likelihood on μ in two different uncertainty assumptions for the inclusive $4\ell b\bar{b}$ final state and an integrated luminosity of 15000 fb^{-1}.

	Signal Significance (σ)	95% CL limit on μ
$4\mu b\bar{b}$	1.03	2.04
$4eb\bar{b}$	0.50	4.69
$2e2\mu b\bar{b}$	1.02	2.08
$4\ell b\bar{b}$	1.43	1.45

Table 4.14: HE-LHC analysis - Expected significance and upper limit at the 95% CL on the signal strength μ for the four final states studied, in two different uncertainty assumptions, for HE-LHC (15000 fb^{-1}).

Prospects for λ_{HHH}

Prospects for the sensitivity of the analysis to the measurement of the Higgs self-coupling λ_{HHH} at HE-LHC are also derived, assuming that a HH signal exists with the properties predicted by the SM. The scan of the likelihood as a function of the κ_λ coupling is shown in Figure 4.22: the confidence interval on κ_λ corresponds to $[-0.1, +6.4]$ at 68% CL and to $[-0.7, +7.2]$ at 95% CL in the inclusive $4\ell\mathrm{b}\bar{\mathrm{b}}$ final state. Table 4.15 summarizes the confidence intervals on κ_λ at 68% CL and 95% CL in all four final states, considering both statistical and systematic uncertainties.

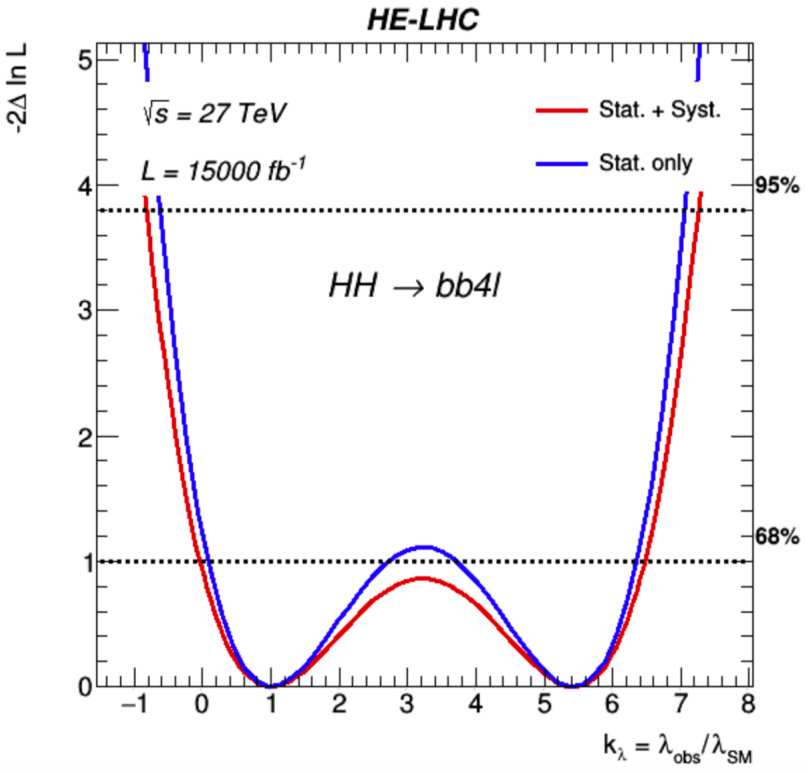

Figure 4.22: HE-LHC analysis - Expected negative log-likelihood on the self-coupling modifier κ_λ in two different uncertainty assumptions for the inclusive $4\ell\mathrm{b}\bar{\mathrm{b}}$ final state and an integrated luminosity of 15000 fb^{-1}.

	68% CL intervals on κ_λ	95% CL intervals on κ_λ
$4\mu bb$	$[-0.3, +6.7]$	$[-1.3, +7.7]$
$4eb\bar{b}$	$[-2.0, +8.3]$	$[-3.9, +10.5]$
$2e2\mu b\bar{b}$	$[-0.4, +6.9]$	$[-1.5, +8.0]$
$4\ell bb$	$[-0.1, +6.4]$	$[-0.7, +7.2]$

Table 4.15: HE-LHC analysis - Confidence intervals on κ_λ at 68% CL and 95% CL in the four final states studied, considering both statistical and systematic uncertainties.

4.5 Results of the analysis at FCC-hh

The same procedure adopted in the HL- and HE-LHC scenarios has been adopted in the FCC-hh study. The expected event yields, shown in Table 4.16, are normalized to an integrated luminosity of 30 ab^{-1} for the HH signal and the considered background processes. The invariant mass spectrum of the four leptons after the full event selection is shown in Figure 4.23 where the same considerations regarding the $t\bar{t}Z$ background in the HL scenario hold.

Channel	$4\mu b\bar{b}$	$4eb\bar{b}$	$2e2\mu b\bar{b}$	$4\ell b\bar{b}$
$t\bar{t}H$	366	229	576	1162
ggH	100	62	155	317
ZH	17	10	26	52
$t\bar{t}Z$	60	30	90	179
Sum of backgrounds	543	331	847	1710
$HH \to 4\ell b\bar{b}$ signal	156	96	238	489
Total expected	699	427	1085	2199

Table 4.16: FCC-hh analysis - Number of expected background and signal events after the full event selection for an integrated luminosity of 30 ab^{-1}.

Precision on the cross section

The negative log-likelihood of the SM cross section is shown in Figure 4.24, and the precision on the expected SM value of the signal strength μ under the three different systematic uncertainties assumptions discussed in Section 3.6.3 is reported in Table 4.17. At 95% CL the precision on the measurement is expected to be 19% when including statistical uncertainties only, 21% if a 1% systematic uncertainty is assumed on signal and background processes, 34% if the systematic uncertainties rise to 3%.

	68% CL precision on μ	95% CL precision on μ
Stat. only	10%	19%
Stat + sys. (1%)	11%	21%
Stat + sys. (3%)	17%	34%

Table 4.17: FCC-hh analysis - Expected precision at 68% CL and 95% CL on the signal strength in the three uncertainties scenarios for the inclusive $4\ell b\bar{b}$ final state and an integrated luminosity of 30 ab^{-1}.

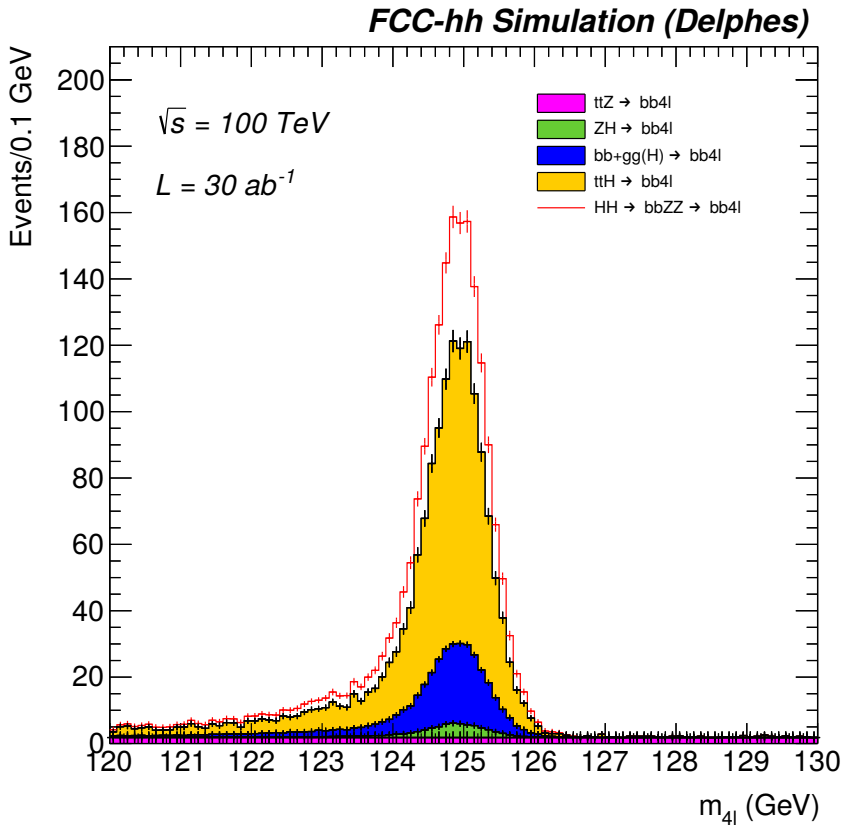

Figure 4.23: FCC-hh analysis - Distribution of the four-lepton reconstructed invariant mass in the inclusive $4\ell b\bar{b}$ final state for an integrated luminosity of 30 ab^{-1}.

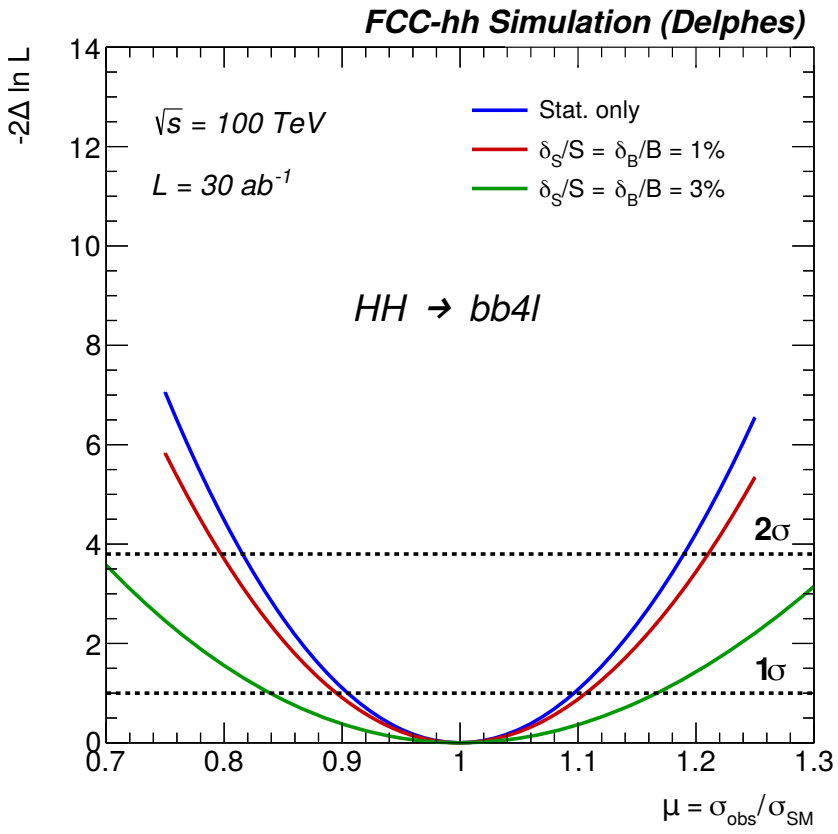

Figure 4.24: FCC-hh analysis - Expected negative log-likelihood on μ in two different uncertainty assumptions for the inclusive $4\ell b\bar{b}$ final state and an integrated luminosity of 30 ab^{-1}.

Precision on λ_{HHH}

The negative log-likelihood of the self-coupling modifier κ_λ is shown in Figure 4.25, and the expected precision on κ_λ is summarized in Table 4.18. Without systematic uncertainties the precision is 28% at 95% CL, it becomes 31% when assuming a 1% systematic uncertainty on the signal and the backgrounds, and decreases to 51% when assuming a 3% systematic uncertainty.

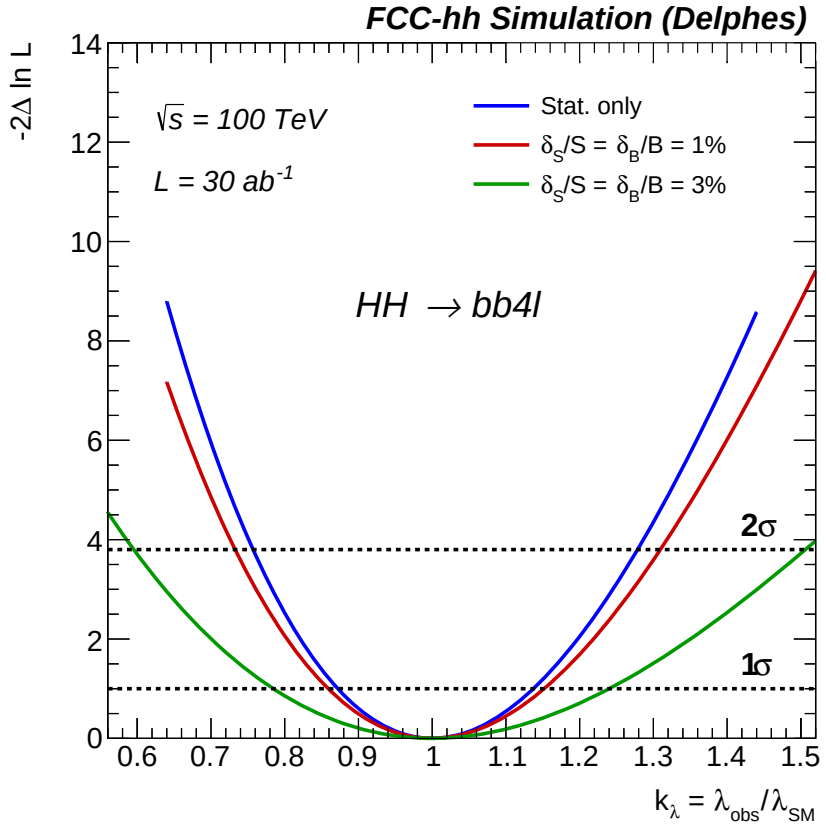

Figure 4.25: FCC-hh analysis - Negative log-likelihood on the self-coupling modifier κ_λ for the inclusive $4\ell\mathrm{b}\bar{\mathrm{b}}$ final state in the three uncertainties scenarios and an integrated luminosity of 30 ab^{-1}.

	68% CL precision on κ_λ	95% CL precision on κ_λ
Stat. only	14%	28%
Stat + sys. (1%)	15%	31%
Stat + sys. (3%)	24%	51%

Table 4.18: FCC-hh analysis - Expected precision at 68% CL and 95% CL on κ_λ in the three uncertainties scenarios for the inclusive $4\ell b\bar{b}$ final state and an integrated luminosity of 30 ab^{-1}.

4.6 Comparison of the results in the different scenarios

The study of this decay channel in many different scenarios, in terms of energy and integrated luminosity, allows to have a complete overview of its current and future sensitivity to the HH cross section and Higgs boson self-coupling. In Table 4.19, the results obtained for the limit on the signal strength and the signal significance are reported, including systematic uncertainties, for the Run 2, HL-LHC and HE-LHC studied scenarios.

	Significance (σ)	95% CL limit on μ
Run 2 (2018) - observed	0.244	229.5
Run 2 (2018) - expected	0.012	230.0
Full Run 2	0.015	155.5
HL-LHC	0.37	6.6
HE-LHC	1.43	1.45

Table 4.19: Upper limit at 95% CL and significance of the signal for the Run 2, HL-LHC and HE-LHC scenarios studied including both statistical and systematic uncertainties.

As expected, the increased cross section due to the higher center-of-mass energy, and statistics, give the opportunity to reach better precision in the future LHC scenarios with respect to the current results obtained with CMS Run 2 data. That is confirmed by the results obtained at FCC-hh, where a precision on the signal strength of 17% (34%) is reached at 68% (95%) CL, assuming a systematic uncertainty of 3% on signal and background processes.

The study at future scenarios included also the determination of the confidence intervals on the parameter κ_λ: a comparison of the results obtained in the HL-LHC and HE-LHC phases is reported in Table 4.20.

	68% CL intervals on κ_λ	95% CL intervals on κ_λ
HL-LHC	$[-2.0, +8.0]$	$[-3.9, +9.9]$
HE-LHC	$[-0.1, +6.4]$	$[-0.7, +7.2]$

Table 4.20: Confidence intervals on κ_λ at 68 and 95% CL including both statistical and systematic uncertainties for the HL-LHC and HE-LHC scenarios.

Also in this case, the higher energy conditions of the HE-LHC scenario allows to narrow the confidence interval in κ_λ. At FCC-hh, where a direct measurement of this parameter would be possible in this channel, the 68%

(95% CL) precision on the Higgs self-coupling modifier would be of about 24% (51%), assuming a systematic uncertainty of 3% on signal and background processes.

Chapter 5

The μ-RWELL for future high energy physics experiments

Gaseous detectors are a fundamental component of high energy physics experiments, especially at the LHC, for their excellent performances: good efficiency, spatial and time resolution, even up to very large surfaces. New developments on gaseous detectors have recently been proposed to let these devices cope with very high particle rates: these are a new generation of detectors, the micropattern gaseous detectors (MPGDs), flexible and improved devices that allow to overcome some limitations affecting traditional gaseous detectors. As already discussed in Section 2.4 of Chapter 2, new MPGDs realized with the GEM technology are currently under installation and integration in the CMS muon spectrometer, and further stations with the same technology will be installed during LS3 to be able to provide an efficient, robust and reliable system for the HL-LHC phase. Another type of MPGD that was originally considered for the CMS upgrade but, more importantly, is the baseline for the IDEA detector designed for the FCC-ee [94] and CepC [140] projects, is the μ-RWELL detector, recently developed by the LNF - Detector Development Group (DDG).

Part of my thesis work was devoted to test and verify the detector capabilities in high radiation environment and in large surface detectors. For this reason, aging studies were conducted on a μ-RWELL prototype at the GIF++ facility at CERN, described in Section 5.4, and homogeneity studies were performed on a large surface μ-RWELL detector during a beam test at CERN, described in Section 5.5.

5.1 Introduction to gaseous detectors

Gaseous detectors have been widely used in particle physics for radiation detection since the beginning of the 20^{th} century, where three main types of gaseous detectors were built: the ionization chamber, the proportional counter and the Geiger-Müller counter. Then from the late 1960's, the multi-wire proportional chamber was invented and opened the path for new types of detectors such as the drift chamber and the time projection chamber. The first three devices have the same structure, but they are operated in different modes, exploiting different phenomena.

The basic structure can be summarized with a cylinder container with conducting walls (cathode) and a thin end window. The cylinder is filled with a suitable gas, as explained in more details in Section 5.1.3. A conducting wire is suspended along its axis, with a positive voltage relative to the walls $+V_0$ applied (anode). The resultant electric field is:

$$E = \frac{1}{r} \frac{V_0}{\ln(b/a)} \tag{5.1}$$

where r is the distance from the axis, b is the inner radius of the cylinder, a is the radius of the wire [141]. When a ionizing particle passes through the container, it produces a certain number of electron-ion pairs, whose mean number is proportional to the energy deposited by the particle in the gas volume. Under the action of the electric field, electrons are accelerated towards the anode, while ions towards the cathode, where they are collected. The signal collected and observed depends on the intensity of the field.

5.1.1 Energy loss in gases

The energy loss of a charged particle in a medium, a gas in this case, is due to two types of reactions: excitation and ionization.

The excitation of an atom X

$$X + p \rightarrow X^* + p \tag{5.2}$$

where p is a charged particle, is a resonant reaction that requires the correct amount of energy to be transferred, and has a typical cross section in noble gases of the order of 10^{-17} cm^2.

The ionization of the atom X

$$X + p \rightarrow X^+ + p + e^- \tag{5.3}$$

instead does not require a specific energy, and has a cross section one order of magnitude higher, $\sigma \simeq 10^{-16}$ cm^2. The electrons and ions created by an

ionizing crossing particle constitute the primary ionization: if the primary electrons produced have enough energy, they produce a secondary ionization. This value does not depend much on the particle type, and only weakly on the gas type. The average value of the energy w needed to create an ionization (about 30 eV for one electron-ion pair) determines the efficiency and the energy resolution of a detector, since the resolution for a particle with energy E is:

$$\sigma_E = 2.35\sqrt{\frac{F \cdot w}{E}} \tag{5.4}$$

where F is the Fano factor for a gas medium, that is around 0.2 for pure Argon [141].

5.1.2 Transport of electrons and ions in gases

After being produced in the ionization process, electron-ion pairs are able to move inside the gas, thanks to two phenomena: diffusion and drift.

Diffusion When no electric field is applied to the gas medium, electrons and ions diffuse uniformly from the creation point, suffering multiple collisions with the gas molecules and thus loosing their energy. At thermal energy, the average velocity of the particles is described by the Maxwell distribution:

$$v = \sqrt{\frac{8kT}{\pi m}} \tag{5.5}$$

where k is the Boltzmann constant, T is the temperature and m is the mass of the particle. At room temperature the electron velocity is $\sim 10^6$ cm/s while the positive ions move at about 10^4 cm/s. The consequence is the recombination with photon emission:

$$X^+ + e^- \rightarrow X + h\nu \tag{5.6}$$

where $h\nu$ is the energy of the emitted photon. The rate of recombination depends on the concentration of positive and negative ions:

$$\frac{dn}{dt} = bn^- n^+ \tag{5.7}$$

where b is a gas-dependent constant and n^+ and n^- are the positive and negative ion concentrations respectively [141].

Drift When an electric field is applied to the gas medium, the produced electrons and ions are accelerated along the field lines towards the anode and the cathode, respectively. Since the particles drift in a medium, they collide with the gas molecules: this limits the maximum average velocity. The drift velocity is defined as:

$$v = \mu \cdot E \tag{5.8}$$

where μ is the mobility of a charge and E is the electric field strength. The drift velocity of ions is lower than the diffusion velocity described previously, and depends linearly on the ratio E/p where p is the gas pressure, but for electrons it can be much higher (1000-10000 times larger than the ions one), thanks to their low mass, and depends linearly on E.

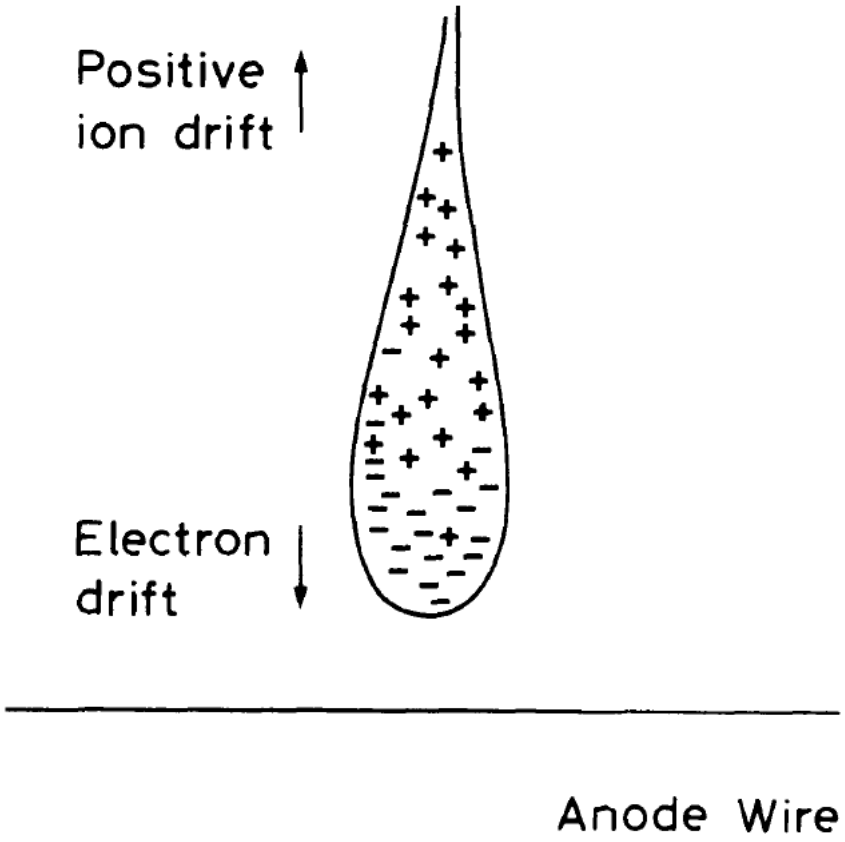

Figure 5.1: Liquid-drop shape of the avalanche, with the electrons at the head and ions in the tail [141].

Avalanche multiplication As already anticipated, when primary electrons produced in the first ionization have enough energy to ionize gas molecules, they produce secondary electrons, that can produce tertiary ionization and so on. The result is an avalanche multiplication. Because of the greater mobility of electrons with respect to ions, the avalanche has a liquid-drop shape, with electrons concentrated near the head and the ions in the tail, as shown in Figure 5.1. If λ is the mean free path of the electron for a secondary ionizing collision, then $\alpha = 1/\lambda$ is the probability of an ionization per path length unit. This is better known as the first Townsend coefficient. If there are n electrons, then there will be

$$dn = n\alpha dx \tag{5.9}$$

new electrons created in a path of dx length. Integrating, this yields to the total number of electrons created in a path x:

$$n = n_0 \exp(\alpha x) \tag{5.10}$$

where n_0 is the initial number of electrons. The multiplication factor, or gain, is then defined as:

$$M = \exp\left[\int_{r_1}^{r_2} \alpha(x)dx\right] \tag{5.11}$$

The multiplication factor is physically limited to about $M < 10^8$ or $\alpha x < 20$, after which breakdown occurs: this is called the Raether limit [142].

5.1.3 Gas mixtures

The baseline gas used in gaseous detectors is always a noble gas, since they require low electric fields to initiate the avalanche. The most common noble gas used in gas detectors is Argon, thanks to its low cost and low ionization energy. A noble gas alone however cannot lead to gains greater than 10^3-10^4 before reaching the breakdown regime due to the high excitation energy: the excited argon atoms formed in the avalanche deexcite emitting high energy photons capable of ionizing the cathode and causing other avalanches. The problem is solved adding a polyatomic gas: their molecules act as quenchers by absorbing the radiated photons and dissipating the energy through dissociation or elastic collisions. Gains up to 10^6 can thus be obtained. The gain can be further increased adding an electronegative gas, that absorbs photons and traps electrons extracted from the cathode before they cause the avalanche. A gain of 10^7 can be obtained before entering the Geiger-Müller regime, with no proportionality between primary and total ionization.

One of the drawbacks of the usage of polyatomic gases is the formation of solid or liquid polymers due to the recombination of dissociated organic molecules. This leads to an accumulation of the polymers on the electrodes, causing the Malter effect, that consists in the presence of dark currents that alter the performance of the detector [143]. This effect is much more common with organic quenchers. For this reason the main quenchers used for gaseous detectors are CO_2 and CF_4. However, in the choice of the gas mixture a new aspect must be included: greenhouse gases (GHG). Various gas mixtures including fluorinate-gases (F-gases), such as CF_4, are subjected to a new regulation of the European Union that is trying to reduce the amount of these gases employed in old devices and ban their usage for new detectors [144]. CERN experiments are already implementing this regulation, adopting recirculation and recuperation strategies in the gas lines of the existing detectors using GHG gases, such as RPCs and CSCs [145]. Other studies are ongoing to find alternative GHG-free mixtures, with similar properties and performances [146]. For this reason, the GEM detectors that will be included in the upgrade of the muon system are planned to be flushed with an Ar/CO_2 mixture that excludes CF_4 completely.

5.1.4 Operational regimes of gaseous detectors

Figure 5.2 summarizes the different operational regimes of gaseous detectors, reporting the number of collected ions as a function of the intensity of the electric field:

- The first region is the *recombination region*, where the electric field is not strong enough to allow the electrons and ions collection, since they recombine under their own electrical attraction, emitting a photon.

- In the second region the recombination does not occur, since the electric field is strong enough to allow electron-ion pairs collection at the electrodes. A detector working in this region is called *ionization chamber*.

- In the third region, the electric field is so strong that not only electron-ion pairs are created and collected, but the freed electrons have enough energy to ionize in their turn the gas molecules and produce a secondary ionization. These electrons produce other electron-ion pairs, resulting in an avalanche. The number of electron-ion pairs is proportional to the primary electrons, with the proportional constant called "gain" (see Eq. 5.11: for this reason the detectors operating in this regime are called *proportional chambers*. Increasing the voltage would cause a distorted

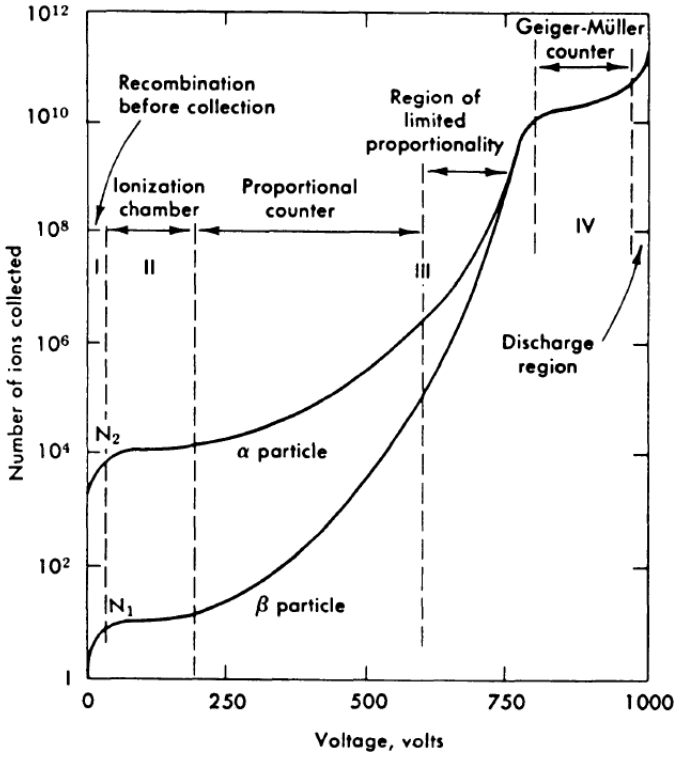

Figure 5.2: Number of ions collected as a function of the applied voltage in a single wire gas chamber [141].

field close to the anode, where electrons are collected more rapidly than the ions, with a limited proportionality effect between the primary and total electrons produced.

- If a quenching gas is added to the gas mixture the discharge is stopped and the *Geiger-Müller* regime is reached. In this region there is no longer proportionality between primary and total ionization, and the number of collected ions is in a plateau with very high gains. Increasing the field beyond this point would lead to discharges occurring regardless of the presence of a ionizing particle or not, with an increasing risk of damage for the detector components.

Multi-wire proportional chambers (MWPC), invented by Nobel awarded Charpak in 1968 [147], represent the evolution from the basic proportional counters just described: they are composed of a series of parallel and equidistant anode wires placed between two cathode planes, as shown in Figure 5.3. With all wires at the same potential, the radial field obtained is uniform

far from the wire plane, and allows high gains thanks to the dependence of the field on $1/r$. After MWPCs were introduced, other new types of detectors have been explored, such as the drift chamber and the time projection chamber. These detectors, used in the modern LHC experiments, exploit the combined information of drift velocity and arrival time of the signal to obtain the spatial information on the coordinate parallel to the field one.

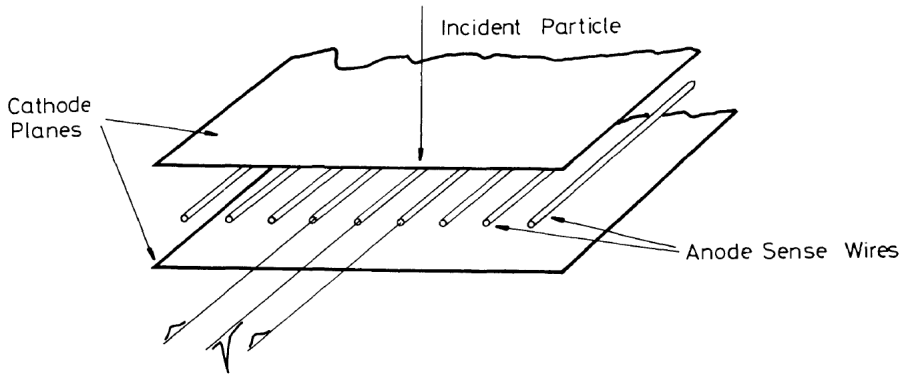

Figure 5.3: Basic configuration of a multiwire proportional chamber [141].

5.1.5 Limitations of traditional gaseous detectors

Even if almost all classical gaseous detectors show great performances at low costs, with the possibility to adapt their geometry to the various experiments needs, they have some limitations, that lead to the development of the micropattern gaseous detectors (MPGD) technology. Taking as baseline the MWPC, the first limitation is the stability of the mechanical anode wires structure, especially in large area detectors. When the electric field is applied between anode wires and cathode planes, a little displacement of one wire reflects on a major attraction to one side and less to the opposite, increasing the risk of a discharge that can damage the detector [148]. Another limit is the rate capability, that is the maximum rate of particles up to which the detectors maintains good performances. Since a huge quantity of ions are produced during the avalanche, and since their drift velocity is much smaller than the electron's one, the number of collected electrons is lower than that produced, and an amount of ions is always present close to the wire, modifying the field. The effect is a drop in the gain, that leads to a lower efficiency of the detector. Finally, aging effects generally affect the traditional gaseous detectors, as already mentioned, for what concerns the polymerization processes due to organic quenchers, usually seen around the anode wires, or corrosive processes due to the presence of F-radicals.

5.2 Micro pattern gaseous detectors

In order to overcome the limitations set by classical gaseous detectors, the Microstrip Gas Chamber (MSGC) was introduced in 1988 by Oed [149]. The basic structure of this detector, shown in Figure 5.4, consists of a series of thin metal strips engraved on an insulating substrate, alternately connected as anodes and cathodes, with the drift electrode placed on the opposite side, defining the electric field of the drift region. The electrons drift along the field lines and in proximity of the anode strips the avalanche occurs. Ions are collected by the cathode strips.

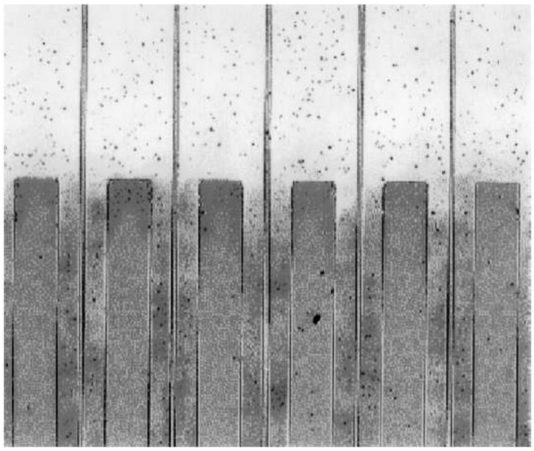

Figure 5.4: Zoomed view of a Microstrip Gas Chamber plates [150].

MSGC were the first prototype of this new generation of gaseous detectors, characterized by a high granularity with small (below 1 mm) distance between the anode and the cathode electrodes [151]. In these detectors there is a clear separation between the drift region and the amplification region: in the drift region, with low electric field, ionization electrons simply drift towards the amplification region, where a very high electric field causes the avalanche multiplication. This separation and the concentration of the avalanche only in the amplification region allow an improvement of the spatial resolution of one order of magnitude, and improve the rate capability thanks to the reduced path of the ions towards the cathode strips. The main problem affecting MSGCs is the occurrence of sparks that can damage the thin electrodes, induced by the presence of dust or other impurities inside the detector [152, 153].

Starting from the MSGC, many different new MPGD have been developed and employed in high-energy physics experiments: micro-mesh gaseous detectors (MicroMegas) [154], selected by the ATLAS experiment at CERN

for the upgrade of the New Small Wheel, and GEM detectors, already installed in the LHCb muon system and selected for the upgrade of the CMS detector, being only few examples.

5.3 The μ-RWELL technology

Other new detectors have been developed starting from the working principle of a single GEM foil (see Section 2.4), introducing improvements such as resistive electrodes to suppress sparks in order to reach higher gains in a safe regime. One of them is the μ-RWELL detector, recently developed by the LNF - Detector Development Group (DDG) of Frascati, that is a new MPGD composed of two elements: the cathode PCB and the μ-RWELL-PCB, which is the core of the detector since it forms both the amplification stage, and the readout [155]. The cathode is a simple FR4 foil with a thin copper layer on one side, while the μ-RWELL-PCB is realized with a suitable patterned Kapton® foil, sputtered with a resistive layer on its bottom side and coupled to a standard readout PCB, as shown in Figure 5.5.

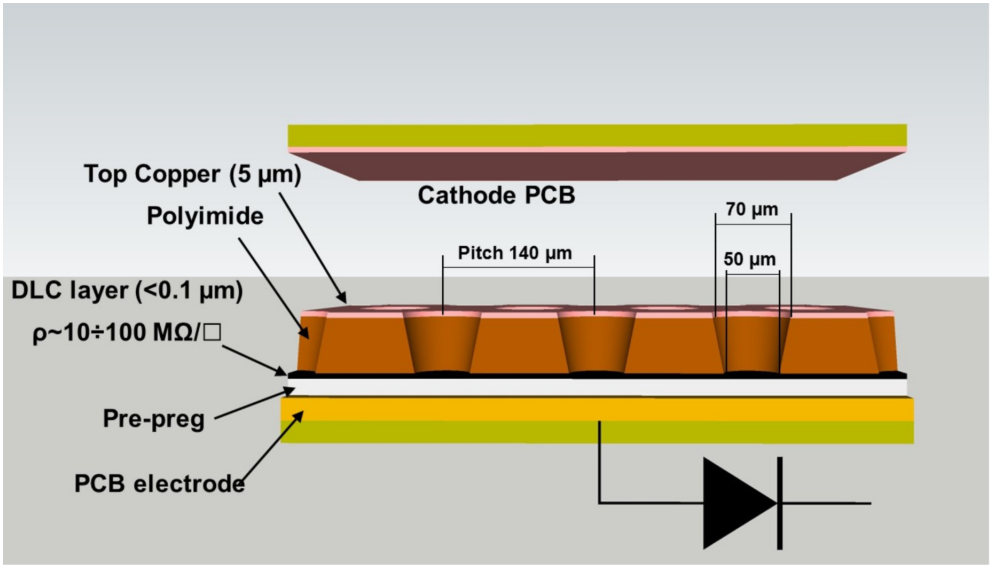

Figure 5.5: Schematic view of the μ-RWELL detector [156].

The amplification stage is manufactured, as for GEMs, with standard photolitographic technique. The geometrical parameters are actually similar to the GEM foils: 50 μm Kapton® thickness, 5 μm copper layer on the top side; conical wells with opening diameter of 70 μm and base diameter 50 μm. The holes are distributed honeycomb-like with a pitch of 140 μm.

The Kapton® foil has on the other side a resistive layer, realized with a $100 \div 200$ nm thin Diamond-Like-Carbon (DLC) [157], and then is glued to the readout PCB. With this structure, the drift gas is delimited by the cathode and the top of the Kapton® foil, while the amplification stage is realized inside the wells: when a proper voltage is applied between the sides of the foils, the avalanche of the electrons originated in the drift gas gap occurs. The charge is then collected on the resistive layer, introduced to suppress the discharge amplitude, with a mechanism similar to the one used in the RPCs: the streamer generated in the gas gap inside the amplification layer induces a current on the resistive layer, generating a local drop of the amplifying voltage and the suppression of the multiplication process. The charge induced on the resistive layer spreads with a time constant τ that depends on the surface resistivity ρ and the capacitance per unit area c as:

$$\tau = \rho c = \rho \frac{\varepsilon_0 \varepsilon_r}{t} \tag{5.12}$$

where t is the distance between the resistive and readout layers [158, 159]. This mechanism of charge suppression allows to reach high gains, of the order of 10^4 with a single amplification stage, in a safe spark-free regime [155]. On the other hand, the Ohmic behavior of the detector does not allow very high rate capabilities and makes the described configuration of this detector more suitable for "low" rate applications (50-100 kHz/cm^2), leading to an intense R&D program dedicated to the development of new very high-rate configurations.

5.3.1 Low rate configuration

The layout of the μ-RWELL described earlier is based on a single-resistive layer with ground on the edge of the active area, forming a 2D current evacuation. This simple layout has been designed for low rate applications, for particle fluxes lower than 100 kHz/cm^2, such as the upgrade of the CMS muon system with GE2/1 chambers. The two prototypes studied for my thesis work, that will be described in more details in the next sections, have been realized with this technique.

5.3.2 High rate configuration

New layouts have been developed to build a detector able to stand higher incident fluxes, of the order of 1 MHz/cm^2 or higher [160]. This can be performed changing the grounding layout of the DLC, speeding up the charge evacuation. A new tested layout has been realized with a double-resistive

layer: a first DLC film is sputtered on the bottom of the amplification stage, and connected to a second DLC film by means of metalized vias. Then a second matrix of vias connects the second DLC layer to the readout electrodes, providing the final grounding of the whole resistive stage, with a 3D current evacuation layout. The vias density is typically $\leq 1/\text{cm}^2$. A second approach has been taken to create a prototype for high rates: a single-resistive layout with a grounding grid (SG) network. In this case, a conductive grid is deposited on the DLC layer to act as a 2D current evacuation system meanwhile reducing the charge paths to the ground. To avoid discharges on the DLC over the grids, this design requires the introduction of small dead zones in the amplification stage above the grid lines.

5.3.3 Properties of the μ-RWELL detector

Many different prototypes have been realized and tested to study the detector performances in different configurations. The basic single-resistive layer for low rates has proved to stand fluxes of the order of tens of kHz/cm^2 without losing efficiency [159]. With the high rate prototypes, instead, a rate capability up to 10 MHz/cm^2 with a detection efficiency of the order of 97% has been achieved [160]. The spatial resolution depends largely on the type of readout and DLC resistivity: with a surface resistivity of the order of 100 $\text{M}\Omega/\square$ a resolution of $\sim$ 60 μm has been obtained [155]. A time resolution of 6 ns has been achieved both with a small and a large area prototypes operated at a gain of about 10000 [161], the latter being the same prototype used to perform the longevity studies described in the next section.

An important advantage of this technology is the simple structure, composed of very few components, that does not require any complex time-consuming assembly procedure. Compared to a GEM detector, for example, it has only one amplification stage, reducing material and costs of almost a factor three and does not require any stretching of the GEM foils, which is a very delicate procedure, since here the Kapton® foil is glued directly on the readout plane. This advantage makes this technology very suitable for future experiments, where large area detectors are required, and easily mass produced by industry, reducing production costs.

For this thesis work, two other tests were performed on two different μ-RWELL prototypes. An aging test was performed to monitor the response of the detector under high irradiation, equivalent to several years of operations in the HL-LHC environment, for example. Furthermore, to test the response of a large area detector, the largest μ-RWELL detector ever built was tested in a beam facility, studying its homogeneity and efficiency.

5.4 Aging tests at the GIF++ facility

Aging is one of the main problems affecting the traditional gaseous detectors, primarily due to polymerization phenomena, leading to significant and often permanent degradation of the performances. For this reason, it is important to perform tests to evaluate the detector deterioration, simulating its lifetime in an experiment. For this purpose, a longevity study was performed at the Gamma Irradiation Facility (GIF++) at CERN on a low-rate μ-RWELL detector.

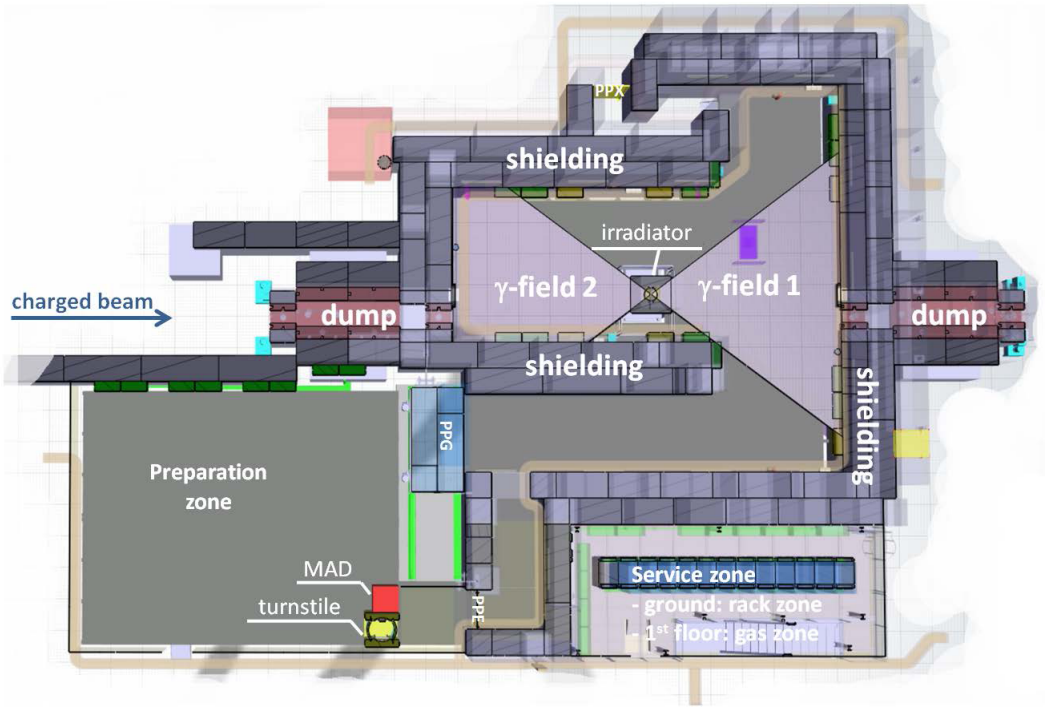

Figure 5.6: Schematic view of the GIF++ facility at CERN [162].

5.4.1 The GIF++ facility at CERN

The Gamma Irradiation Facility (GIF++) [162] is a test area placed at CERN, in the SPS North Area (Prévessin site), where a high intensity gamma-ray source is located for longevity studies. The source exploited is the ^{137}Cs isotope, that emits 662 keV photons with an activity of 14 TBq (certified in December 2015). This allows to simulate similar conditions to the ones expected at HL-LHC, for example, where the main source of background in the CMS muon system is composed of neutron-induced photons,

with an energy of 0.1-10 MeV [87]. In Figure 5.6 a sketch of the facility is shown: with a surface of 100 m^2, it is composed of two different areas, the upstream (30 m^2) and the downstream (70 m^2) areas.

The irradiation region is shielded by concrete walls 1.6 m thick, that divide it from the preparation area, where detectors are placed temporarily for preliminary tests, the gas zone, where all the services regarding the gas systems are placed, and the rack zone, where high voltage systems, electronics and data acquisition systems are located. The ^{137}Cs source is placed at the same height of the 150 GeV muon beam from the secondary SPS beam line H4, that can be used for combined tests. The irradiation fields, upstream and downstream, are defined by an opening angle of 37° on the horizontal and vertical planes and, thanks to proper lenses, are uniform in x-direction, depending only on the perpendicular distance from the source (z-coordinate). In order to understand the properties of the GIF++ irradiation field, simulations have been performed, showing the photon flux in the $x - z$ plane: Figure 5.7(top) shows the emitted field intensity while Figure 5.7(bottom) shows the simulated absorbed dose rate in air. For each irradiation zone, the intensity of the field can also be modulated and reduced from its nominal intensity, with an array of 3×3 lead attenuation filters, for a total of 24 different nominal attenuation factors between 1 and 46415.

5.4.2 Description of the setup

The detector that has been installed in the GIF++ facility is the same large area prototype used for the time resolution measurement described in the Section 5.3.3: a μ-RWELL detector ($\sim 1.2 \times 0.5$ m^2), realized with the CMS 10° GE1/1 shape in the low-rate single-resistive scheme, with a DLC surface resistivity of about 70 M$\Omega/\square$, shown in Figure 5.8. During construction, the detector has been divided in two vertical regions, left and right, and this resulted in two sectors powered and readout independently. The prototype has also a horizontal segmentation in 8 sectors per side, for a total of 16 different sectors, as schematically reported in Figure 5.9. In particular, only four sectors were connected to the high voltage, and then subject to aging: sectors number 3-left, 3-right, 5-left and 7-right, as illustrated in Figure 5.9.

The high voltage was provided by a CAEN module placed in the rack area, connected to the detector by 35 m long HV cables routed under the GIF++ floor. The drift gap of this detector is 7 mm, while the readout is realized with 800 μm strips, that were not connected to electronics because the test was performed in current mode. The high voltage and the current meter could be operated remotely to control and access measurements during operation without dead times. The gas system, realized with stainless steel tubes to

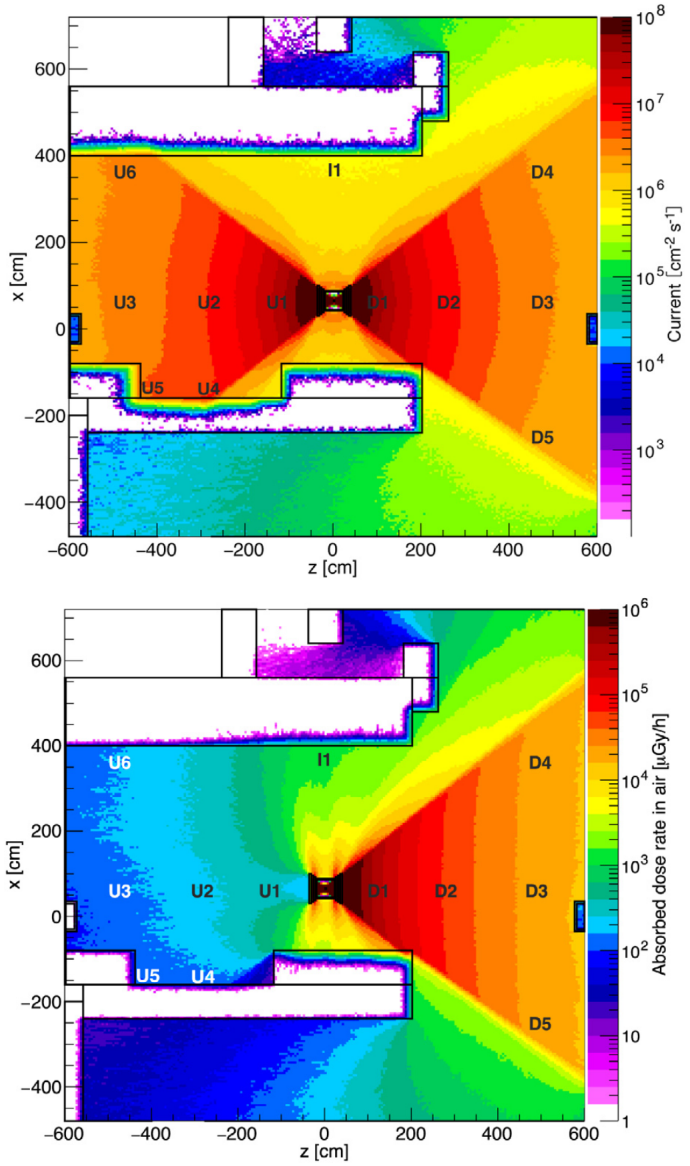

Figure 5.7: Simulated photons current in air in the $x-z$ plane (top), absorbed dose rate in air in the $x-z$ plane with only the downstream side of the source on (bottom). [162].

avoid contamination from plastic materials, was equipped with flow-meters and a pressure monitoring system along the line, to regulate and monitor the gas flow to the detector. The detector was flushed with Ar/CO_2 (70/30), with a flux of 10 ℓ/h.

The detector has been placed in the downstream area of the GIF++

Figure 5.8: GE1/1 μ-RWELL detector for the GIF++ longevity test.

facility, at about 1 m from the source, as shown in Figure 5.10, exposed to a photon flux up to 10^8 Hz/cm^2 (see Figure 5.7). In addition, the environmental parameters like atmospheric pressure, temperature and humidity, within the experimental irradiated area were monitored.

The GE1/1 μ-RWELL detector was operated at a gain of about 1000 for the first two months of irradiation, started at the beginning of April 2017, to understand the behavior of the chamber in this challenging high-radiation environment. Then the gain was raised to 4000 for the actual longevity test, that started in June 2017 and ended in June 2019, for a total of 24 months of irradiation.

5.4.3 Results of the longevity test

Figure 5.11 shows the total integrated charge per unit of detector area as a function of time, for the full irradiation period with gain 4000, together

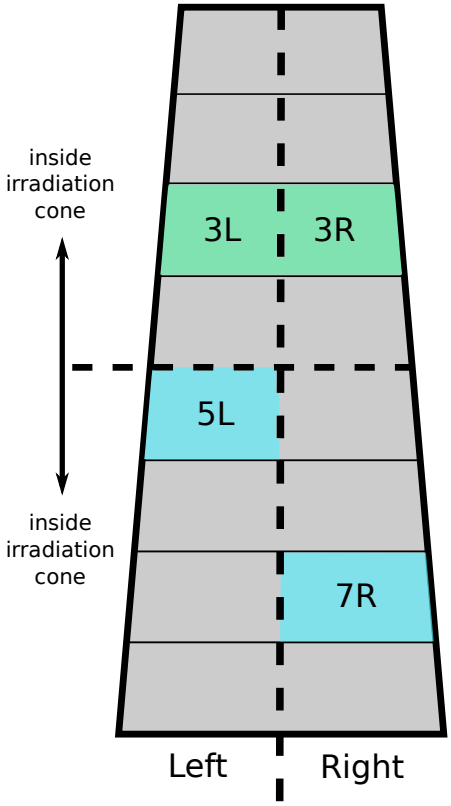

Figure 5.9: Schematic representation of the HV sectors of the GE1/1 μ-RWELL detector for the GIF++ longevity test.

with the charge individually integrated by the cathode, top-left, and top-right planes of the μ-RWELL.

Due to the position of the detector with respect to the source, only sectors 3-left and 3-right were placed inside the irradiation cone, thus integrating charge, while sectors 5-left and 7-right were not irradiated. To correct the total integrated charge for these two sectors, the mean current drawn by the chamber during periods with source switched off has been computed, since it is reasonably equivalent to the current drawn by the two sectors not irradiated with the source on, and then subtracted to the total current. The periods characterized by a flat trend of the integrated charge are due to full months in which the intensity of the source was attenuated to allow measurements for other GIF++ users. The total integrated charge after two years of operations, from the two irradiated sectors, is about 130 mC/cm^2. Comparing the integrated charge at the GIF++, that includes the duty cycle

Figure 5.10: GE1/1 μ-RWELL setup inside the GIF++ facility at ~ 1 m to the source.

of the facility, to the expected integrated charge in the ME0 station after ten years of HL-HLC (283 mC/cm^2), one obtains an acceleration factor of about 2.3. The integrated charge at the GIF++ is then equivalent to a 5-year irradiation period at HL-LHC in the ME0 position.

The normalized total current, and individual contributions from the cathode, top-left and top-right planes of the μ-RWELL, are shown in Figure 5.12 as a function of the integrated charge. Only periods with source on with no attenuation filters have been considered. The currents are normalized to the average current drawn by the detector during the first month of irradiation with chamber at gain 4000, June 2017, when no aging effects could yet be affecting the detector, reported in Table 5.1.

From Figure 5.12 it is clear that even though the current drawn by the top-left plane remains constant for the whole irradiation period, the total current drawn by the top-left and cathode planes suffers a drop of about

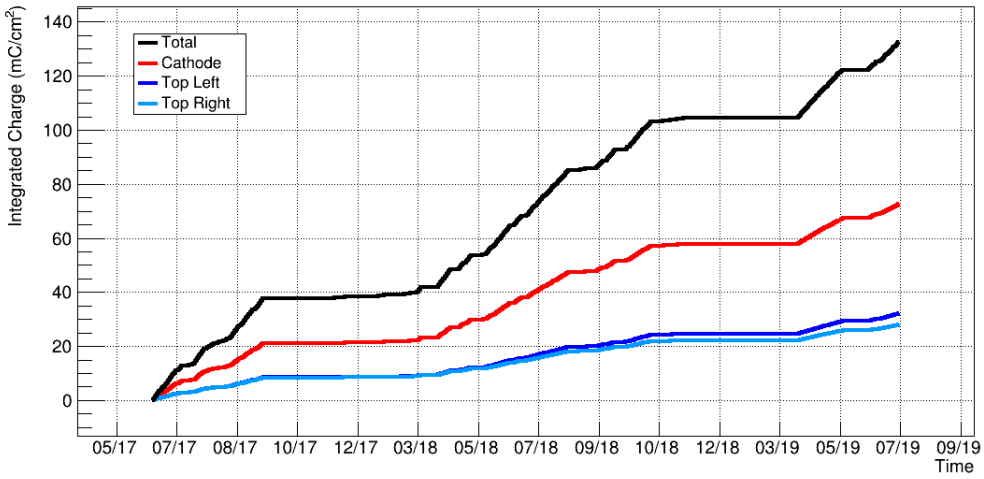

Figure 5.11: Total and individual planes integrated charge per unit of detector area as a function of time; the flat regions correspond to periods of time during which the source was switched off or strongly attenuated.

	Mean current (nA)
cathode	1010
top-left	400
top-right	400
total	1810

Table 5.1: Mean current drawn by each plane together with the total current drawn by the detector.

20% with respect to the initial irradiation period.

To fully understand this result, further tests and investigations are needed, including a proper visual inspection of the amplification and cathode layer of the detector, that could probably highlight some discrepancies between the top-left and top-right sections. Furthermore, this result is in partial disagreement with the one recently obtained in beam tests with the same technology prototypes performed at the Paul Scherrer Institute (PSI) by the LNF - Detector Development Group (DDG) of Frascati (private communication). During this latter test, two μ-RWELL detectors were tested together with two GEM detectors used as reference, exploiting a π-beam of 270 MeV/c at the PiM1 facility of the PSI. The two μ-RWELL detectors integrated 200 mC/cm^2 and 110 mC/cm^2 (due to the different position with respect to the beam line), during a 8 days irradiation period. During the analysis pro-

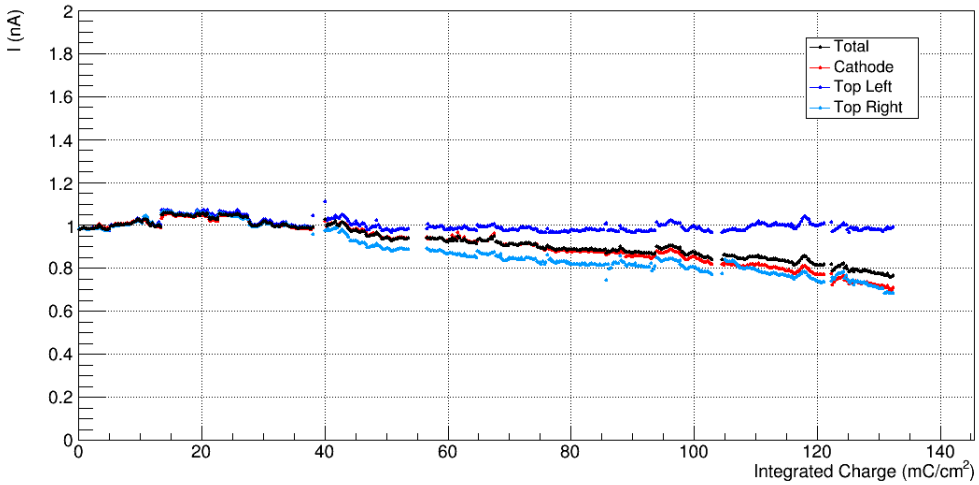

Figure 5.12: Total and individual planes current as a function of the total integrated charge.

cess, the current read out from the μ-RWELL detectors has been corrected for temperature and pressure fluctuations and normalized to the one read out from the GEM detectors, to be insensitive to the beam conditions. After this process, the current of both μ-RWELL detectors under study appears to be stable, with no trends, and with maximum fluctuations of the order of 10%, not compatible with the results obtained during the GIF++ longevity study just described.

5.5 Homogeneity studies on a large surface detector

One of the main purposes of the development of new MPGD detectors, alternative to GEMs and MicroMegas, is the possibility to be able to construct large area detectors with simple building techniques, easily transferable to industry with low costs. It is important to ensure that in large area detectors the response is uniform and the detection efficiency does not depend on the position of the incident particle. For this reason, the largest μ-RWELL ever built was assembled and tested in a beam line facility at CERN to verify the homogeneity of the response across all the surface.

5.5.1 Description of the setup

A large area μ-RWELL detector was realized with the same structure of a CMS 20° GE2/1 detector, a 2×1 m^2 trapezoidal chamber, with the M4 sector equipped with active area and connectors, as reported schematically in Figure 5.13.

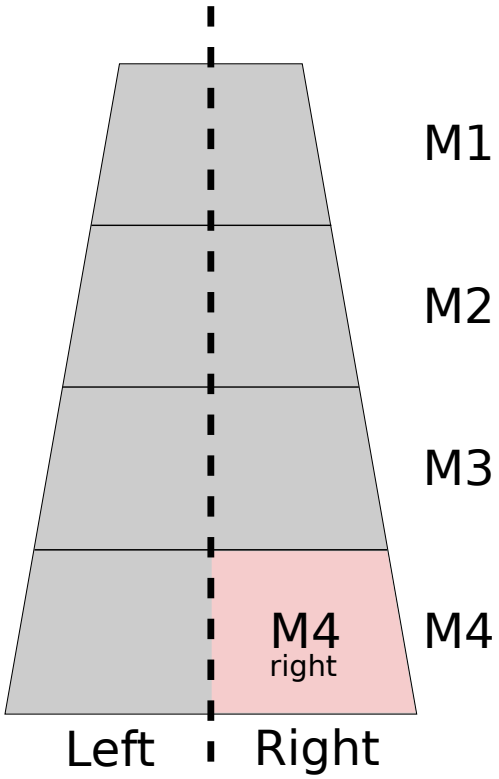

Figure 5.13: CMS GE2/1 M4 sector μ-RWELL scheme.

The detector, with a drift gas gap of about 7 mm, had a single-resistive layer configuration, and was flushed with a Ar/CO_2 (70/30) gas mixture, with a flux of 10 ℓ/h. The test was performed at CERN, exploiting the 150 GeV muon beam of the H4 beam line, in July 2017. To study the homogeneity of the response, the detector was placed along the beam line on a remotely controllable moving platform, in order to allow to scan all the active area across the muon beam, as shown in Figure 5.14. The beam line was also equipped with two plastic scintillators used as trigger, two small 10×10 cm^2 GEM detectors flushed with Ar/CO_2 (70/30) gas mixture, used to reconstruct the track of the muons. Both GEMs and M4 chambers were

connected to the same high-voltage system, with a CAEN module placed inside the experimental area. The acquisition system, used for both GEMs and M4, was based on the Scalable Readout System (SRS), developed by the RD51 Collaboration at CERN [163]. This system, interfaced with APV25 chips, allows to read the analog signals, with a 25 ns sampling [164]. Signals were then digitized by the Frontend Card of the SRS and then processed by the GEM Reconstruction And Analysis Libraries (GRAAL) software, developed in the context of the R&D for the BES III experiment, that has been used to reconstruct raw data from the different detectors [165].

Figure 5.14: GE2/1 μ-RWELL detector on the movable platform in the H4 beam line.

5.5.2 Results of the homogeneity study

Before studying the response across all the surface of the detector, a proper amplification field working point was chosen. To do that, the efficiency with respect to the reference chambers was computed in a fixed position at different amplification voltages: as shown in Figure 5.15, the plateau was reached at 520 V. For this reason, the amplification voltage was set to 530

V, slightly above the starting point of the plateau, and was kept fixed to this value during all the homogeneity test. The detector was moved in the $x - y$ plane, to scan a large portion of the surface in subsequent sets of measurements, as schematically shown in Figure 5.16 where all the tested portions of the M4 are marked. Due to time constraints during the short beam test period, only the M4-right part was equipped with readout electronics and tested.

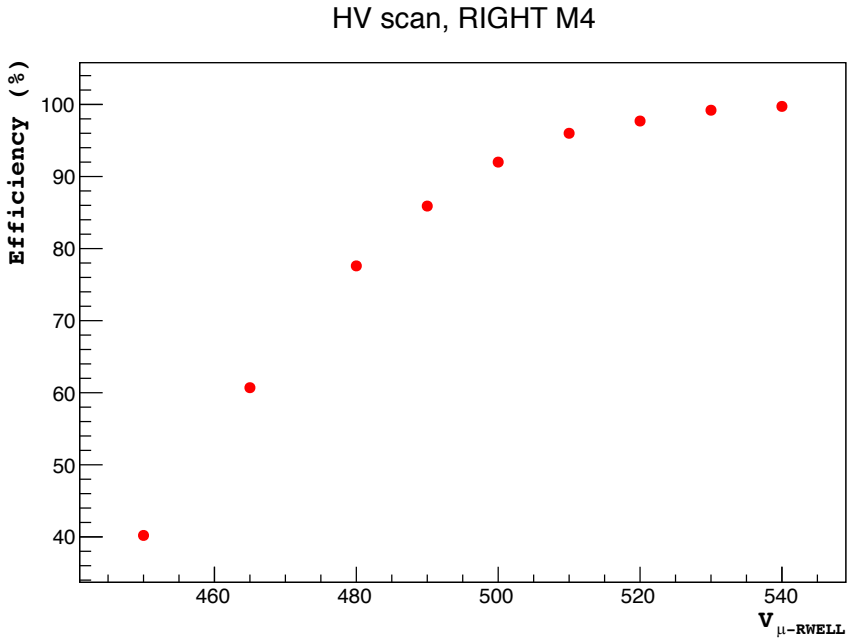

Figure 5.15: Efficiency as a function of the amplification voltage applied to the μ-RWELL-PCB.

Analysis procedure A first rough efficiency measurement can be obtained defining the efficiency of the M4 chamber as the number of triple coincidences between the two tracker GEM detectors and the M4, divided by the double coincidence of the two GEMs. With this definition, the results obtained in the top and bottom regions of the M4-right are reported in Figure 5.17(top) and Figure 5.17(bottom) respectively, as a function of the distance of the measurement from the left edge of the M4-right detector. The efficiency is above 98% in all the positions studied.

However, a more accurate procedure should be used, requiring a match in the muon expected position on the M4-right surface, extrapolated from the two GEM detectors. For this purpose, the M4 detector and the two trackers

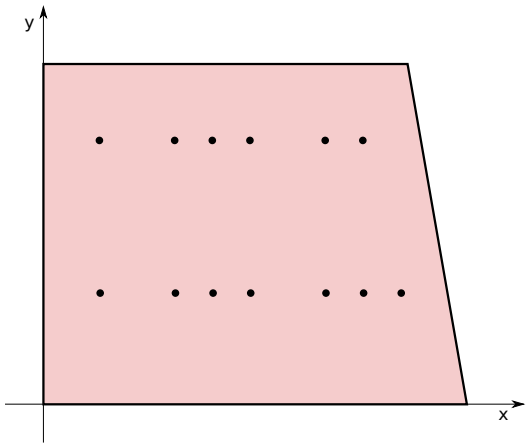

Figure 5.16: Scheme of the tested regions of the M4-right surface: the dots represent the projected center of the muon beam (average radius of 5 cm) on the detector surface in the different positions.

needed to be aligned. Since during the beam test, the position of the M4 chamber was not fixed, an alignment per each tested position was then performed. Events with only one cluster signal in each GEM have been selected, and the residuals distribution of the cluster position in the M4-right chamber with respect to the expected position extrapolated from the two GEMs were studied. The position reconstructed from the M4-right was thus corrected shifting the x or y coordinate by a factor equal to the mean value of the residuals distribution. After the alignment, the computation of the efficiency required the signal in the M4-right chamber to be within a $\pm 3\sigma$ distance in the $x - y$ plane, computed from the correspondent residuals distribution, with respect to the expected position extrapolated from the trackers. The 2D map of the efficiency scan performed on a large portion of the M4-right detector is shown in Figure 5.18, where the white color represents the portion of the surface that had not been tested. Except for a small region, where the efficiency is $\sim 90\%$, the efficiency in all the tested surface is well above 97%.

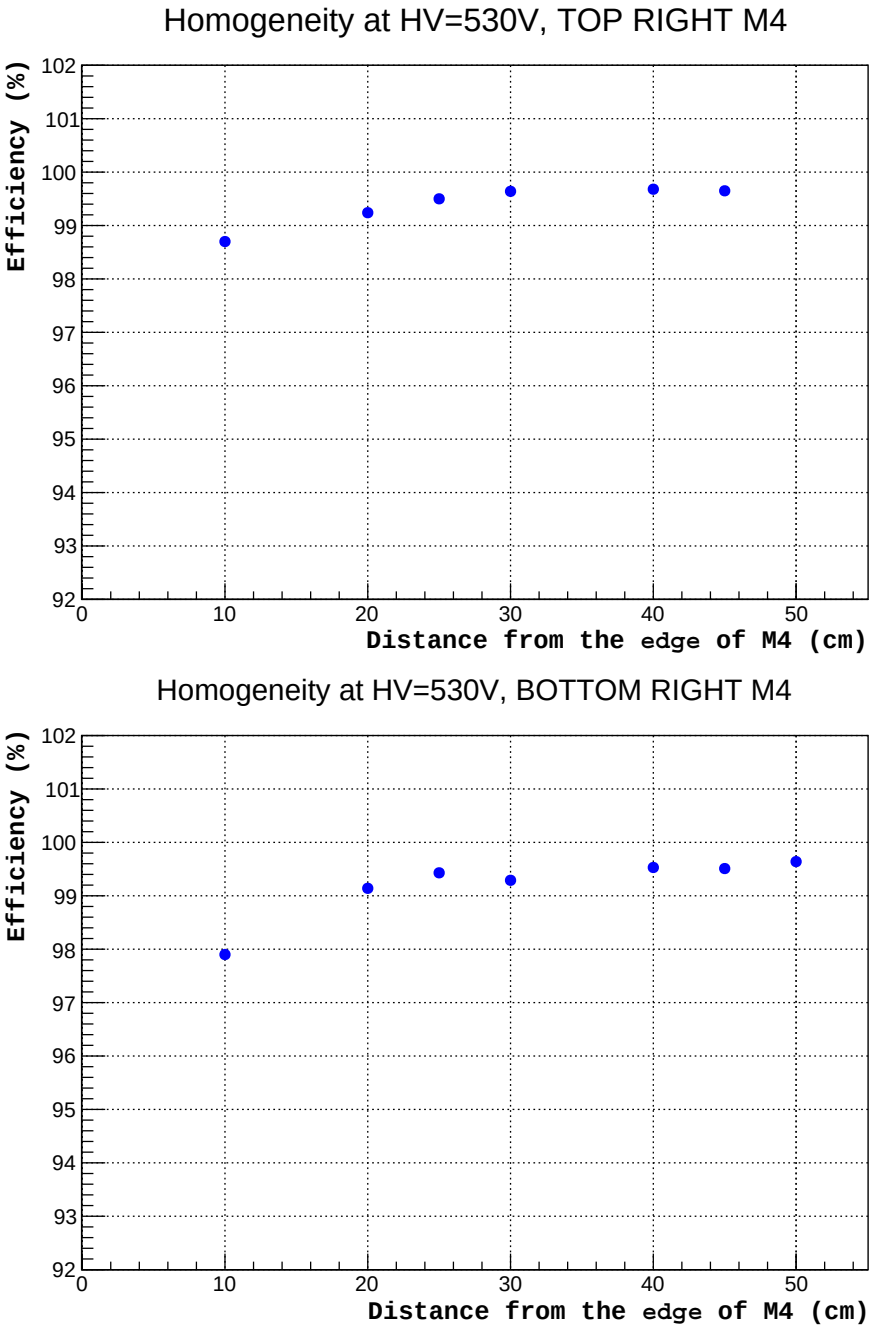

Figure 5.17: First estimation of the efficiency for the top (top), and bottom (bottom) region of the M4-right tested.

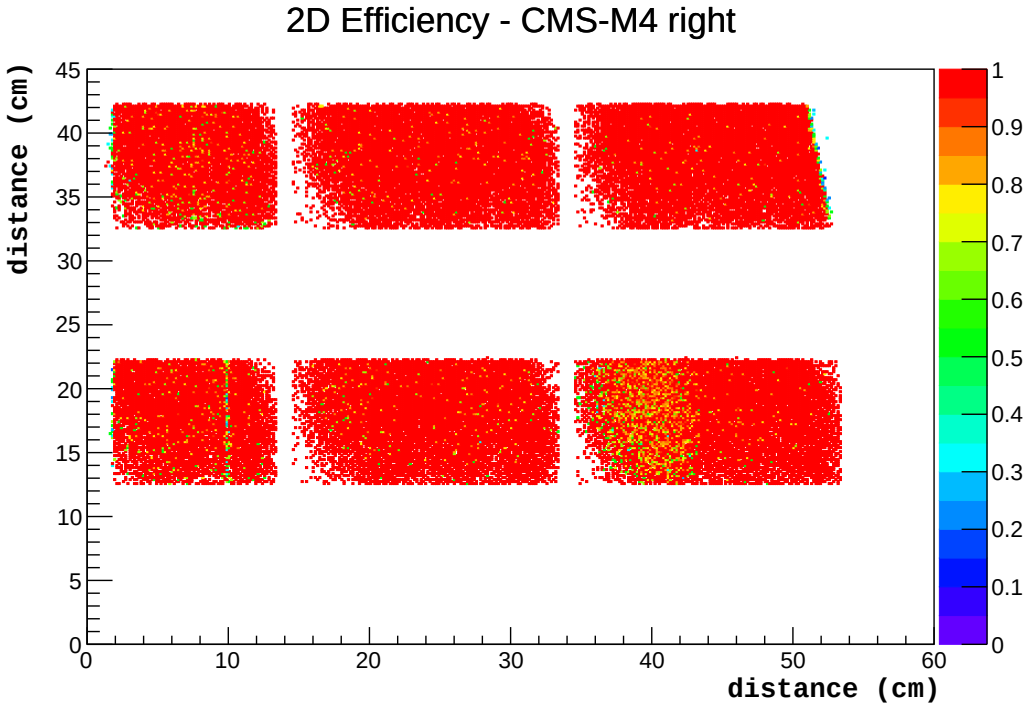

Figure 5.18: Efficiency of the M4-right μ-RWELL detector.

Conclusions and perspectives

The discovery of the Higgs boson marked a milestone in the history of physics, since it completes the standard model (SM) with its last missing piece and opens up the study of its scalar sector. Now it is fundamental to explore and study the Higgs self-interaction processes as a probe of the scalar sector of the SM. To study this type of processes, the HH $\rightarrow$ ZZ(4ℓ)b$\bar{\text{b}}$ final state has been chosen in the context of this thesis, exploiting the rare but clean final state provided by the four isolated leptons, and taking advantage of the high branching fraction of the b$\bar{\text{b}}$ decay. Beyond the standard model (BSM) physics processes, such as the presence of new resonances or anomalous couplings, would alter the double Higgs production (HH) cross section and self-coupling λ_{HHH}, directly accessible with HH searches. To give a unique overview of the capabilities of the chosen decay channel, the analysis has been conducted in different experimental scenarios. The limit on the signal strength μ obtained with the data collected by the CMS experiment at a center-of-mass energy of 13 TeV during 2018, has been set to about 230 times the SM. Performing the study exploiting the simulation of the CMS upgrade detector foreseen for the High Luminosity phase of LHC (HL-LHC), one obtains a limit of 6.5 times the SM predictions. Going to the possible subsequent High Energy scenario (HE-LHC), with a center-of-mass energy of 27 TeV, this limit improves further, to 1.5 times the SM. Finally, thanks to the increased statistics and larger signal cross section, the study performed in a future high energy hadron circular collider (FCC-hh) has led to the measurement of the HH cross section with a precision of 17%. The combination of the results obtained in the HL-LHC scenario with the ones obtained in other four decay channels has set to a limit of 0.77 times the SM cross section and a combined significance of 2.6 σ, assuming a HH signal with the properties predicted by the SM. Furthermore, the perspective on the Higgs self-coupling has allowed to put stringent boundaries on the value of the self-coupling modifier, up to a precision of 24% on its value at FCC-hh.

The unprecedented experimental conditions of the new scenarios justify the need for upgrades to the existing detectors, and the design and construc-

tion of future accelerators. A very promising technology useful to build large area detectors for new experiments is the μ-RWELL detector. The test conducted on a μ-RWELL prototype to verify the behavior of the detector in a high radiation environment is still ongoing to fully understand the results obtained. The homogeneity test on a large area μ-RWELL prototype, to verify the feasibility and robustness of large surface detectors realized with this technology, without compromising the excellent performances, resulted in a uniform detection efficiency higher than 97%.

This thesis is the conclusion of a three-year study, and gives a unique overview of the potentiality of the $HH \to ZZ(4\ell)b\bar{b}$ channel in many different experimental scenarios. In the future, these results will be further improved: the $HH \to ZZ(4\ell)b\bar{b}$ channel will be combined with other $4\ell + X$ final states, thus including $4\ell WW$, $4\ell\gamma\gamma$ and $4\ell\tau\tau$ decay channels, and performed on the full Run 2 dataset, to increase the sensitivity of the measurement. All the studies on HH processes will be subsequently performed on the data that will be collected during Run 3 and the HL-LHC era, and will certainly allow to clarify many open questions related to the SM and to its possible BSM extensions, keeping the double Higgs production at the forefront of the CMS and future experiments physics program.

Bibliography

[1] Halzen, F., and Martin, A. D., Quarks and Leptons: An Introductory course in Modern Particle Physics. *John Wiley and Sons* (1984).

[2] Perkins, D. H., Introduction to High Energy Physics. *Cambridge Univ. Press* (2000).

[3] Griffiths, D., Introduction to Elementary Particles. *John Wiley and Sons* (1987).

[4] Particle Data Group, Review of particle physics. *Phys. Rev. D 98* (Aug 2018), 030001. doi:10.1103/PhysRevD.98.030001.

[5] Glashow, S. L., Partial Symmetries of Weak Interactions. *Nucl. Phys. 22* (1961), 579–588. doi:10.1016/0029-5582(61)90469-2.

[6] Weinberg, S., A Model of Leptons. *Phys. Rev. Lett. 19* (1967), 1264–1266. doi:10.1103/PhysRevLett.19.1264.

[7] Salam, A., Weak and Electromagnetic Interactions. *Conf. Proc. C680519* (1968), 367–377.

[8] Englert, F., and Brout, R., Broken Symmetry and the Mass of Gauge Vector Mesons. *Phys. Rev. Lett. 13* (1964), 321–323. doi:10.1103/PhysRevLett.13.321.

[9] Higgs, P. W., Broken Symmetries and the Masses of Gauge Bosons. *Phys. Rev. Lett. 13* (1964), 508–509. doi:10.1103/PhysRevLett.13.508.

[10] Guralnik, G. S., Hagen, C. R., and Kibble, T. W. B., Global Conservation Laws and Massless Particles. *Phys. Rev. Lett. 13* (1964), 585–587. doi:10.1103/PhysRevLett.13.585.

[11] Kibble, T. W. B., Symmetry breaking in non Abelian gauge theories. *Phys. Rev. 155* (1967), 1554–1561. doi:10.1103/PhysRev.155.1554.

[12] 't Hooft, G., Renormalizable Lagrangians for Massive Yang-Mills Fields. *Nucl. Phys. B35* (1971), 167–188. doi:10.1016/0550-3213(71)90139-8.

[13] Graham, R., and Tél, T., Potential for the complex ginzburg-landau equation. *Europhysics Letters (EPL) 13*, 8 (dec 1990), 715–720. doi:10.1209/0295-5075/13/8/008.

[14] Goldstone, J., Field Theories with Superconductor Solutions. *Nuovo Cim. 19* (1961), 154–164. doi:10.1007/BF02812722.

[15] LEP Working Group for Higgs boson searches, ALEPH, DELPHI, L3, OPAL, Search for the standard model Higgs boson at LEP. *Phys. Lett. B565* (2003), 61–75. doi:10.1016/S0370-2693(03)00614-2, arXiv:hep-ex/0306033.

[16] Aaltonen, T., et al. Combined CDF and D0 Upper Limits on Standard Model Higgs Boson Production with up to 8.2 fb^{-1} of Data. In *Proceedings, 46th Rencontres de Moriond on Electroweak Interactions and Unified Theories: La Thuile, Italy, March 13-20, 2011* (2011). arXiv:1103.3233.

[17] The ATLAS Collaboration, Observation of a new particle in the search for the Standard Model Higgs boson with the ATLAS detector at the LHC. *Phys. Lett. B716* (2012), 1–29. doi:10.1016/j.physletb.2012.08.020, arXiv:1207.7214.

[18] The CMS Collaboration, Observation of a New Boson at a Mass of 125 GeV with the CMS Experiment at the LHC. *Phys. Lett. B716* (2012), 30–61. doi:10.1016/j.physletb.2012.08.021, arXiv:1207.7235.

[19] Baglio, J., and Djouadi, A., Higgs production at the LHC. *JHEP 03* (2011), 055. doi:10.1007/JHEP03(2011)055, arXiv:1012.0530.

[20] LHC Higgs Cross Section Working Group, Handbook of LHC Higgs Cross Sections: 4. Deciphering the Nature of the Higgs Sector. doi:10.23731/CYRM-2017-002, arXiv:1610.07922.

[21] LHC Higgs Cross Section Working Group, Handbook of LHC Higgs Cross Sections: 2. Differential Distributions. *CERN Yellow Reports: Monographs* (2012). doi:10.5170/CERN-2012-002, arXiv:1201.3084.

[22] The ATLAS Collaboration, Combined search for the Standard Model Higgs boson in pp collisions at $\sqrt{s}$=7 TeV with the

ATLAS detector. *Phys. Rev. D 86* (Aug 2012), 032003. doi:10.1103/PhysRevD.86.032003.

[23] The ATLAS Collaboration and The CMS Collaboration, Combined Measurement of the Higgs Boson Mass in *pp* Collisions at $\sqrt{s}$ = 7 and 8 TeV with the ATLAS and CMS Experiments. *Phys. Rev. Lett. 114* (2015), 191803. doi:10.1103/PhysRevLett.114.191803, arXiv:1503.07589.

[24] The CMS Collaboration, Study of the mass and spin-parity of the Higgs boson candidate via its decays to Z boson pairs. *Phys. Rev. Lett. 110*, 8 (2013), 081803. doi:10.1103/PhysRevLett.110.081803, arXiv:1212.6639.

[25] The CMS Collaboration, Precise determination of the mass of the Higgs boson and tests of compatibility of its couplings with the standard model predictions using proton collisions at 7 and 8 TeV. *Eur. Phys. J. C75*, 5 (2015), 212. doi:10.1140/epjc/s10052-015-3351-7, arXiv:1412.8662.

[26] Aad, G., Abbott, B., Abdallah, J., Abdinov, O., and Aben, R., Measurements of the Higgs boson production and decay rates and coupling strengths using pp collision data at $\sqrt{s} = 7$ and 8 TeV in the ATLAS experiment. *The European Physical Journal C 76*, 1 (Jan 2016), 6.

[27] The ATLAS Collaboration and The CMS Collaboration, Measurements of the Higgs boson production and decay rates and constraints on its couplings from a combined ATLAS and CMS analysis of the LHC pp collision data at $\sqrt{s} = 7$ and 8 TeV. *JHEP 08* (2016), 045. doi:10.1007/JHEP08(2016)045, arXiv:1606.02266.

[28] The ATLAS Collaboration, Observation of $H \to b\bar{b}$ decays and VH production with the ATLAS detector. *Phys. Lett. B786* (2018), 59–86. doi:10.1016/j.physletb.2018.09.013, arXiv:1808.08238.

[29] The ATLAS Collaboration, Observation of Higgs boson production in association with a top quark pair at the LHC with the ATLAS detector. *Phys. Lett. B784* (2018), 173–191. doi:10.1016/j.physletb.2018.07.035, arXiv:1806.00425.

[30] The CMS Collaboration, Observation of $t\bar{t}H$ production. *Phys. Rev. Lett. 120*, 23 (2018), 231801. doi:10.1103/PhysRevLett.120.231801, arXiv:1804.02610.

[31] The CMS Collaboration, Observation of Higgs boson decay to bottom quarks. *Phys. Rev. Lett. 121*, 12 (2018), 121801. doi:10.1103/PhysRevLett.121.121801, arXiv:1808.08242.

[32] The ATLAS Collaboration, Cross-section measurements of the Higgs boson decaying into a pair of τ-leptons in proton-proton collisions at $\sqrt{s} = 13$ TeV with the ATLAS detector. *Phys. Rev. D99* (2019), 072001. doi:10.1103/PhysRevD.99.072001, arXiv:1811.08856.

[33] The CMS Collaboration, Observation of the Higgs boson decay to a pair of τ leptons with the CMS detector. *Phys. Lett. B779* (2018), 283–316. doi:10.1016/j.physletb.2018.02.004, arXiv:1708.00373.

[34] The ATLAS Collaboration. Combined measurements of Higgs boson production and decay using up to 80 fb^{-1} of proton-proton collision data at $\sqrt{s} = 13$ TeV collected with the ATLAS experiment. Tech. Rep. ATLAS-CONF-2018-031, CERN, Geneva, Jul 2018. http://cds.cern.ch/record/2629412.

[35] The CMS Collaboration, Combined measurements of Higgs boson couplings in proton-proton collisions at $\sqrt{s} = 13\,\text{TeV}$. *Eur. Phys. J. C79*, 5 (2019), 421. doi:10.1140/epjc/s10052-019-6909-y, arXiv:1809.10733.

[36] Di Vita, S., Grojean, C., Panico, G., Riembau, M., and Vantalon, T., A global view on the Higgs self-coupling. *JHEP 09* (2017), 069. doi:10.1007/JHEP09(2017)069, arXiv:1704.01953.

[37] Baglio, J., Djouadi, A., Gröber, R., Mühlleitner, M. M., Quevillon, J., and Spira, M., The measurement of the Higgs self-coupling at the LHC: theoretical status. *JHEP 04* (2013), 151. doi:10.1007/JHEP04(2013)151, arXiv:1212.5581.

[38] Frederix, R., Frixione, S., Hirschi, V., Maltoni, F., Mattelaer, O., Torrielli, P., Vryonidou, E., and Zaro, M., Higgs pair production at the LHC with NLO and parton-shower effects. *Phys. Lett. B732* (2014), 142–149. doi:10.1016/j.physletb.2014.03.026, arXiv:1401.7340.

[39] Randall, L., and Sundrum, R., A Large mass hierarchy from a small extra dimension. *Phys. Rev. Lett. 83* (1999), 3370–3373. doi:10.1103/PhysRevLett.83.3370, arXiv:hep-ph/9905221.

[40] Oliveira, A., Gravity particles from Warped Extra Dimensions, predictions for LHC. arXiv:1404.0102.

[41] Barger, V., and Ishida, M., Randall-Sundrum Reality at the LHC. *Phys. Lett. B709* (2012), 185–191. doi:10.1016/j.physletb.2012.01.073, arXiv:1110.6452.

[42] Schabinger, R. M., and Wells, J. D., A Minimal spontaneously broken hidden sector and its impact on Higgs boson physics at the large hadron collider. *Phys. Rev. D72* (2005), 093007. doi:10.1103/PhysRevD.72.093007, arXiv:hep-ph/0509209.

[43] Dawson, S., and Lewis, I. M., NLO corrections to double Higgs boson production in the Higgs singlet model. *Phys. Rev. D92*, 9 (2015), 094023. doi:10.1103/PhysRevD.92.094023, arXiv:1508.05397.

[44] Branco, G. C., Ferreira, P. M., Lavoura, L., Rebelo, M. N., Sher, M., and Silva, J. P., Theory and phenomenology of two-Higgs-doublet models. *Phys. Rept. 516* (2012), 1–102. doi:10.1016/j.physrep.2012.02.002, arXiv:1106.0034.

[45] Djouadi, A., Maiani, L., Moreau, G., Polosa, A., Quevillon, J., and Riquer, V., The post-Higgs MSSM scenario: habemus MSSM? *European Physical Journal C 73* (11 2013), 2650. doi:10.1140/epjc/s10052-013-2650-0.

[46] Efrati, A., and Nir, Y., What if $\lambda_{hhh} \neq 3m_h^2/v$. arXiv:1401.0935.

[47] Goertz, F., Papaefstathiou, A., Yang, L. L., and Zurita, J., Higgs boson pair production in the D=6 extension of the SM. *JHEP 04* (2015), 167. doi:10.1007/JHEP04(2015)167, arXiv:1410.3471.

[48] Carvalho, A., Dall'Osso, M., De Castro Manzano, P., Dorigo, T., Goertz, F., Gouzevich, M., and Tosi, M., Analytical parametrization and shape classification of anomalous HH production in the EFT approach. arXiv:1608.06578.

[49] Carvalho, A., Dall'Osso, M., Dorigo, T., Goertz, F., Gottardo, C. A., and Tosi, M., Higgs Pair Production: Choosing Benchmarks With Cluster Analysis. *JHEP 04* (2016), 126. doi:10.1007/JHEP04(2016)126, arXiv:1507.02245.

[50] The ATLAS Collaboration, Combination of searches for Higgs boson pairs in pp collisions at $\sqrt{s}$ =13 TeV with the ATLAS detector. arXiv:1906.02025.

[51] The CMS Collaboration, Combination of searches for Higgs boson pair production in proton-proton collisions at $\sqrt{s} = 13$ TeV. *Phys. Rev. Lett. 122*, 12 (2019), 121803. doi:10.1103/PhysRevLett.122.121803, arXiv:1811.09689.

[52] Baconnier, Y., Brianti, G., Lebrun, P., Mathewson, A. G., Perin, R., and Baconnier, Y. LHC: the Large Hadron Collider accelerator project. Tech. rep., CERN, Geneva, 1993. https://cds.cern.ch/record/257706.

[53] LHC Study Group. The Large Hadron Collider: conceptual design. Tech. Rep. CERN-AC-95-05-LHC, CERN, Oct 1995. https://cds.cern.ch/record/291782.

[54] Mobs, E. The CERN accelerator complex. Complexe des accélérateurs du CERN. Tech. Rep. OPEN-PHO-ACCEL-2016-009, CERN, Jul 2016. https://cds.cern.ch/record/2197559.

[55] Evans, L., and Bryant, P., LHC Machine. *JINST 3* (2008), S08001. doi:10.1088/1748-0221/3/08/S08001.

[56] Apollinari, G., Béjar Alonso, I., Brüning, O., Lamont, M., and Rossi, L., High-Luminosity Large Hadron Collider (HL-LHC): Preliminary Design Report. *CERN Yellow Reports: Monographs* (2015). doi:10.5170/CERN-2015-005.

[57] Apollinari, G., Béjar Alonso, I., Brüning, O., Fessia, P., Lamont, M., Rossi, L., and Tavian, L., High-Luminosity Large Hadron Collider (HL-LHC): Technical Design Report V. 0.1. *CERN Yellow Reports: Monographs* (2017). doi:10.23731/CYRM-2017-004.

[58] Zimmermann, F., et al., High-Energy LHC Design. 022009. doi:10.1088/1742-6596/1067/2/022009.

[59] Abada, A., Abbrescia, M., and AbdusSalam, S. S., HE-LHC: The High-Energy Large Hadron Collider. *The European Physical Journal Special Topics 228*, 5 (Jul 2019), 1109–1382. doi:10.1140/epjst/e2019-900088-6.

[60] The CMS Collaboration, The CMS Experiment at the CERN LHC. *JINST 3* (2008), S08004. doi:10.1088/1748-0221/3/08/S08004.

[61] The CMS Collaboration. CMS, Tracker Technical Design Report. Tech. Rep. CERN-LHCC-98-06, CMS-TDR-5, 1998. http://weblib.cern.ch/abstract?CERN-LHCC-98-6.

[62] Dominguez, A., et al. CMS Technical Design Report for the Pixel Detector Upgrade. Tech. Rep. CERN-LHCC-2012-016. CMS-TDR-11, Sep 2012. https://cds.cern.ch/record/1481838.

[63] The CMS Collaboration. The CMS electromagnetic calorimeter project: Technical Design Report. Tech. Rep. CERN-LHCC-97-033, Geneva, 1997. https://cds.cern.ch/record/349375.

[64] The CMS Collaboration. The CMS hadron calorimeter project: Technical Design Report. Tech. Rep. CERN-LHCC-97-031, Geneva, 1997. https://cds.cern.ch/record/357153.

[65] The CMS Collaboration. The CMS magnet project: Technical Design Report. Tech. Rep. CERN-LHCC-97-010, Geneva, 1997. https://cds.cern.ch/record/331056.

[66] The CMS Collaboration. The CMS muon project: Technical Design Report. Tech. Rep. CERN-LHCC-97-032, Geneva, 1997. https://cds.cern.ch/record/343814.

[67] Gasparini, F., et al., Bunch crossing identification at LHC using a mean-timer technique. *Nucl. Instrum. Meth. A336*, 1 (1993), 91 – 97. doi:10.1016/0168-9002(93)91082-X.

[68] The CMS Collaboration. CMS TriDAS project: Technical Design Report, Volume 1: The Trigger Systems. Tech. Rep. CERN-LHCC-2000-038, 2000. https://cds.cern.ch/record/706847.

[69] The CMS Collaboration. CMS: The TriDAS project. Technical design report, Vol. 2: Data acquisition and high-level trigger. Tech. Rep. CERN-LHCC-2002-026, 2002.

[70] The CMS Collaboration, Particle-flow reconstruction and global event description with the CMS detector. *JINST 12*, 10 (2017), P10003. doi:10.1088/1748-0221/12/10/P10003, arXiv:1706.04965.

[71] Billoir, P., Progressive track recognition with a kalman-like fitting procedure. *Computer Physics Communications 57*, 1 (1989), 390 – 394. doi:10.1016/0010-4655(89)90249-X.

[72] The CMS Collaboration, Description and performance of track and primary-vertex reconstruction with the CMS tracker. *JINST 9*, 10 (2014), P10009. doi:10.1088/1748-0221/9/10/P10009, arXiv:1405.6569.

[73] The CMS Collaboration, Performance of CMS Muon Reconstruction in pp Collision Events at $\sqrt{s} = 7$ TeV. *JINST 7* (2012), P10002. doi:10.1088/1748-0221/7/10/P10002, arXiv:1206.4071.

[74] Baffioni, S., Charlot, C., Ferri, F., Futyan, D., Meridiani, P., Puljak, I., Rovelli, C., Salerno, R., and Sirois, Y. Electron reconstruction in CMS. Tech. Rep. CMS-NOTE-2006-040, CERN, Geneva, Feb 2006. https://cds.cern.ch/record/934070.

[75] The CMS Collaboration, Performance of electron reconstruction and selection with the CMS detector in proton-proton collisions at $\sqrt{s} = 8$ TeV. *JINST 10*, 06 (2015), P06005. doi:10.1088/1748-0221/10/06/P06005, arXiv:1502.02701.

[76] Kottakki, K. K., Bhushan, M., and Bhartiya, S., Monte Carlo gaussian sum filter for state estimation of nonlinear dynamical systems. *IFAC-PapersOnLine 49*, 1 (2016), 65 – 70. doi:https://doi.org/10.1016/j.ifacol.2016.03.030.

[77] The CMS Collaboration, Performance of Jet reconstruction in CMS at 13 TeV. *PoS ICHEP2016* (2016), 736. doi:10.22323/1.282.0736.

[78] Cacciari, M., Salam, G. P., and Soyez, G., FastJet User Manual. *Eur. Phys. J. C72* (2012), 1896. doi:10.1140/epjc/s10052-012-1896-2, arXiv:1111.6097.

[79] Cacciari, M., Salam, G. P., and Soyez, G., The anti-k_t jet clustering algorithm. *JHEP 04* (2008), 063. doi:10.1088/1126-6708/2008/04/063, arXiv:0802.1189.

[80] The CMS Collaboration, Determination of jet energy calibration and transverse momentum resolution in CMS. *JINST 6*, 11 (Nov 2011), 11002. doi:10.1088/1748-0221/6/11/P11002, arXiv:1107.4277.

[81] Contardo, D., Klute, M., Mans, J., Silvestris, L., and Butler, J. Technical Proposal for the Phase-II Upgrade of the CMS Detector. Tech. Rep. CERN-LHCC-2015-010. LHCC-P-008. CMS-TDR-15-02, Geneva, Jun 2015. https://cds.cern.ch/record/2020886.

[82] The CMS Collaboration. The Phase-2 Upgrade of the CMS L1 Trigger Interim Technical Design Report. Tech. Rep. CERN-LHCC-2017-013. CMS-TDR-017, CERN, Geneva, Sep 2017. https://cds.cern.ch/record/2283192.

[83] The CMS Collaboration. The Phase-2 Upgrade of the CMS Tracker. Tech. Rep. CERN-LHCC-2017-009. CMS-TDR-014, CERN, Geneva, Jun 2017. https://cds.cern.ch/record/2272264.

[84] The CMS Collaboration. The Phase-2 Upgrade of the CMS Barrel Calorimeters. Tech. Rep. CERN-LHCC-2017-011. CMS-TDR-015, CERN, Geneva, Sep 2017. https://cds.cern.ch/record/2283187.

[85] The CMS Collaboration. The Phase-2 Upgrade of the CMS Endcap Calorimeter. Tech. Rep. CERN-LHCC-2017-023. CMS-TDR-019, CERN, Geneva, Nov 2017. https://cds.cern.ch/record/2293646.

[86] Martelli, A. The CMS HGCAL detector for HL-LHC upgrade. In *5th Large Hadron Collider Physics Conference (LHCP 2017) Shanghai, China, May 15-20, 2017* (2017). arXiv:1708.08234.

[87] The CMS Collaboration. The Phase-2 Upgrade of the CMS Muon Detectors. Tech. Rep. CERN-LHCC-2017-012. CMS-TDR-016, CERN, Geneva, Sep 2017. https://cds.cern.ch/record/2283189.

[88] Colaleo, A., Safonov, A., Sharma, A., and Tytgat, M. CMS Technical Design Report for the Muon Endcap GEM Upgrade. Tech. Rep. CERN-LHCC-2015-012. CMS-TDR-013, CERN, Jun 2015. https://cds.cern.ch/record/2021453.

[89] Sauli, F., GEM: A new concept for electron amplification in gas detectors. *Nucl. Instrum. Meth. A386*, 2 (1997), 531 – 534. doi:https://doi.org/10.1016/S0168-9002(96)01172-2.

[90] Bouclier, R., Dominik, W., Hoch, M., Labbe, J. C., Million, G., Ropelewski, L., Sauli, F., Sharma, A., and Manzin, G., New observations with the gas electron multiplier (GEM). *Nucl. Instrum. Meth. A396* (1997), 50–66. doi:10.1016/S0168-9002(97)00648-7.

[91] Sauli, F., The gas electron multiplier (GEM): Operating principles and applications. *Nucl. Instrum. Meth. A805* (2016), 2–24. doi:10.1016/j.nima.2015.07.060.

[92] The CMS Collaboration. Technical proposal for a mip timing detector in the CMS experiment Phase 2 upgrade. Tech. Rep. CERN-LHCC-2017-027. LHCC-P-009, CERN, Geneva, Dec 2017. https://cds.cern.ch/record/2296612.

[93] Abada, A., Abbrescia, M., and AbdusSalam, S. S., FCC Physics Opportunities. *The European Physical Journal C 79*, 6 (Jun 2019), 474. doi:10.1140/epjc/s10052-019-6904-3.

[94] Abada, A., Abbrescia, M., and AbdusSalam, S. S., FCC-ee: The Lepton Collider. *The European Physical Journal Special Topics 228*, 2 (Jun 2019), 261–623. doi:10.1140/epjst/e2019-900045-4.

[95] Abada, A., Abbrescia, M., and AbdusSalam, S. S., FCC-hh: The Hadron Collider. *The European Physical Journal Special Topics 228*, 2 (Jun 2019), 755–1107. doi:10.1140/epjst/e2019-900045-4.

[96] Alwall, J., Frederix, R., Frixione, S., Hirschi, V., Maltoni, F., Mattelaer, O., Shao, H. S., Stelzer, T., Torrielli, P., and Zaro, M., The automated computation of tree-level and next-to-leading order differential cross sections, and their matching to parton shower simulations. *JHEP 07* (2014), 079. doi:10.1007/JHEP07(2014)079, arXiv:1405.0301.

[97] Alioli, S., Nason, P., Oleari, C., and Re, E., NLO vector-boson production matched with shower in POWHEG. *JHEP 07* (2008), 060. doi:10.1088/1126-6708/2008/07/060, arXiv:0805.4802.

[98] Frixione, S., Nason, P., and Oleari, C., Matching NLO QCD computations with Parton Shower simulations: the POWHEG method. *JHEP 11* (2007), 070. doi:10.1088/1126-6708/2007/11/070, arXiv:0709.2092.

[99] Sjoostrand, T., Ask, S., Christiansen, J. R., Corke, R., Desai, N., Ilten, P., Mrenna, S., Prestel, S., Rasmussen, C. O., and Skands, P. Z., An Introduction to Pythia 8.2. *Comput. Phys. Commun. 191* (2015), 159–177. doi:10.1016/j.cpc.2015.01.024, arXiv:1410.3012.

[100] Agostinelli, S., et al., GEANT4: A Simulation toolkit. *Nucl. Instrum. Meth. A506* (2003), 250–303. doi:10.1016/S0168-9002(03)01368-8.

[101] Allison, J., et al., GEANT4 developments and applications. *IEEE Trans. Nucl. Sci. 53* (2006), 270. doi:10.1109/TNS.2006.869826.

[102] Ovyn, S., Rouby, X., and Lemaitre, V., DELPHES, a framework for fast simulation of a generic collider experiment. arXiv:0903.2225.

[103] de Favereau, J., Delaere, C., Demin, P., Giammanco, A., Lemaître, V., Mertens, A., and Selvaggi, M., DELPHES 3, A modular framework for fast simulation of a generic collider experiment. *JHEP 02* (2014), 057. doi:10.1007/JHEP02(2014)057, arXiv:1307.6346.

[104] Brun, R., and Rademakers, F., ROOT - An Object Oriented Data Analysis Framework. *Nucl. Inst. Meth. A389* (1997), 81–86. doi:http://root.cern.ch/.

[105] Bertolini, D., Harris, P., Low, M., and Tran, N., PileUp Per Particle Identification. *JHEP 10* (2014), 059. doi:10.1007/JHEP10(2014)059, arXiv:1407.6013.

[106] Borowka, S., Greiner, N., Heinrich, G., Jones, S. P., Kerner, M., Schlenk, J., Schubert, U., and Zirke, T., Higgs Boson Pair Production in Gluon Fusion at Next-to-Leading Order with Full Top-Quark Mass Dependence. *Phys. Rev. Lett. 117*, 1 (2016), 012001. doi:10.1103/PhysRevLett.117.079901, 10.1103/PhysRevLett.117.012001, arXiv:1604.06447.

[107] Borowka, S., Greiner, N., Heinrich, G., Jones, S. P., Kerner, M., Schlenk, J., and Zirke, T., Full top quark mass dependence in Higgs boson pair production at NLO. *JHEP 10* (2016), 107. doi:10.1007/JHEP10(2016)107, arXiv:1608.04798.

[108] de Florian, D., and Mazzitelli, J., Higgs pair production at next-to-next-to-leading logarithmic accuracy at the LHC. *JHEP 09* (2015), 053. doi:10.1007/JHEP09(2015)053, arXiv:1505.07122.

[109] Degrassi, G., Giardino, P. P., and Gröber, R., On the two-loop virtual QCD corrections to Higgs boson pair production in the Standard Model. *Eur. Phys. J. C76*, 7 (2016), 411. doi:10.1140/epjc/s10052-016-4256-9, arXiv:1603.00385.

[110] The NNPDF Collaboration, Parton distributions for the LHC Run II. *JHEP 04* (2015), 040. doi:10.1007/JHEP04(2015)040, arXiv:1410.8849.

[111] Bagnaschi, E., Degrassi, G., Slavich, P., and Vicini, A., Higgs production via gluon fusion in the POWHEG approach in the SM and in the MSSM. *JHEP 02* (2012), 088. doi:10.1007/JHEP02(2012)088, arXiv:1111.2854.

[112] Nason, P., and Oleari, C., NLO Higgs boson production via vector-boson fusion matched with shower in POWHEG. *JHEP 02* (2010), 037. doi:10.1007/JHEP02(2010)037, arXiv:0911.5299.

[113] Hartanto, H. B., Jager, B., Reina, L., and Wackeroth, D., Higgs boson production in association with top quarks in the POWHEG BOX.

Phys. Rev. D91, 9 (2015), 094003. doi:10.1103/PhysRevD.91.094003, arXiv:1501.04498.

[114] Luisoni, G., Nason, P., Oleari, C., and Tramontano, F., $HW^{\pm}/HZ$ + 0 and 1 jet at NLO with the POWHEG BOX interfaced to GoSam and their merging within MiNLO. *JHEP 10* (2013), 083. doi:10.1007/JHEP10(2013)083, arXiv:1306.2542.

[115] Gao, Y., Gritsan, A. V., Guo, Z., Melnikov, K., Schulze, M., and Tran, N. V., Spin determination of single-produced resonances at hadron colliders. *Phys. Rev. D 81* (2010), 075022. doi:10.1103/PhysRevD.81.075022, arXiv:1001.3396.

[116] Grazzini, M., Kallweit, S., and Rathlev, D., ZZ production at the LHC: fiducial cross sections and distributions in NNLO QCD. *Phys. Lett. B750* (2015), 407–410. doi:10.1016/j.physletb.2015.09.055, arXiv:1507.06257.

[117] Campbell, J. M., and Ellis, R. K., MCFM for the Tevatron and the LHC. *Nucl. Phys. Proc. Suppl. 205* (2010), 10. doi:10.1016/j.nuclphysbps.2010.08.011, arXiv:1007.3492.

[118] Campbell, J. M., Ellis, R. K., and Williams, C., Bounding the Higgs width at the LHC using full analytic results for $gg \to e^-e^+\mu^-\mu^+$. *JHEP 04* (2014), 060. doi:10.1007/JHEP04(2014)060, arXiv:1311.3589.

[119] Bonvini, M., Caola, F., Forte, S., Melnikov, K., and Ridolfi, G., Signal-background interference effects in $gg \to H \to WW$ beyond leading order. *Phys. Rev. D 88* (2013), 034032. doi:10.1103/PhysRevD.88.034032, arXiv:1304.3053.

[120] Catani, S., and Grazzini, M., An NNLO subtraction formalism in hadron collisions and its application to Higgs boson production at the LHC. *Phys. Rev. Lett. 98* (2007), 222002. doi:10.1103/PhysRevLett.98.222002, arXiv:hep-ph/0703012.

[121] Grazzini, M., NNLO predictions for the Higgs boson signal in the H $\to$ WW $\to \ell\nu\ell\nu$ and H $\to$ ZZ $\to 4\ell$ decay channels. *JHEP 02* (2008), 043. doi:10.1088/1126-6708/2008/02/043, arXiv:0801.3232.

[122] Grazzini, M., and Sargsyan, H., Heavy-quark mass effects in Higgs boson production at the LHC. *JHEP 09* (2013), 129. doi:10.1007/JHEP09(2013)129, arXiv:1306.4581.

[123] CMS Collaboration. Measurements of properties of the Higgs boson in the four-lepton final state at $\sqrt{s} = 13$ TeV. Tech. Rep. CMS-PAS-HIG-18-001, CERN, Geneva, 2018. https://cds.cern.ch/record/2621419.

[124] The CMS Collaboration. Measurement of the properties of the Higgs boson in the four-lepton final state at $\sqrt{s} = 13$ TeV. CMS Physics Analysis Note CMS-AN-15-277, 2016.

[125] JetMETPOG. Jet ID for 2018, 2018. CMS Twiki, https://twiki.cern.ch/twiki/bin/view/CMS/JetID13TeVRun2018.

[126] JetMETPOG. Jet PU ID for 2017, 2017. CMS Twiki, https://twiki.cern.ch/twiki/bin/viewauth/CMS/PileupJetID.

[127] BTAGPOG. B-tagging for 2018, 2018. CMS Twiki, https://twiki.cern.ch/twiki/bin/viewauth/CMS/BtagRecommendation102X.

[128] Anderson, I., Bolognesi, S., Caola, F., Gao, Y., Gritsan, A. V., Martin, C. B., Melnikov, K., Schulze, M., Tran, N. V., Whitbeck, A., and Zhou, Y., Constraining anomalous HVV interactions at proton and lepton colliders. *Phys. Rev. D 89* (2014), 035007. doi:10.1103/PhysRevD.89.035007, arXiv:1309.4819.

[129] Bolognesi, S., Gao, Y., Gritsan, A. V., Melnikov, K., Schulze, M., Tran, N. V., and Whitbeck, A., On the spin and parity of a single-produced resonance at the LHC. *Phys. Rev. D 86* (2012), 095031. doi:10.1103/PhysRevD.86.095031, arXiv:1208.4018.

[130] The CMS Collaboration, Constraints on the spin-parity and anomalous HVV couplings of the Higgs boson in proton collisions at 7 and 8 TeV. *Phys. Rev. D92*, 1 (2015), 012004. doi:10.1103/PhysRevD.92.012004, arXiv:1411.3441.

[131] The CMS Collaboration. Prospects for HH measurements at the HL-LHC. Tech. Rep. CMS-PAS-FTR-18-019, 2018.

[132] Contino, R., et al., Physics at a 100 TeV pp collider: Higgs and EW symmetry breaking studies. *CERN Yellow Rep.*, 3 (2017), 255–440. doi:10.23731/CYRM-2017-003.255, arXiv:1606.09408.

[133] ATLAS, CMS, LHC Higgs Combination Group. Procedure for the LHC Higgs boson search combination in summer 2011. Tech. Rep. ATL-PHYS-PUB-2011-011, CMS-NOTE-2011-005, 2011.

[134] Lista, L., Statistical Methods for Data Analysis in Particle Physics. *Lect. Notes Phys. 941* (2017), 1–257. doi:10.1007/978-3-319-62840-0.

[135] Neyman, J., and Pearson, E. S., On the problem of the most efficient tests of statistical hypotheses. *Philosophical Transactions of the Royal Society of London. Series A, Containing Papers of a Mathematical or Physical Character 231* (1933), 289–337.

[136] Wilks, S. S., The Large-Sample Distribution of the likelihood ratio for testing composite hypotheses. *Annals Math. Statist. 9*, 1 (1938), 60–62. doi:10.1214/aoms/1177732360.

[137] Junk, T., Confidence level computation for combining searches with small statistics. *Nucl. Instrum. Meth. A434* (1999), 435–443. doi:10.1016/S0168-9002(99)00498-2, arXiv:hep-ex/9902006.

[138] Read, A. L., Presentation of search results: the CLs technique. *Journal of Physics G: Nuclear and Particle Physics 28*, 10 (sep 2002), 2693–2704. doi:10.1088/0954-3899/28/10/313.

[139] Cowan, G., Cranmer, K., Gross, E., and Vitells, O., Asymptotic formulae for likelihood-based tests of new physics. *Eur. Phys. J. C71* (2011), 1554. doi:10.1140/epjc/s10052-011-1554-0, 10.1140/epjc/s10052-013-2501-z, arXiv:1007.1727.

[140] CEPC Study Group Collaboration, CEPC Conceptual Design Report: Volume 2 - Physics I& Detector. arXiv:1811.10545.

[141] Leo, W. R., Techniques for Nuclear and Particle Physics Experiments: A How to Approach. *Springer-Verlag Berlin Heidelberg* (1987). doi:10.1007/978-3-642-57920-2.

[142] Knoll, G. F., Radiation detection and measurement; 4th ed. *Wiley* (2010).

[143] Malter, L., Thin film field emission. *Phys. Rev. 50* (Jul 1936), 48–58. doi:10.1103/PhysRev.50.48.

[144] Regulation (EU) No 517/2014 of the European Parliament and of the Council of 16 April 2014 on fluorinated greenhouse gases and repealing Regulation (EC) No 842/2006.

[145] Saviano, G., et al., Properties of potential eco-friendly gas replacements for particle detectors in high-energy physics. *JINST 13*, 03 (2018), P03012. doi:10.1088/1748-0221/13/03/P03012, arXiv:1505.00701.

[146] Capeans, M., Guida, R., and Mandelli, B., Strategies for reducing the environmental impact of gaseous detector operation at the CERN LHC experiments. *Nucl. Instrum. Meth. A845* (2017), 253–256. doi:10.1016/j.nima.2016.04.067.

[147] Charpak, G., Bouclier, R., Bressani, T., Favier, J., and Zupancic, C., The use of multiwire proportional counters to select and localize charged particles. *Nucl. Instrum. Meth. 62* (1968), 262–268. doi:10.1016/0029-554X(68)90371-6.

[148] Sauli, F. Principles of operation of multiwire proportional and drift chambers. Tech. Rep. CERN-77-09, 1977.

[149] Oed, A., Position sensitive detector with microstrip anode for electron multiplication with gases. *Nucl. Instrum. Meth. A263* (1988), 351–359. doi:10.1016/0168-9002(88)90970-9.

[150] Sauli, F., and Sharma, A., Micropattern gaseous detectors. *Annual Review of Nuclear and Particle Science 49*, 1 (1999), 341–388. doi:10.1146/annurev.nucl.49.1.341.

[151] Angelini, F., Bellazzini, R., Brez, A., Massai, M., Spandre, G., and Torquati, M., A microstrip gas avalanche chamber with two-dimensional readout. *Nucl. Instrum. Meth. A283*, 3 (1989), 755 – 761. doi:https://doi.org/10.1016/0168-9002(89)91452-6.

[152] Angelini, F., Bellazzini, R., Brez, A., Massai, M., Raffo, R., Spandre, G., and Spezziga, M., Operation of msgcs with gold strips built on surface-treated thin glasses. *Nucl. Instrum. Meth. A382*, 3 (1996), 461 – 469. doi:https://doi.org/10.1016/S0168-9002(96)00767-X.

[153] Bouclier, R., Capeáns, M., Million, G., Ropelewski, L., Sauli, F., Temmel, T., Cooke, R., Donnel, S., Sastri, S., and Sonderer, N., High rate operation of micro-strip gas chambers on diamond-coated glass. *Nucl. Instrum. Meth. A369*, 1 (1996), 328 – 331. doi:https://doi.org/10.1016/0168-9002(95)00812-8.

[154] Giomataris, Y., Rebourgeard, P., Robert, J. P., and Charpak, G., MICROMEGAS: A High granularity position sensitive gaseous detector for high particle flux environments. *Nucl. Instrum. Meth. A376* (1996), 29–35. doi:10.1016/0168-9002(96)00175-1.

[155] Bencivenni, G., De Oliveira, R., Morello, G., and Lener, M. P., The micro-Resistive WELL detector: a compact spark-protected

single amplification-stage MPGD. *JINST 10*, 02 (2015), P02008. doi:10.1088/1748-0221/10/02/P02008, arXiv:1411.2466.

[156] Handbook of particle detection and imaging, vol. 1 and vol.2. *Springer* (2012). doi:10.1007/978-3-642-13271-1.

[157] Ochi, A., Homma, Y., Yamazaki, Y., Yamane, F., Takemoto, T., Kawamoto, T., Kataoka, Y., Masubuchi, T., Kawanishi, Y., and Terao, S. Carbon Sputtering Technology for MPGD detectors. In *Proceedings, 3rd International Conference on Technology and Instrumentation in Particle Physics (TIPP 2014): Amsterdam, Netherlands, June 2-6, 2014* (2014), vol. TIPP2014, p. 351.

[158] Dixit, M. S., and Rankin, A., Simulating the charge dispersion phenomena in micro pattern gas detectors with a resistive anode. *Nucl. Instrum. Meth. A566* (2006), 281–285. doi:10.1016/j.nima.2006.06.050, arXiv:physics/0605121.

[159] Bencivenni, G., De Oliveira, R., Felici, G., Gatta, M., Morello, G., Ochi, A., Lener, M. P., and Tskhadadze, E., Performance of μ-RWELL detector vs resistivity of the resistive stage. *Nucl. Instrum. Meth. A886* (2018), 36–39. doi:10.1016/j.nima.2017.12.037.

[160] Bencivenni, G., De Oliveira, R., Felici, G., Gatta, M., Giovannetti, M., Morello, G., Ochi, A., Poli Lener, M., and Tskhadadze, E., The μ-RWELL layouts for high particle rate. *JINST 14*, 05 (2019), P05014. doi:10.1088/1748-0221/14/05/P05014, arXiv:1903.11017.

[161] Bencivenni, G., et al., The μ-RWELL detector. *JINST 12*, 06 (2017), C06027. doi:10.1088/1748-0221/12/06/C06027.

[162] Pfeiffer, D., Gorine, G., Reithler, H., Biskup, B., Day, A., Fabich, A., Germa, J., Guida, R., Jaekel, M., and Ravotti, F., The radiation field in the Gamma Irradiation Facility GIF++ at CERN. *Nucl. Instrum. Meth. A866* (2017), 91–103. doi:10.1016/j.nima.2017.05.045, arXiv:1611.00299.

[163] Martoiu, S., Muller, H., Tarazona, A., and Toledo, J., Development of the scalable readout system for micro-pattern gas detectors and other applications. *JINST 8*, 03 (mar 2013), C03015–C03015. doi:10.1088/1748-0221/8/03/c03015.

[164] Jones, L. L., French, M. J., Morrissey, Q. R., Neviani, A., Raymond, M., Hall, G., Moreira, P., and Cervelli, G., The APV25 deep submicron readont chip for CMS detectors. doi:10.5170/CERN-1999-009.162.

[165] Farinelli, R., Research and development in cylindrical triple-GEM detector with μTPC readout for the BESIII experiment. *Ferrara University.* (2018). arXiv:1904.06548.

Ringraziamenti

Giunta al termine di questo percorso, vorrei ringraziare tutti quelli che ne hanno fatto parte, e che mi hanno aiutato a raggiungere questo traguardo.

Grazie Sylvie, per avermi dato la possibilità di continuare il mio percorso di formazione già cominciato con te durante la tesi magistrale, e grazie Paolo per avermi messa in contatto con tante realtà e gruppi di lavoro diversi.

Grazie a tutto il gruppo CMS di Bologna, in particolare Fabrizio, Daniele B., Francesca, Gianni e Luigi per il supporto, le indicazioni e il conforto durante tutti questi anni. Grazie ancora Luigi per esserci sempre stato.

Grazie a tutti i miei colleghi di test beam e studio di rivelatori, in particolare Giulio, Riccardo, Gaia, Gianni e Marco, per aver provato ad insegnarmi tutto quello che sanno sui rivelatori, ed aver condiviso con me fatiche e gioie inaspettate.

Grazie a tutti i gruppi di analisi di cui ho avuto il piacere di far parte, in special modo Maria, Roberto, Giacomo e Luca per tutto quello che ho potuto imparare da voi.

Grazie a tutti i colleghi che sono diventati amici, per il tempo, le risate e il bene che mi avete donato: Carlo, Nico, Massi, Maria Teresa, Dima, Ilaria (e Andrea), Ciccio, Alessandra, Angela, Gianfranco, Budda, Manu, Leonardo, Fabio ed Elisa.. grazie! In particolare grazie Leonardo, Fabio ed Elisa perché con voi mi son sentita sempre a casa (#D040bestoffice!), e grazie Manu, ti voglio bene.

Grazie Bruna: la tua amicizia mi ha sempre accompagnato durante i periodi difficili, ma anche più belli, fatti di compartecipazione ai racconti delle nuove esperienze, gioia condivisa e costante affetto. Sono felice di quello che stiamo diventando, e sono sicura che continueremo così!

Grazie Daddi, papà e mamma: siete un punto di riferimento, mi avete sempre supportato e spronato a migliorare, e so che ci sarete sempre. Grazie mamma perché senza di te semplicemente non sarei, tornare nei tuoi abbracci è ormai raro ma insostituibile.

Grazie Giuseppe perché ci sei sempre stato, perché mi capisci e sostieni come nessun altro, perché in questi anni ho potuto condividere con te ogni pensiero, difficoltà e gioia: sei la persona migliore che potessi incontrare su questo cammino.

Infine, sperando di non sembrare presuntuosa, grazie alla mia forza di volontà, che non mi ha mai abbandonata!